Experimental and Numerical Analysis of Flow Mixing in Packed Beds

Dissertation

zur Erlangung des akademischen Grades

Doktoringenieur

(Dr.-Ing.)

vorgelegt von

M.Sc. Ali Mohammed Ridha Al-Khalaf

geb. am 26.02.1964

in Najaf, Irak

genehmigt durch die

Fakultät für Verfahrens- und Systemtechnik

der Otto-von-Guericke-Universität Magdeburg

Gutachter:

Prof. Dr.-Ing. E. Specht, Universität Magdeburg

Prof. Dr.-Ing. D. Thevenin, Universität Magdeburg

Dr.-Ing. Anne Giese, Gas- und Wärme-Institut Essen e.V.

Promotionskolloquium am 20.03.2017

Preface

This dissertation is submitted to Otto von Guericke University Magdeburg for the degree of Doctor of Engineer. The research described herein was conducted under the supervision of Prof. Dr.-Ing. Eckehard Specht between March 2013 and July 2016. To the best of my knowledge, this work is original, except where suitable references are made to previous works. Neither this nor any substantially similar dissertation has been submitted for any degree, diploma or qualification at any other university or institution.

Ali Al-Khalaf
Magdeburg, Germany
July 05, 2016

Acknowledgments

I would like to express my gratitude to my home university, **University of Technology/ Iraq.** Without that, I was not able to work and research here in Germany. Which provides me this golden opportunity to pursue and completing my Doctoral degree.

I would like to express my sincere gratitude to my supervisor **Prof. Dr.-Ing. Eckehard Specht**, for providing me the opportunity to work with him and pursue a doctoral degree, and for his constant advice, encouragement and financial support. His knowledge, experience and patience have benefited me immensely.

Best thank and grateful appreciation to **Prof. Dr.-Ing. habil. Ulrich Krause**, **Prof. Dr.-Ing. Dominique Thevenin**, and **Dr.-Ing. Anne Giese** who accepted to review my thesis.

I whole heartedly thank my research group **Dr. Hermann Woche, Dr.-Ing. Nallathambi**, **Dr.-Ing. Sandaka**, **Abdulkadir**, **Bassem**, **Gaurav**, **Haozhi**, **Jakob**, **Kamyar**, **Nyein Nyein**, **Qayyum**, **Tino** and **Yuan** for their friendship and many happy and enjoyable times. And of course, our sweet and warm-hearted secretary **Christin Hasemann** for helping me to solve the official issues.
The continuous discussions with **Dr. Nabeh Al-durobi** improved the understanding of CFD work among my hall study. He sincerely provided me his valuable suggestion in solve the CFD problems I faced. A special thanks to **Dr. Ralf Praetor** who teach me the professional CFD work at the beginning of my study, my deepest gratitude goes to my loyal friend **Dr.-Ing. Janan Al-Karawi** for the continuous support throughout my living in Magdeburg.

I would like to take this opportunity to express my warm thankfulness to my **Mother**, who gave me all her spirit in order to achieve what I wish. Another big thanks to my wife **Bushra** and children **Jumana**, **Daniah** and **Hussein** without them I could not continue, they charged my heart with more love and affection.
Also I would like to thank all my family members and friends for their unconditional love and support.

Abstract

Shaft kilns are widely used in the production of lime. In RCE-type shaft kilns, fuel is injected through fuel lances in the radial direction. In PFR-type shaft kilns, fuel is injected through lances that extend vertically to the bottom of the preheating zone. The knowledge of the temperature distribution and radial gas mixing plays an important role in designing lime shaft kilns, but these aspects remain poorly understood

This work involves in experimental and numerical studies. In the experimental part, gas measurements through a packed bed are performed in a model of a shaft kiln with dimensions of (624*364*600) mm. This model, named the test box in this study, has two inlets, i.e., one for air and one for N2. Air enters the box from the bottom, and N2 is injected either radially or axially in accordance with the manner of fuel injection in RCE and PFR kilns, respectively. Both structured and unstructured packed beds are considered to be in the test box. Two packing forms, simple cubic (SC) and body-centered cubic (BCC) using 52 mm ceramic spheres, are studied for the structured bed, and two types of small particles (monodispersed 4 mm glass beads and polydispersed 2-6 mm cement clinker) are considered for the unstructured bed.

Three-dimensional computational fluid dynamics (CFD) simulations corresponding to the experimental setup are conducted. Two models are used in the numerical study, i.e., a real particle model (RPM) and a porous media model (PMM). In the RPM, three methods (gap, overlap and bridge) are applied to prevent highly skewed elements near the contact point between (particle–particle, particle–wall). The prediction results of the CFD calculations revealed that the gap method in the RPM yields results that best agree with the experimental data. The bridge method takes longer to produce results.

The results obtained under the PMM, in the case of axial injection, are in a good agreement with the results from both the RPM and experiments. The mixing in the bed is measured under different operating conditions, namely, different measurement heights, injection velocities, volumetric flow rate ratios, flow conditions and injection positions.

Zusammenfassung

Schachtöfen werden für die Herstellung von Kalk verwendet. In RCE-Schachtöfen wird der Brennstoff durch Lanzen in radialer Richtung eingespritzt, während in GGR-Schachtöfen der Brennstoff vertikal am Ende der Vorwärmzone durch Lanzen eingespritzt wird. Die Kenntnis der Temperaturverteilung und der radialen Gasmischung spielt eine wichtige Rolle bei der Entwicklung der Kalkschachtöfen, was jedoch noch nicht genug erforscht ist.

Diese Arbeit beinhaltet sowohl experimentelle als auch numerische Untersuchungen. Im experimentellen Teil werden die Gasmessungen an einem gepackten Bett als Modell des Schachtofens mit Abmessungen von (624 * 364 * 600) mm durchgeführt. Dieses Modell, welches als Testbox in dieser Studie genannt ist, hat zwei Einlässe, einen für Luft und einen für N_2. Luft tritt in den Kasten von unten ein. N_2 wird entweder radial oder axial in Übereinstimmung mit der Art und Weise der Brennstoffeinspritzung in dem RCE- bzw. GGR-Schachofen injiziert. Sowohl strukturierte als auch unstrukturierte gepackte Betten werden in der Testbox betrachtet. Für das strukturierte Bett werden zwei Verpackungsformen, einfach kubisch (SC) und kubisch raumzentriert (BCC) mit Keramikkugeln von 52 mm untersucht. Für das unstrukturierte Bett werden zwei Arten von kleinen Partikeln (monodisperse 4 mm Glasperlen und polydisperse Zementklinker 2-6 mm) verwendet.

Dreidimensionale numerische CFD-Strömungssimulationen wurden entsprechend dem Versuchsaufbau durchgeführt. Zwei Modelle, reales Partikelmodell (RPM) und poröses Medien-Modell (PMM), werden in der numerischen Studie verwendet. In RPM werden drei Methoden (Spalt, Überlappung und Brücke) angewendet, um das hohe schiefe Element in der Nähe der Kontaktstelle zwischen Partikel-Partikel, Partikel-Wand zu verhindern. Die Ergebnisse der CFD-Berechnungen ergaben, dass das Spaltverfahren in RPM zur besten Übereinstimmung mit den experimentellen Daten führt. Die Brücke-Methode braucht länger Zeit, um Ergebnisse zu produzieren.

Die PMM-Ergebnisse zeigen im Fall einer axialen Injektion eine gute Übereinstimmung mit den beiden Ergebnissen der RPM und der Experimente.
Das Mischen im Bett wird unter verschiedenen Betriebszuständen wie Messhöhe, Spritzgeschwindigkeit, Volumenstrom-Verhältnis, Strömungsverhältnisse und Injektionsposition untersucht. Es wurde festgestellt, dass das Volumenstromverhältnis beim Mischen einen signifikanten Effekt hat.

Contents

Preface i
Acknowledgments ii
Abstract iii
Zusammenfassung iv
Contents v
Nomenclatures viii
1. Introduction 1
1.1 Shaft Kiln 1
1.1.1 Principle mechanism 1
1.1.2 Common problems in typical shaft kilns 4
1.1.3 Gas flow 5
1.1.4 Control 5
1.2 Flow Pattern 6
1.2.1 Void fraction 6
1.2.2 Pressure drop 7
1.3 Heat and mass transfer 12
1.3.1 Convection 12
1.3.2 Influence of shape and size distribution 13
1.3.3 Influencing parameter 13
1.4 Modeling of lime shaft kiln problems 14
2. Literature review 15
2.1 Modeling of shaft kilns 15
2.1.1 Modeling a fixed packed bed of spheres 17
2.1.2 Packing arrangement 17
2.1.3 Aspect ratio 25
2.1.4 Meshing structure 26
2.1.5 Flow regimes and turbulence 30
2.2 Modeling of Packed Bed using Porous Medium 33
3. Experimental work 36
3.1 Experimental Apparatus 36
3.2 Detailed description of the experimental apparatus 36
3.2.1 Test box with beds 36
3.2.2 Distribution space with perforated plate 38
3.3 Experimental results and discussion 41
3.3.1 Measuring height 41
3.3.2 Lance diameter 43

3.3.3 Volumetric flow rate 44
3.3.4 Volumetric flow rate ratio 48
3.3.5 Lance position 50
3.3.6 Velocity profiles 52
4. Computational Fluid Dynamics in Packed Bed 54
4.1 Computational Fluid Dynamics 54
4.2 Computation of fluid motions 54
4.3 Governing Equations 54
4.3.1 Continuity Equation 54
4.3.2 Navier-Stokes Equation 55
4.3.3 Selection of turbulence model 55
4.3.4 Types of turbulence models 55
4.3.5 Standard k-ϵ turbulence model 55
4.3.6 Influence of turbulence model 56
4.3.7 Species transport model 58
4.4 Near-wall treatments 58
4.5 Boundary conditions 60
4.6 Solution of CFD problem 60
4.6.1 Relaxation factor 60
4.6.2 Residual value 60
4.7 CFD simulation process 61
4.7.1 Pre-processing 61
4.7.2 Solving 61
4.7.3 Post-processing 61
4.8 CFD modeling of packed bed 61
4.8.1 Types of models 61
4.8.2 Real particle model (RPM) 62
4.8.3 Description of the geometry and the grid 62
4.8.4 Contact points 64
4.8.5 Real box domain meshing 67
4.8.6 Definition of the simulation models and materials 69
5. Results of RPM 78
5.1 CFD modeling using RPM 78
5.2 Simulation results with the RPM (axial flow with cross injection) 78
5.2.1 Influence of contact point treatment method 78
5.2.2 Influence of bed height and contact treatment methods 79
5.2.3 Influence of lance position 80
5.2.4 Influence of lance diameter 82

5.2.5 Influence of volumetric flow 84
5.2.6 Influence of volumetric flow rate ratio 84
5.2.7 Velocity profiles 86
5.3 Simulations results of RPM (axial flow with parallel injection) 88
5.3.1 Influence of contact point treatment method 89
5.3.2 Influence of the flow rate ratio for the two bed arrangements 91
5.3.3 Influence of the axial lance injection position 93
5.4 Comparison between cross and parallel injection 95
6. CFD Results of PMM 98
6.1 Porous media model 98
6.1.1 Viscous and inertial resistance 98
6.1.2 Ergun equation for a packed bed 99
6.1.3 Superficial velocity 99
6.1.4 Model definition and Boundary conditions 100
6.2 Geometry and computational mesh 101
6.3 Simulation results of the PMM (axial flow with cross injection) 103
6.3.1 Influence of the turbulence model and the order of the upwind schemes 103
6.3.2 Influence of measurement height 104
6.3.3 Influence of porosity value 104
6.3.4 Influence of lance position 108
6.3.5 Influence of lance diameter 111
6.3.6 Influence of particle size with different bed porosities 114
6.3.7 Comparison between results of the PMM and the RPM 115
6.4 Simulations results of the PMM (axial flow with parallel injection) 117
6.4.1 Influence of the lance position and the porosity value 117
6.4.2 Influence of lance position with different bed porosities 119
6.4.3 Influence of the particle size and the porosity value 121
6.4.4 PMM comparison with RPM 123
6.5 Comparison between cross and parallel injection 123
References 127
List of Publications 130
Curriculum Vitae 131

Nomenclatures

Variables	Description	Unit
A	Area	m^2
B	Width	m
d_p	Particle diameter	m
d_L	Lance diameter	m
Dh	Hydraulic diameter	m
H	Height	m
I	Turbulence intensity, 0.16 ($Re^{\wedge-0.125}$)	-
L	Length	m
N	Box equivalent diameter-to-particle diameter ratio	-
Re	Reynolds number	-
U	Velocity	m/s
$\dot{V}_{ax}$	Air axial flow rate	m^3/s
$\dot{V}_i$	N_2 injection flow rate	m^3/s
$\dot{V}_R$	N_2 to air flow rate ratio	-
X_L	Lance position in X direction	m
ΔP	Pressure drop	Pa
φ	Porosity	-
μ	Dynamic viscosity	kg/m.s
ρ	Density	kg/m^3

Abbreviations

BCC	Body-centered cubic
CFD	Computational fluid dynamics
SC	Simple cubic
RPM	Real Particle Model
PMM	Porous Media Model

1. Introduction

1.1 Shaft Kiln

1.1.1 Principle mechanism

Shaft kilns and cupola furnaces are used for the mass conversion and melting of granular and coarse materials. The material is transported through a vertical shaft by gravity. The hot gas flows counter current to the material. For calcination processes, the term shaft kiln is typically used, whereas the term cupola furnace is typically used for melting processes. The term blast furnace is common when reducing iron ore. In the following, for the general description, the term shaft kiln is used. Table 1-1 summarizes typical characteristic values of common shaft kilns [1].

Table 1-1: Typical characteristics of common shaft kilns

Characteristics		**Normal shaft**	**Mixed-Feed**	**Annular**	**PFR**
Output capacity, t/d		150 –300	100 - 200	200 - 600	200 - 800
Inner diameter, m		2.0 – 3.0	2.5 – 6	3.0 – 4.5	2.5 – 3.5*
Cross-sect. area, m^2		3 –7	6 – 30	20 - 23	6 - 10*
Height of solid bed, m		10 – 15	15 - 20	15 - 25	15 – 20
Output flux, $t/d/m^2$		40 – 45	10 - 25	15 - 30	20 - 30*
Solid velocity, m/h		1.8 – 2.0	0.5 – 1.0	0.6 – 0.7	0.6 – 1.4
Air flux, $m^3_{STP}/m^2/s$		0.6 - 0.7	0.1 - 0.12	0.6 - 0.8	0.8 - 1.1
Min. particle size, mm		30	20	30	20
Max. particle size, mm		150	200	250	160
Total press. drop, mbar		200 – 250	10 - 30	200 - 400	300 - 400
Typical type of fuel		natural/lean gas lignite	anthracite coke	natural/lean gas coal/oil	natural/lean gas lignite/pet coke
Energy supply	MJ/kg_{lime}	3.8 - 4.8	3.9 - 4.5	3.8 - 4.1	3.3 - 4.0
	$kcal/kg_{lime}$	910 – 1150	930 - 1080	910 - 980	790 - 950

Max. solid temp., °C		1400 – 1500	1100 - 1300	1100 - 1200	1100 - 1200
Max. gas temp., °C		1500 – 1600	1300 - 1400	1200 - 1300	1200 - 1300
Lime	type	hard-burnt	hard/middle	middle/soft	soft-burnt
	reactivity	low	low/medium	medium/high	high

* Data given for one shaft

From the table, it can be seen that, in lime calcination, the material needs a large reaction enthalpy for the mass conversion. This results in a higher energy consumption and a lower outflow flux. The energy supply is relatively large in coke-fired melting furnaces. Air has to be burnt with an excess air number of lower than one so that CO is produced to protect the iron from oxidation. The flue gas leaving the furnace contains a CO concentration of 20 – 25%. This gas is later burnt to preheat the combustion air. Coke must be used as fuel because it builds a carrier framework for the material and the hot melt flow. Figure 1.1 schematically shows a shaft kiln as an example for the calcination of limestone. Limestone particles are filled in a container, weighed on a balance, lifted to the top of the kiln and poured into the shaft. The material passes a sluice before it falls onto the packed bed. The gas has to be separated for cleaning. On the way down, the particles are initially preheated from the hot gas and then calcinated after reaching the reaction temperature.

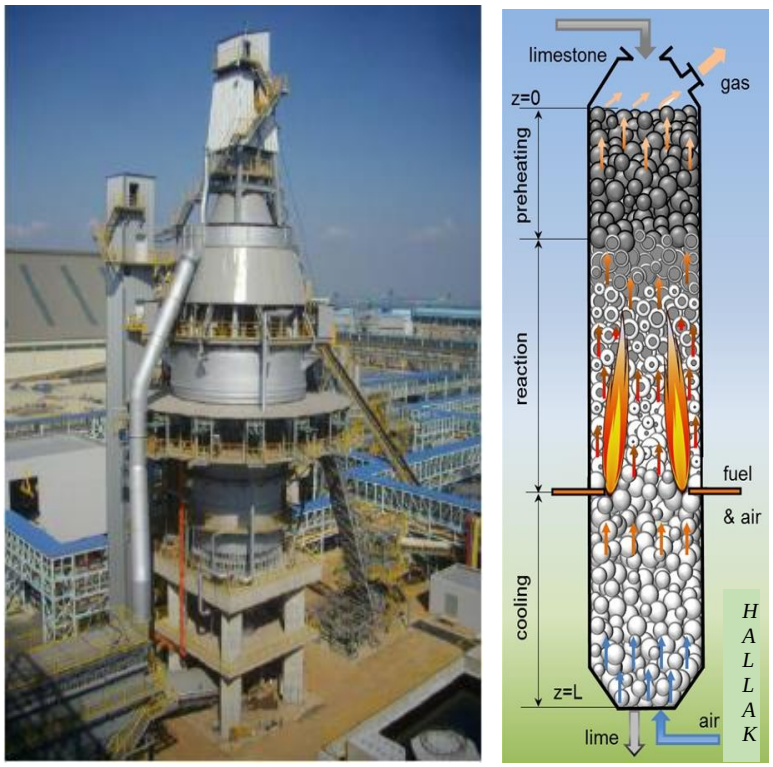

Figure 1.1: Actual image and schematic of a lime shaft kiln.

To provide an energy supply, fuel and air are injected into burners placed in the wall; see Figure 1.2 [2]. Immediately after leaving the burner, the jet hits particles and is converted into the vertical direction. The penetration depth of the burner jet in the horizontal direction is therefore very low. As a consequence, burners are necessary inside the bed.

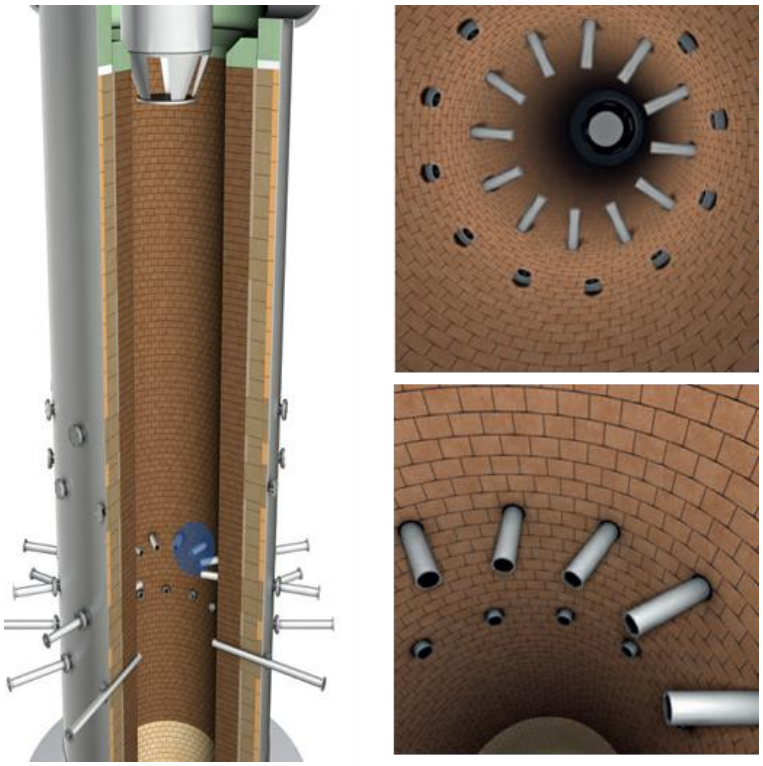

Figure 1.2: Firing system and burner arrangement in lime shaft kiln

The figure shows a central burner with axial supply. Many designs exist to improve horizontal mixing in the cross section; the homogenization of the temperature and concentration in the cross section is a main problem for shaft kilns. Calcination occurs above the burners. Below the burners, the lime has to be cooled down. Therefore, a part of the combustion air flows from the bottom in the counter current direction through the packed bed. Figure 1.3 shows a normal shaft kiln as an example of a typical profile of the mean temperature of the solid and of the gas. To explain the process, it makes sense to divide the kiln into zones. After inserting particles at ambient temperature, they are heated by the hot combustion gas in the counter current. The decomposition of the limestone according to the reaction $CaCO3 = CaO + CO2$ can start after reaching temperatures of 810°C – 840°C, depending on the $CO2$ concentration of the gas because of equilibrium conditions. This is the end of the preheating zone and the beginning of the reaction zone. The end of this zone has to be reached before the injection level of the fuel. Behind this injection lies the cooling zone. Here, the particles have to be cooled down to temperatures of approximately 50°C – 80°C. The ambient air in the counter current serves as a cooling agent. Above the level where fuel injection occurs, the temperature of the gas increases rapidly. After the particle temperature is exceeded, heat can be transferred to facilitate the endothermic reaction.

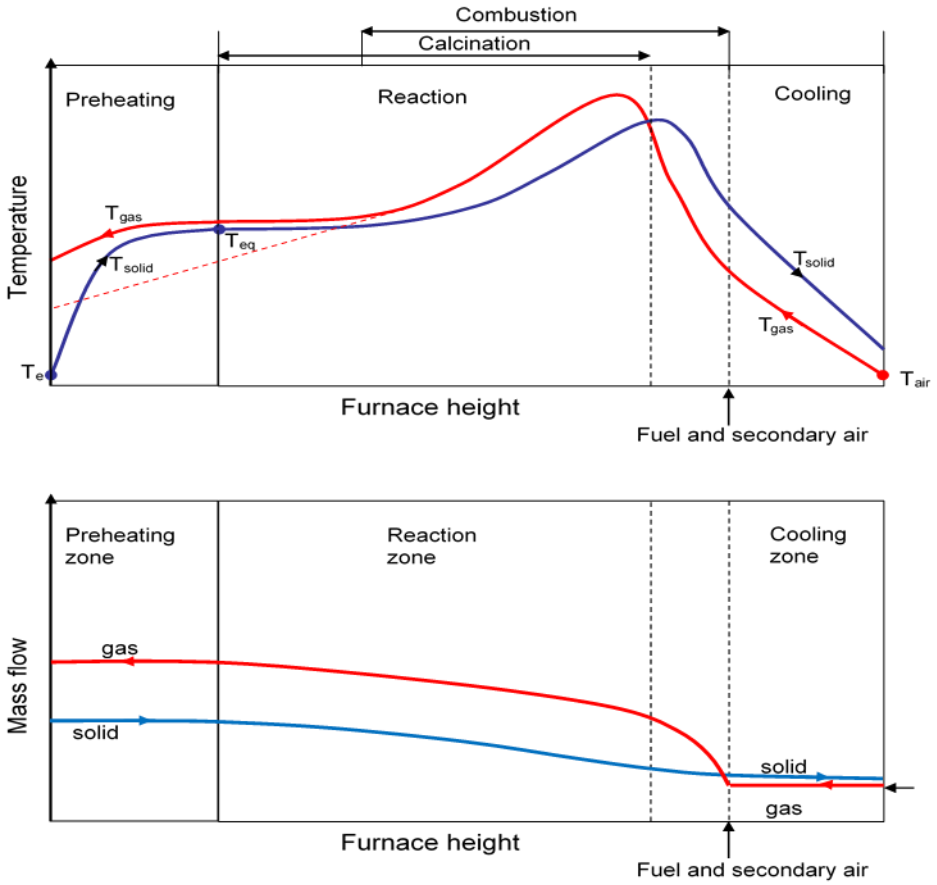

Figure 1.3: Typical temperature and mass flow profiles of solid and gas in a normal shaft kiln.

1.1.2 Common problems in typical shaft kilns

Typical shaft kilns achieve quite efficient heat transfer in the preheating and cooling zones. In the calcination zone, however, these furnaces suffer from many heating problems such as “hot spots” or cool channels, refractory over-heating, and surplus heat. In recent years, shaft kilns have seen dramatic developments toward optimal kiln designs. Today, considering increasing energy prices and the extremely competitive situation in industrialized regions, it is necessary to develop improved shaft kilns, create new kilns and improve existing kilns. The optimization of modern kilns continues to overcome these problems related to kilns. The most important factors in the modernization of shaft kilns are improving the quality of the product, the flexibility in fuel applications, increased capacity, improvements in kiln operation, enhanced range of the stone grain size, environmental issues and increased availability and safety. Therefore, not considering one of these factors will cause problems. This section presents the shaft kiln problem in two parts; first part presents the main problems facing the industry, and the second part is related to shaft kiln simulation and modeling.

1.1.3 Gas flow

Pressure drop

The gas flow through the packed bed causes a large pressure drop. Therefore, a classification of the solid is necessary to minimize the pressure drop. The pressure drop is influenced by the reciprocal value of the void fraction to the third power and by the reciprocal particle size. The void fraction is the fraction of the gas volume to the volume of the kiln. In a packed bed with particles of different sizes, the small particles fall into the gap between the large particles and reduce the void fraction. The pressure drop in the bed of arbitrary shape of particles is higher than the pressure drop in the bed of equal size particles. As a consequence, the particles have to be sieved and classified before being inserted into kilns. The ratio between the diameters of the largest and smallest particle in a kiln should be less than two. The lower limit of the particle size for an economic pressure drop is approximately 30 mm; these small particles have to be calcinated in rotary kilns. Particles greater than approximately 150 mm are not used because their calcination time would be too long.

Radial homogenization

The penetration depth of radially injected gas jets is relatively low, as previously mentioned. From industrial experience, it is known that the penetration depth is approximately in the range of 1 to 1.5 m. In lime shaft kilns, internal burners are commonly used to improve the fuel distribution. Lances can be arranged from the top or from the bottom into the bed.

1.1.4 Control

The controlling of such kilns is very difficult because of the limited possibilities for measurement. It is nearly impossible to measure temperatures and concentrations in the kiln. Thermocouples cannot be placed through the walls and placed inside the bed because they would be cut off due to the movement of the bed. For the transient measurement of temperatures, small pipes with thermocouples inside can be placed on top of the packed bed and transported between the particles through the kiln. However, in the hot region of the kiln, where the temperatures are of greatest interest, the pipes are typically crushed. The thermocouple measures only a mixture of the gas and solid temperature.

Measurements of the temperature and concentration of the gas are possible behind the sluice and before injection into the kiln. The problem is to obtain representative values of the cross section. The distribution above the bed cannot always be assumed as homogeneous. An error in the measurements occurs because of false air and leakages. If the material comes out in the solid state, e.g., in lime calcinations, it is difficult to measure the particle temperature. The particles do not exhibit a uniform temperature. The core is hotter than the surface. Additionally, the temperatures depend on the size and shape.

A controlling of the kilns is therefore possible only with input and output data. Another problem for such control is the time lag of the kiln. It takes more than a day to transverse the kiln. The thick wall of the kiln requires multiple days to reach steady state. Therefore, the kiln requires a few days to reach new stationary conditions after parameters are changed. To achieve a better control, mathematical simulations of the processes are required.

1.2 Flow Pattern

1.2.1 Void fraction

Shaft kilns are basically packed bed reactors with an upward flow of hot gases passing counter current to the downward flow of feed consisting of solid particles. A packed bed is characterized by the void fractionΨ, which is defined as

$$\Psi = \frac{\text{Bed volume} - \text{Packing volume}}{\text{Bed volume}}. \qquad (1\text{-}1)$$

The void fraction is influenced by

- the method of packing (random or regular, loose or dense),
- the particle shape (sphere, cylinder, etc.), and
- the particle size distribution.

For an infinitely extended regular packing of equally sized large spheres, the void fraction is
0.476 for simple cubic packing (SC),
0.395 for cubic space centered packing (BCC), and
0.259 for cubic face centered packing (FCC).

Figure 1.4 shows three types of sphere packing.

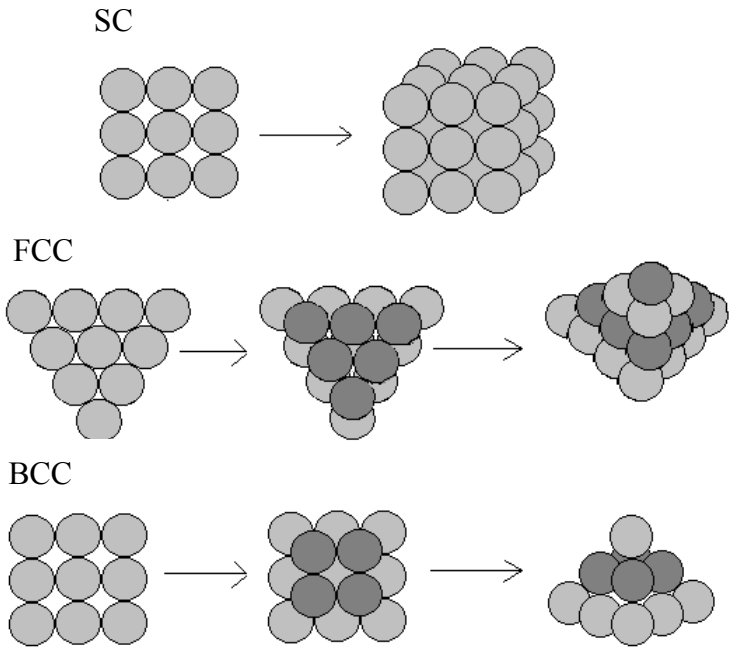

Figure 1.4: sphere packing

For the random packing of equally sized large spheres, the void fraction is

0.4 - 0.42 for loose packing
0.36 - 0.38 for dense packing.

1.2.2 Pressure drop

The pressure drop is a very important parameter of the shaft kiln because it determines the power of the blower. It can be described by two different models:

- Model based on the hydraulic diameter
- Model based on one-particle cross-flow

Hydraulic diameter model

The **hydraulic diameter** is defined as

$$d_h = \frac{\text{Volume of bed available for flow}}{\text{Surface of particles}} = \frac{\text{Void fraction}}{\text{Specific surface}} = \frac{\Psi}{O}$$

where O is the specific surface area [m^2/m^3] of the packed bed. If the bed consists of particles with a volume V_p and surface area A_p, then the specific surface area is obtained as

$$O = \frac{A_p}{V_p} \cdot (1 - \Psi). \qquad (1\text{-}2)$$

For spherical particles with diameter d, we obtain

$$O = \frac{6}{d} \cdot (1 - \Psi). \qquad (1\text{-}3)$$

Using the above-mentioned equations, we obtain

$$d_h = \frac{2}{3} \cdot \left(\frac{\Psi}{1 - \Psi} \right) \cdot d. \qquad (1\text{-}4)$$

There are two equations, according to Ergun and Brauer, which can be used to determine the pressure drop of packed beds. The Ergun equation is based on the model conception that the real packed bed can be replaced by a parallel connection of flow channels, and the pressure drop calculation is similar to a one-phase pipe flow but with the hydraulic diameter of the packed bed as the characteristic dimension. This equation is presented as

$$\Delta p = \int_{z=0}^{L} 150 \cdot \frac{(1-\Psi)^2}{\Psi^3} \cdot \frac{\rho \cdot \nu \cdot w}{\overline{d}^2} \cdot dz + \int_{z=0}^{L} 1.75 \cdot \frac{(1-\Psi)}{\Psi^3} \cdot \frac{\rho \cdot w^2}{\overline{d}} \cdot dz \qquad (1\text{-}5)$$

where w denotes the velocity in the kiln if no packing was present, called the superficial velocity:

$$w = \frac{\dot{V}}{A}. \qquad (1\text{-}6)$$

Here, $\dot{V}$ is the volumetric flow through the kiln and A is its cross section area. Normally, the volumetric flow at standard temperature and pressure conditions (STP) is known. If the mass flow is constant, the velocity changes with the temperature.

The first term of the Ergun equation describes the change in pressure by the viscous force, and the second term describes that by the inertia force. The constants are based on experimental data for many shapes of particles, but the equation is most accurate for spherical particles.

Figure 1.5 shows the pressure drop using the Ergun equation in two cases. In the first case, both terms of the equation are used, and in the second case, only the second term of the equation is used. It can be seen that the difference is not significant. This is because the inertia force is dominant because the flow turns after each particle. Therefore, it is more convenient to use only the second term of the equation to determine the pressure drop of kilns.

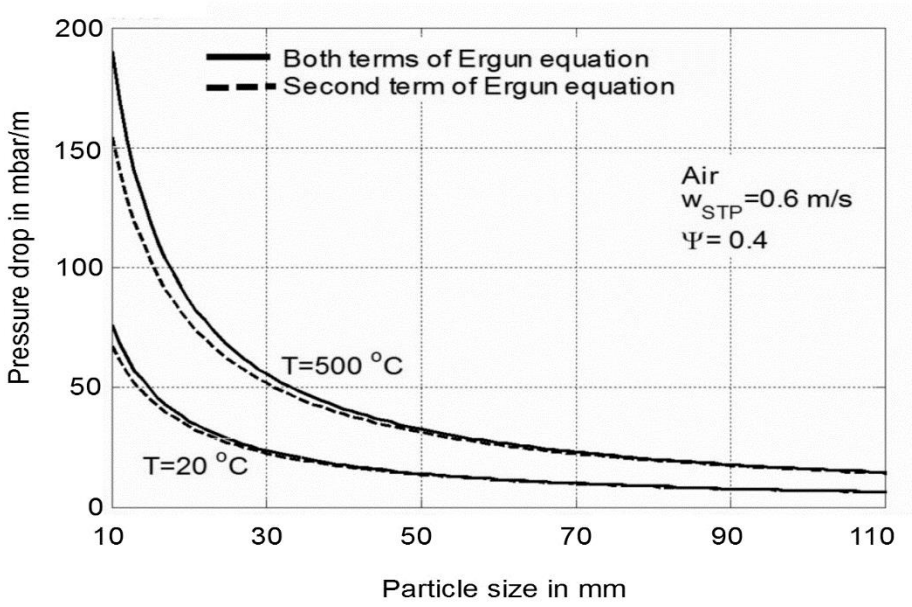

Figure 1.5: Pressure drop calculated by Ergun equation

The single-particle cross-flow model

Another equation for the pressure drop based on the cross-flow can be used. The pressure drop is calculated from the Euler number, with

$$dp = \int_{z=0}^{L} \frac{3}{4} \cdot \frac{1-\Psi}{\Psi^2} \cdot \frac{\rho \cdot w^2}{\bar{d}} \cdot Eu \cdot dz. \qquad (1\text{-}7)$$

Figure 1.6 demonstrates the influence of the particle size on the pressure drop. The calculation was performed for a void fraction of 0.4 and a superficial velocity of 1 m/s as an example. It can be seen that there is a strong increase in the pressure drop in the case where the particle sizes are smaller than approximately 30 mm. Hence, shaft kilns are operated with solid particles greater than 30 mm to avoid an excessive pressure drop.

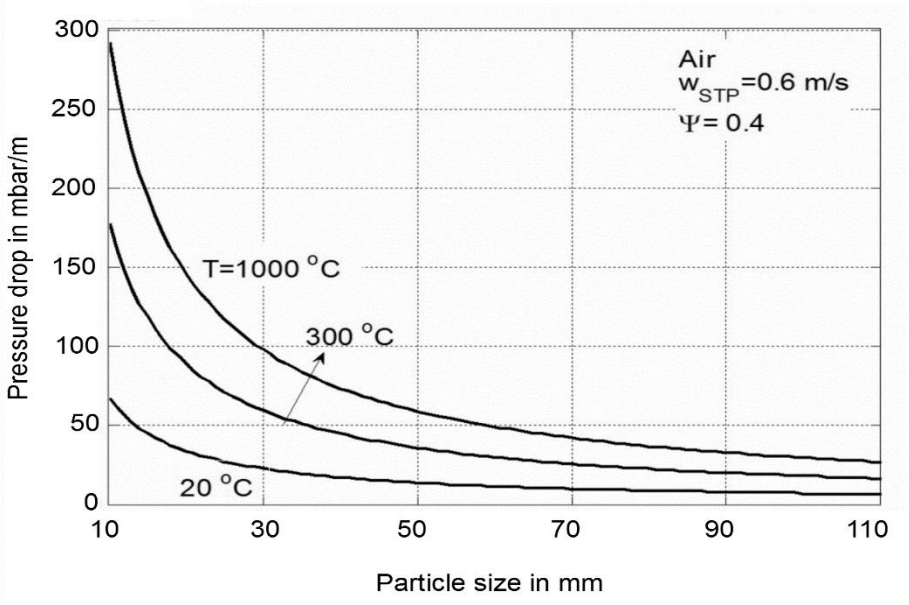

Figure 1.6: Influence of particle size on pressure drop

According to Eq. (1-5), the pressure drop is strongly influenced by the void fraction. Figure 1.7 shows the effect of the void fraction on the pressure drop. It increases with decreasing void fraction to nearly the third power. Therefore, low values of the void fraction have to be avoided.

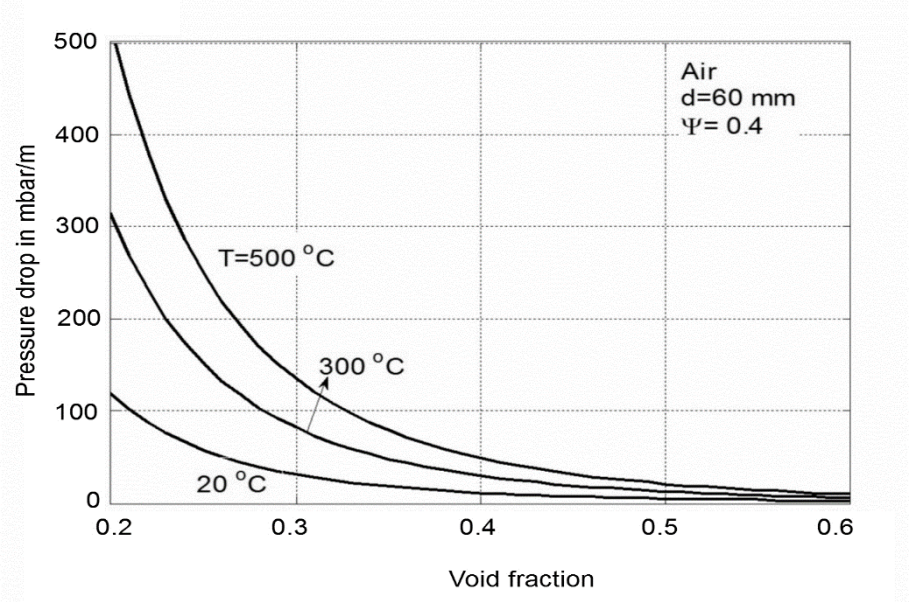

Figure 1.7: Pressure drop as a function of the void fraction of a packed bed

Figure 1.8 shows the effect of two different particle sizes on the void fraction. In this figure, the volume fraction of the fine particles is defined as $Q_f = V_f/V_s$, where V_f denotes the total volume of the fine particles and V_s represents the total volume of the solid phase. The diameter of the coarse particle is d_c, and that of the fine particle is d_f. If the particles have the same diameter, then the packing is called monodispersed, and the void fraction is approximately 0.4. If there are only a few fine particles, these particles fill in the gaps created by the large particles. As a result, the free bed volume and therefore the void fraction decreases considerably according to the theoretical function ψ_1 until the gaps are filled. Then, the minimum value of the void fraction is reached, which is the square of the void fraction of the monodispersed packing. With higher fractions of the fine particles, the void fraction increases again according to the function ψ_2. The minimum value of the void fraction depends on the diameter ratio between the coarse and fine particles. A lower ratio results in a higher minimum void fraction. If the ratio between the largest and finest particle is lower than two, the decrease in the void fraction is relatively small. Under this condition, the pressure drop is not significantly increased.

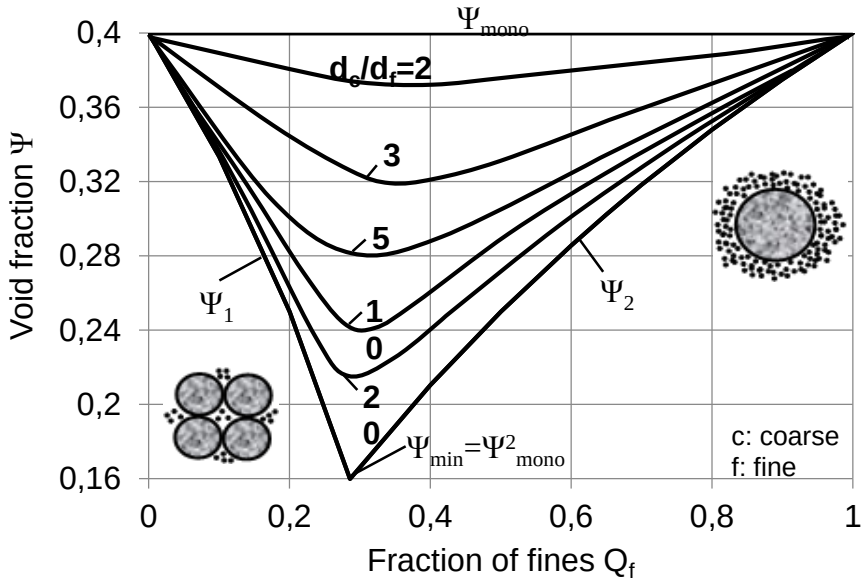

Figure 1.8: Bed porosity of bi-dispersed packing of spheres

Another effect on the void fraction is the wall effect, which causes loose packing in the region close to the wall of the packed bed. This effect is presented in Figure 1.9. In the region near the wall, the void fraction is approximately equal to 1. However, in the radial direction, the void fraction decreases from the wall to the center, and it is nearly constant after a distance corresponding to one particle diameter. The consequence is that, near the wall, the flow has a much lower pressure drop. Therefore, the flow prefers the near-wall region, which results in a much higher velocity [1].

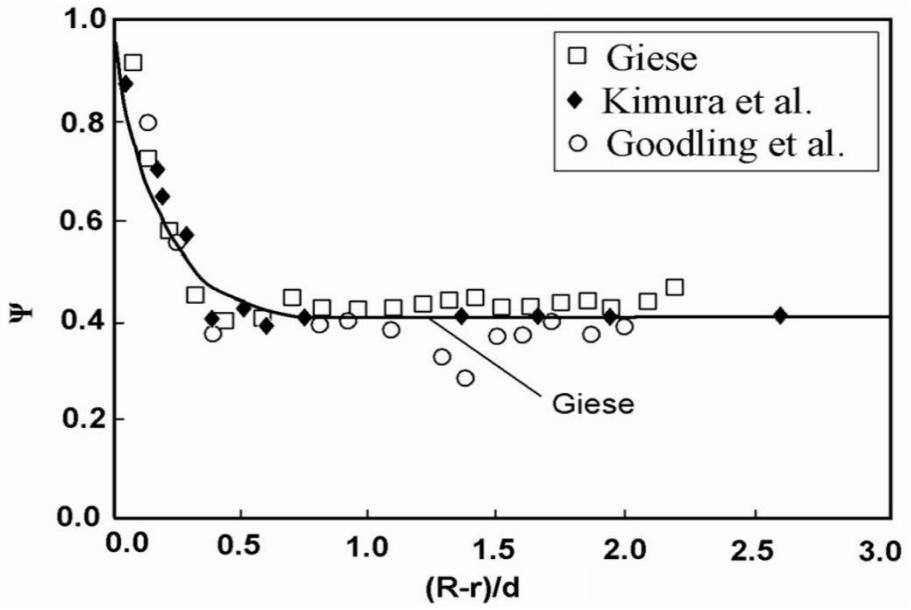

Figure 1.9: Radial porosity profile

1.3 Heat and mass transfer

1.3.1 Convection

Model based on hydraulic diameter

One approach to estimating the heat transfer coefficient in a packed bed is given by Jeschar (1964), in which a packed bed can be described as a bundle of parallel pipes. The heat transfer coefficient is based on the established Nusselt correlation

$$\mathrm{Nu} = 2 + 1.12 \cdot \mathrm{Re}^{\frac{1}{2}} \cdot \mathrm{Pr}^{\frac{1}{3}} \cdot \left(\frac{1-\Psi}{\Psi} \right)^{\frac{1}{2}} + 0.005 \cdot \mathrm{Re} \qquad (1\text{-}8)$$

where ψ is the void fraction of the packed bed. The Nusselt number is defined as

$$\mathrm{Nu} = \frac{\alpha \cdot d}{\lambda_G} \qquad (1\text{-}9)$$

where d is the size of the particle and λ_G is the gas thermal conductivity. The Reynolds number Re in Eq. (1-8) is defined as

$$\mathrm{Re} = \frac{w.d}{\nu \cdot \psi} \qquad (1\text{-}10)$$

where w is the gas velocity if no packing was present (superficial velocity) and υ is the gas kinematic viscosity. The Prandtl number is defined as

$$\mathrm{Pr} = \frac{\nu \cdot \rho_G \cdot c_{pG}}{\lambda_G} \qquad (1\text{-}11)$$

where ρ_G is the density and C_{pG} is the specific heat capacity of the gas.

Model based on the flow over a single particle

Another common model used to determine the heat transfer coefficient in a packed bed was given by Gnielinski (1978), where the Nusselt number is based on the cross flow over a simple sphere. The laminar and turbulent Nusselt functions for a cross-flow are given as

$$\mathrm{Nu}_{\mathrm{lam}} = 0.664 \cdot \mathrm{Re}^{\frac{1}{2}} \cdot \mathrm{Pr}^{\frac{1}{3}} \qquad (1\text{-}12)$$

Figure 1.10 compares both Nusselt functions for void fractions of 0.4 and 0.6 and Prandtl number for a gas of 0.7. Both models obtain a similar result. Therefore, the Nusselt function described in Eq. (1-8) is preferred because it is a slightly simpler equation.

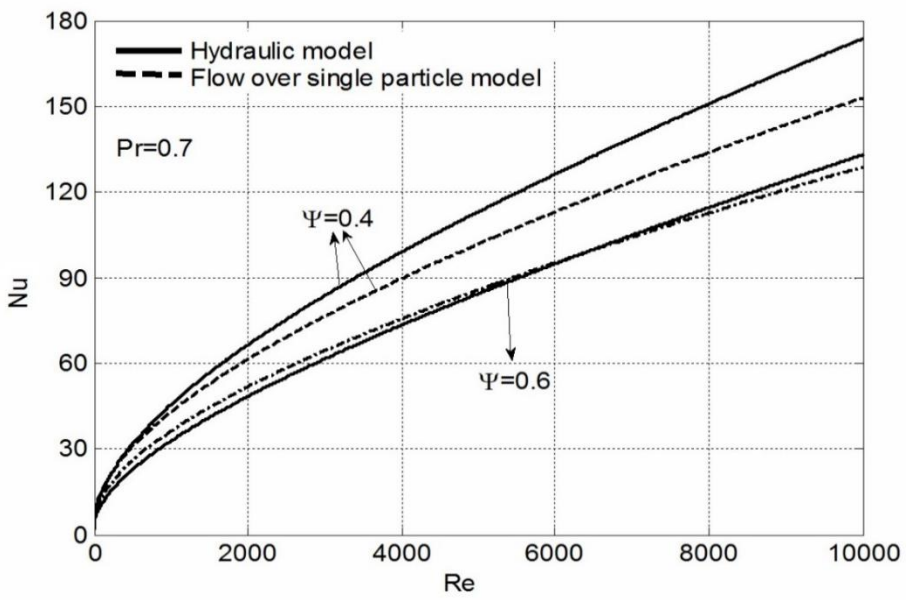

Figure 1.10: Comparing two heat transfer models

1.3.2 Influence of shape and size distribution

The packed beds of kilns consist of particles characterized a certain size distribution. If only a mean heat transfer coefficient is required for the bed, the Nusselt and Reynolds numbers have to be formed with the Sauter-diameter:

$$\bar{d} = \left[\sum_{i=1}^{n} \left(\frac{V_i}{V} \cdot \frac{1}{d_i} \right) \right]^{-1} \qquad (1\text{-}13)$$

1.3.3 Influencing parameter

Figure 1.11 shows the influence of the superficial velocity and the gas temperature on the heat transfer coefficient. It can be seen that the heat transfer coefficient increases significantly with increasing superficial velocity and gas temperature. It can also be seen that a smaller particle size results in a higher heat transfer coefficient.

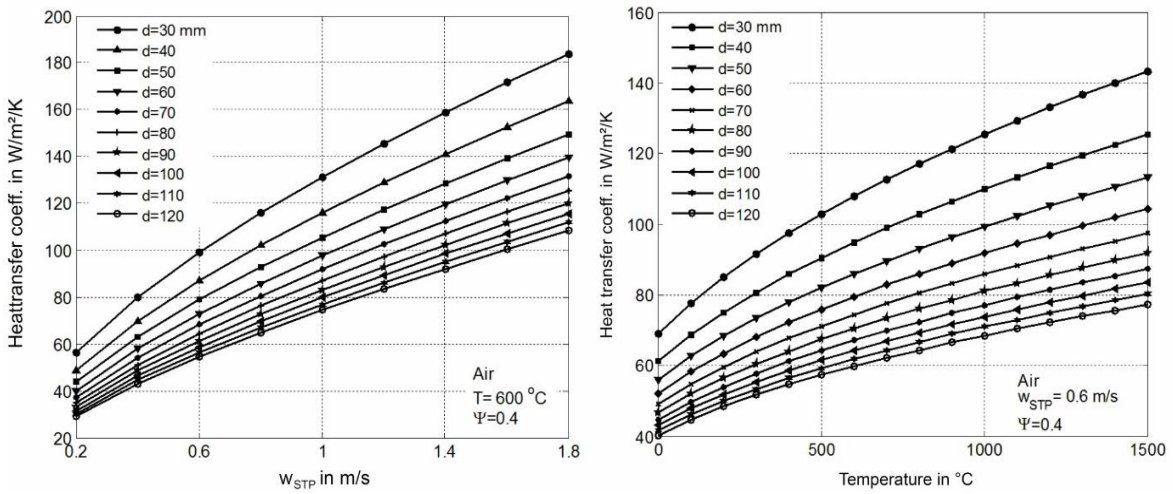

Figure 1.11 shows the influence of the superficial velocity and the gas temperature on the heat transfer coefficient

1.4 Modeling of lime shaft kiln problems

Due to the large geometry of industrial lime shaft kilns, 30 m in height and 3 m in diameter; large stones moving in the vertical direction; and the complicated systems involved; measurements of temperature and concentration profiles are not possible because in most cases the measurement instruments would be damaged. Many attempts in past decades have been aimed at addressing these above-described problems. However, the optimization is usually very empirical and costly because the response to a change in any of the operating parameters is noticeable only after a couple of days. In addition, reproducing this process in a laboratory-scale furnace is expensive.

However, the modeling of lime shaft kilns is relatively complex because of the complex phenomena that occur inside the kiln, such as the counter-current mode of operation, chemical reactions, and heat and mass transfer, all of which occur simultaneously. Developing mathematical models for the thermodynamic process of a shaft kiln using any programmable software cannot provide accurate predictions due to the over simplifications of the processes involved. For example, the temperature distribution in the radial direction and the gases concentrations along the kiln cannot be predicted well, and other parameters must be studied to describe the complete process. CFD approaches being applied to study the physical and chemical processes within lime shaft kilns are essential to investigating the effective parameters on the kiln operation.

Because of the lack of knowledge of fluid phenomena in kilns, a CFD mathematical model for a small box was used in this work to exam the cross mixing through the bed, and the flow structure is computed by solving the mathematical equations that govern the flow in the entire flow domain. The results were validated with experimental results from a test rig representing two packing types, regular packing for 52 mm ceramic spheres as a simple cubic (SC) and a body-centered cubic (BCC) arrangement. These two models were implemented in a CFD code using a real particle model (RPM), as in reality. In addition, irregular packing for 4 mm small glass beads was used. This model was too complex to be created as an FBM; thus, a porous media model (PMM) was adopted.

2. Literature review

2.1 Modeling of shaft kilns

The complex phenomena that occur inside the kiln make the modeling of lime shaft kilns relatively complex because of the counter-current mode of operation, chemical reactions, and heat and mass transfer, all of which occur simultaneously. The trend in most of these models has always been toward providing grouped parameters to facilitate a simple description of the physical processes. Considering the difficulties of experimental measurements inside lime kilns, the processes of kilns remain poorly understood, and there are many problems that have to be solved. A fundamental understanding of the processes occurring in a shaft kiln is required to obtain high lime quality and thermal efficiency.
In this study, only the essential work that falls under the modeling of cross flow mixing in a rectangular box as a test rig is reviewed due to the difficulties of studying the dynamic processes of gases inside the shaft kiln. First, the principles of modeling shaft kilns using CFD are clarified. Then, the modeling aspects for a packed bed of spheres, such as the packing arrangement, aspect ratio, mesh structure and flow regimes, are discussed. Then, the modeling of a packed bed as a PMM is discussed.

Zhiguo Xu et al. [3] numerically investigated the flow of a structured packed bed with jet injections using CFD. They constructed geometries with a tube-to-particle diameter ratio (aspect ratio N) of 20 for use in CFD models. The results showed that the jet behavior was independent of the bed height. Furthermore, the influence of the nozzle's shape on the radial mixing of gases in the beds was investigated. Additionally, they proved that the jet flow pattern is slightly influenced by the heat transfer between the solid and gas phases. Based on these simplifications, they created a 3D geometric model with a 30° segment and bed height of approximately 0.8 m. In addition, they illustrated that an increase in the lance depth may be helpful for protecting the refractory wall from becoming overheated, but this has only a slight effect on the overall radial temperature distribution. Further, the mixing between combustion gas and the cooling air can be improved by reducing the burner diameter or by preheating the combustion air. However, their model still suffers from certain limitations. For example, during the 3D geometry creation, they used porous media conditions at the inlet and outlet of the domain, which may affect the flame distribution. Additionally, their 3D discrete particle model was verified based on the pressure drop accuracy, which may have no influence on the flame distribution. Figure 2.1.

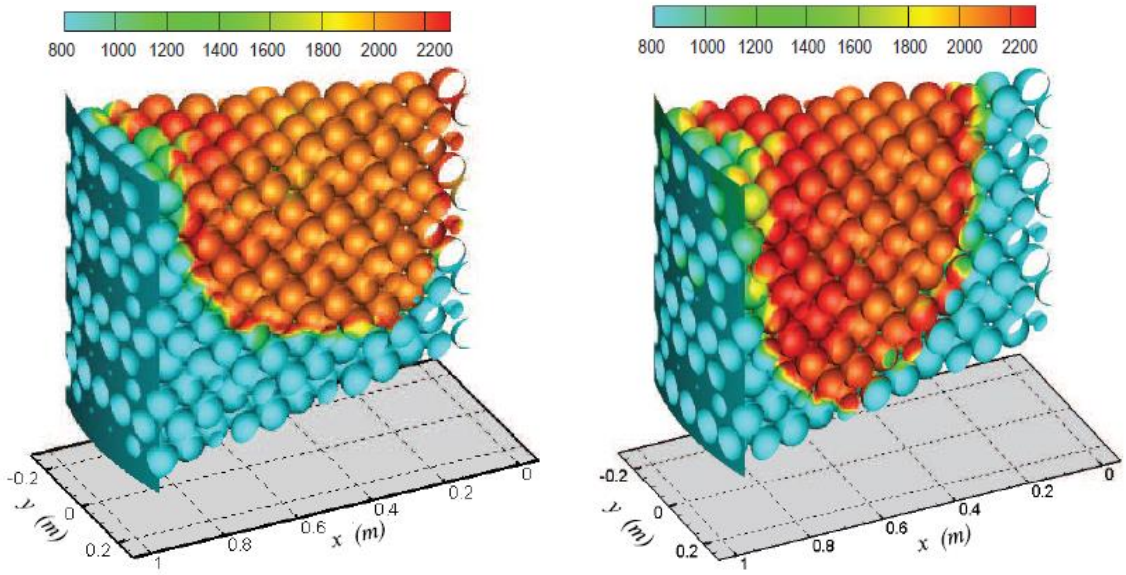

Case I **Case II**

Figure 2.1: Temperature contours on the surfaces of particles of Case I (x_L= 100 mm), Case II (x_L = 200 mm), d_P= 100 mm; Legend shows temperature in K.

Zhou et al. [4] coupled a discrete particle simulation (DPS) with CFD modeling to investigate the gas–solid flow within a blast furnace (BF). The results showed that the DPS–CFD approach can generate the static zone without global assumptions or arbitrary treatments. The obtained results confirmed that increasing the gas flow rate can increase the size of the static zone. T. Bluhm-Drenhaus and Simsek [5] investigated the heat and mass transfer in a lime shaft kiln through a coupled numerical scheme for a fluid and solid phase transport. The three-dimensional transport of mass, momentum and energy in the gas phase is modeled using CFD, whereas the discrete element method (DEM) is employed for the mechanical movement and the conversion reaction of the solid material. They studied the effects of interphase heat transfer and chemical conversion (calcination) in simulations of laboratory-scale experiments on single reacting spheres. Anthony G. Dixon et al. [6] validated the CFD simulations of heat transfer in fixed beds of spheres by comparing the results with experimental measurements in a pilot-scale rig. The comparisons were made for two ranges of particle Reynolds numbers: $2200 < Re < 27000$ for a tube-to-particle diameter ratio $N = 5.45$ and $1600 < Re < 5600$ for $N = 7.44$. The CFD simulations were compared to the experimental data; trends as a function of Re, N and bed depth were captured, and the quantitative agreement of the temperature profiles was reasonable.

Rasul and Saotayanan [7] developed a 2D model to simulate thermodynamic processes for a shaft kiln of magnesia briquettes. The combustion, particle-gas dynamics and heat transfer processes that occur inside the shaft kiln were modeled by an Eulerian multiphase model and species transport with a finite volume chemical reaction model. The results showed a discrepancy in the model of the gas-particle dynamics, with an inaccurate prediction of the gas and particles interaction. Additionally, their results predicted temperatures within the kiln that were extremely high, in stark contrast to practical conditions.

In addition, some studies have been conducted to study the pressure drop in packed beds. Baker and Tabor [8] compared computational simulations of air flow through a packed column containing 160 spherical particles at an aspect ratio of N = 7.14 with experimental and theoretical results for equivalent beds. The experimental measurements indicated a pressure drop across the column and were compared with the correlation of Reichelt (1972) using the fitting coefficients of Eisfeld and Schnitzlein (2001). The results were found to correlate strongly with the experimental data and the correlation in the literature. Furthermore, the flow structure was studied. Calis et al. [9] demonstrated that a CFD code (CFX-5.3) could be applied to predict the pressure drop characteristics of packed beds of spheres with a tube-to-particle diameter ratio of 1.00 to 2.00, therein obtaining an average error of nearly 10%.

2.1.1 Modeling a fixed packed bed of spheres

In shaft kilns, the raw material is charged at the top of the kiln, and the product is withdrawn from the bottom. This causes the material to move excessively slowly downward through the kiln. Packed beds have been used extensively in engineering processes such as filtration, heat and mass storage and industrial catalysis. These beds can be defined based on the number of particles dumped into a container. The particles form a structure that contains voids or pores, through which a fluid is free to penetrate. These particles are static and unable to move. This section presents the principles and methods of modeling a fixed packed bed. It includes the geometric properties and the physics of the flow in a packed bed.

2.1.2 Packing arrangement

There are two special categories of packing: randomly packed beds and structured packed beds. Randomly packed beds have been predominant for decades because of their ease of use and low price compared to other packing methods, as is well represented in the literature [10-14]. The arrangement of particles and how they are ordered within the bed are highly influential in regard to where a fluid can pass through the media. In addition, packed beds can be loosely packed or densely packed, based on the number of particles packed into a known volume. The random shapes and sizes of particles in packings play an important role; when a fluid passes through a packing, it flows through a network of voids and channels formed by the particles, resulting in an overall fluid flow and pressure drop. Usually, a packing can be characterized by a few parameters such as the particle size and particle shape. Most numerical studies and many experimental investigations have been performed for packings consisting of spherical particles [15-20] because the simple spherical geometry allows for a relatively easy and well-defined generation of the packing as spheres. Furthermore, the packing of spheres more strongly reflects the wall effects. For any structured packing, there is a representative unit cell that is in principle sufficient to completely describe the packing. This work examines cross and axial flow mixing through a packed bed of small, large, regular, irregular, rough and smooth particles to determine which parameters are the most important in terms of influencing the flow mixing.

Gunjal and Vivek [20] used the unit-cell approach to understand fluid flow through the array of spheres. They considered different periodically repeating arrangements of particles, such as simple cubical (SC), 1-D rhombohedral ($\varepsilon = 0.4547$), 3-D rhombohedral ($\varepsilon = 0.2595$), and face-centered cubical (FCC) ($\varepsilon = 0.302$) geometries, as shown in Figure 2.2.

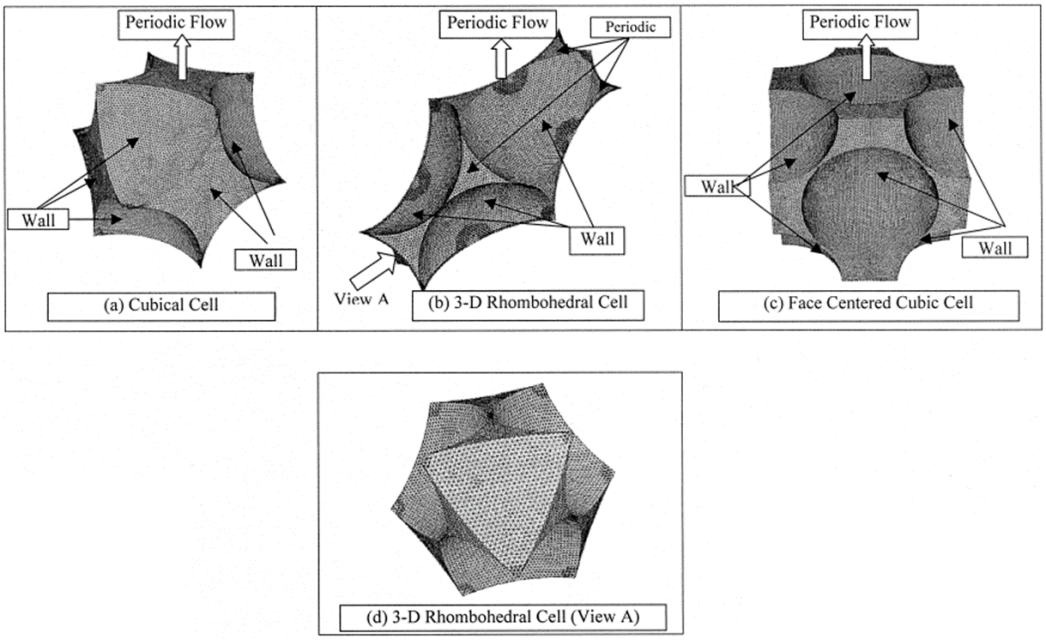

Figure 2.2: Different unit cell arrangements [20]

Their simulations were conducted at different particle Reynolds numbers in a laminar flow regime (representative values of 12 and 204) and in a turbulent flow regime (representative values of 1000 and 2000). For the SC and FCC unit cells, only one fourth of the domain was used for the flow simulations because of the inherent symmetry. They found that, in the laminar flow regime, the predicted magnitude of the dimensionless maximum velocity increased with increasing particle Reynolds number. However, for the turbulent flow regime, the magnitude of the dimensionless maximum velocity was almost independent of the particle Reynolds number and much lower than that observed in the laminar flow regime. The predicted values of the Nusselt numbers for the FCC arrangement showed reasonable agreement with the correlations of the particle-to-fluid heat transfer in packed beds. The predicted values of the Nusselt number for the SC arrangement were much lower than those obtained for the FCC arrangement. Additionally, the velocity distribution in the 1-D rhombohedral geometry was found to be more sensitive to the value of particle Reynolds number than that in the 3-D rhombohedral geometry. In the turbulent flow regime, the magnitude of the dimensionless maximum velocity was almost independent of the particle Reynolds number and much lower than that observed in the laminar flow regime. Furthermore, the predicted velocity distributions for the SC and 1-D rhombohedral geometries showed sharp peaks, which indicate a large void volume faction with low velocities. However, for the FCC and 3-D rhombohedral geometries, the predicted velocity distribution is quite flat. Yuh Ferng and Kun-Yueh [21] conducted simulations of flow and heat transfer through a high-temperature gas-cooled reactor (HTGR) with a pebble bed with respect to two arrangements, BCC and FCC; see Figure 2.3.

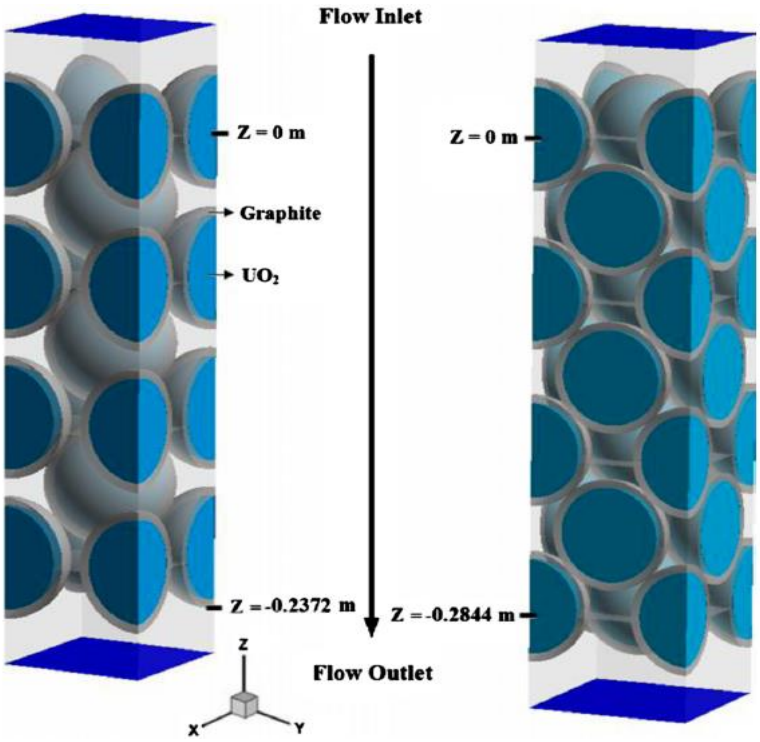

Figure 2.3: Schematic of simulation domain for each pebble arrangement

Based on the simulation results, higher heat transfer capability and lower pebble temperature are predicted in the pebbles under the FCC arrangement. In addition, they concluded that, with a more compact arrangement and smaller flow area, the characteristics of higher flow velocities and larger cross flows for pebbles under the FCC arrangement are more obvious than those under the BCC-lattice geometry; see Figure 2.4.

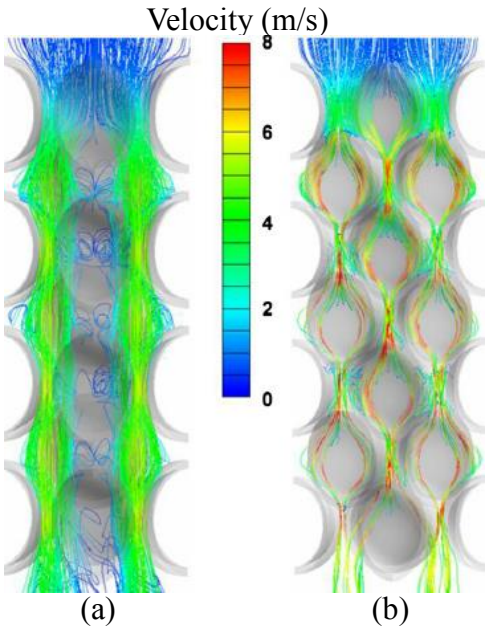

Figure 2.4: Comparison of calculated flow stream lines within the pebbles for the BCC (a) and FCC (b) arrangement

The temperature contours in Figure 2.5 provide a clear comparison between the BCC (a) and FCC (b) arrangements. The higher heat transfer capability is revealed in the FCC-arranged pebbles due to the more compact lattice and higher flow acceleration. The temperatures of the pebbles in an FCC lattice were then predicted to be lower than those in a BCC lattice, and the temperature distribution of a selected pebble was determined for both pebble arrangements. The higher temperature difference (~80 K) between the front and rear locations for a pebble in a BCC arrangement was also revealed and compared with that (~75 K) in an FCC arrangement.

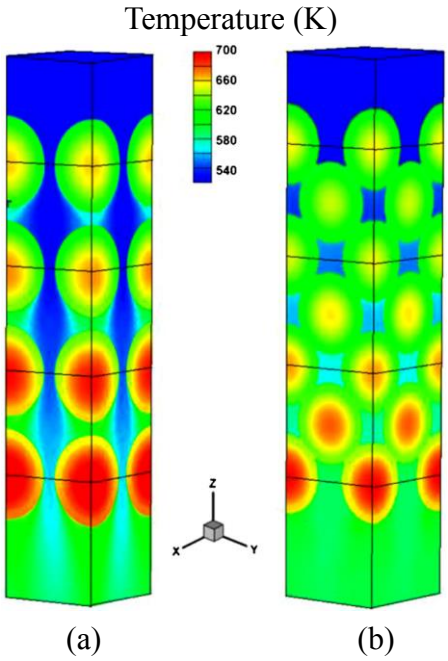

Figure 2.5: Comparison of temperature contours for the BCC (a) and FCC (b) arrangement

Shanshan Bu et al. [22] experimentally studied the flow transitions in three structured packed beds of spheres, i.e., with SC, BCC and FCC packing forms, with the electrochemical technique. Three flow regimes in the packed beds, i.e., the laminar, transition and turbulent flow regimes, were identified, with particle Reynolds numbers (Re) ranging from 20 to 1100. The microelectrodes were placed at the tube wall and inner particle surfaces to test the local flow fluctuations at the pore level; see Figure 2.6.

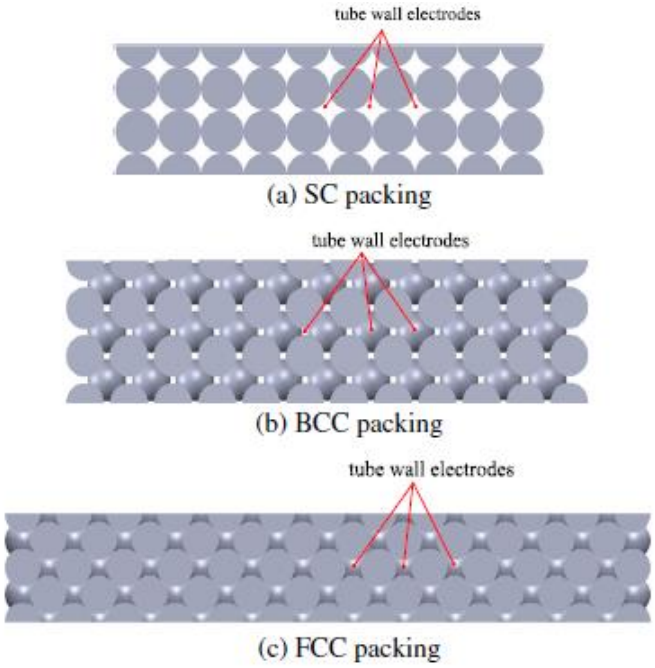

Figure 2.6: Locations of tube wall electrodes

The results were compared with the results of random packed beds from the literature. The flow transition in an SC packed bed is later than that in an FCC packed bed, considering both the end of the laminar flow regime and the onset of turbulent flow. The flow transition of the inner probes in a BCC packed bed is close to the results in random packed beds. SC and FCC packings obtain similar results near the tube wall and in the center pores, whereas for the BCC packed bed, the onset of turbulence of the tube wall probes is much later than that of the inner probes. The transition regime in the SC packed bed occurs at Reynolds numbers ranging from 260 to 430 for most electrodes, and for a BCC packed bed, laminar flow ends at Re = 130, the onset of turbulent flow for the inner probes occurs at approximately Re = 350, and that of the tube wall probes occurs at approximately Re = 580. For an FCC packed bed, the transition regime covers the range $70 < Re < 250$ for most electrodes.

Yang and Wang [23] conducted simulations of flow and heat transfer inside small pores of some novel structured packed beds; see Figure 2.7. They investigated different types of particle shapes, e.g., spherical, ellipsoidal and nonuniform spherical particles, as shown in Figure 2.8. They adopted the three-dimensional Navier-Stokes equationsand RNG k-ε turbulence model with a scalable wall function for their computations. The effects of the packing form and particle shape were investigated in detail. The major findings are as follows: With the proper selection of the packing form and particle shape, the pressure drop in the structured packed beds can be greatly reduced, and the overall heat transfer performance can be improved. In addition, the effects of both the packing form and the particle shape are significant on the flow and heat transfer in structured packed beds. The results revealed that the overall heat transfer efficiency of the SC packing is the highest for a given particle shape and is the lowest for the FCC packing. With the same physical parameters, the overall heat transfer efficiencies of the BCC and FCC packings are much higher than those of random packings, and the overall heat transfer efficiency of the SC packing is lower than that of random packing. Therefore, for the high-porosity case, random packing is recommended, whereas for the low-porosity case, structured packing forms, such as the BCC and FCC

packings, are recommended for applications. In addition, with the same packing form, such as FCC packing, the variations in the pressure drops and heat transfer performances of the spherical (FCC) and flat ellipsoidal particle (FCC-1) models are similar but are higher than those of the long ellipsoidal particle model (FCC-2). The overall heat transfer performance of the FCC-2 model is higher than those of the FCC and FCC-1 models. Furthermore, with the same packing form and particle shape, such as BCC packing with spheres, the pressure drop and heat transfer of the non-uniform packing (BCC-1) are higher than those of the uniform packing (BCC), whereas the overall heat transfer performance of the BCC-1 packing is lower.

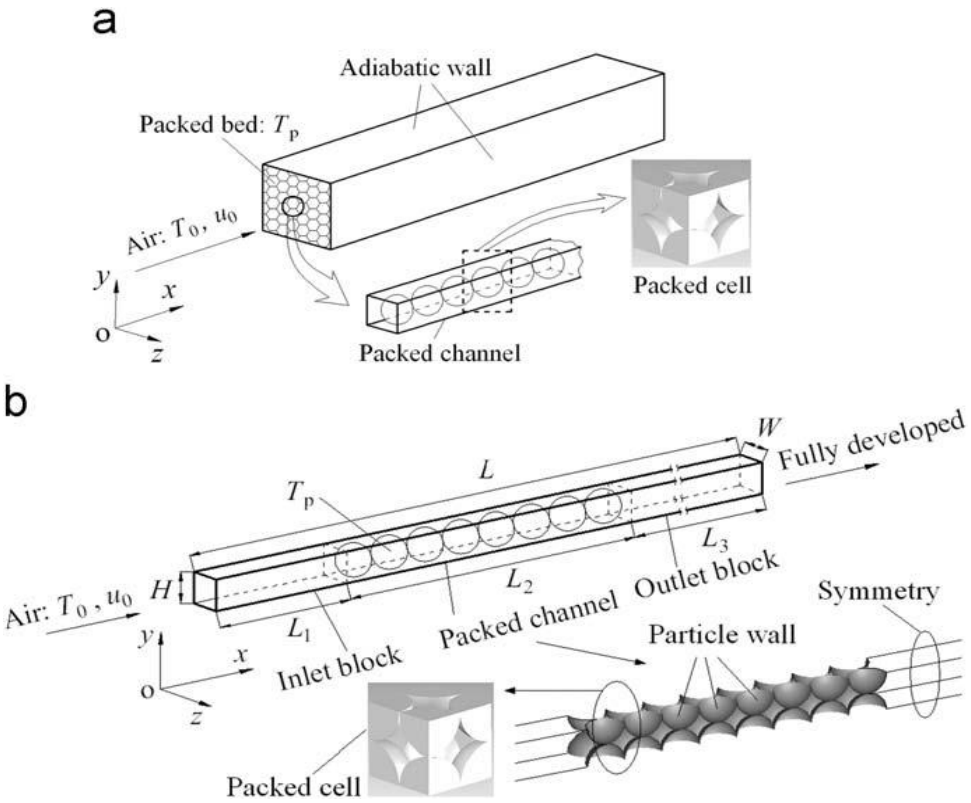

Figure 2.7: Physical model: (a) structured packed bed and (b) representative computational domain

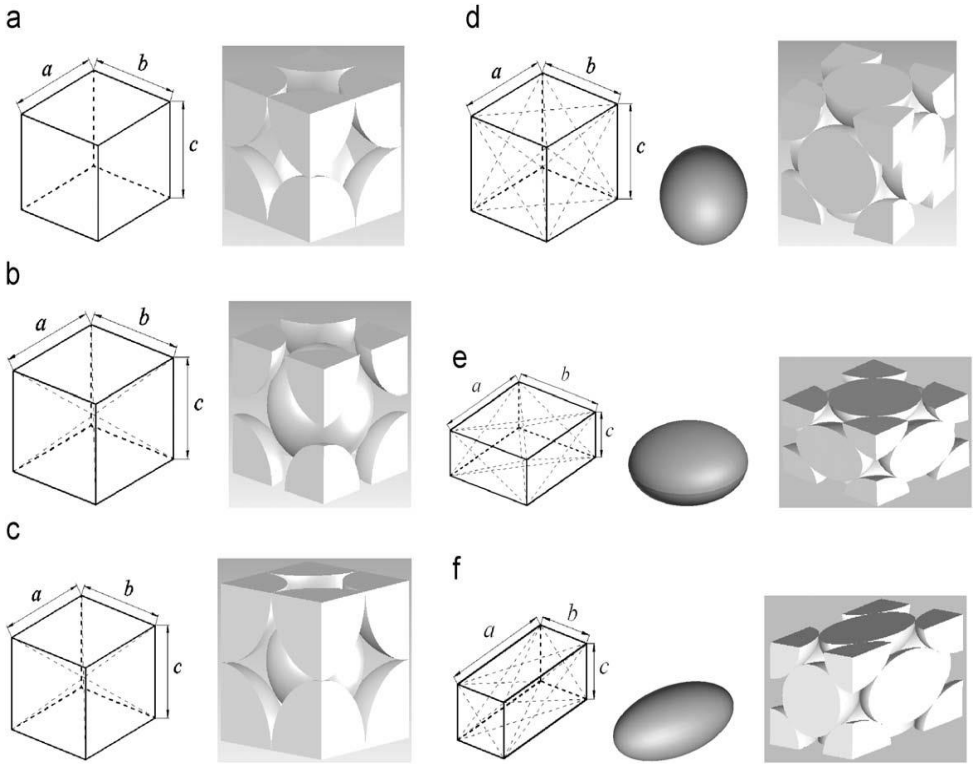

Figure 2.8: Different packed cells: (a) SC (Sphere); (b) BCC (Uniform sphere); (c) BCC-1 (Nonuniform sphere); (d) FCC (Sphere); (e) FCC-1(Flat ellipsoid) and (f) FCC-2 (Long ellipsoid)

P. Ward et al. [24] used the spectral-element CFD code Nek5000 to conduct both large eddy simulation (LES) and direct numerical simulation (DNS) of fluid flow through a single FCC sphere lattice with periodic boundary conditions; see Figure 2.9. They are also determined how the Reynolds number affects the development of asymmetries within the flow patterns: if the Reynolds number increases, the degree of symmetry also increases. The DNS was conducted with a Reynolds number of 3898 based on the inlet flow velocity and pebble diameter. In addition to the DNS, a series of LES runs were conducted at various Reynolds numbers to compare how varying the Reynolds number affected the development of turbulence. One simulation was conducted with Re = 2445, another with Re = 4551, and a third with Re = 5867. The Reynolds numbers were calculated using the inlet velocity and controlled by varying the viscosity.

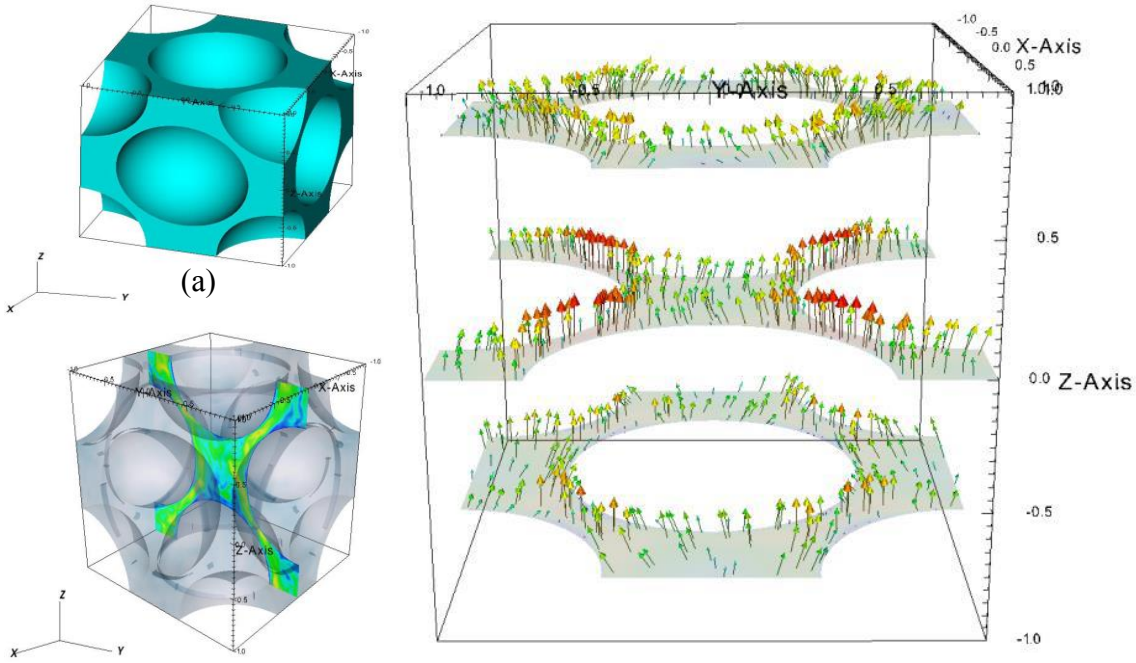

Figure 2.9: (a) Simulation domain (b) Instantaneous velocity field in the domain (c) Vector plot of velocity magnitude on three planes, each orthogonal to the z-axis.

Table 2.1 lists several works on the type of bed arrangement and different porosities.

Table 2.1: Different packed bed porosity studies

Name &Year	Field	Work	Re. No.	Bed Arrangement	Particles No.	dp mm	Porosity
Y. Ferng (21) (2013)	Fluid flow And H.T.	CFD	3716 4887	BCC FCC	8 14	25	0.38 0.29
S. Bu (22) (2015)	Fluid flow	Exp.	20-1100	SC BCC FCC	70-150	12	0.22 0.41 0.22
J. Yang (23) (2010)	Fluid flow	CFD	10 1000	SC BCC, FCC	12	12	0.49 0.34 0.28
P. Ward (24) (2014)	Fluid flow	CFD	2445 4551 5867	FCC	4	unit cell	0.26

2.1.3 Aspect ratio

The primary dimensionless property used to characterize a packed bed is the ratio between the equivalent diameter (dp) of the particle and the container diameter (D). This is referred to as the aspect ratio, which is given as

$$A_{ratio} = \frac{D}{d_p}$$

Packed beds are categorized as being of low or high aspect ratio; a tube of sand would be considered to have a high aspect ratio, whereas a tube of snooker balls would be considered to have a low aspect ratio. However, A_{ratio} = 50 is often suggested as a reasonable value to distinguish between a low- and high-aspect-ratio bed. In shaft kilns, A_{ratio} can be between 60 to 80. Usually, packed bed models with low tube-to-particle diameter ratios have been developed where temperature and flow profile gradients are mild and can be averaged. Michiel Nijemeisland and Anthony G. Dixon [25] developed a 3D model for a packed bed of spheres for N=2 and N=4. Values of the pressure drop obtained from simulations of an N=2 geometry were validated using experimental values. Flows of beds with fixed tube-to-particle diameters are sufficient for reactor design purposes. However, for flow features that contribute to the transport of heat and mass, their strong local gradients can influence reaction kinetics.

S. Sachdev et al. [26] used more practical 3D models for N=4 and N=8 with structured spherical packing; see Figure 2.10. CFD (COMSOL Multiphysics) was used to obtain the results. The nature of the results for the N=4 and N=8 models was similar, but there were differences in the values of the velocity, pressure and temperature. The values of the results obtained for the N=8 model can be considered as more practical because the packing arrangement is more realistic.

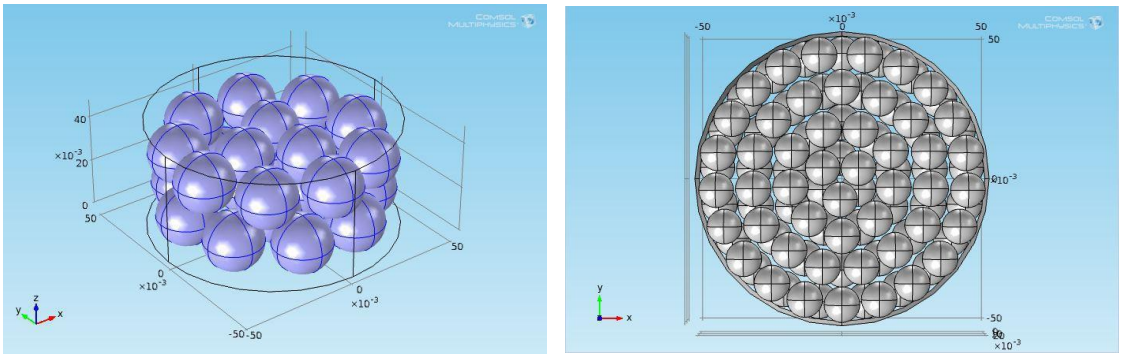

N=4 geometry N=8 geometry

Figure 2.10: Aspect Ratio

For more details about the fluid flow type and different aspect ratios, several works are listed in Table 2.2.

Table 2.2: Different aspect ratios (N) studies

Name and Year	Field	Type of work	Re. No.	Aspect ratio (N)	Particles No.	d_P mm	Porosity
Z. Xu [1] (2010)	Fluid flow	CFD	2000-12000	20	----------	100	0.4
A. Dixon [4] (2012)	Heat transfer	CFD and Exp.	2200-27000 1600-5600	5.4 7.4	1000 1250	18 13	----------
A. Dixon [25] (2013)	Fluid flow and heat	CFD	500-10000	4-8	250-800	25.4	0.43-0.46
K. Vollmari [26] (2015)	Fluid flow and pressure drop	CFD and Exp.	90-1500 50-1000	15 22	--------	7 5	0.4

2.1.4 Meshing structure

Packed beds often contain spherical media. When spheres are in contact with each other, they produce an infinitely small contact point, which is difficult for mesh generation software discretization algorithms to fully describe at this stage. This phenomenon has become one of the major constraints when analyzing packed beds using CFD approaches. Contact point problems, or highly skewed elements, do not appear in the laminar flow [29]. However, when the flow is developing toward the turbulent regime, a converged solution is unachievable. This is due to the increasing flow velocities in the fluid element around the contact points. Therefore, the mathematical domain has to be modified to reduce the skewed elements around the contact points using one of three commonly used methods (gap, overlap, and bridge). These methods have been studied by many researchers but for axial flow. This study also used these methods but for cross flow mixing through the packed bed.

The gap approach for CFD was used by (Calies et al., 2004; Nijemeisland & Dixon, 2001). The overlap method was advanced by (Guardo, Coussirat, Larrayoz, Recasens and Eguesquiza 2004), and the development of the bridge approach was facilitated by (Ookawara, Kuroki, Street and Ogawa 2007).

Anthony G. Dixon et al. [25] provided a systematic investigation into the use of different modification methods to enable CFD meshing around particle-to-particle and particle-to-wall contact points for spheres packed in a tube, therein focusing on higher flow rates typical of industrial steam reformers ($500 < Re < 10{,}000$). Three methods for flow and heat transfer were studied in test configurations, thereby allowing qualitative trends to be identified and

quantitative estimates to be made of the errors introduced by the contact point modifications; see Figure 2.11.

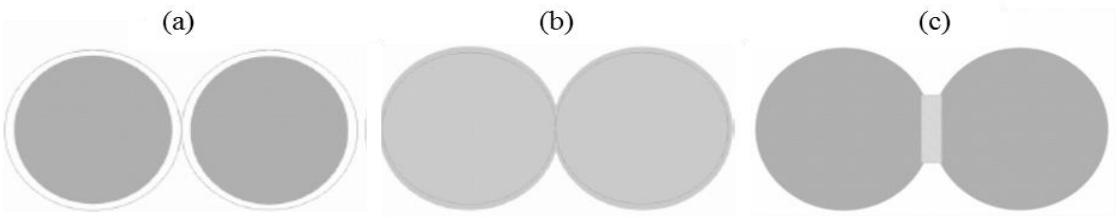

Figure 2.11: Schematics of the three contact point modifications: (a) Gaps; (b) Overlaps; (c) Bridges

This study's results indicate that global methods such as contracting or expanding all the spheres uniformly produce unacceptably high errors in both the drag coefficient and the particle-particle heat transfer rate unless the expansion or contraction is extremely small. For heat transfer work, any type of fluid gap leads to unrealistic temperature profiles and large errors in the heat flow, and overlapping particles produce an excessive heat transfer rate. They recommended the bridges method with a suitably defined effective thermal conductivity for the bridge material.

Eppinger and Seidler [17] presented a new meshing method for fixed beds consisting of spherical particles by flattening the area near particle-particle and particle-wall contact points to avoid bad cell qualities; see Figure 2.12 (a, b). The CFD simulations were performed for tube-to-particle diameter ratios of $3 \leq D/d \leq 10$ in the laminar, transitional and turbulent flow regimes and were compared with results from the literature concerning porosity and pressure drop. The whole process, consisting of the random fixed bed generation with DEM, CAD model generation, meshing and running the CFD simulation, was fully automated.

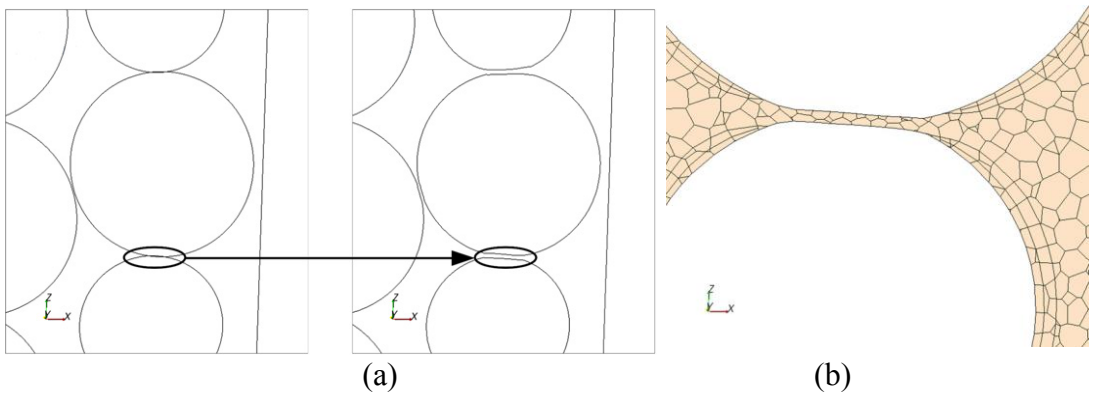

Figure 2.12: (a) Modification of near contact points. (b) Fluid cell in the artificial gap between two spheres

The modeling approach for a radially varying velocity is a significant improvement over the plug flow assumption. Nevertheless, this model cannot account for regions with stagnant or back flow. The influence of such regions has to be investigated.

In Figure 2.13, all volume cells with zero or negative velocity are displayed. The volume fraction of this region increases with increasing Re-number and reaches a value of approximately 13%. This influences the residence time distribution: the residence time is short in the near-wall region, whereas the residence time in regions with stagnant or back flow is high. They found that CFD simulations of fixed bed reactors with a small D/d ratio are helpful and reasonable for obtaining a better understanding of lab-scale packed bed reactors. Additionally, the number of cells increases when the number of spheres increases at the same D/h ratio. Their findings are supported by models with low aspect ratios (3-10), but in our work, the aspect ratio is 9.

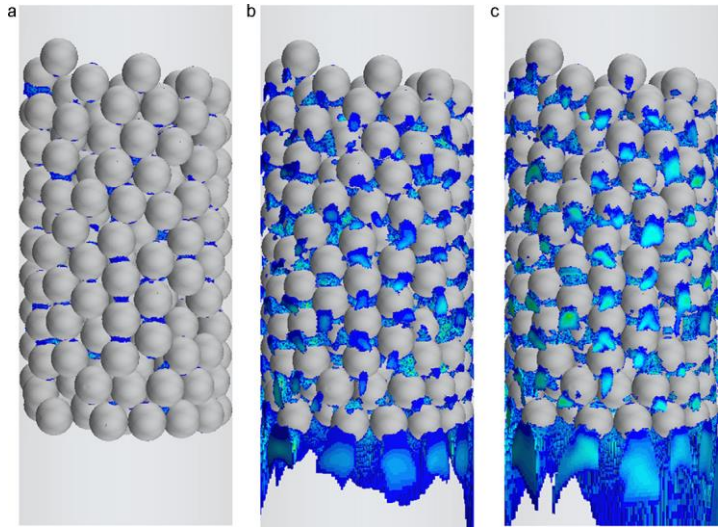

Figure 2.13: Regions with zero or negative velocities for (a) Re_P = 1, (b) Re_P = 100 and (c) Re_P = 1000

There remain doubts about when the turbulence model should be valid in a packed bed because there are no reliable guidelines for predicting the flow transition in complex geometries such as fixed bed reactors and extraction equipment [30].

The numerical treatment of the inter-pebble regions in the modeling of a packed bed geometry was studied by Lee and Park [31] for the CFD analysis of a pebble bed reactor, where the pebbles are in contact with each other. They assumed a closely packed geometry of the BCC type for the PBR to examine the effects of the treatments with different contact pebble spacings in simulations of the PBR core. Two cases, PB-1 and PB-2, were considered in the simulation of the PBR, a 1 mm gap and contact regions between adjacent pebbles; see Figure 2.14.

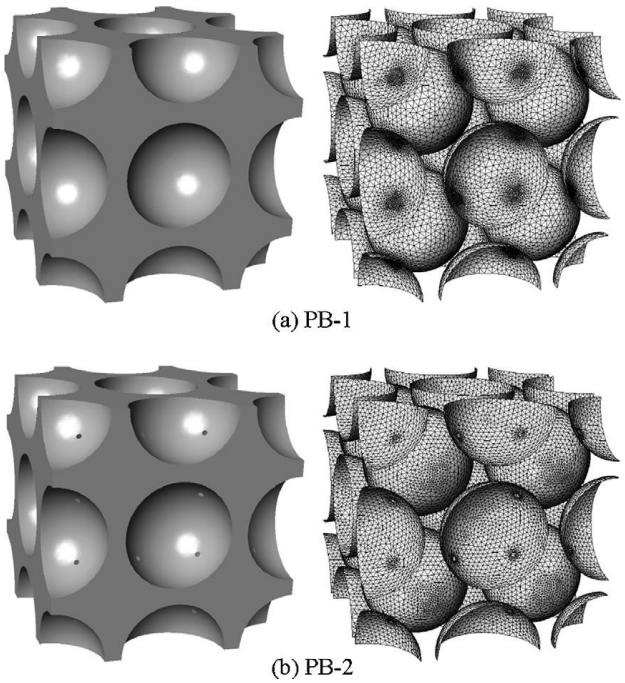

Figure 2.14: Packed bed geometries and grid systems

The modeling results for PB-2 indicated generation of additional hot spots on the pebble surface, where the local temperatures were significantly higher than those of the other regions. Large vortices were generated in the vicinity of the contact regions due to the blockage of the coolant flow. This finally caused a decrease in the local heat transfer in these regions. From these results, it is evident that the treatment of the contacts among the pebbles with approximated gaps may give inaccurate information about the local flow fields despite the advantages of this method in terms of the simplification of the calculations as well as that of the problems in mesh generation. However, their results showed numerous differences in the flow fields and heat transfer compared to the cases using the gap approximation; see Figure 2.15.

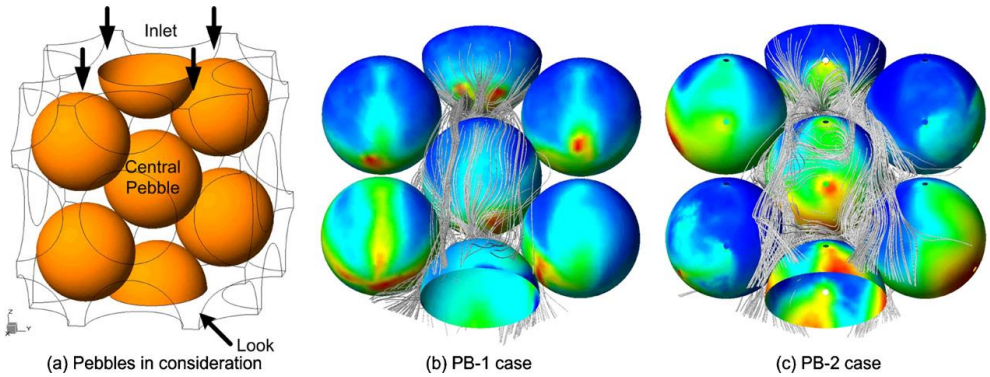

Figure 2.15: Instantaneous flow path of coolant near the central pebble and surface temperature distribution

Augiera and Idouxa [32] investigated the flow transport and heat transfer properties inside packed beds of spherical particles by CFD simulations. They studied the treatment of contact

points between particles with a few particles. A dense packing (φ= 33%) of spheres using a DEM was adopted. Then, they computed the heat and mass transfer properties of fluid flow in the packed bed at low to moderate Reynolds numbers (1 < Re < 80). They showed that a contraction of particles is necessary to perform finite-volume flow simulations inside packed beds. Furthermore, they used two different volumes of hundreds of particles with and without walls. They found that the contraction of particles applied to the packing leads to underestimates. However, they easily corrected this using a function of the porosity modification induced by the contraction; see Figure 2.16 (a, b).

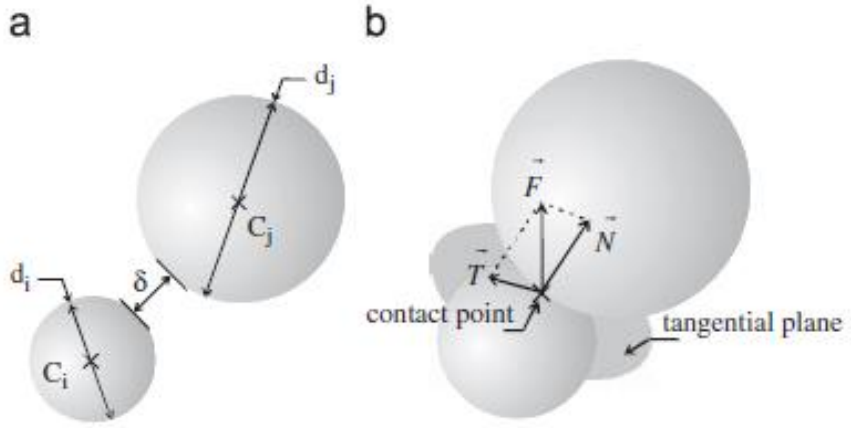

Figure 2.16: (a) Geometrical parameter and gap between particles, (b) contact force components between particles

2.1.5 Flow regimes and turbulence

The study of flows through packed beds is complex and difficult due to the disordered characteristics. In a high-aspect-ratio bed, the flow is disturbed, but it can be considered homogeneous due to the relatively uniform size of the voids. In a low-aspect-ratio bed, the bed structure is considerably more disturbed, with large voids increasing the velocity channeling. The flow through packed beds can also be characterized by the Reynolds number. The flow can be described as laminar (Redp < 10), transitional (10 < Redp < 300) or turbulent (Redp > 300). In many applications of packed beds, the Re number is defined as

$$Re_{dp} = \frac{\rho U dp}{\mu}$$

Freunda and Zeiser [33] used new numerical methods to simulate in detail single-phase reacting flows in such reactors. They developed a three-dimensional (3D) structure of random packings to resolve local homogeneities for various tube-to-particle diameter ratios (aspect ratio = 5), L/dp = 7.5, and φ = 0.444, with approximately 150 spheres in total.

This study demonstrated that the simulations provide knowledge that very often cannot (or only with much effort) be obtained in such detail by experimental approaches. The results showed that the local structure of the packed bed has a significant impact on the global fluid dynamical characteristics. Furthermore, axially and circumferentially averaged radial velocity profiles predict velocity peaks of approximately 2.5–3 times the superficial velocity in the

near-wall region, and locally maximum velocities occur that are more than 8 times higher than the superficial velocity. They also concluded that a packing with almost the same mean porosity features pressure drops varying by more than 4%.

Hassan [34] performed a simulation of turbulent transport for a gas through the gaps of the spherical fuel using a large eddy simulation in an HTGR. His study facilitated the understanding of highly three-dimensional, complex flow phenomena caused by flow curvature in the pebble bed. Resolving all the scales of a turbulent flow is too costly, whereas applying highly empirical turbulence models to complex problems can produce inaccurate simulation results. He concluded that the LES could help in understanding the highly complicated flow structure induced by the curvature of the pebbles. Note that the LES is a time-dependent method. Eddies were created and destroyed quickly between the pebbles due to the high Reynolds number in the simulation.

The temperature distribution within the packed bed was calculated. As shown in Figure 2.17, it is clear that a higher temperature is obtained at several local positions where fluid separation occurs. It should be noted that the difference between the high temperature (red) and low temperature (blue) is approximately 5°C.

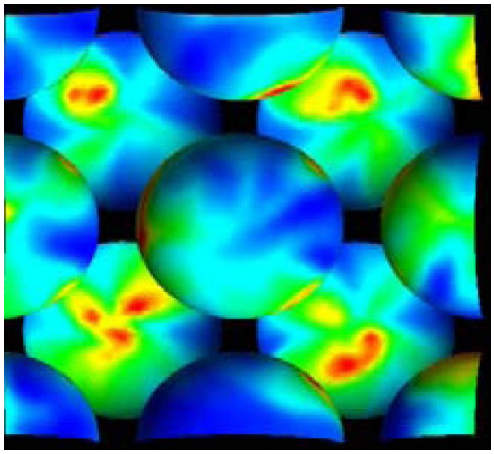

Figure 2.17: Temperature distributions on the pebbles of the packed bed at the outlet region.

A new pseudo-continuous model was developed by Eisfelda and Schnitzleinb [35] for the fluid flow within packed bed reactors by formulating the Navier–Stokes equations for a statistically described domain geometry. This technique gives an additional term for representing the fluid solid interaction due to the particle boundaries in the packing. They found a good agreement with correlations and experiments for the predictions of the pressure drop and the radial distribution of the axial velocity. The maximum deviation of the pressure drop was 16.4%. They found that such large deviations occur only at very low Reynolds numbers and at very low aspect ratios. The velocity predictions are compared to experimental work, and a good agreement is obtained for Reynolds numbers of Re_{dp} = 4 and 532. They concluded that the pressure drop is influenced by the aspect ratio and low Reynolds numbers.

Freund and Bauer [19] studied the fluid flow and mass transport by presenting a clear and comprehensive approach that can serve as a strategy for the detailed numerical simulation of the fluid flow and mass transport in fixed beds. They simulated the fluid flow and mass transport for SC and random packing geometries, and they discussed axial and radial porosity distributions, therein noting that the oscillating behavior is damped with increasing wall distance under the random packing. They obtained a detailed 3D flow field by applying the lattice Boltzmann method for the calculation of the flow field under the random packing geometry and compared their results to experimental MRI data. The agreement between experimental and simulation results was good. They showed that, for uniform (SC) packing, the flow oscillation is strong and remains unchanged through the bed.

For additional details about the fluid flow type and turbulence models, several works are listed in Table 2.3.

Table 2.3: Different turbulence models studies

Name and Year	Field	Type of work	Re. No.	Turbulence model and method
M. Baker [8] 2010	Fluid flow	CFD and Exp.	700-5000	k-ω
T. Atmakidis [15] 2009	Pressure drop	CFD	63	Monte Carlo
A. Dixon [27] 2013	Fluid flow and heat	CFD	500-10000	(SST)k-ω
K. Vollmari [28] 2015	Fluid flow and pressure drop	CFD and Exp.	90-1500 50-1000	DEM
H. Bai [44] 2009	Fluid flow and pressure drop	CFD and Exp.	2000-20000	RNG k-Є

2.2 Modeling of Packed Bed using Porous Medium

There are two main approaches for the CFD simulation of the geometry of closely packed pebbles: the porous approach and the realistic approach. In the porous approach, an averaged concept of porosity is applied to simulate the closely packed geometry. Van Rooyen et al. [36] demonstrated that a model with the porous approach could accurately predict the distributions of flow velocity, pressure, temperature, etc. within hollow fiber bundles.

The widely applied resistance model for flow through porous media was proposed by Ergun (1952). This model is called the Ergun equation, which is often used to analyze the resistance or pressure drop for flow through porous media (Vafai and Tien [37]; Khaled and Vafai [38]; Jiang et al. [39]).
The Ergun equation, which has been considered for porous media in recent decades, is expressed as

$$\frac{\Delta P}{L} = 150.\frac{(1-\varepsilon)^2}{\varepsilon^3}.\frac{\mu.U}{d_p^2} + 1.75.\frac{1-\varepsilon}{\varepsilon^3}.\frac{\rho.U^2}{d_p}$$

The first term on the right is for the viscous energy loss in laminar flow when the modified Reynolds number ($R_{ep} = (\frac{D_p \rho v}{\mu})(1-\varepsilon)^2$) is less than 10, and the second term on the rate denotes the kinetic energy loss primarily in turbulent flow when the modified Reynolds number is higher than 100. The Ergun equation is examined from the perspective of its dependence upon the flow rate, the properties of the fluids, the porosity, the orientation, the size, the shape, and the particle surfaces. According to the Ergun equation, the orientation of the randomly packed beds does not have an influence in the exact mathematical formulation.
Wu and Yu [40] developed a new model for the resistance of flow through porous media. Their model is expressed as a function of porosity, the ratio of the pore diameter to the throat diameter, the diameter of the particles, and fluid properties. The two empirical constants, 150 and 1.75, in the Ergun equation are replaced by two expressions, which are explicitly related to the pore geometry.

Hellström and Lundström [41] modeled the flow through porous media considering inertia-force effects. They used an empirically derived Ergun equation to describe the mechanisms of the flow. They performed a micromechanically based study of moderate Re flow between parallel cylinders using a CFD approach. The high-quality CFD simulations were performed with the commercial software ANSYS CFX using grid refinement techniques, and the iteration error was sufficiently small. Their main results were that the Ergun equation fits the simulated data well up to Re = 20, although the inertia effects must be considered when the Re is greater than 10.

The porous approach was applied by Rasul et al. [7] to model and simulate the thermodynamic process of vertical shaft kilns. The combustion, particle-gas dynamics and heat transfer processes were modeled by an Eulerian multiphase model and species transport and finite volume chemical reaction model. Although the authors declared that the simulated results showed a reasonably good agreement with designed data, the temperature profile through the kiln seemed too high to be realistic due to the steady state assumption and the exclusion of the decomposition process of dolomite.

Wu and Ferng [30] adopted pebble bed geometry for HTGRs. They investigated the thermal-hydraulic behaviors in a segment of pebbles predicted by the RANS CFD model using porous and realistic approaches for the complicated geometry. They revealed the advantages of each approach's methodology for a closely packed pebble geometry by comparing the calculated results. A CFD simulation with the porous approach for the pebble geometry can quickly and reasonably capture the averaged behaviors of the thermal-hydraulic parameters as the gas flows through the core, including the pressure drop and temperature increase. For realistic approaches they used a segment of 28 pebbles, including 16 full pebbles, 16 half pebbles, and 16 quarter pebbles. The corresponding mesh distributions for the two approaches are shown in Figure 2.18, where (a, b) show the three-dimensional (3D) views of the mesh models for the realistic and porous approaches for the closely packed spheres.

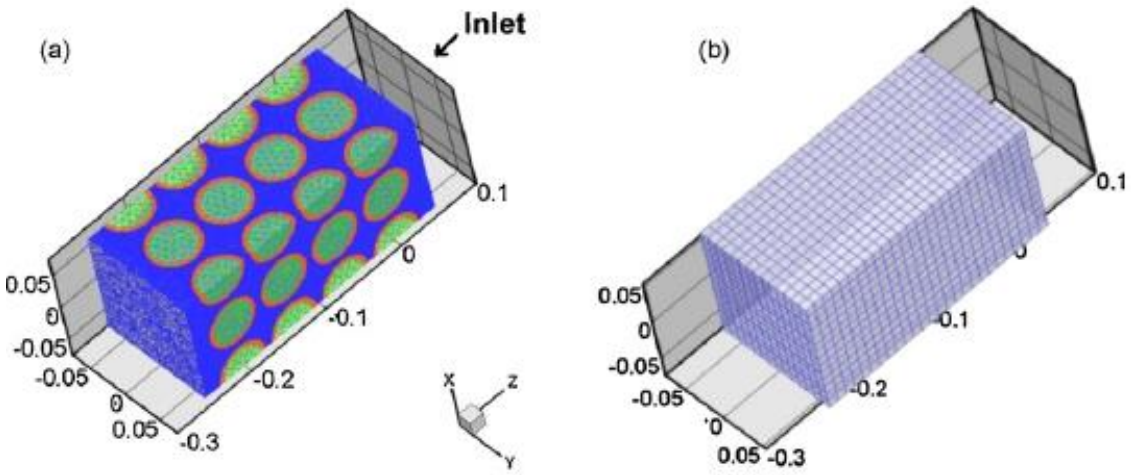

Figure 2.18: Schematics of mesh models (a) in 3D form for the realistic approach and (b) in 3D form for the porous approach [30]

In the realistic approach, approximately 2 million meshes are used in their simulation; however, only approximately 26,000 uniform grids are used in the porous approach. The computation time for the simulation with the realistic approach is 62,414 sec, and that for the porous approach is approximately 26 sec. They concluded that the realistic approach can reasonably simulate the thermal-hydraulic characteristics within the closely packed sphere geometry, including the vortices and flow separation in the pores and the temperature variation around the sphere surfaces. However, these characteristics cannot be captured by a CFD simulation with the porous approach; see Figure 2.19.

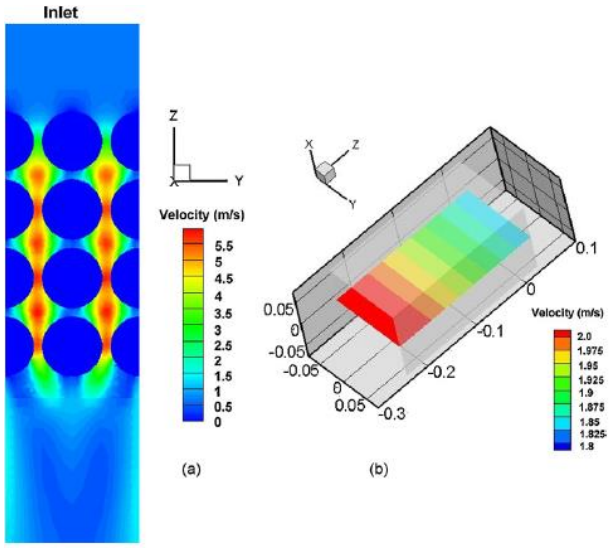

Figure 2.19: 2D temperature contours for (a) the realistic approach and (b) the porous approach [30]

The above studies showed that there is substantial knowledge of flow transition, mass transfer and pressure drop in randomly and structured packed beds. In a shaft kiln, for the heat treatment of granular material, the fuel and a part of the combustion air are injected radially. The cooling air flows from the bottom. The mixing behavior of these two flows is important for the temperature distribution in the cross section and therefore the quality of the product. These kilns have a diameter of up to 4 meters. The industrial processing shows that the penetration depth of the radial flow is relatively low. This mixing behavior remains poorly researched. This study addresses a numerical and an experimental investigation.

Therefore, two beds were used in the experiment in this study:

1) A structured bed with ceramic spheres 52 mm in diameter in a SC and BCC packing's of bed.
2) An unstructured bed with glass beads 4 mm in diameter and clinker non-spherical particles 2-6 mm in diameter.

3. Experimental work

3.1 Experimental Apparatus

Experimental measurements inside the shaft kilns are very expensive and very complicated because the kilns are designed for production purposes and not for measurements. The experimental setup was constructed to investigate the flow mixing in the packed bed. A schematic representation of the experimental system is shown in Figure 3.1. This system consists of cubic boxes as a packed bed, serve boxes for the distribution of air from the bottom of the packed bed, a centrifugal air blower, a package of nitrogen bottles, a rotameter, a gas analyzer, a data evaluation system and control devices for the monitoring and adjusting the operating parameters.

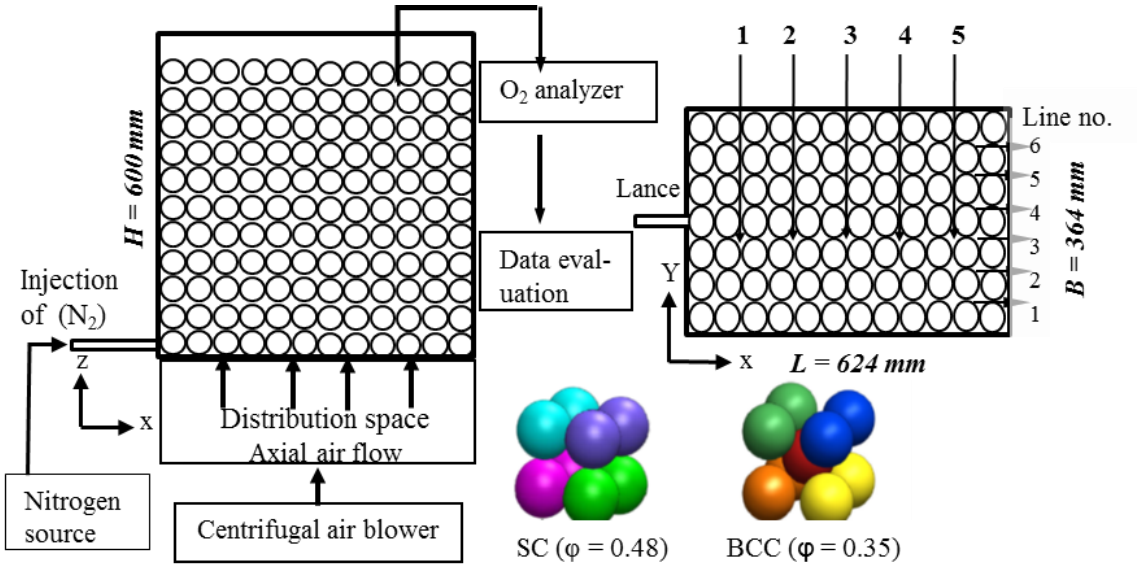

Figure 3.1: Schematic description of the experimental setup for the structured bed.

3.2 Detailed description of the experimental apparatus

3.2.1 Test box with beds

The test section box has a length L = 0.624 m, width B = 0.364 m and height H = 0.6 m. Figure 3.2 shows the packed beds constructed using the structured and unstructured packing of spheres and glass beads.

a **b**

Figure 3.2: Test box a) structured bed with ceramic spheres and (b) unstructured bed with glass beads.

The structured packing of ceramic spheres with a diameter d_P = 52 mm consists of an SC or BCC packed bed. The unstructured packing includes a monodispersed particle bed constructed using small glass beads of d_P = 4 mm and a polydispersed particle bed of arbitrary shape and size of cement clinker particles of d_P = 2-6 mm. Figure 3.3 shows the two structured packing forms, i.e., SC and BCC (a), and two unstructured beds (b).

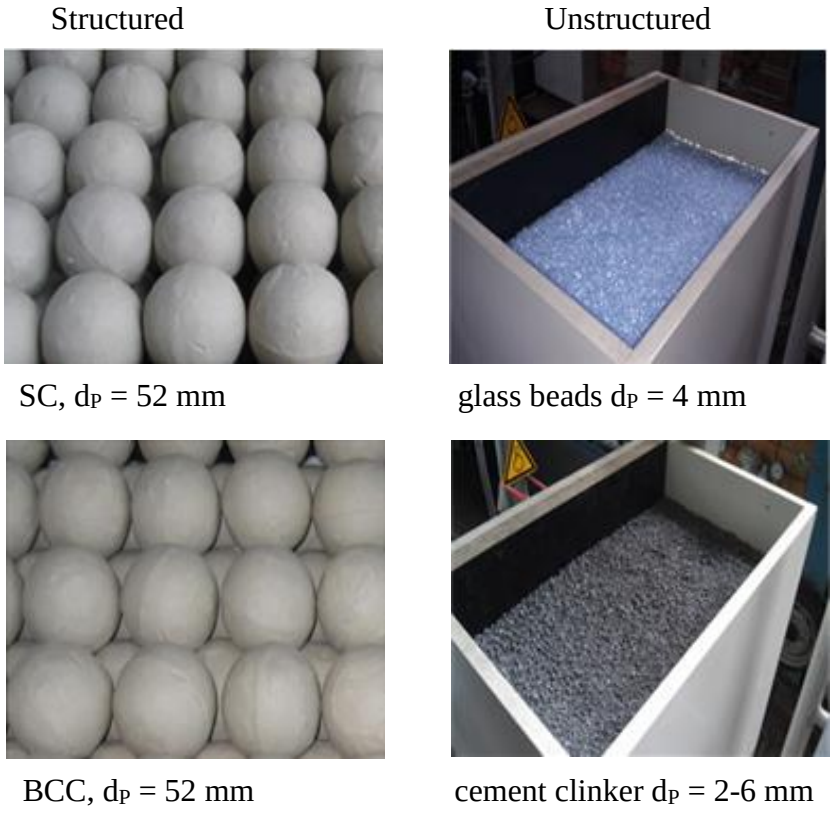

Figure 3.3: (a) Structured bed packing (b) Unstructured bed particles

The structured bed is identified by three parameters: layers, columns and rows. The layers parameter is the number of spheres in the vertical direction (box height), the columns parameter is the number of spheres in the cross-flow direction (box length), and the rows parameter is the number of spheres in the Y direction (box width). For the first setting, i.e., SC, the ceramic spheres, with diameter of 0.052 m, are lying on top of each other, as represented in Figure 3.3(a). This structure results in 11 layers, with 7 columns and 12 rows of ceramic spheres, for a total of 924 spheres. This arrangement leads to a porosity of $\varphi = 0.48$, which agrees with the nominal porosity for this arrangement. For the second setting, i.e., BCC, the spheres constituting the next layer lie in the hollow space of the lower layer. The offset of the spheres results in 7 layers with 7 columns and 12 rows and 6 layers with 6 columns and 11 rows of ceramic spheres, totaling 984 spheres. Therefore, the local porosity of this arrangement is $\varphi = 0.35$, and the nominal porosity is $\varphi = 0.39$. The porosity of unstructured packing for the cement clinker is $\varphi = 0.35$, and that for glass beads is $\varphi = 0.4$.

Each of these materials affects the flow form due to the use of particles of different shapes and sizes, as well as different porosities resulting from the different arrangements.

Table 3.1 shows the relationship between porosity with packing settings.

Table 3.1: Description of porosity in each packing setting

Bed	d_P (mm)	Packing	Porosity	Bed height (m)	Bed volume (m^3)
Ceramic spheres	52	structured SC	0.48	0.572	0.130
Ceramic spheres	52	structured BCC	0.35	0.489	0.111
Cement clinker	2-6	unstructured	0.35	0.5	0.1136
Glass beads	4	unstructured	0.4	0.5	0.1136

3.2.2 Distribution space with perforated plate

During the experiments, two gases, air and nitrogen, were mixed together. Ambient air was blown through the packed bed from the bottom of the test section box through a perforated plate with 66 holes, each hole having a diameter of 20 mm, therein presenting a high flow resistance and an open area of 9% (high flow resistance). A serve box has been arranged (placed) below the perforated plate to ensure a good distribution of the injected air.

The volumetric flow rate of the air was measured using a rotameter with an error of ±0.015 $m^3.s^{-1}$. Different series of axial air flow rates ($\dot{V}_{ax}$ =40, 83, 150 and 250 $m^3.h^{-1}$) were tested. Figure 3.1 shows the top view of the five locations for the measurements. A lance was attached to the box, from which nitrogen was injected perpendicular to the air flow. The

volumetric flow rate of the nitrogen, coming from a package of N_2 bottles, was measured using a rotameter with an error of ±0.01 $m^3\ s^{-1}$. Three injection flow rates ($\dot{V}_i$ =5, 15 and 25 $m^3.h^{-1}$) were tested. Three lances, with inner diameters of 6, 12 and 20 mm, were used. The experiments were performed with the lance at positions of 0, 0.156 and 0.312 m. To inject the nitrogen gas into the test chamber, a hole 26 mm in diameter was drilled into the lateral-end face of the test room. It was located at a height of 26 mm, i.e., in the middle of the lowest layer of packing material. Through this hole, a lance was inserted as shown in Figure 3.2 a.

The molar concentration of the oxygen was measured at different positions in the bed using a gas analyzer with an accuracy of ±0.2 vol. %, resolution of 0.01 vol. % and a response time of 20 sec. Figure 3.4 shows the flue gas analyzer. The lance was placed in the bed, and a small part of the gas mixture was vacuumed out. The measurements could be performed from three directions, i.e., the X, Y and Z directions, because the lance of the gas analyzer could be inserted through the gap between the spheres. There were five measuring positions in the X-direction (0.104, 0.208, 0.312, 0.416 and 0.520 m) for the ceramic sphere packing shown in Figure 3.1. There were 11 fixed positions for the cement clinker and glass bead particles. The measurements were performed at two different heights in the Z direction (0.260 and 0.468 m) by fixing the lance of the gas analyzer to ensure the correct location at which the probe was placed. Concentration profiles were used to analyze the experiments at varying operating parameters and for the comparison with the results under the utilized parameters. The results of these experiments are compared with the results obtained from CFD simulations. The mixing is limited by the extent of the O_2 distributed through the bed, which in turn depends mainly on the supplied amount of nitrogen.

Figure 3.4: Testo 350 XL flue gas analyzer

The measurements could be taken from three directions, X, Y and Z, under the SC arrangement, and the lance of the gas analyzer could be inserted through the gaps between the spheres. However, under the BCC arrangement, the measurements could only be taken in the second layer from the top in the Z direction because there is no gap between the spheres. Therefore, to obtain measurements at different levels, it was necessary to make a hole through the spheres. The measurements were taken at three different levels in the Z direction, i.e., at 0.26 m and 0.468 m under the SC setting and at 0.459 m under the BCC setting. Experiments

were conducted by varying the following parameters: lance diameter, lance position, porosity, measurement level, injection flow rate and axial flow rate.

For the unstructured packing, the test room was packed by pouring the particles into the room. A fine metal mesh was placed at the bottom of the test room to prevent small particles from dropping through the perforated plate into the distribution space box. Two types of packing material are used, cement clinker and glass beads, by emptying the test section, refilling it, and taking a set of measurements.

The operating conditions considered for the experiments are listed in Table 3.2 and Table 3.3.

Table 3.2: The operating conditions for the SC packing bed

Air flow			Nitrogen flow				Volume flow ratio
$m^3 \cdot h^{-1}$	Superficial Velocity ($m \cdot s^{-1}$)	Real velocity ($m \cdot s^{-1}$)	$m^3 \cdot h^{-1}$	Lance diameter (mm) 6	12	20	
				Velocity, $m \cdot s^{-1}$			
40	0.050	0.102	5	-	12.5	4.5	0.125
			15	-	37.0	13.5	0.375
			25	-	62.4	22.4	0.625
83	0.101	0.210	5	50	12.5	4.5	0.060
			15	150	37.0	13.5	0.180
			25	-	62.4	22.4	0.301
150	0.183	0.381	5	50	12.5	4.5	0.033
			15	150	37.0	13.5	0.099
			25	-	62.4	22.4	0.166
250	0.306	0.637	5	-	12.5	4.5	0.020
			15	-	37.0	13.5	0.060
			25	-	62.4	22.4	0.100

Table 3.3: The operating conditions for the BCC packing bed

Air flow			Nitrogen flow				
				Lance diameter (mm)			Volume flow ratio
$m^3 \cdot h^{-1}$	Superficial Velocity ($m \cdot s^{-1}$)	Real velocity ($m \cdot s^{-1}$)	$m^3 \cdot h^{-1}$	6	12	20	
				Velocity, $m \cdot s^{-1}$			
40	0.050	0.142	5	-	12.5	4.5	0.125
			15	-	37.0	13.5	0.375
			25	-	62.4	22.4	0.625
83	0.101	0.288	5	50	12.5	4.5	0.060
			15	150	37.0	13.5	0.180
			25	-	62.4	22.4	0.301
150	0.183	0.523	5	50	12.5	4.5	0.033
			15	150	37.0	13.5	0.099
			25	-	62.4	22.4	0.166
250	0.306	0.874	5	-	12.5	4.5	0.020
			15	-	37.0	13.5	0.060
			25	-	62.4	22.4	0.100

3.3 Experimental results and discussion

3.3.1 Measuring height

The effect of the measuring height on the O_2 concentration is first discussed using the SC arrangement for the case of a structured bed. The lance of the gas analyzer was inserted from the top into the gap between the particles and placed at a level of 0.26 m and 0.468 m. The volumetric flow rate ratio ($\dot{V}_R$) of the injection flow of N_2 ($\dot{V}_i$) to the axial flow of air ($\dot{V}_{ax}$) was 0.625. Figure 3.5 shows the measured O_2 concentration versus the injection direction for different lance positions (x_L). When the lance was at 0 m (x_L= 0 m), the O_2 concentration increased slowly with increasing distance from the injection position and reached a value of approximately 10%. Then, it increased with an increasing slope. The O_2 concentration increased much faster after X = 0.4 m and reached approximately 19%. The N_2, therefore, did not penetrate past this position. The profiles for the O_2 concentration are also shown for the other two positions of the lance, i.e., x_L= 0.156 m and x_L= 0.312 m. The O_2 concentration remained almost constant at a value of 10% for different measurement positions.

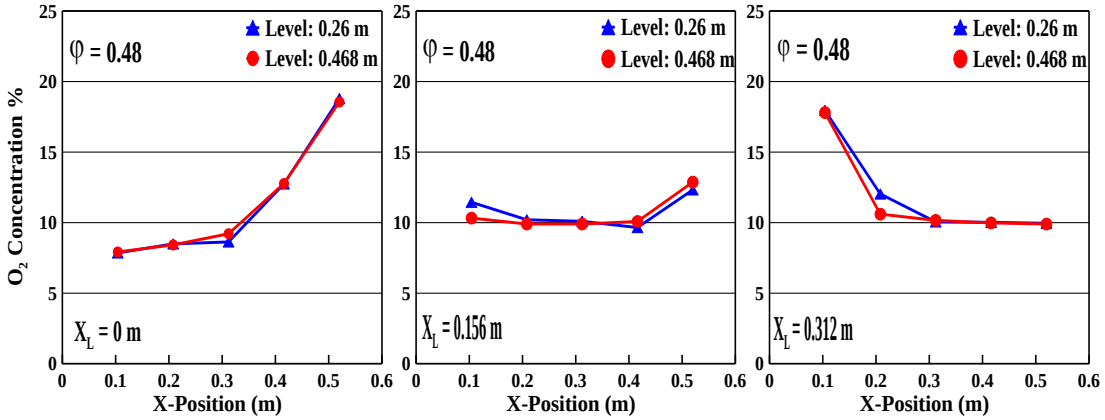

Figure 3.5: Effect of measurement level on the O_2 concentration with different lance positions for the structured bed (d_P = 0.052 m, d_L= 0.02 m, $\dot{V}_R$ = 0.625)

It can be noted that the O_2 concentration is independent of the level of the measurement. Therefore the next measurements are performed only at one position, i.e., 0.459 m, for the case of the BCC arrangement due to the complexity of the structure. Therefore, measurements are shown in the figures only at a position of 0.468 m for the SC packing so that the results could be composed.

For an unstructured bed composed of glass bead particles (d_p=4 mm), 11 fixed points were used for measurements, and the measurements were taken at two heights in the Z direction: 0.223 m and 0.473 m. Figure 3.6 shows the schematic diagram of the experimental setup for the unstructured bed.

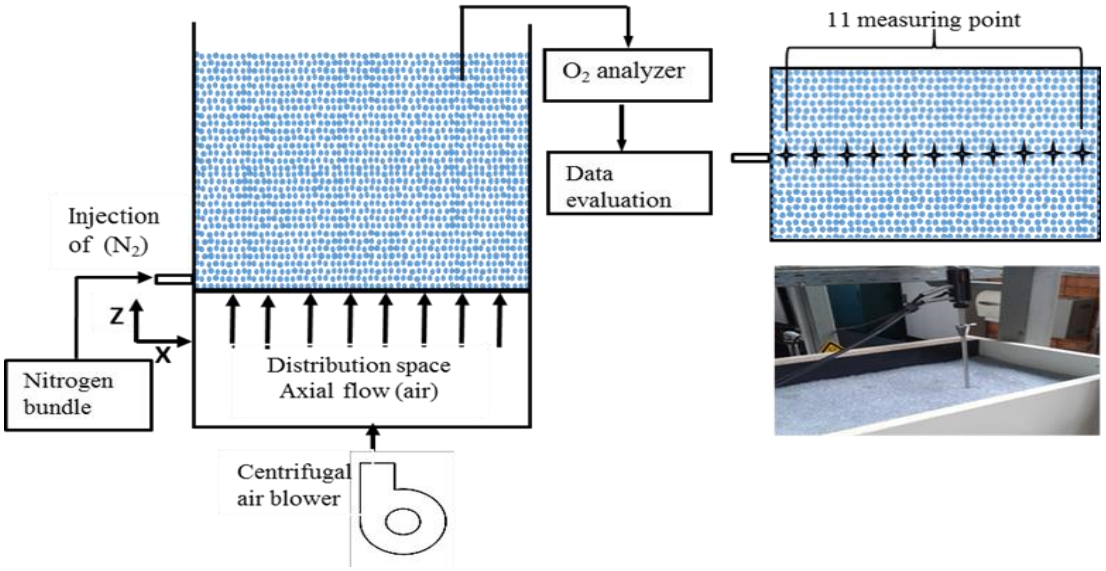

Figure 3.6: Schematic description of the experimental setup for the unstructured bed

Figure 3.7 shows the effect of the measuring level on the O_2 concentration for different lance positions for an unstructured bed of porosity 0.4 with 3 different lance positions. The measurement level does not affect the O_2 concentration. In the case of an unstructured bed also, there is a different profile for the O_2 concentration that persists compared to the case of the structured bed. Furthermore, a sharp increase in the O_2 concentration could be seen after 0.15 m in the injection direction for lance positions of 0 and 0.156 m. Symmetric curves are noticed for the O_2 concentration at both sides of the injection when the injection position is 0.312 m; in addition, the O_2 concentration has a value of 0% until 0.1 m from the injection position at both sides. The value increases and finally reaches 21%.

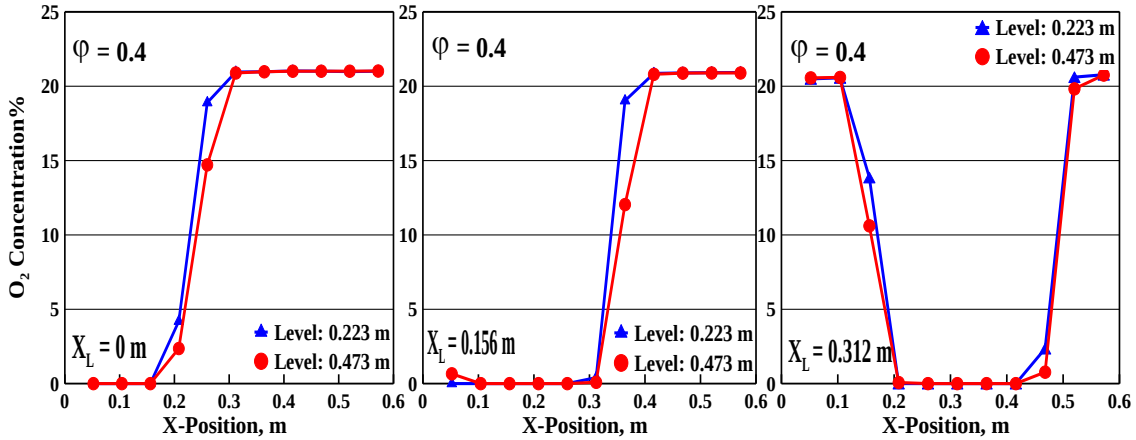

Figure 3.7: Effect of measuring level on the O_2 concentration with different lance positions for the unstructured bed (d_P = 0.004 m, d_L= 0.02 m, $\dot{V}_R$ = 0.625)

3.3.2 Lance diameter

Figure 3.8 a, b demonstrates how the three different lance diameters (6, 12, and 20 mm) affect the O_2 concentration. For a structured bed with φ = 0.48, the concentration curve for the case of the high volume ratio for all injection velocities exhibits a linear trend. However, for the low volume ratio, the O_2 concentration achieves a higher value at the first position of the measurement, later decreases to a minimum and finally increases again with increasing distance from the injection position. As a result, the distribution in the bed is not good at low $\dot{V}_R$; at higher $\dot{V}_R$, the concentration profile in the bed is uniform. For the case of an unstructured bed (small particles) with φ = 0.4, it can be concluded that the O_2 concentration does not change if the diameter of the lance changes for different $\dot{V}_R$.

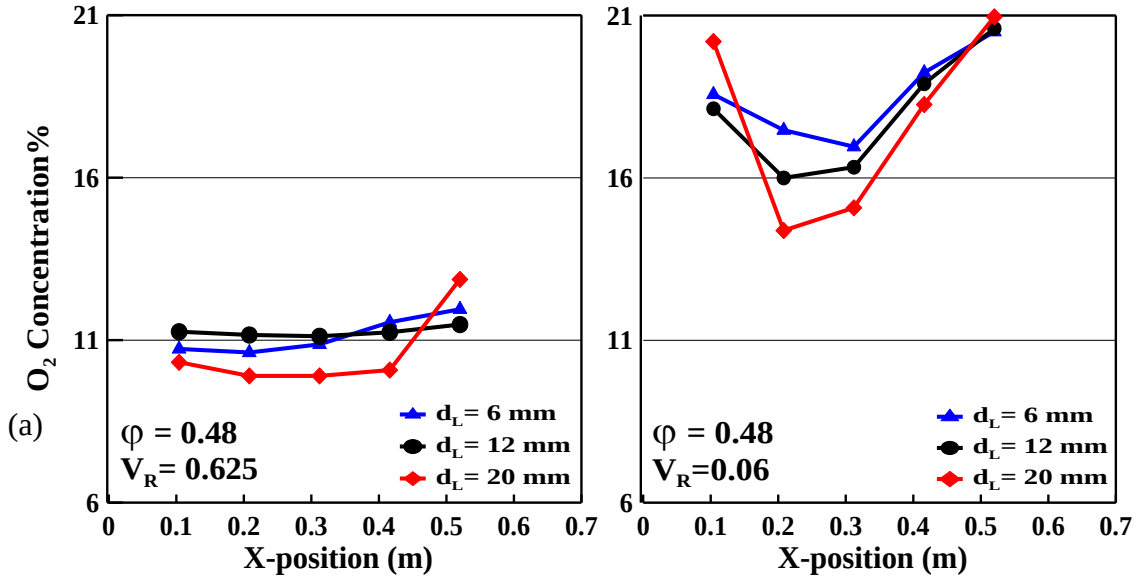

(a)

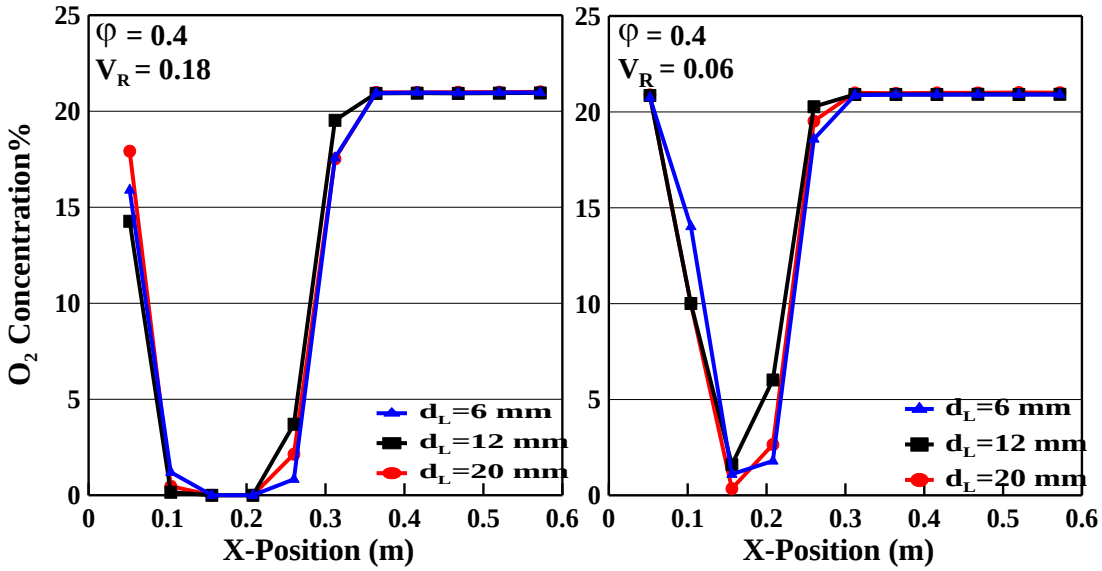

(b)

Figure 3.8: Effect of the lance diameter (injection velocity) on the O_2 concentration for a) ceramic spheres at measuring level of 0.468 mm and b) glass beads at measuring level of 0.473 mm; x_L= 0.156 m.

3.3.3 Volumetric flow rate

Effect of air (axial flow rate)

For the structured bed, under both arrangements (SC and BCC), Figure 3.9 shows the effects of the axial flow rate on the O_2 concentration in the bed. The upper curves are for the SC packing with a porosity of 0.48, and the lower curves are for the BCC packing with a porosity of 0.35. The measurements were conducted using injection flow rates of $\dot{V}_i$ = 5 $m^3.h^{-1}$ and $\dot{V}_i$ = 25 $m^3.h^{-1}$. The lance position in both cases was 0.312 m. The figure shows that the

O_2 concentration is 21% for the first three measurement points for the case of the SC arrangement when $\dot{V}_i$ = 5 $m^3.h^{-1}$. This means that there is no penetration of N_2 upstream. The minimum lies at the measuring position of 0.416 m.Then, by decreasing the axial flow rate, the O_2 concentration decreases due to the conservation of mass. For the BCC arrangement, only the first two measurement points were identical at 21%. There was minimal N_2 penetration upstream; however, in the range of the measuring positions, a minimum could again be found. For higher injection flow rates, i.e., $\dot{V}_i$ = 25 $m^3.h^{-1}$, the effect of the axial flow rate of air on the O_2 concentration is shown. The concentration of O_2 is 21% only for the first two measuring positions for a bed with higher porosity, i.e., 0.48. Then, the O_2 concentration decreases and remains relatively constant downstream. As a consequence of this high injection flow rate, N_2 exhibits minimal penetration downstream. A minimum in the profile does not occur, in contrast to the case of low $\dot{V}_i$. For the bed with the low porosity of φ = 0.35, the profiles are similar for the first three measurement points. However, at 0.416 m, a minimum again can be found. This means that the injection flow rate $\dot{V}_i$ does not achieve as high of a high penetration as for φ =0.48.

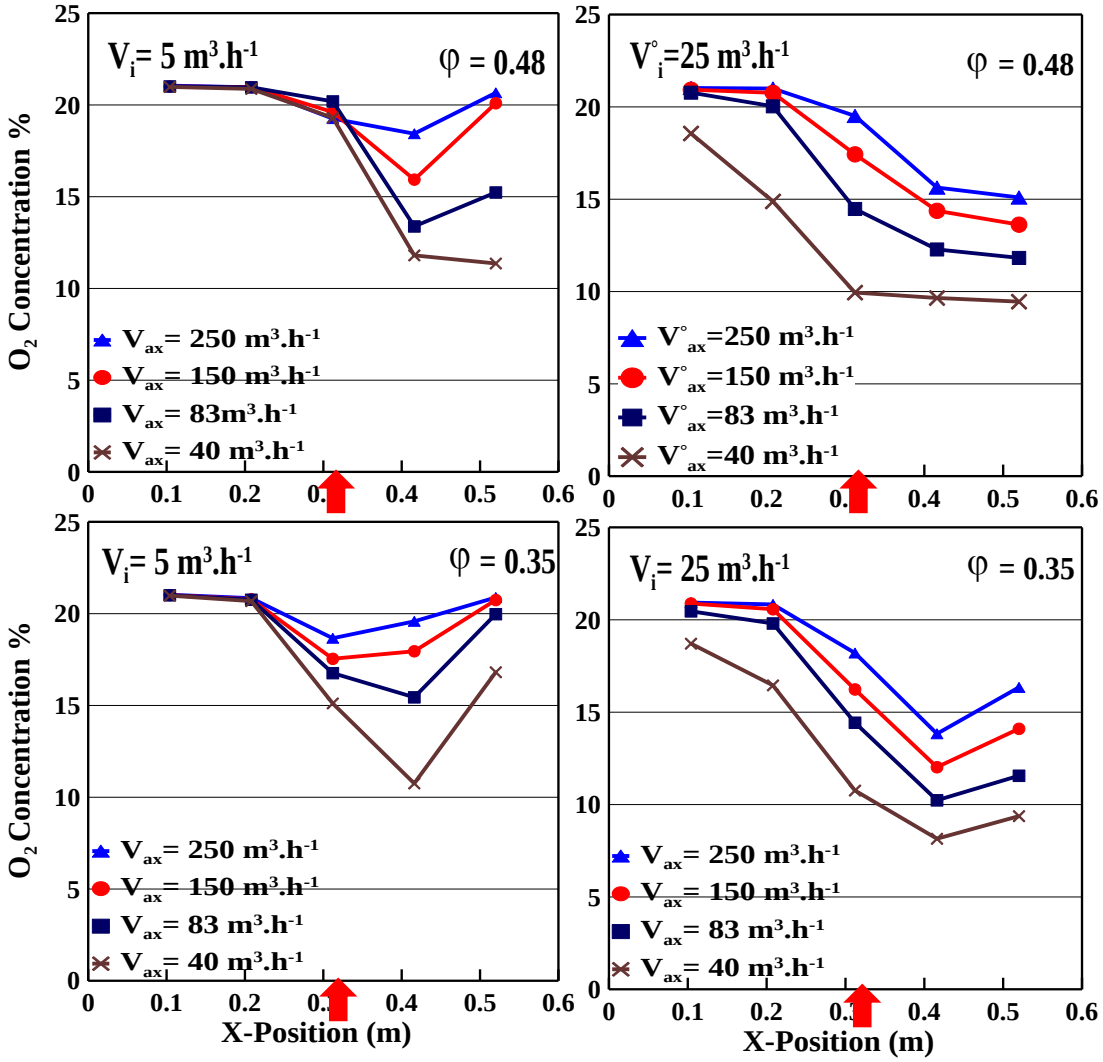

Figure 3.9: Effects of axial flow rate on the O_2 concentration for two structured beds, SC at measuring level of 0.468 mm and BCC at measuring level of 0.459 mm , with x_L= 0.312 m and d_L= 0.02 m

Figure 3.10 shows the effect of the axial flow rate on the O_2 concentration for two unstructured beds, glass beads with $\varphi = 0.4$ and clinker with $\varphi = 0.35$, at $x_L = 0.312$ m and $d_L = 0.02$ m. In both cases, the behavior of the O_2 concentration curves is similar in general. From the two cases, it can be seen that the width of the jet curves in the case of $\dot{V}_i$ = of 25 $m^3.h^{-1}$ is greater than that for $\dot{V}_i$ = 5 $m^3.h^{-1}$. In addition, by comparing two beds at the low injection flow rate of $\dot{V}_i$ = 5 $m^3.h^{-1}$, the figures show that the minimum value of the O_2 concentration for the cement clinker bed is higher than that for the bed of glass beads. The inhomogeneity caused by the arbitrary shape of the cement clinker particles could affect the N_2 penetration through the bed.

Thus, for the future, the comparison shall be made between structured beds with both arrangements and the unstructured bed with glass beads only.

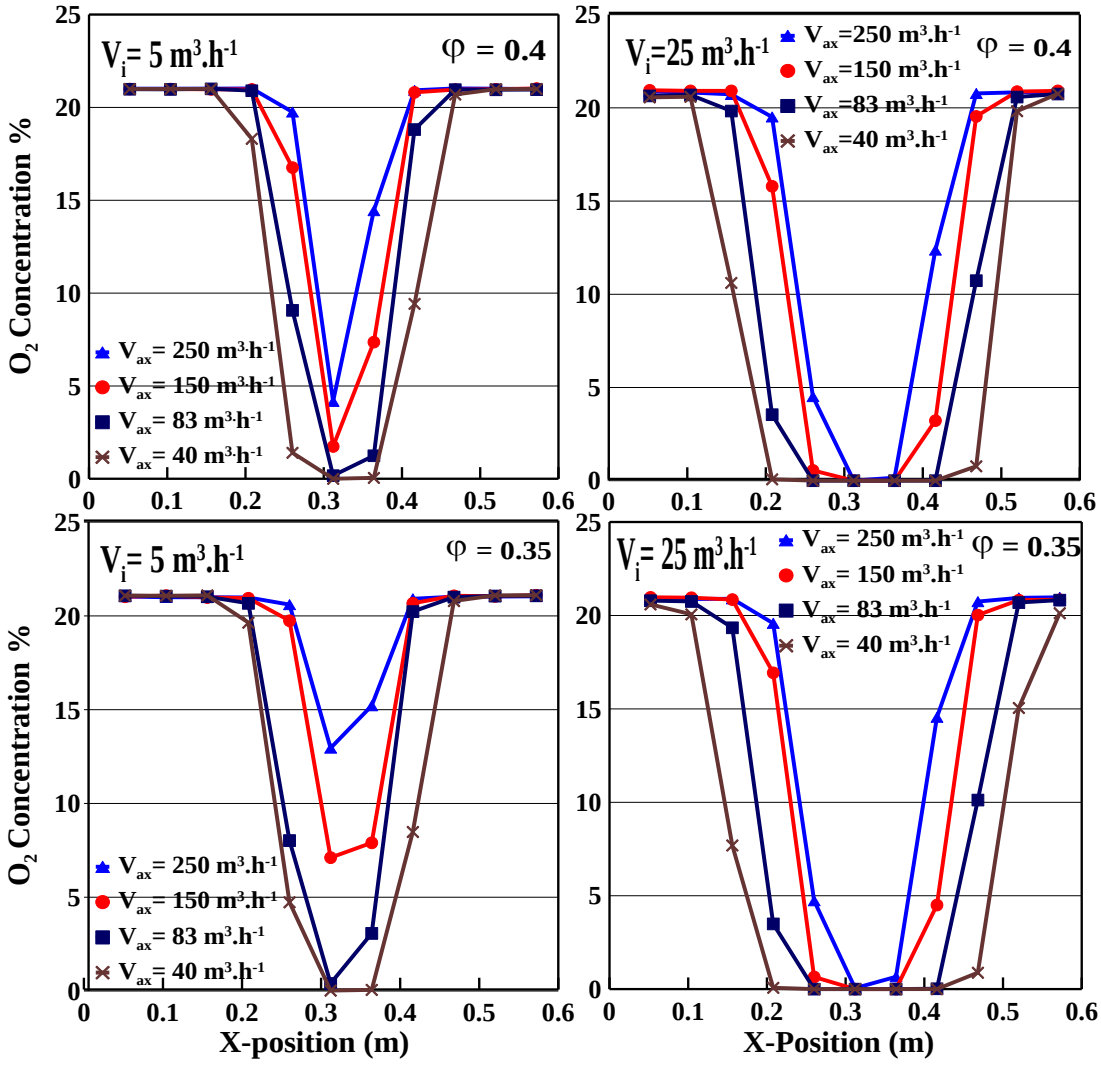

Figure 3.10: Effect of the axial flow rate on the O_2 concentration for two unstructured beds, glass beads with $\varphi = 0.4$ and clinker with $\varphi = 0.35$ at measuring level of 0.473 mm, $x_L = 0.312$ m and $d_L = 0.02$ m

Effect of N_2 (injection flow rate)

Figure 3.11 shows the effect of the injection flow rate on the O_2 concentration for two structured beds, SC and BCC, at x_L = 0.312 m and d_L= 0.02 m and for different air flow rates, $\dot{V}_{ax}$ =40 $m^3.h^{-1}$ and 250 $m^3.h^{-1}$. For the case of a low axial flow rate $\dot{V}_{ax}$ = 40 $m^3.h^{-1}$, the O_2 concentration decreases up to the fourth measuring position for both structured beds, SC and BCC; then, the curves remain flat up to the last measurement position under the SC packing, whereas they continue increasing in the case of the BCC packing.For a high axial flow rate of 250 $m^3.h^{-1}$, the first three measurement points for φ = 0.48 corresponded to an O_2 concentration of 21%, which means that there was no penetration of N_2 into the opposite side of the injection. For the low N_2 flow of 5 $m^3.h^{-1}$, a minimum is obtained. Therefore, the jet does not penetrate into the end of the box. However, for the higher N_2 flows, the jet reached the end of the box. The concentration of O_2 is constant, and hence, the value of 21% is obtained only at the first two measuring positions for φ = 0.35. Here, the N_2 penetrates slightly in the injection direction. A minimum then occurs for all three N_2 flows, and the jets do not penetrate into the end of the box for the lower porosity case.

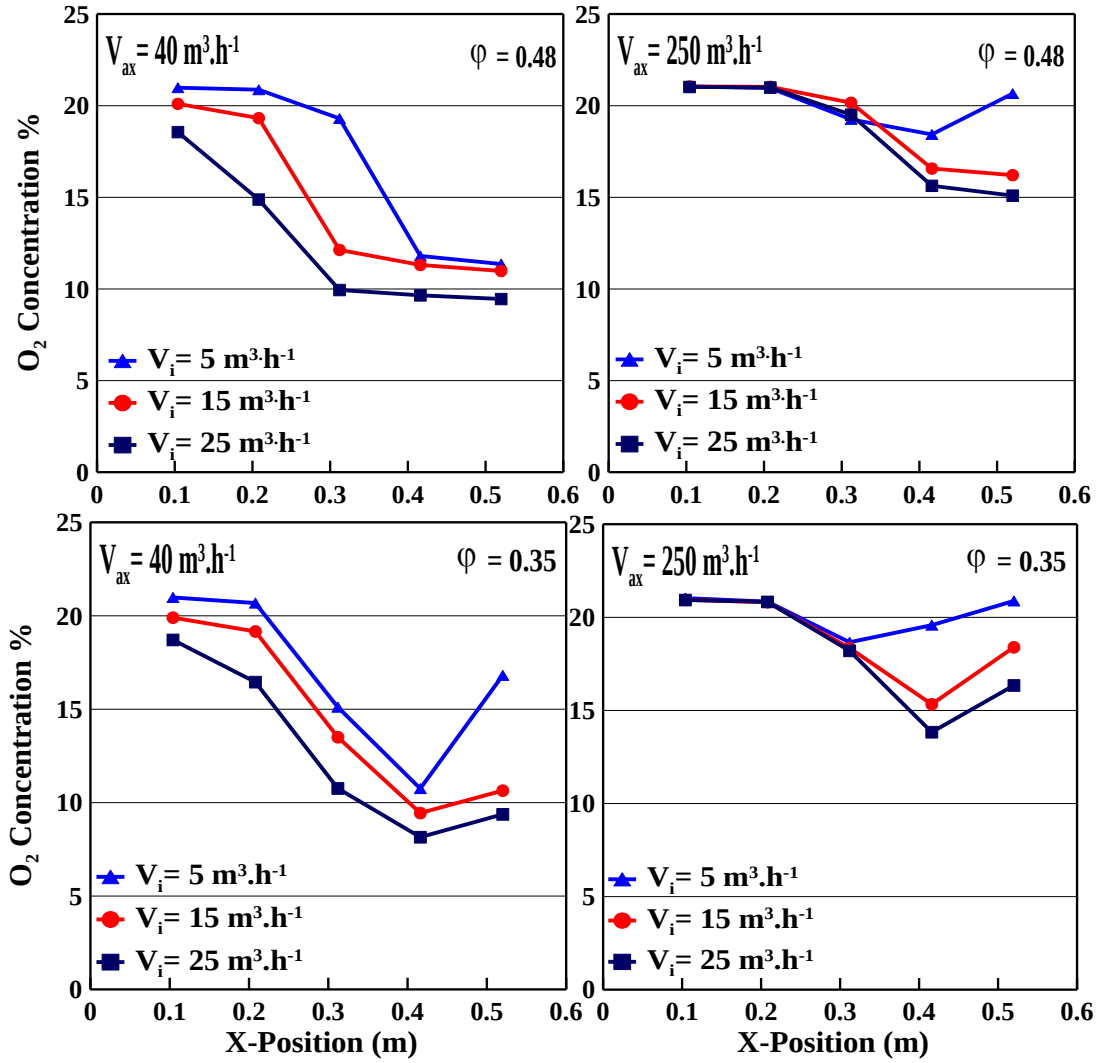

Figure 3.11: Effect of injection flow rate on the O_2 concentration for two structured beds, SC & BCC at measuring level of 0.468, 459 mm respectively, where x_L = 0.312 m and d_L= 0.02 m

Figure 3.12 shows symmetrical curves on both sides of the injection point, with the minimum value of the O_2 concentration being less than that in the structured bed due to the effect of the bed density. In the case of the unstructured bed, the effect of increasing the axial flow to 250 $m^3.h^{-1}$ appears in the small width of the jet.

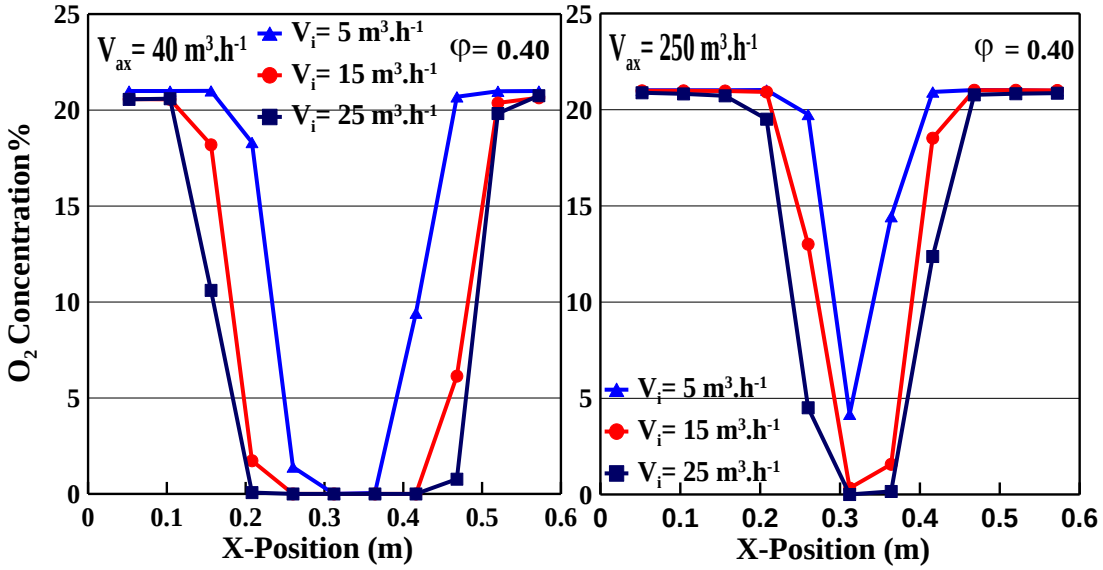

Figure 3.12: Effect of injection flow rate on the O_2 concentration for unstructured bed (glass beads) with φ = 0.4, at x_L = 0.312 m and d_L= 0.02 m

3.3.4 Volumetric flow rate ratio

The volumetric flow rate ratio can be adjusted by the injection and axial flow rates. Thus, the same ratio can be obtained with different combinations. For example, a volumetric flow rate ratio of 0.1 can be obtained by combining an injection flow rate of 25 m^3/h with an axial flow rate of 250 $m^3.h^{-1}$ or by using 15 m^3/h and 150 $m^3.h^{-1}$ for the injection and axial flow rates, respectively. Figure 3.13 presents the effects of the obtained volumetric flow rate ratio on the O_2 concentration with a lance position of 0.312 m. Clearly, the curves present similar trends in both arrangements, SC and BCC.

For the bed with φ = 0.48, the O_2 concentration decreased behind the injection position until the end of the box. This means that the N_2 only penetrates in the injection direction until the end of the box. Under the BCC setting with φ = 0.35, the O_2 concentration decreases at 0.2 m before the injection, reaches a minimum at 0.4 m and then increases to 0.21 at the end of the box. This means that the N_2 penetrates slightly in the injection direction but does not reach the end of the box. A bed of BCC packing has a lower penetration depth than for SC. The profiles are nearly independent of the ratio $\dot{V}_R$.

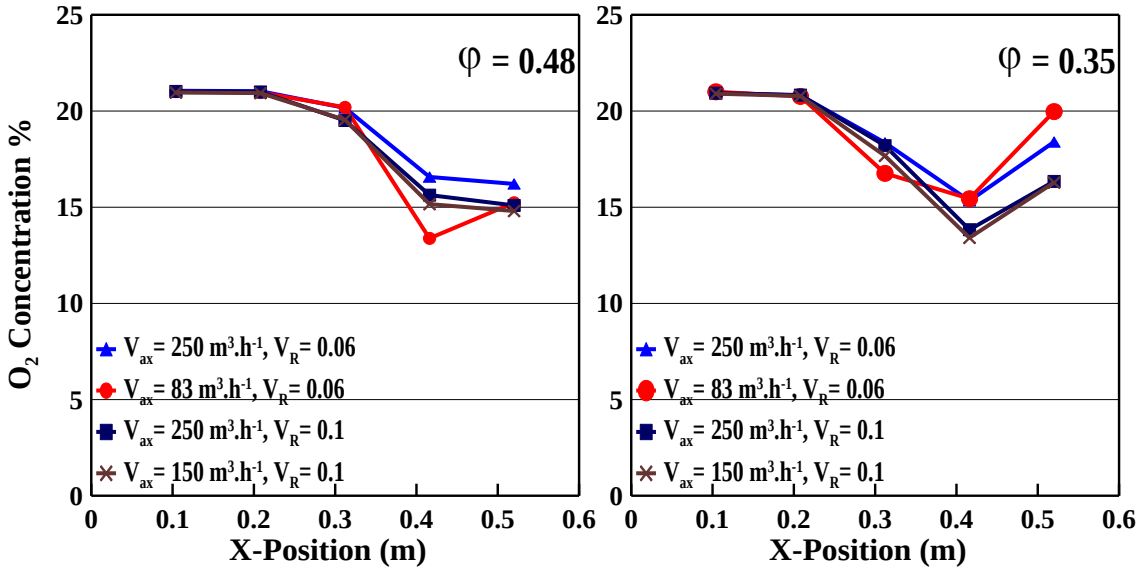

Figure 3.13: Effect of volumetric flow ratio on O_2 concentration for both structured beds, SC and BCC, with x_L= 0.312 m and d_L= 0.02 m

For the unstructured bed with φ = 0.4, the curves are identical despite the two different volume ratios; in addition, the profiles here are independent of $\dot{V}_R$, as shown by Figure 3.14.

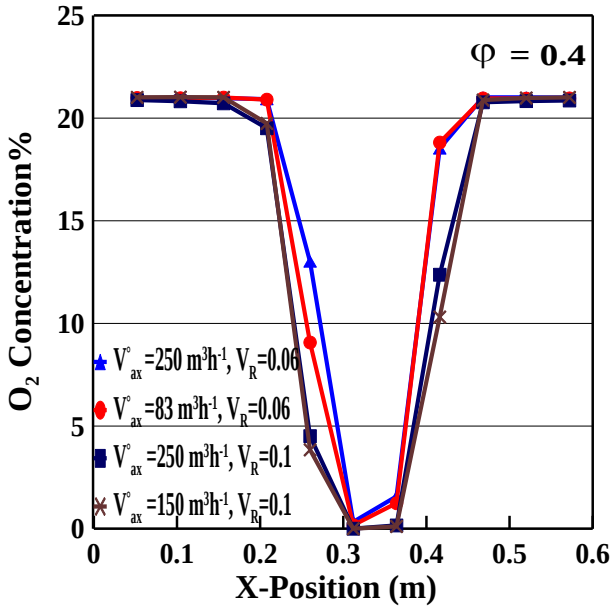

Figure 3.14: Effect of volumetric flow rate ratio on O_2 concentration for the unstructured bed with φ = 0.4 at x_L= 0.312 m and d_L= 0.02 m

3.3.5 Lance position

Figure 3.15 shows the effect of the lance position (x_L= 0, 0.156, 0.312 m) on the O_2 concentration for different volumetric flow rate ratios in two beds with φ = 0.48 and 0.35. The upper two figures are for the SC arrangement, and the injection positions of 0.156 and 0.312 m were shifted to the position at 0 m. This means that the injection always starts at 0 m. The first figure, where $\dot{V}_R$ = 0.625, clearly shows that all profiles decreased together and formed a jet of N_2. The O2 concentration at the lance position of 0.312 m formed the left side of the jet, and that of the lance position of 0 m formed on the right side. The whole profile can only be seen when the lance is at a position of 0.156 m. Therefore, it can be concluded that the shape of the jet is independent of the lance position. The figures for the other values of $\dot{V}_R$ show that when less N_2 is injected, the width of the jet decreases. It seems that the O_2 minimum is shifted slightly toward the 0 mm position with increasing $\dot{V}_R$. For $\dot{V}_R$ = 0.625, the minimum of the jet is at approximately 0.2 m, and when decreasing $\dot{V}_R$, the minimum moves toward 0.1 m.

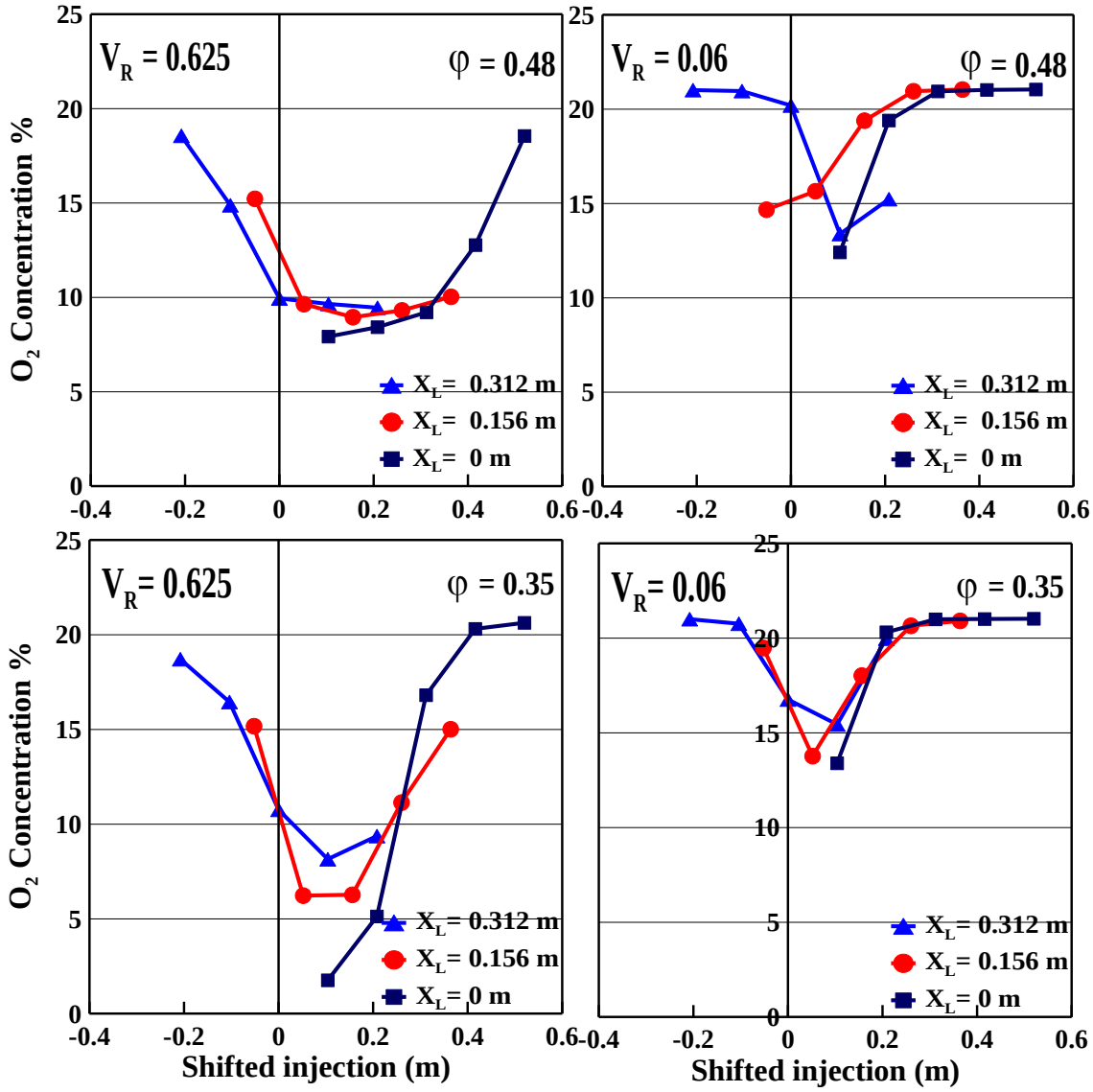

Figure 3.15: Effect of the lance position x_L on the O_2 concentration for both structured beds, with d_L= 0.02 m

The curves of the O_2 concentration for the case of the BCC packed bed with $\varphi = 0.35$ is shown in the lower figures. As described above, the position of the injection is 0 mm i.e. at the wall of the box. It can also be concluded that the shape of the jet is independent of the lance position. By comparing the figures for $\dot{V}_R = 0.625$ and 0.06, it can be seen that the minimum O_2 concentration for $\varphi = 0.35$ is lower than that for $\varphi = 0.48$, especially for the 0 mm injection position because of the confinement between the wall and the bed. Moreover, the N_2 jet is wider in the SC bed than in the BCC bed. This effect cannot be as clearly seen for the lower value of $\dot{V}_R = 0.06$. For $\dot{V}_R = 0.625$, the minimum of the jet is at approximately 0.1 m. When decreasing $\dot{V}_R$, the minimum moves toward 0.05 m for $\dot{V}_R = 0.06$.

Figure 3.16 shows the effect of the lance position on the O_2 concentration for the unstructured bed, where $d_L = 0.02$ m for the unstructured bed. The curves are wider at higher values of $\dot{V}_R$. With decreasing $\dot{V}_R$, the shape of this jet changes gradually. The minimum of the O_2 concentration has a smaller value than in the case of the structured bed. Furthermore, the minimum of the jet is close to the position of 0 mm.

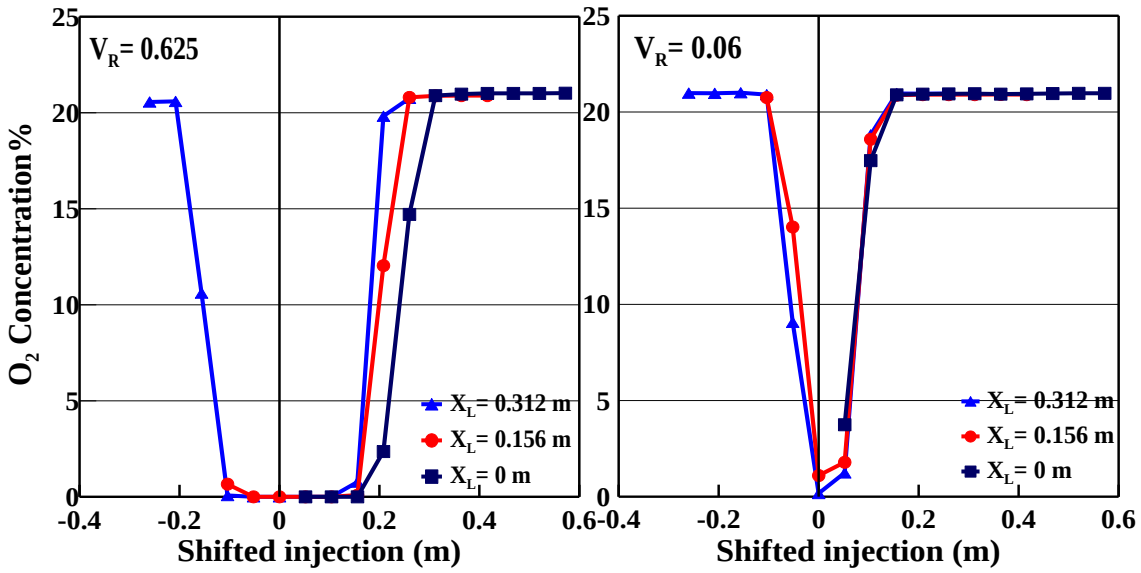

Figure 3.16: Effect of the lance position on the O_2 concentration for the unstructured bed, $d_L = 0.02$ m

3.3.6 Velocity profiles

Figure 3.17 a represents the velocity distribution of the six lines, with 11 points per line for each sphere; Figure 3.17 b shows these lines. The velocity measurements were performed using a hot wire having an error of approximately ±0.01 $m.s^{-1}$. Actually, there were some problems in obtaining the absolute velocity during the measurements due to the human error when fixing the hot wire, but the tendency of the distribution is acceptable. From the figure, it can be concluded that there is no difference in the mixing velocity distribution through the cross lines at the outlet of the box. Therefore, all data are collected at line 3.

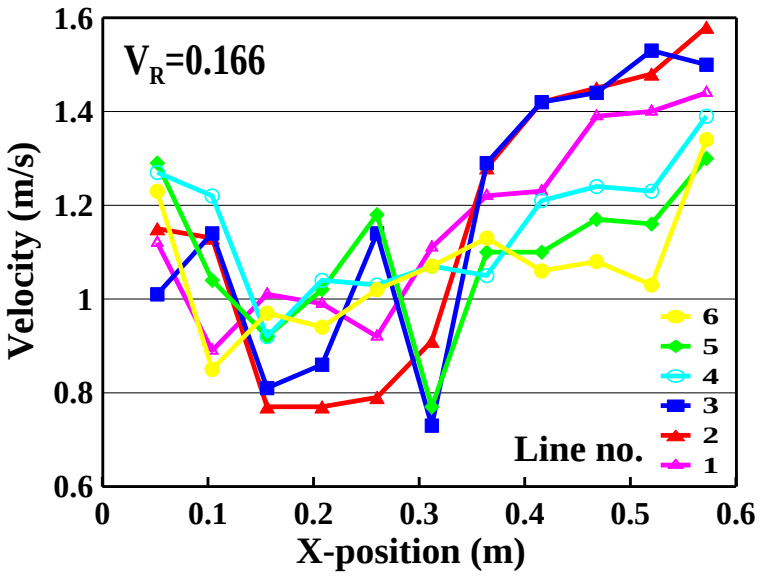

(a)

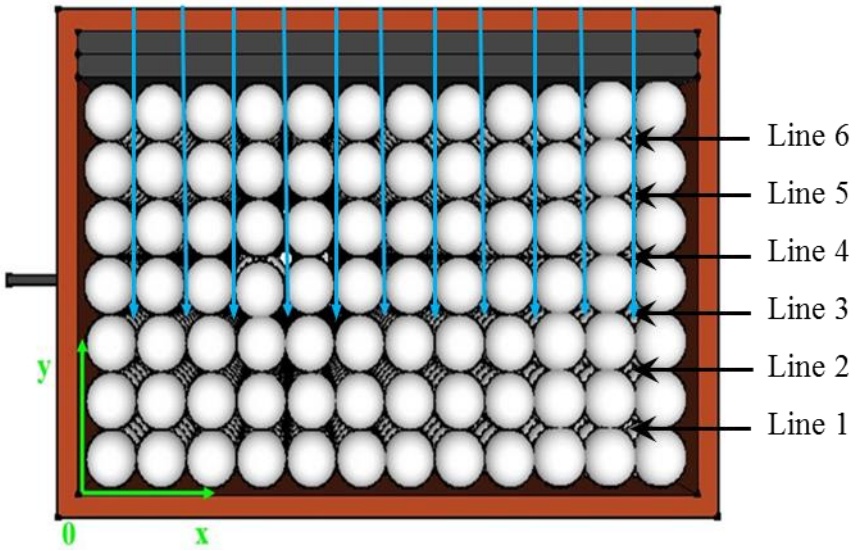

(b)

Figure 3.17: a) Mixing velocity distribution for different lines at the outlet plane at x_L= 0.156 m and d_L= 0.02 m b) Measuring Lines.

Figures 3.18 shows the average of the mixing velocity distribution for a volumetric flow rate ratio of 1.25. The figure shows that the average mixing velocity at the outlet is 0.65 for the SC bed and 0.43 for the BCC bed. Moreover, the curve of the mixture velocity remains constant up to the injection position at x_L= 0.312 m but then increases until the end of the box for the SC bed. The effect of the channeling of the air near the wall of the box for the BCC bed due to the change in porosity could also be observed.

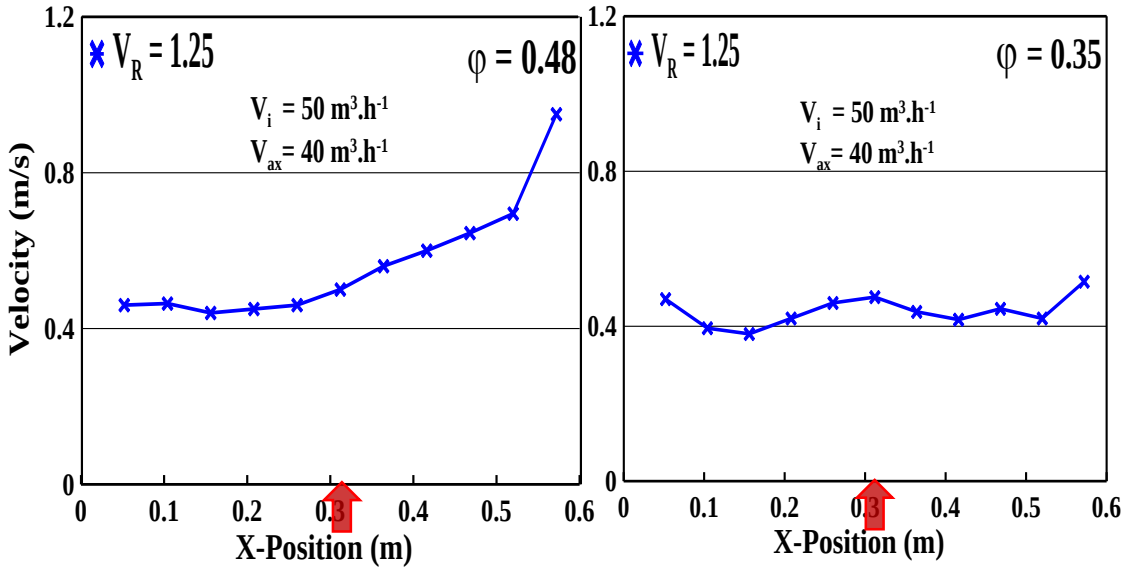

Figure 3.18: Comparison between the experimental mixing velocity distributions for structured beds at x_L = 0.312 m and d_L= 0.02 m

4. Computational Fluid Dynamics in Packed Bed

4.1 Computational Fluid Dynamics

CFD codes make it possible to numerically solve flow, mass, and energy balances in complicated flow geometries such as a packed bed. The differential forms of these balances are applied to a large number of control volumes, which together constitute the computational domain. The size and number of control volumes (mesh density) are user-defined and strongly influence the accuracy of the solutions. After boundary conditions have been implemented, the flow and energy balances are solved by an iteration process that continues until a satisfactory result has been obtained.

The general equations used for conservation of mass (the continuity equation), conservation of momentum, and conservation of energy and the finite volume method (FVM) used to discretize the domain are all described in standard references on the subject [43]. Here, particular care is given to the choice of turbulence model and to the treatment of flow near solid surfaces.

4.2 Computation of fluid motions

Today, thousands of companies worldwide benefit from the use of the ANSYS FLUENT software as an integral part of the design and optimization phases of their product development. Advanced solver technology provides fast and accurate CFD results. The CFD software package must be able to numerically solve the equations that govern the flow of fluids and determine the way in which a fluid will flow for a given situation. FLUENT, one of the ANSYS commercial CFD packages, solves the Navier-Stokes equations for conservation of mass and momentum when it is set to calculate laminar flow without heat. Additional equations are solved for heat transfer, species mixing or reactions or turbulent cases. The basic equations and background of these equations are stated in the FLUENT 6.2 User's Guide [44].

4.3 Governing Equations

Turbulent flow is assumed for all runs due to the high flow rates; then, the RANS equations are solved. The CFD model uses the equations for conservation of mass, momentum, energy and species. These equations are then discretized by the FVM. A turbulence model, namely, the standard k– ϵ model with standard wall treatment, is used for the enclosed domain.

4.3.1 Continuity Equation

The continuity equation states that the rate of increase of the mass in a control volume is equal to the difference between the rate of mass in and the rate of mass out of the control volume. The continuity equation in differential form is given below:

$$\frac{\partial \rho}{\partial t} + \nabla . (\rho \mathrm{u}) = 0 \qquad . \qquad (4.1)$$

If ρ is a constant, as in the case of incompressible flow, the mass continuity equation simplifies to a volume continuity equation,

$$\nabla.u = 0 \qquad (4.2)$$

which physically means that the local volume dilation rate is zero

4.3.2 Navier-Stokes Equation

The Navier-Stokes equation is the equation of motion for a Newtonian fluid with constant viscosity and density. The equation is greatly simplified when applied to 2D flow with the assumption that the velocity is only in the axial (z) direction, i.e., V_r =0 and V_θ =0:

$$-\frac{dp}{dz} + \rho g_z + \mu \left[\frac{1}{r}\frac{d}{dr}\left(r\frac{dv_z}{dr}\right)\right] = 0 \quad . \quad (4.3)$$

4.3.3 Selection of turbulence model

No single turbulence model is universally accepted as being superior for all classes of problems. The choice of turbulence model depends on considerations such as the physics involved in the flow, the class of problem, the level of accuracy required, the available computational resources and the amount of time available for the simulation. The nature of the flow through packed beds is complex and difficult to study due to the disorderly characteristics. In a bed with a high aspect ratio (tub-to-particle diameter ratio), the flow is disordered but can be considered homogeneous statistically due to the relatively uniform size of the voids. In a bed with a low aspect ratio, the bed structure is considerably more disordered, and large voids increase velocity channeling. ANSYS FLUENT offers seven turbulence models [44].

4.3.4 Types of turbulence models

Turbulence models can be classified into two broad types. The first type includes the classical models of RANS turbulence models; models of the second type are based on space-filtered averaging such as the Large-Eddy Simulation. In this study, RANS turbulence models are presented. Normally, RANS models are employed for the Navier-Stokes equations so that the small-scale turbulent fluctuations do not have to be directly resolved. Additionally, the Reynolds-averaged method relies on averaging out all the unsteadiness within the flow and considers all unsteadiness as being a result of turbulence. Therefore, the RANS approach greatly reduces the required computational effort and is widely adopted for practical engineering applications.

ANSYS Fluent offers different types of turbulence models based on the RANS approach. To illustrate their affect, six different types of models have been studied: Standard k − ε, RNG k − ϵ, Realizable k − ϵ, Standard k − ω, SST k − ω and Transition SST. More information regarding equations and empirical constants can be found in the ANSYS documentation [44].

4.3.5 Standard k-ϵ turbulence model

For fluid flow with high Reynolds numbers, the rate of dissipation of kinetic energy (ϵ) is equal to the viscosity multiplied by the fluctuating vorticity. An exact transport equation for the fluctuating vorticity, and thus the dissipation rate, can be derived from the Navier-Stokes equation, whereas the equation for turbulent kinetic energy is obtained empirically.

The standard K-Є model is by far the most popular and most widely used turbulence model, especially for industrial applications. It is a semi-empirical model and consists of two transport equations, one for the specific turbulent kinetic energy (K) and one for the turbulent dissipation rate (Є).

The K-Є model consists of the turbulent kinetic energy equation

$$(u.\nabla)\, k = \nabla.\left[\left(\mu + \frac{\mu_T}{\sigma_k}\right)\nabla k\right] + P_k - \rho\epsilon \qquad (4.4)$$

and the dissipation rate equation

$$(u.\nabla)\, \epsilon = \nabla.\left[\left(\mu + \frac{\mu_T}{\sigma_e}\right)\nabla\epsilon\right] + C_{e1}P_k\frac{\epsilon}{k} - C_{e2}\,\rho\,\frac{\epsilon^2}{k} \qquad (4.5)$$

where P_k represents

$$P_k = \mu_T\,[\nabla u{:}(\nabla u + (\nabla u)^T)] \qquad (4.6)$$

and C_{e1}, C_{e2}, σ_k and σ_e are turbulence model parameters (constants). In the implementation of this model, the Kolmogorov-Prandtl expression for the turbulent viscosity is used:

$$\mu_T = \rho C_\mu \frac{k^2}{\epsilon} \qquad (4.7)$$

4.3.6 Influence of turbulence model

A packed bed with a low aspect ratio exhibits full turbulence throughout. Conversely, a packed bed with a very high aspect ratio (such as a porous medium) (A ratio > 500) displays no turbulence due to the pore size being smaller than the smallest turbulent structures.

ANSYS FLUENT will, by default, solve the standard conservation equations for turbulence quantities in the porous medium. In this default approach, turbulence in the medium is treated as though the solid medium has no effect on the turbulence generation or dissipation rates. This assumption may be reasonable if the permeability of the medium is quite large and if the geometric scale of the medium does not interact with the scale of the turbulent eddies.

Figure 4.1(a) shows the influence of six turbulence models on the O_2 concentration and the contour plots at the symmetry plane. The calculations were performed with $\dot{V}_R$ = 0.625 for the injection position x_L= 0.156 m and with a lance diameter of d_L = 0.02 m. The CFD results show that all turbulence model curves lie close to each other. Therefore, for the steady-state case, the turbulence models have small effect on the calculations. Figure 4.1(b) shows three contour planes for each turbulence models. The plane for the air inlet from the bottom, the symmetry plane and the XZ plane are at Y = 0.57 m.

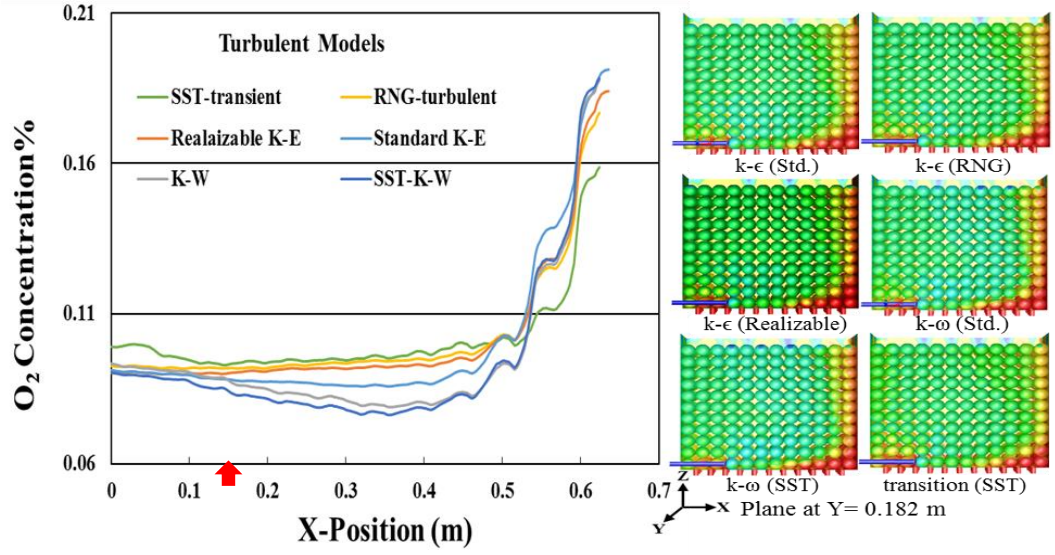

Figure 4.1: (a) The O_2 concentration for different turbulence models and the contour plots at the symmetry plane for RPM (gap method) with $\dot{V}_R$ = 0.625 at x_L= 0.156 m and d_L= 0.02 m

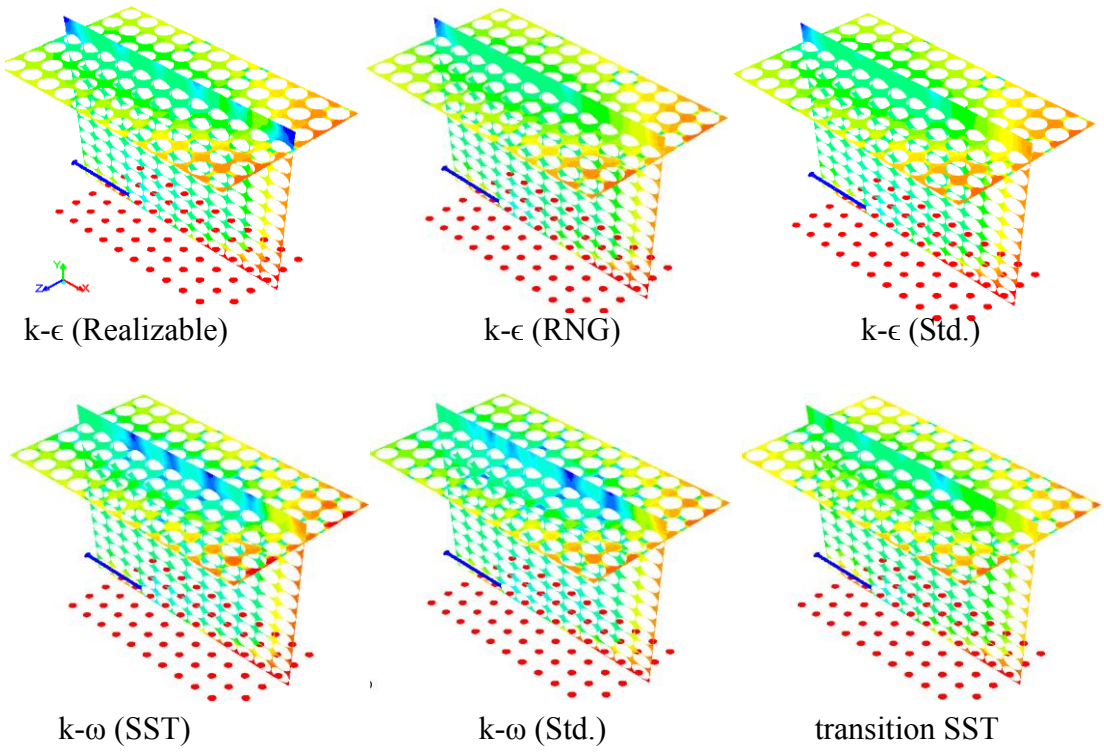

Figure 4.1: (b) Three isometric contour planes for six turbulence models

Considering these calculations and previous studies, the standard k-ϵ model with the standard wall function is chosen and applied in this study.

4.3.7 Species transport model

In this model, the mixing and transport of chemical species can be modeled using conservation equations describing convection, diffusion, and reaction sources for each component species. In other words, ANSYS FLUENT predicts the local mass fraction of each species, Y*i*, through the solution of a convection diffusion equation for the *i*th species. This conservation equation takes the following general form:

$$\frac{\partial}{\partial t}(\rho Y_i) + \nabla.(\rho \vec{u}\, Y_i) = -\nabla.\vec{J}_i + R_i + S_i \qquad (4.8)$$

where *Ri* is the net rate of production of species *i* by chemical reaction, *Si* is the rate of creation by addition from the dispersed phase plus any user-defined sources, and *Ji* is the diffusion flux of species *i*, which arises due to concentration gradients. In turbulent flows, FLUENT computes the mass diffusion by

$$\vec{J}_i = (\rho D_{i,m} + \frac{\mu_t}{Sc_t})\,\nabla Y_i \qquad (4.9)$$

where *Di,m* is the diffusion coefficient for species *i* in the mixture and Sc_t is the turbulent Schmidt number, defined as

$$Sc_t = \frac{\mu_t}{\rho D_t} \qquad (4.10)$$

where μ_t is the turbulent viscosity and D_t is the turbulent diffusivity.

4.4 Near-wall treatments

The near-wall modeling significantly impacts the numerical solutions. In packed bed, spheres surfaces are presumed as walls, which are the main source of mean vorticity and turbulence. Therefore, the accurate representation of the flow in the near-wall region determines the successful prediction of wall-bounded turbulent flows. Numerous experiments have shown that the near-wall region can be largely subdivided into three layers, as shown in Figure 4.2 [1]. In the inner layer, called the viscous sub-layer, the flow is almost laminar. The outer layer, where flow is turbulent, is called the fully turbulent layer; further, there is an interim region between the viscous sub-layer and the fully turbulent layer where the effects of molecular viscosity and turbulence are equally important [44].

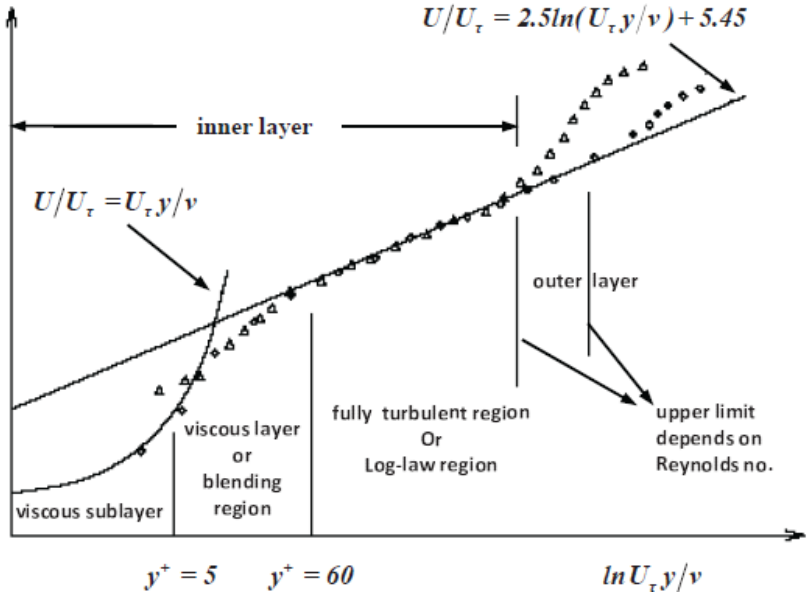

Figure 4.2: Subdivisions of the near-wall region [1]

There are two approaches for modeling the near-wall region. In one approach, the viscosity-affected inner region (viscous sub-layer and buffer layer) is not resolved. Instead, semi-empirical formulas called "wall functions" are used to bridge the viscosity-affected region between the wall and the fully turbulent region. The use of wall functions overcomes the need to modify the turbulence models to account for the presence of the wall. In the other approach, the turbulence models are modified to allow the viscosity-affected region to be resolved with a mesh all the way to the wall, including the viscous sub-layer. For purposes of discussion, this will be termed the near-wall modeling approach. These two approaches are depicted schematically in Figure 4.3. According to the guidelines presented in the FLUENT documentation, the value of y+ should be approximately equal to 1 or at least less than 5 when an enhanced wall treatment is used [44]. Near-wall model approach are used in this work.

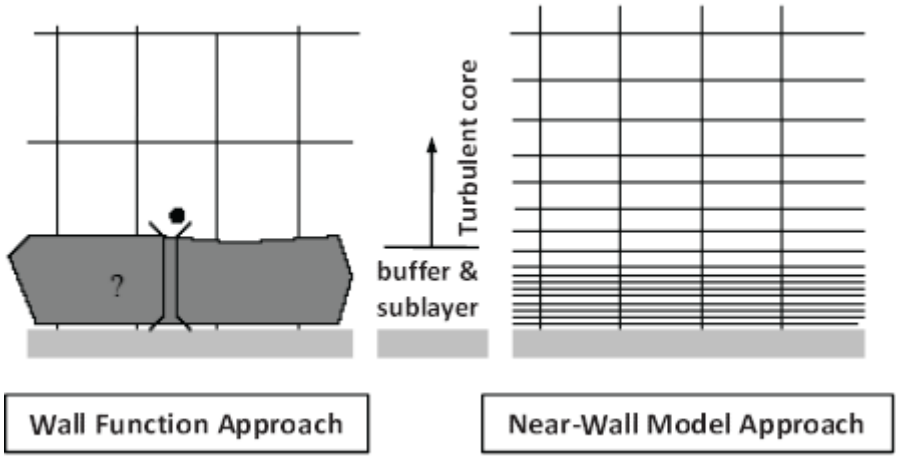

Figure 4.3: Schematic representation of the mesh for a wall function and a near-wall model approach

4.5 Boundary conditions

After geometry and mesh generation, the boundary conditions should be specified according to the fluid or solid. The boundary conditions determine the flow and thermal variables on the boundaries of the physical model. There are a number of classifications of boundary conditions, such as flow inlet and exit boundaries: pressure inlet, velocity inlet, inlet vent, intake fan, pressure outlet, outflow, outlet fan, and exhaust fan. Wall and repeating boundaries include the following: wall, symmetry, and periodic axis. Internal cell zones are either fluid or solid. In this study, the physical model has two inlets, the velocity inlet and the pressure outlet (Pgauge = 0). A plane divides the computational model as a symmetry, and all outer walls and spheres act as wall boundaries.

4.6 Solution of CFD problem

When the computational domain is generated with its mesh, the completed geometry is imported into the solver, and the CFD calculations can be started. However, before this, the boundary conditions on the system as well as the parameters of the iteration process have to be set. There are two main iteration parameters that are to be set before the simulation is run.

4.6.1 Relaxation factor

The relaxation factor is multiplied by the change in the iteration step before it is applied to the result for the next iteration step. The relaxation factor is included to suppress oscillations in the flow solution that arise from numerical errors. When this factor is greater than one, the process is called over-relaxed. In an over-relaxed process, the step change is large, and convergence should be achieved quickly. However, it is not recommended to over-relax a process unless it is very stable. In a less stable or nonlinear system, such as turbulent flow cases, over-relaxation may lead to a divergence of the process. When the relaxation factor is less than one, the process is called under-relaxed. In this case, the iteration process is slower because the step change is small but not likely to diverge.

4.6.2 Residual value

The residual value is the difference between the current and former iteration value and is taken as a measure of convergence. Normally, when the residuals go to zero, the solution converges. Therefore, in this study, all the convergence criteria are set to be less than 10^{-3}. These cut-off values for convergence are set for all elements in the model, i.e., temperatures, densities, pressures, flow, velocities, species transport and mean mixture fraction. In some cases, such as the prediction of pressure drops, the convergence criteria need to be set to be below 10^{-6} to obtain accurate predictions; however, the computation time can increase significantly in response. Additionally, the Navier-Stoke equations and the species transport equations cannot be solved directly unless they are numerically discretized. A variety of techniques can be used to perform this numerical discretization. One such technique is the FVM. The FVM has been developed specifically to solve the equations of heat transfer and fluid flow and is the most popular method used in CFD. ANSYS Fluent adopts an FVM for the numerical discretizations [44].

4.7 CFD simulation process

Essentially, there are three stages to every CFD simulation process: pre-processing, solving and post-processing.

4.7.1 Pre-processing

This is the first step in building and analyzing a flow model. This step includes building the geometry within a computer-aided design (CAD) package, creating and applying a suitable computational mesh, and setting up the flow boundary conditions and fluid material properties.

4.7.2 Solving

In this stage, the CFD solver performs the flow calculations and produces the results. Selecting of a CFD solver can sometimes be a daunting task due to the bewildering variety of choices. Famous commercial providers of CFD codes include ANSYS, Inc.; CD Adapco; Aerosoft, Inc.; and Cobalt Solutions, and LLG. ANSYS, Inc. provides the FLUENT and CFX solvers and controls approximately half the commercial CFD market. FLUENT′s adaptive and dynamic physics is unique among CFD vendors and works for a wide range of physical models.

4.7.3 Post-processing

Post-processing is the final step of the CFD analysis, and it involves the organization and interpretation of the predicted flow data and the production of CFD images and animations if necessary. Post-processing is integrated into the FLUENT solver, and users can perform sophisticated data analysis easily. FLUENT′s CFD data can also be exported to third-party post-processors and visualization tools, such as EnSight, Field view and Tecplot, as well as to VRML formats.

4.8 CFD modeling of packed bed

4.8.1 Types of models

There are two types of models most commonly used in the field of packed-bed modeling [25]. In the first type of model, the bed is represented as an effective porous medium, with lumped parameters for dispersion and heat transfer. This approach is called the "porous medium approach". The reactions that occur in the porous catalyst particles are represented by source or sink terms in the conservation equations and are corrected for volume fraction and particle transport limitations. The velocity field can be obtained from a modified momentum balance or through the form of the Brinkmen-Forcheimer-extended Darcy equation. These approaches provide an averaged velocity field, usually in the form of a radially varying axial component of the velocity. This approach gives better results for the velocity field than those obtained with the classical assumption of plug flow. The disadvantages of this approach are the continued lumping of transport processes and the lack of detailed flow structure.

This approach was applied by Rasul et al. [7] to model and simulate the thermodynamic process of a vertical shaft kiln. The combustion, particle-gas dynamics and heat transfer processes were modeled by an Eulerian multiphase model and species transport and finite volume chemical reaction model. Although the authors declared that the simulated results showed a reasonably good agreement with designed data, the temperature profile through the kiln seems too high to be realistic due to the steady state assumption and the exclusion of the decomposition process of limestone. Therefore, the practical significance for modeling the heat transfer in shaft kilns producing soft-burnt lime is dubious. Additionally, the simulation was based on a 2-D geometric model. There is no doubt that the kiln can be approximated as axisymmetric; however, the firing system definitely cannot be axisymmetric. In a 2-D model, a gap- or slot-shaped burner is used instead of a group of tube pipes. Thus, the influence of the dimension of the slot and the setting of the boundary condition should be investigated intensively.

For the second type of CFD models, the geometric complexities of the packing are not simplified or replaced by the effective medium, and the flow through the space between particles is calculated by solving the Navier-Stokes equations along with other equations. In this approach, solving the governing equations for the fluid flow itself is relatively simple; however, the geometric modeling and grid generation become complicated, and the computation demands increase significantly. However, it use is worthwhile, as this approach yields very detailed solutions, which are of great importance in understanding the phenomena that occur in the bed. With this "Real particle" approach, the complete characteristics of the flow in the entire flow domain can be described in terms of the main variables such as velocity, pressure, and temperature. Building the geometry is one of the most important and time-consuming processes of CFD analysis.

4.8.2 Real particle model (RPM)

3-D geometric models are more realistic when the spherical particles and the tube-shaped lance are modeled. The simulations presented in this chapter mainly present a general study of the behavior of the flow mixing between the injection flow of N_2 and the main flow (axial flow) of air in our domain.

4.8.3 Description of the geometry and the grid

For designing systems such as industrial shaft kilns, various tests with different parameters are needed to obtain a general trend for the response of the system. It is obviously very costly and time consuming to build such a huge model for testing. Therefore, this study involves understanding cross flow behavior through a packed bed in a small test box (0.624*0.364*0.6 m). To prevent the effect of outlet boundary conditions, an extra height of 50 mm was added to the main box, and the rectangular box was created to simulate the experimental test rig, as shown in Figure 4.4.

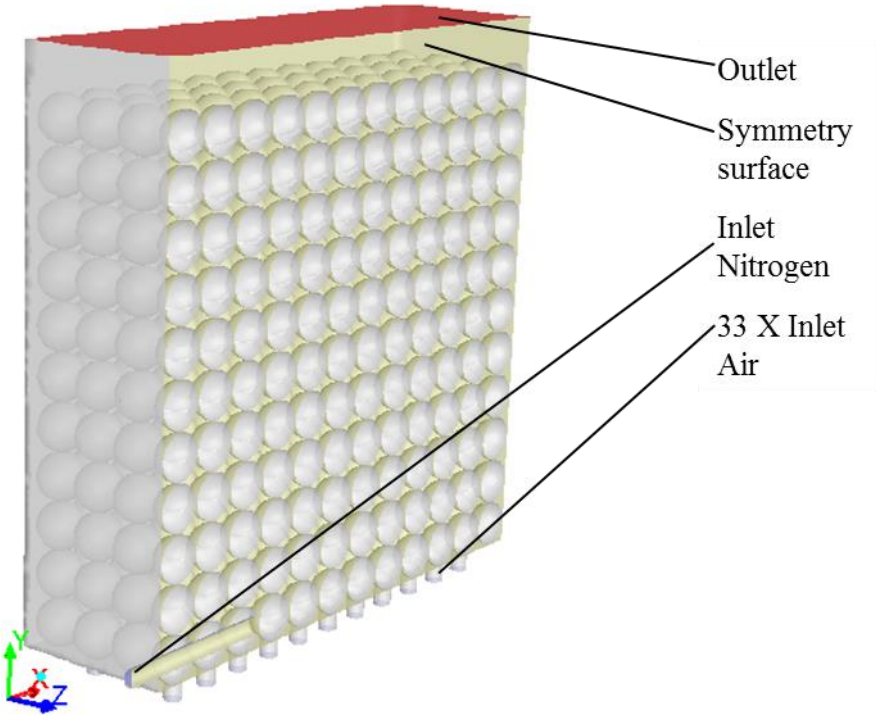

Figure 4.4: CFD isometric view of the symmetrical half domain

SolidWorks version 2014 was used for drawing all the parts of the domain; then, the case was exported from SolidWorks to ANSYS FLUENT, and ANSYS 14 was used to analyze and generate the mesh models for the CFD computation. ANSYS Meshing version 14 was used to mesh the parts of all the domains with high accuracy. The process of meshing includes grid generation and refinement of the mesh specification of the zone type (continuum or boundary type). The meshing was completed using suitable meshing schemes. Figure 4.5 shows the meshing of the domain for the RPM (gap method) in the SC bed.

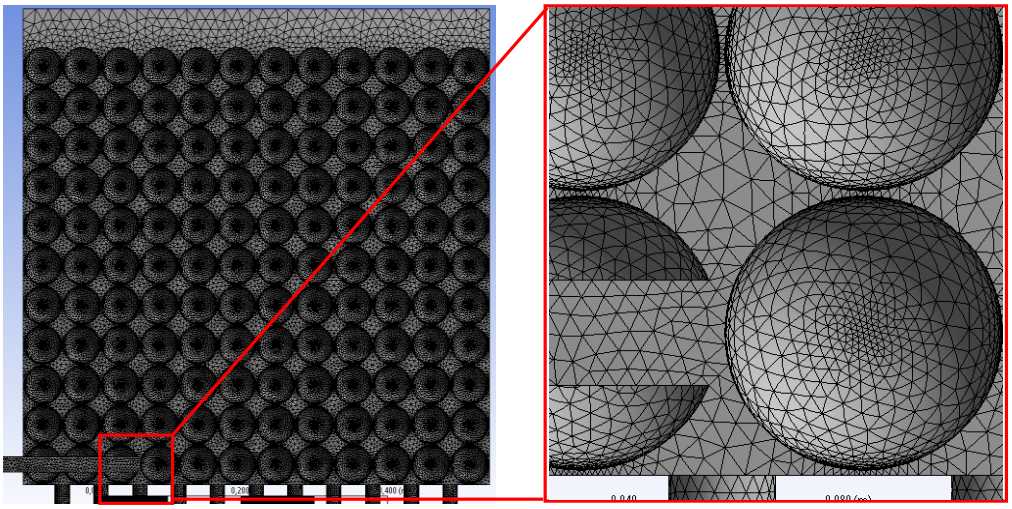

Figure 4.5: The meshing of the domain (SC gap method)

The following steps were considered:

1- Choosing the tetrahedral method for all volumes in this case because it is the best meshing method for the CFD, and it is the only method applicable to complicated geometries.
2- Defining all the boundary inlets, outlets, symmetry and walls.
3- Using the size function for the volume in the domain.

The meshing of the small parts, such as the lance, with a diameter of 6 mm, and the small gap between spheres, which was 1 mm, engaged with the large parts, such as spheres and the box, was very challenging.

4.8.4 Contact points

The meshing of region in the near contact point of wall-particle and particle-particle interfaces is an important subject in geometry generation when the RPM is applied. At these points, the meshing process cannot be conducted due to the very high skewed grid elements around the contact.

Contact point or high skewed elements do not appear in the laminar flow [4]. However, when the flow is developing into a turbulent flow, the convergence of the solution is almost unachievable. This is due to the increasing of the flow velocities in the fluid element around the contact points. In this study, the flow has a high Reynolds number (700 to 4400), which requires a turbulence model to simulate the test section. Therefore, the new mathematical domain of the SC and BCC beds reduces the skewed elements around the contact points by one of three methods (gap, overlap, or bridge). Figure 4.6 shows the contact point for the three methods (gap, overlap, and bridge) in the SC and BCC structured bed. The skewed elements around the contact points can be reduced using any of these methods, i.e., gap, overlap or bridge.

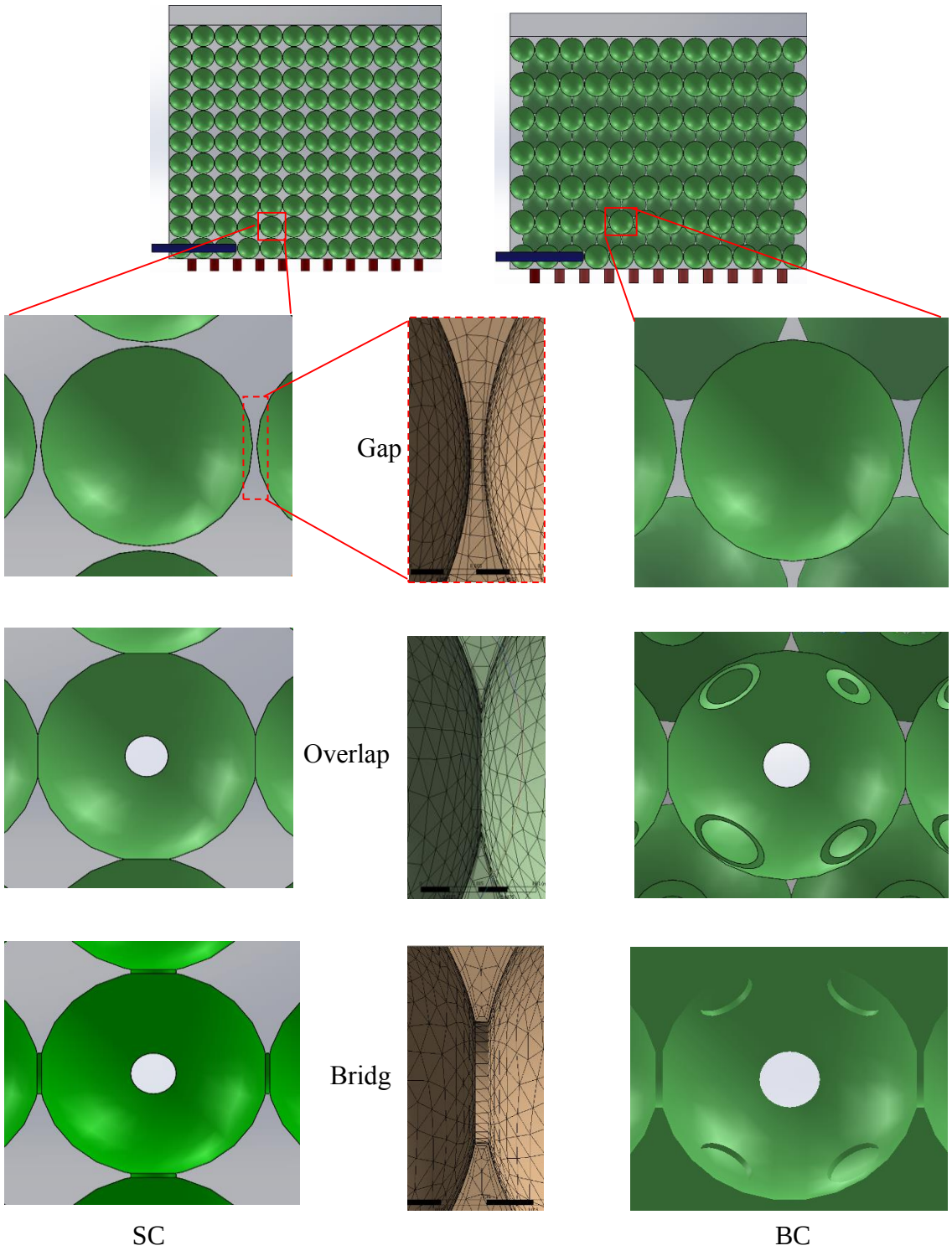

Figure 4.6: Contact point for the three methods (gap, overlap, and bridge) in the SC and BCC structured bed.

These methods have been studied by many researchers but only for axial flow. In this work, these methods are also studied for cross flow mixing through the packed bed. The gap approach for the CFD computation was used by (Calies et al., 2004; Nijemeisland & Dixon, 2001). The overlap method was advanced by (Guardo, Coussirat, Larrayoz, Recasens and Eguesquiza 2004), and the bridge development approach was used by (Ookawara, Kuroki, Street and Ogawa 2007). See Table 4.1.

Table 4.1 lists contact point studies.

Name &Year	Contact point treatment	Field	No. of particle
Calis, Nijenhuis, Paikert, Dautzenberg & Bleek (2001). Dixon and Nijemeisland (2001).	Gap	Pressure drop. Heat transfer & fluid flow.	16 44
Guardo, Coussirat, Larrayoz, Recasens & Egusquiza (2004).	Overlap	Pressure drop& Heat transfer	44
Ookawara, Kuroki, Street & Ogawa (2007)	Bridge	Pressure drop, temperature distribution	240 to 880
Eppinger, Seidler & Kraume (2011) Dixon, Nijemeislandb and Stitt (2013).	Caps	Pressure drop, velocity distribution Drag coefficient	80 to 750 1

The 1 mm space between the spherical particles in the geometrical model was chosen based on previous research performed by Michiel Nijemeisland, Anthony G Dixon [29]. The geometrical model under study approximates the real geometry when a space of 1 mm between particles is used. Therefore, the 1 mm (space and crossing) at the contact points will enlarge and reduce the simulation domain dimensions for gaps and overlaps, respectively. Therefore, the porosity for the gap and overlap will be 0.5083 and 0.4417 in the SC bed, respectively, and 0.3969 and 0.3016 in the BCC bed, respectively.

In the third method, the “bridge” method, a cylinder with a radius = 0.1 of the particle diameter is assumed to be the particle-particle and particle-wall interfaces [27]. Those cylinders will remove the fluid in the narrow gap surrounding the contact point. These cylinders, or bridges, should be meshed together with the particles (spheres). The mesh size in this method is doubled in comparison to the mesh size for the other two methods, and the porosity will be 0.469 in the SC bed and 0.331 in the BCC bed.

Tables 4.2 and 4.3 show the dimensions for each method for the two types of beds. These three methods ensure a reduction in highly skewed elements in the near-wall contact points.

Tables 4.2: SC test section dimensions due to three methods

Test section		SC Bed dimensions (m)		
Real dimensions (m)		Gap	Overlap	Bridge
L	0.624	0.637	0.611	0.624
W	0.364	0.372	0.356	0.364
H	0.572	0.584	0.560	0.572
Volume (m^3)	0.1299	0.1388	0.1218	0.1299
Porosity φ	0.48	0.5083	0.4417	0.4769

Tables 4.3: BCC test section dimensions due to three methods

Test section		BCC Bed dimensions (m)		
Real dimensions (m)		Gap	Overlap	Bridge
L	0.624	0.637	0.611	0.624
W	0.364	0.372	0.356	0.364
H	0.489	0.504	0.474	0.489
Volume (m3)	0.111	0.1194	0.1031	0.111
φ	0.35	0.3969	0.3016	0.335

4.8.5 Real box domain meshing

The mesh was created as mentioned above using the ANSYS workbench. Therefore, we adopted the simplest method for mesh generation. The mesh was generated using the Patch conforming tetra meshing method. Although this method is fully automated, it includes additional mesh controls. To control the mesh size, the element size was specified using the body size option for the entire model. The domain is typically meshed at a cell size equal to dp/52. Decreasing the element size leads to an increased number of nodes and consequently increased computation time.

Tables 4.4 and 4.5 show the total number of mesh elements and the CPU times for the two beds, SC and BCC.

Tables 4.4: Mesh size and CPU time for SC geometry

Case	Description	Sphere diameter (mm)	Pitch (mm)	Number of elements	CPU time (hours)
SC	Gap	52	53	4,642,931	>4
	Overlap		51	4,255,876	4
	Bridge		52	9,629,579	12

Tables 4.5: Mesh size and CPU time for BCC geometry

Case	Description	Sphere diameter (mm)	Pitch (mm)	Number of elements	CPU time (hours)
BCC	Gap	52	53	6,133,000	>5
	Overlap		51	3,926,000	4
	Bridge		52	9,437,000	12

Additionally, special grid design is necessary to address the cases in which the void fraction of the packing is smaller. A smaller void fraction indicates smaller gaps between particles, which may lead to extremely highly skewed cells when a coarse mesh is generated. To solve this problem, a size function is defined. In this function, the cell number in the nearest area of two particles is fixed. A growth rate and a size limit of the cells are given, which means that smaller cells are to be generated in the gaps. In addition, the size increases at a certain rate with increasing void size. Figure 4.7 depicts the grid pattern of the graded mesh in the full-bed model.

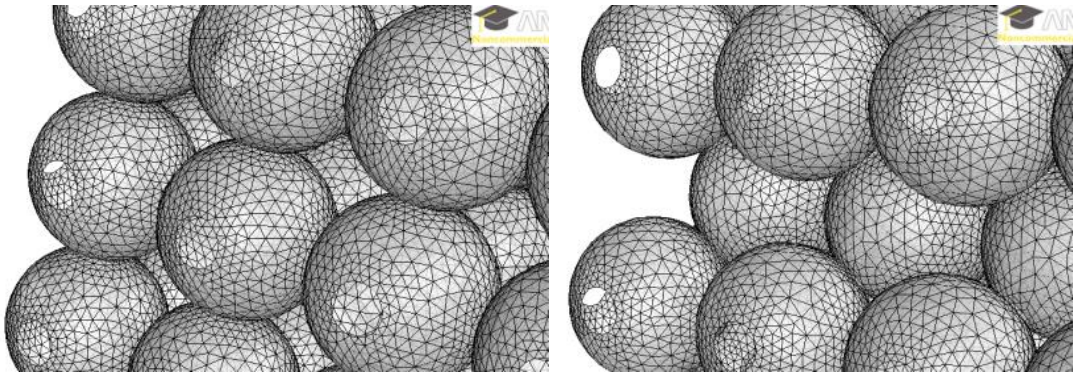

(a) (b)

Figure 4.7: Grid pattern of the graded mesh in the full-bed model: a) SC b) BCC

4.8.6 Definition of the simulation models and materials

According to the porous flow, in general, the distinct flow regimes are largely determined by the particle Reynolds number, e.g., Darcy flow (Rep < 1), Forchheimer flow (1-10 < Rep < 150), unsteady flow (150 < Rep < 300), and fully turbulent flow (Rep > 300) [45].

Here, the Reynolds number for the main flow of air varied from 700 to 4400, and that for the cross flow of nitrogen varied from 2000 to 60,000, which leads to a turbulent flow. The two inlet velocities vary depending on the flow rate values for both air and nitrogen.

The inlet boundary conditions are shown in Table 4.6. The standard k-ε turbulence model with a standard wall function is applied.

Table 4.6: Inlet and outlet boundary conditions

Boundary		D_H, mm	Flow rate ($m^3 \cdot h^{-1}$)	Temperature (k)	Turbulent Intensity (I)
inlet	air	20	40,83,150,250	300	0.05
	N_2	6,12,20	5,15,25	300	0.05
outlet		459	-	300	0.05

The species transport model was employed to calculate the O_2 concentration as a result of cross flow mixing between air and nitrogen. The fluids were taken to be incompressible at a temperature of 300 K. First-order upwind schemes were selected to compute the field variables. The pressure velocity coupling algorithm was the SIMPLE (Semi-Implicit method for Pressure Linked Equations) scheme. Default values for all under-relaxation factors were used, except for the value of the momentum, which was taken as 0.5.

The hydraulic diameter was computed from the following definition:

$$D_H = \frac{4A}{P}$$

where A is the cross sectional area and P is the wetted perimeter.
For a rectangular duct (fully filled),

$$D_H = \frac{2ab}{a+b}$$

.

Figure 4.8 a, b shows the comparison of the simulation results obtained using the three methods for the contact point treatment in the RPM for the SC and BCC beds. The data were obtained for calculation at Z = 0.468 m. This level is at a distance equal to more than 8 times the diameter of the sphere from the injection position. The ratio of the N_2 flow rate to the flow rate of air ($\dot{V}_R = \dot{V}_i/\dot{V}_{ax}$) was 0.625. The simulation results obtained based on the gap method are better fit to experimental data compared to the results obtained using the other two methods.

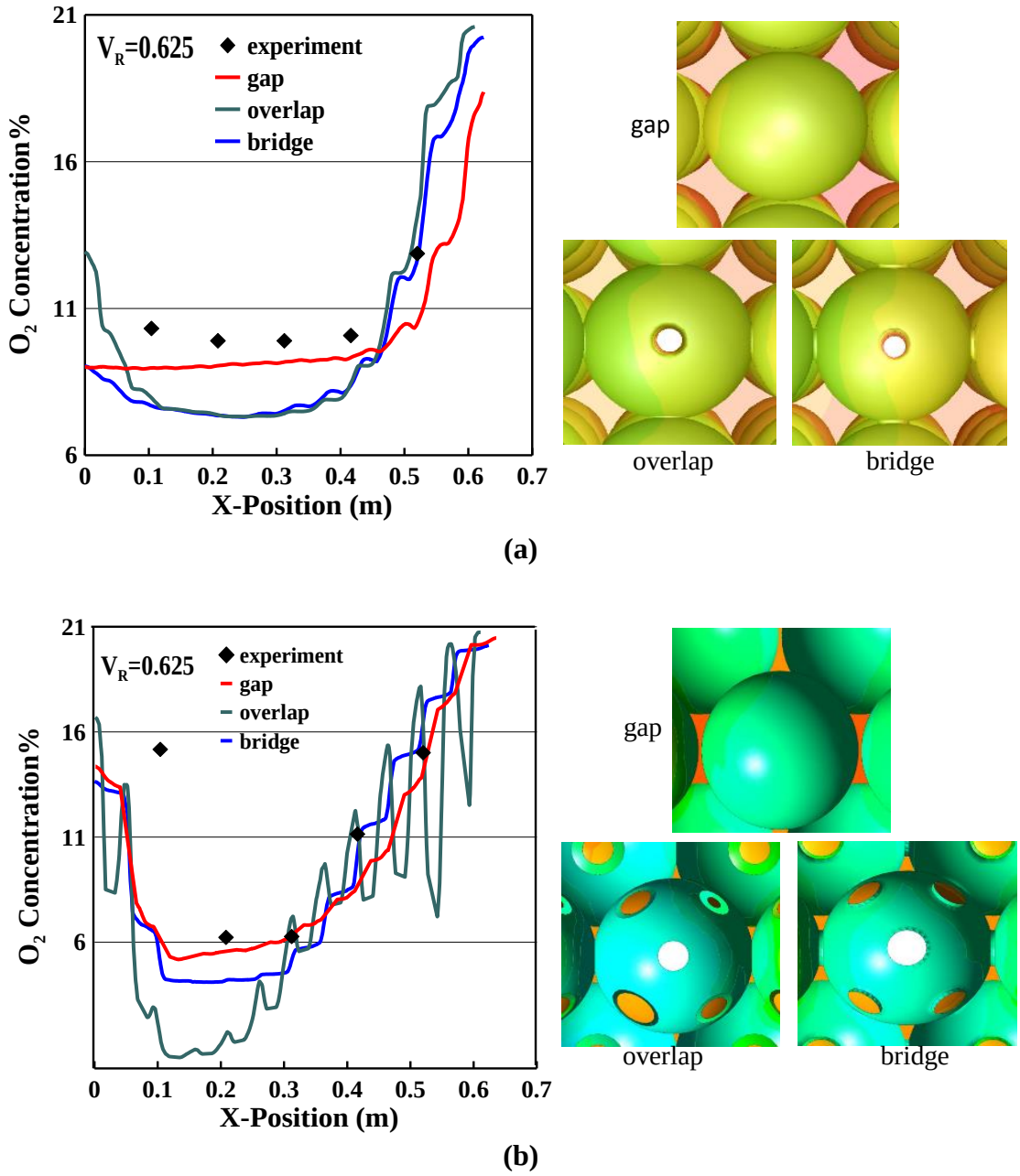

Figure 4.8: Comparison of the three contact treatment methods for (a) SC, (b) BCC and experimental data at x_L= 0.156 m and d_L= 20 mm

Figure 4.9 a, b presents the comparison of the O_2 concentration for the three methods (contact point treatment) with the experimental data at four different volumetric flow rate ratios. The figure demonstrates that the O_2 concentrations for all three methods have nearly the same profile. However, the results obtained using the gap method are much closer to the experimental results, especially with the high volumetric flow rate ratio ($\dot{V}_R$=0.625). The error between the CFD results and the experimental results ranges between 0.02 and 5%, 15 and 32% and 2 and 52% for the gap, overlap and bridge methods, respectively. Table 4.5 shows that the time consumed for the calculation when the bridge method is used is greater than that when the gap and overlap methods are employed. Thus, the gap method is recommended

when the CFD results and the results of the experiments are to be compared, as will be described in the following section.

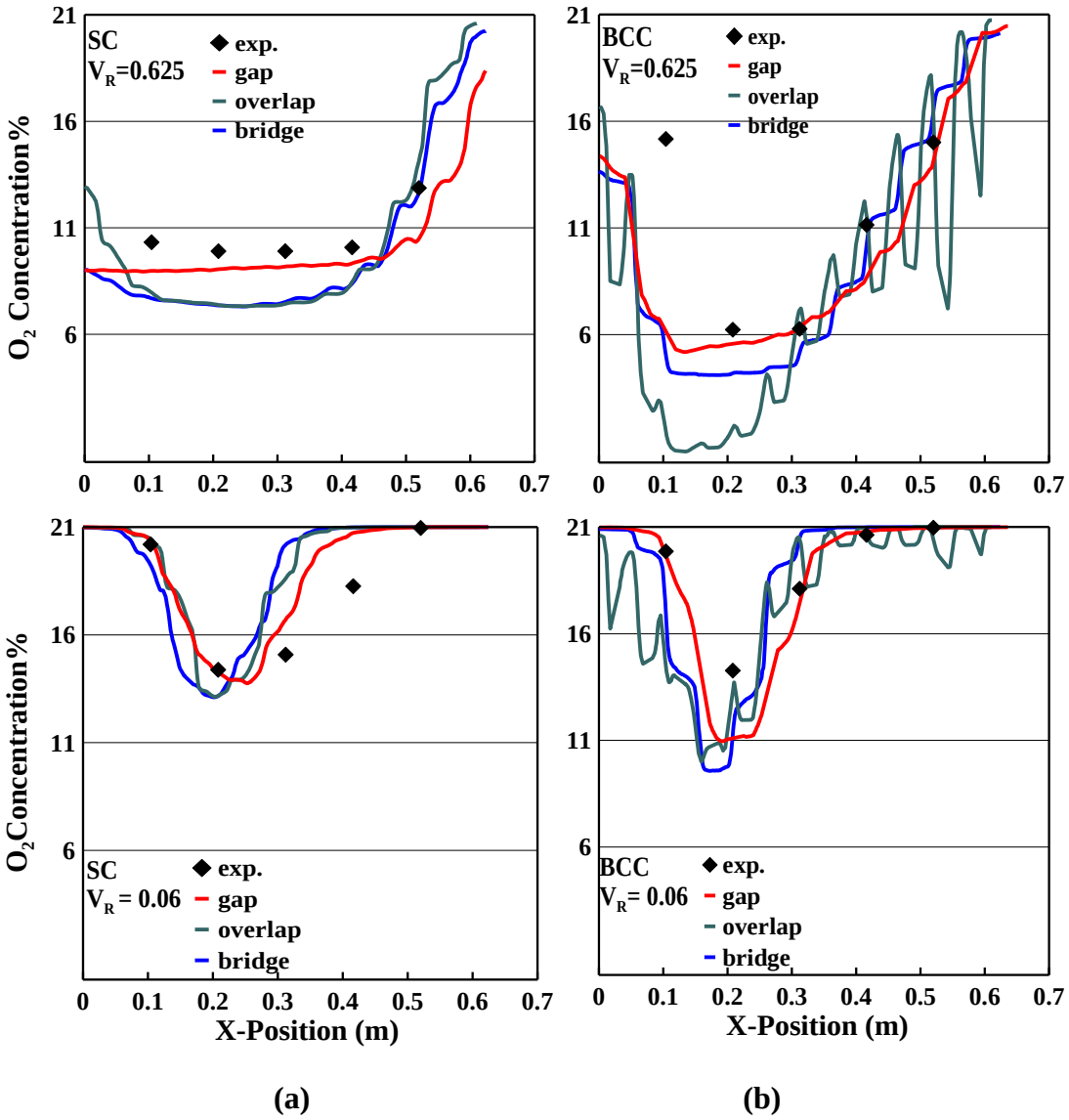

Figure 4.9: Comparison of the three methods with the experimental data for (a) SC and (b) BCC at x_L= 0.156 m and d_L= 20 mm

- *Pressure drop*

Here, spherical particles of the same diameter constitute the packed bed. The Brauer equation can be used to calculate the pressure drop for spherical particles of the same diameter in a packed bed [46]. Thus, the results for the pressure drop obtained by CFD using all these methods (gap, overlap, and bridge) for the contact point treatment are compared with the results for the pressure drop calculated using the Brauer equation.

The Brauer equation is

$$\frac{\Delta P}{L} = 160\left(\frac{(1-\varphi)^2}{\varphi^3}\frac{\mu.U}{d_p^2}\right) + 3.1\left(\frac{(1-\varphi)}{\varphi^3}\frac{\rho.U^2}{d_p}\right)\left[\frac{\mu(1-\varphi)}{\rho.U.d_p}\right]^{0.1}$$

It can be seen in Figure 4.10 (a) that the curve of the pressure drop calculated using the CFD gap method for the SC arrangement shows poorer agreement with the results of the Brauer equation. This is due to the space between particles, which reduces the flow resistance. The pressure drop achieves higher values when calculated using CFD for both the overlap and bridge method for the contact point treatment compared to the results from the Brauer correlation.

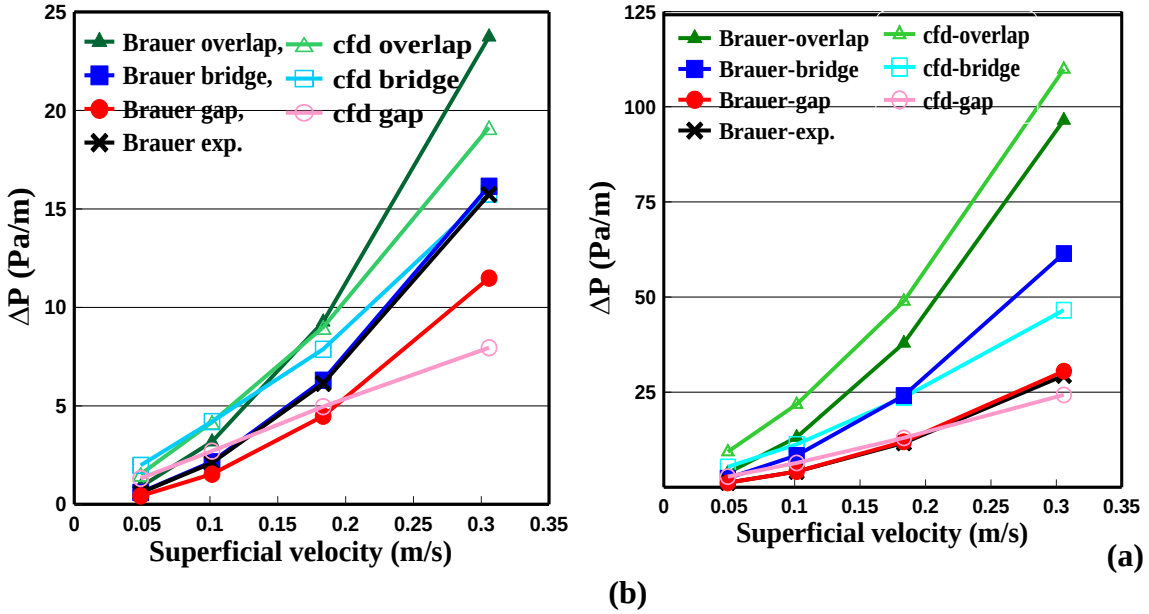

Figure 4.10: CFD calculated pressure drop as a function of superficial velocity for the three contact treatment methods, (a) SC, (b) BCC, and Brauer`s equation at x_L = 0.156 m and d_L = 20 mm.

The crossing area between particles in the overlap method was the main reason for the high pressure drop. The local porosity in the overlap method was 0.44. For the bridge method, the space occupied by the cylinder connecting the two spheres is a very small part of the total volume, which leads to a local porosity of 0.47. Therefore, it can be observed that the numerical results obtained using the bridge method agree fairly well with the pressure drop of the experimental measurements calculated by Breuer's equation. The maximum pressure drop value ranges from 7 to 24 Pa for the SC arrangement, whereas for the BCC arrangement, the porosity is 0.35. The pressure drop increases to the range of 25 to 115 Pa; see Figure 4.10 b. Moreover, a better agreement between the experimental pressure drop and CFD results is obtained under the gap method rather than bridge method. This is due to the increased number of contact points in the BCC bed, which leads to the increased crossing area and increased number of bridges between particles under the overlap and bridge methods, respectively.

- *Velocity magnitude*

Figure 4.11 shows the velocity vector maps of the simulation colored by velocity magnitude in $m.s^{-1}$ at higher $\dot{V}_{ax}$ = 250 $m^3.h^{-1}$. Beds with different arrangements are used to demonstrate the effect of porosity on the flow velocity vectors. CFD modeling of the pressure drop in a structured packed bed has been experimentally validated by many researchers. The results obtained by Xu [3] are five times smaller than those obtained using Breuer's equation. Xu used a larger specific gap, i.e., a 6 mm gap, between particles versus the 100 mm diameter of the particles, and this might have caused the large deviation.

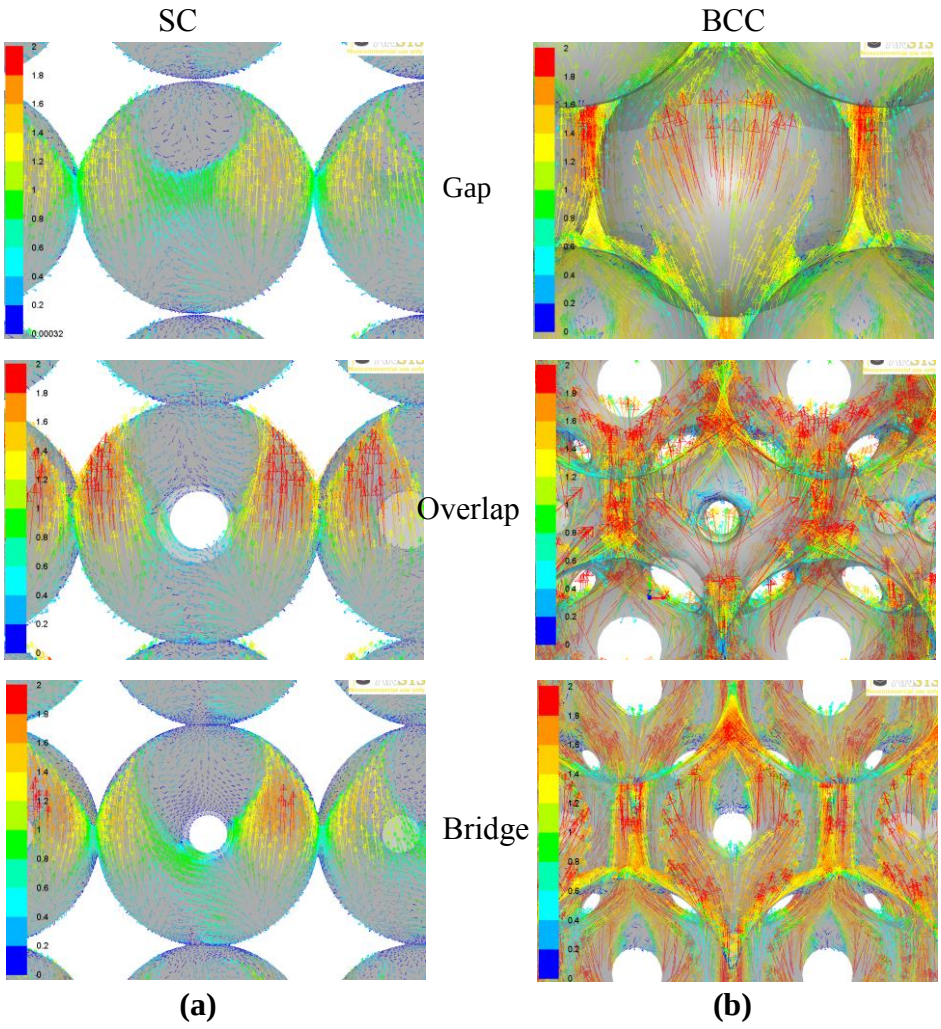

Figure 4.11: Velocity vector maps of the simulation colored by velocity magnitude in $m.s^{-1}$ at higher $\dot{V}_{ax}$ = 250 $m^3.h^{-1}$

Figure 4.12 (a) shows the comparison between the CFD results and the experimental data for the mixing velocity distribution for a volumetric flow rate ratio $\dot{V}_R$ of 1.25. The injection position is 0.156 m, and the lance diameter is 0.02 m. It can be seen that the CFD results agree with the experimental results after the injection position. Actually, the peaks in the simulation results represent the velocity. From the figure, it can be seen that the measured points show a deviation from the simulation results. This is related to the manufacturing of the spheres used

in the experiments. The spheres differ from the exact spheres created in the CFD domain because they have a mold imprint on the surface of the spheres, which could affect the flow. Regarding the experimental results, the figures show that the average mixing velocity at the outlet was 0.65 $m.s^{-1}$. However, for the simulation results, the average mixing velocity was nearly half of the experimental results. Figure 4.12 b presents the contour plot of the mixing velocity at two planes, Z= 0.026 m and Z= 0.57 m, for the RPM. It can be seen that the velocity at the end of the test box is higher than that near the injection position.

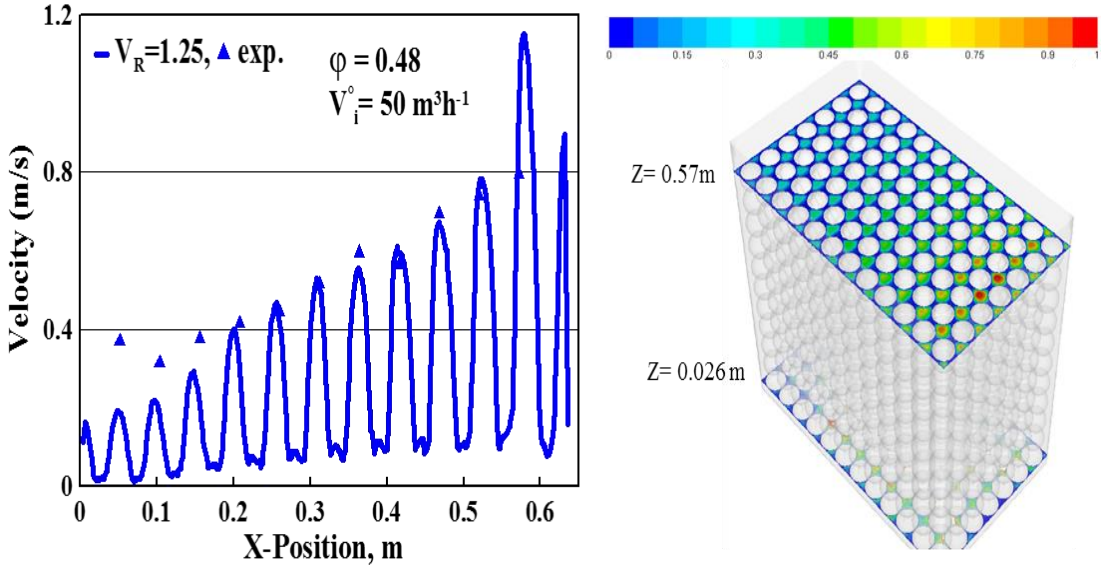

(a) (b)

Figure 4.12: (a) Comparison between CFD results and experimental data for the mixing velocity distribution, (b) Contour plot for mixing velocity at two planes in the Z direction at x_L = 0.156 m and d_L = 0.02 m

4.9 Grid convergence study of RPM

To calculate the concentration of gas mixing through the bed, theoretically, the mesh must be sufficiently fine to yield accurate solutions. Therefore, it is important and necessary to conduct a mesh independence study by increasing the number of mesh elements and monitoring the velocity and pressure drop at a specific position in the bed. Figure 4.13 a, b depicts a series of mesh sizes, ranging from the coarsest mesh, with 29 cells/cm^3, to the finest mesh, with 401 cells/cm^3, for the SC bed and from the coarsest mesh, with 31 cells/cm^3, to the finest mesh, with 646 cells/cm^3, for the BCC bed, as shown in Table 4.7 a, b.

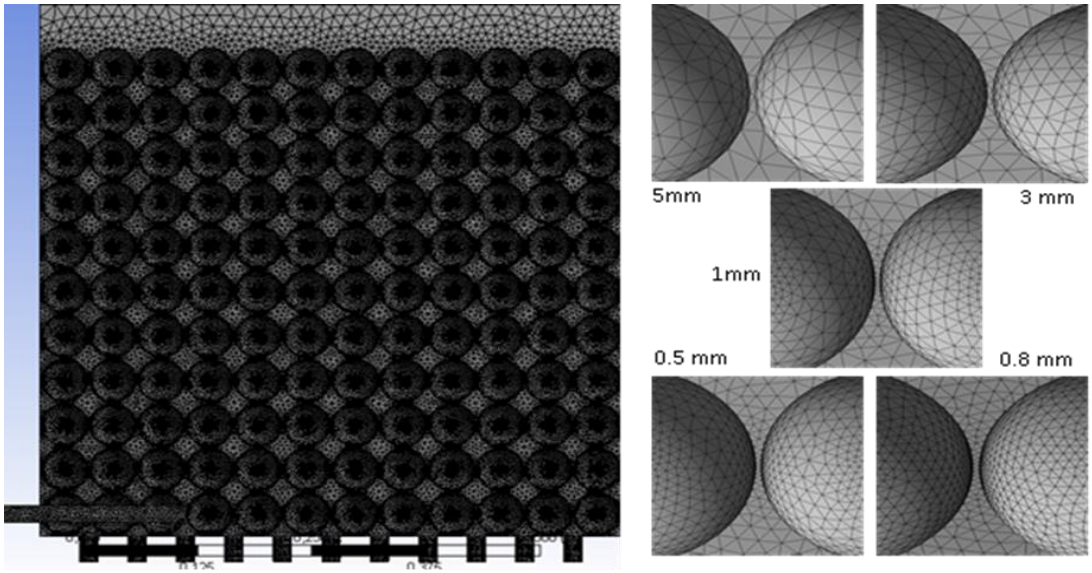

Figure 4.13a: SC Computational mesh geometry with a 1 mm interval size (gap method) with five grades of interval sizes for the mesh

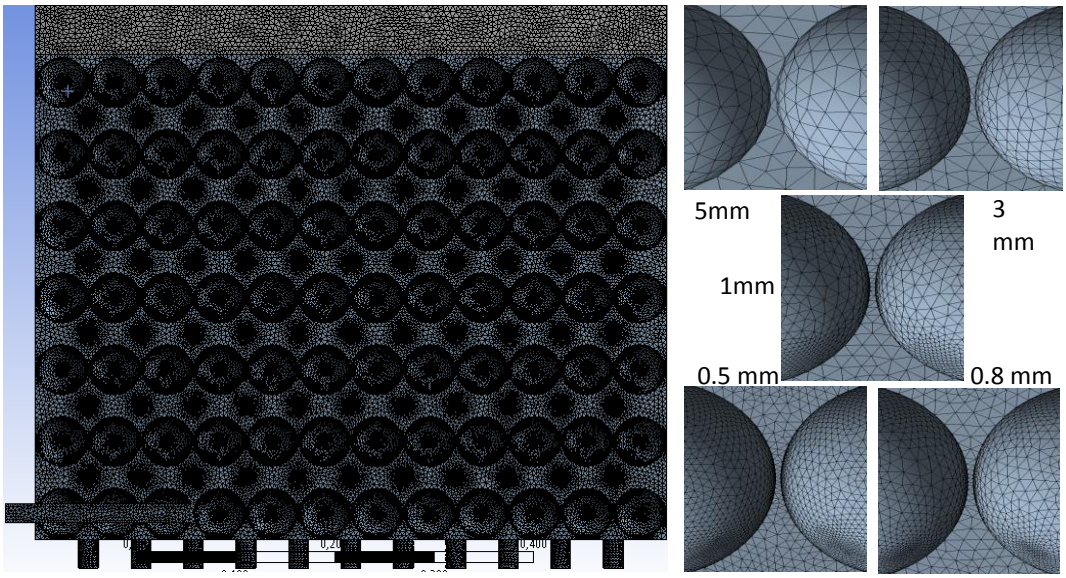

Figure 4.13b: BCC Computational mesh geometry with 1 mm interval size (gap method) with five grade of interval size for the mesh

The results show that the solution of the flow velocity becomes grid independent when a mesh density of 111 cell/cm^3. The mesh pattern on the particle surface indicates the grid structure of the whole domain. It can be noted that the grid is fine in the small gaps and becomes coarser in the larger void area.

Table 4.7 a: The grid used for the grid convergence study and the computational results (u_{air} =3.35 m/s, u_{N2}=22.5 m/s, gap method, SC bed)

Grid	Interval size mm	Cells	Density Cell/cm^3	Y^+ average	Pressure Pa at plane 0.468 m	Velocity m/s at plane 0.468 m	CPU time min
mesh 1	5	1221675	29	7.03	0.560	0.633	35
mesh 2	3	2391425	58	6.07	0.618	0.657	69
mesh 3	1	4642931	111	4.7	0-650	0.657	240
mesh 4	0.8	7606744	182	4.4	0.668	0.660	420
mesh 5	0.5	16699809	401	3.8	0.690	0.659	1275

Table 4.7 b: The grid used for the grid convergence study and the computational results (u_{air} = 3.35 m/s, u_{N2}= 22.5 m/s, gap method, BCC bed)

Grid	Interval size mm	Cells	Density Cell/cm^3	Y^+ average	Pressure Pa at plane 0.459 m	Velocity m/s at plane 0.459 m	CPU time min
mesh 1	5	943689	31	8.47	0.232	1.116	17
mesh 2	3	2306910	76	7.33	0.238	1.172	65
mesh 3	1	6130980	205	5.66	0-331	1.181	495
mesh 4	0.8	9681583	325	5.00	0.362	1.179	594
mesh 5	0.5	19265477	646	4.55	0.418	1.186	1083

Figure 4.14 a shows histograms of the cell equivolume skew, where the mesh contains a few highly skewed elements. Most of the skewed elements are located near particles near contact points. Figure 4.14 b yields the y+ values near the solid wall (sphere walls). The y+ value is a non-dimensional distance value and is important in turbulence modeling for determining the proper size of the cells near walls [21]. Here, the value is less than 5 at the surfaces of the spheres and walls.

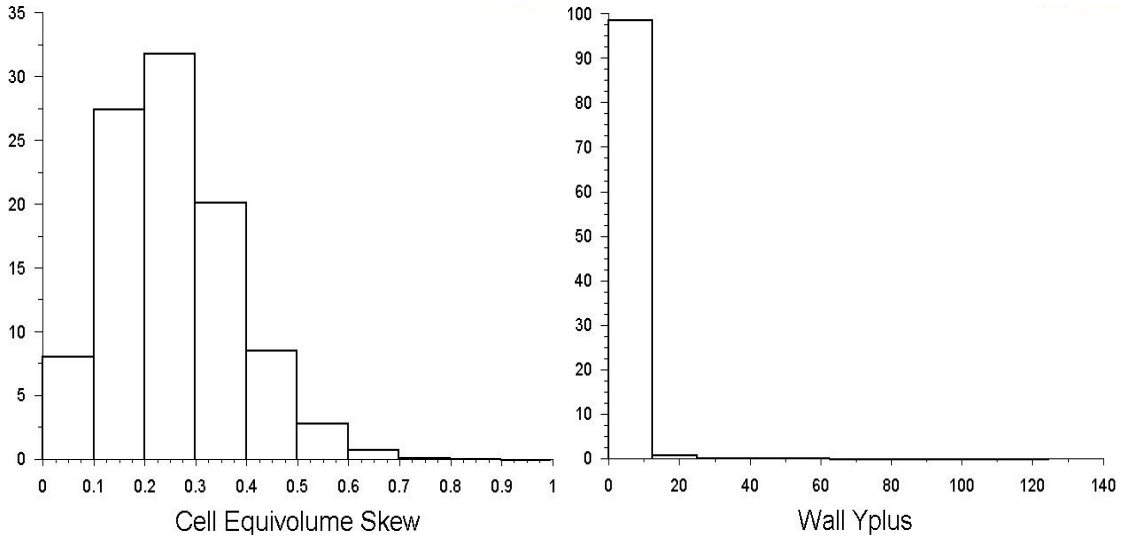

(a) (b)

Figure 4.14: (a) Histograms of the cell equivolume skew. (b) y+ values for the wall region at higher velocities for air and N_2 (u_{air} =3.35 m/s, u_{N2}=22.5 m/s, gap metho

5. Results of RPM

5.1 CFD modeling using RPM

The main purpose of the CFD simulations is to test their ability to simulate the cross flow mixing in a packed bed and to investigate how to improve this mixing using the RPM. The results of the CFD simulations are presented in the form of O_2 molar concentration contour plots and curves. As mentioned in chapter 4, this study involves understanding fluid cross flow behavior through a packed bed in a small test box. Two cases are constructed, a) an axial flow with cross flow and b) an axial flow with parallel flow, to simulate gas mixing in the bed.

5.2 Simulation results with the RPM (axial flow with cross injection)

Simulations are performed to investigate the radial mixing in a packed bed. This study mainly focuses on important parameters such as the position of lance injection, the lance diameter, and the arrangement of the packed beds. A small test rig is used to study the effects of these factors (parameters).

5.2.1 Influence of contact point treatment method

Figure 5.1 (a, b) compares the effect of the contact treatment methods in the CFD simulation on the O_2 concentration for the SC and BCC arrangements when the injection position is at 0.156 m and the volumetric flow rate ratio is taken as $\dot{V}_R$ = 0.625. The computation time under the bridge method is longer than that under the gap and overlap methods. As mentioned before in chapter 4 at tables 4.4 and 4.5 the time taken for the bridge method is longer than the time taken for the gap and overlap methods. The figure represents the comparison of the CFD results from the three methods. In this study, simulations are conducted using the gap method.

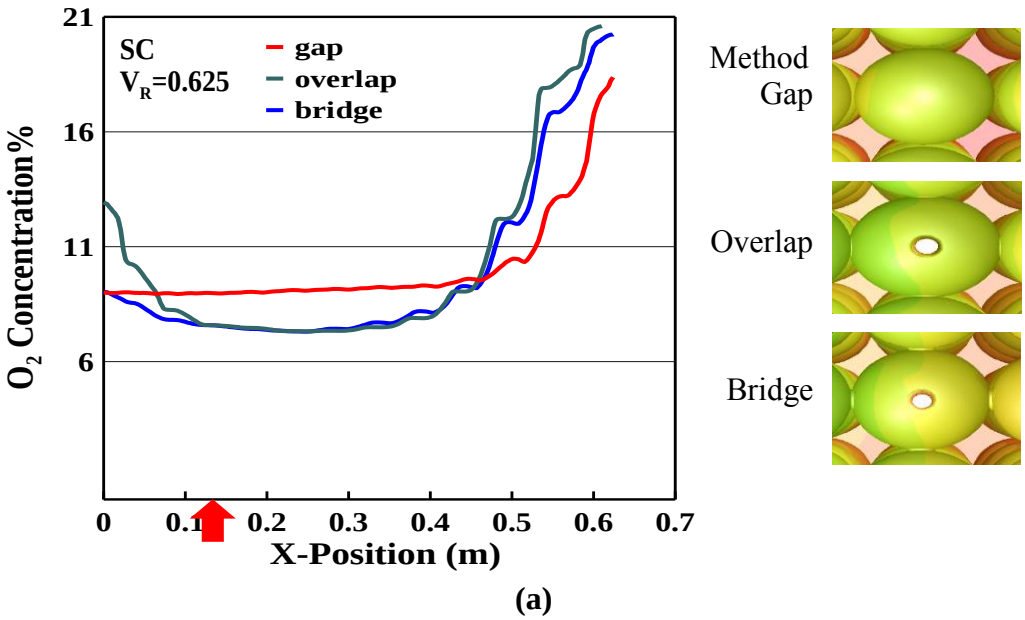

(a)

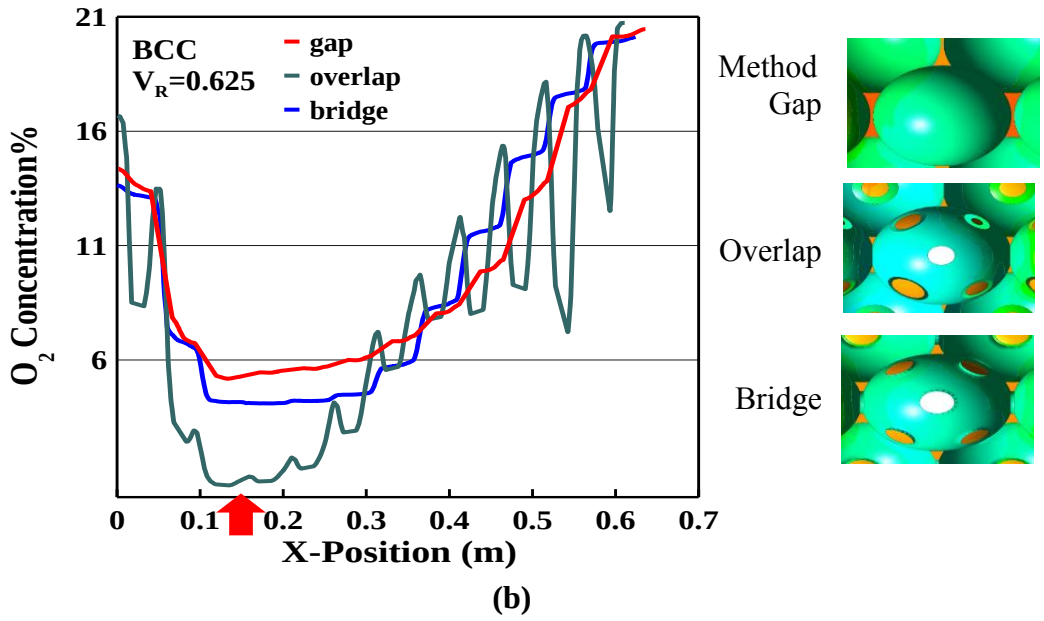

Figure 5.1: Influence of contact treatment methods on the O_2 concentration in a structured bed for a) SC and b) BCC at x_L= 0.156 m and d_L=0.02 m

5.2.2 Influence of bed height and contact treatment methods

Figure 5.2 displays the simulation results of the three methods at Z_1=0.26 m and Z_2=0.468 m for the lance injection position x_L= 0.156 m in an SC bed, and $\dot{V}_R$ = 0.625. Generally, it can be concluded that the oxygen concentration is independent of the measuring level in each method, and the gap method achieves a better fit with the experiment data. Therefore, the measurement points for the next simulations are only at a height of 0.468 m.

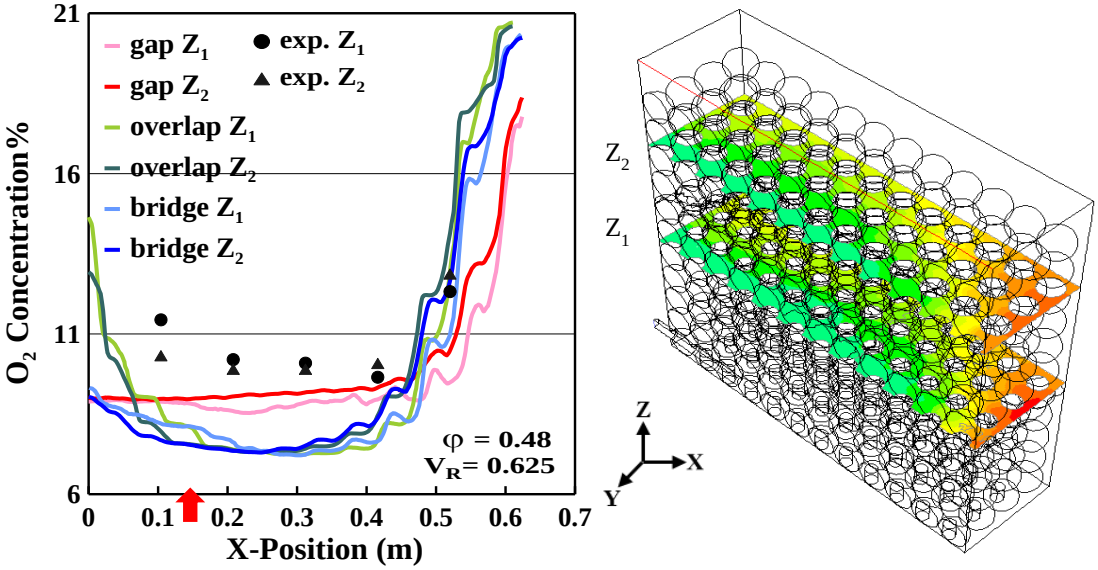

Figure 5.2: Influence of the bed level on the O_2 concentration for the three methods in an SC bed and experiment data, with x_L= 0.156 m and d_L=0.02 m

5.2.3 Influence of lance position

Simulations are performed for three cases with different positions of the lance while keeping the other operating conditions constant; see Figure 5.3. In Case I, x_L is 0 mm, i.e., the lance is on the wall of the test box. In Cases II and III, the lance injection position x_L is 156 mm and 312 mm, respectively. For all cases, the diameter of the lance is 20 mm.

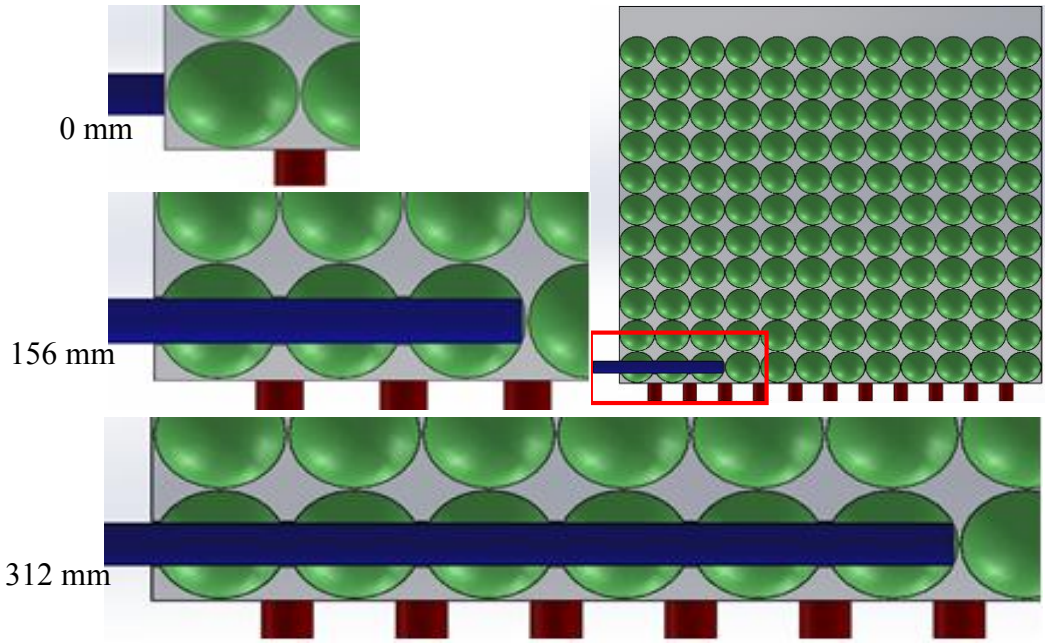

Figure 5.3: Front view for the SC domain with three different lance injection positions

Figure 5.4 (a, b) shows the influence of the lance position (injection position) on the O_2 concentration and the contour plot for high and low $\dot{V}_R$ in a SC structured bed. The curves of the O_2 concentration for a lance position of 0.156 and 0.312 m are drawn such that the reference point of the coordinate system is X= 0. Figure 5.4(a), for $\dot{V}_R$ =0.625, clearly shows that all profiles decreased together and formed a jet of N_2. The lance injection position of 0.312 m formed the left side of the jet, and the lance injection position of 0 m forms the right side of the jet. Only the lance injection position of 0.156 m could show the whole profile. Figure 5.4(b), for low $\dot{V}_R$, shows a smaller width of the jet (the distance between the first two side flat points, on the top of the curve). It seems that the minimum of the jet is shifted slightly toward the injection position with decreasing $\dot{V}_R$. For $\dot{V}_R$ = 0.625, the minimum of the jet was at approximately 0.15 m, and when decreasing the $\dot{V}_R$ to 0.06, the middle moved toward 0.1 m. Additionally, it can be seen that the minimum O_2 concentration for the lance position of 0 m was obtained at a lower position than for the other two lance positions because the flow has only one direction to move. This means that the lance position has a strong influence on the O_2 concentration profiles in the bed. Moreover, the oxygen displacement is wider than that with a lower volume ratio.

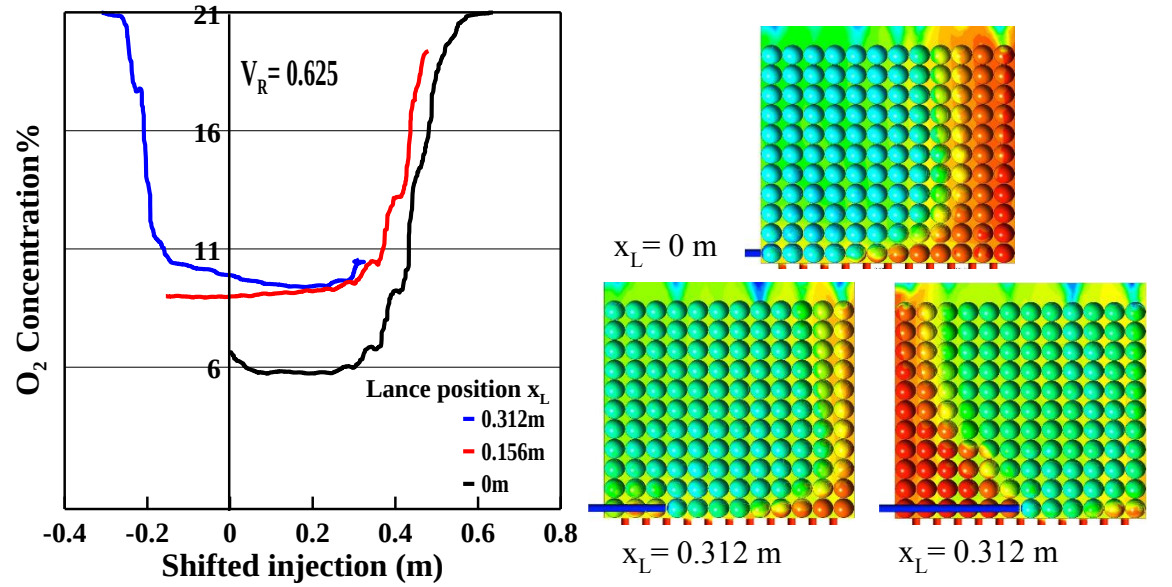

(a)

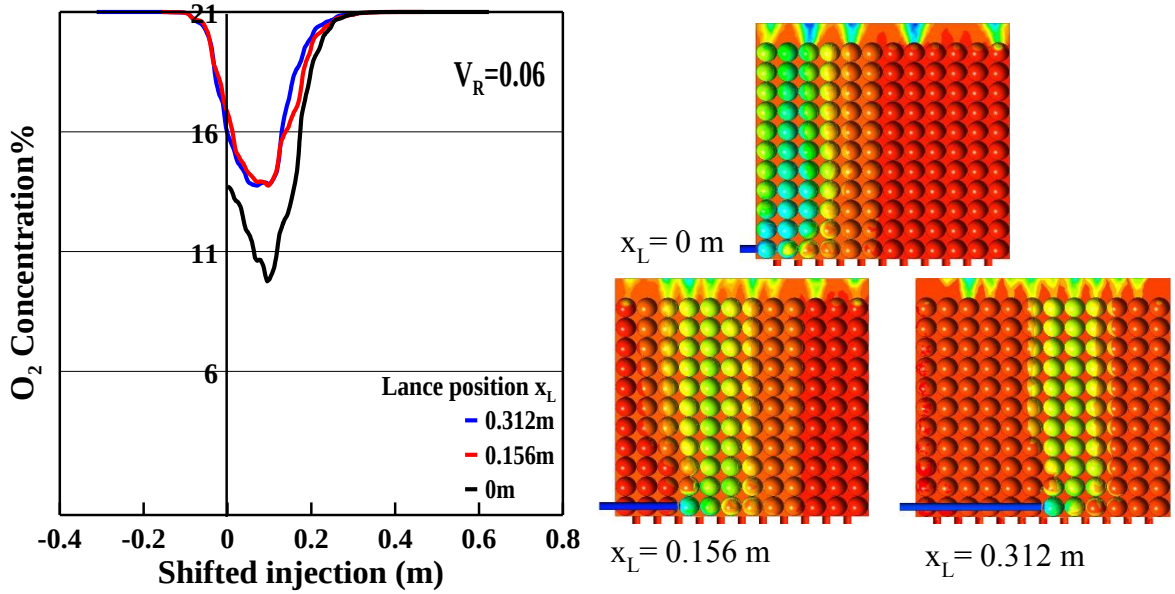

(b)

Figure 5.4: Influence of lance position on the O_2 concentration and contour plots for the SC structured bed for (a) $\dot{V}_R$ = 0.625 and (b) $\dot{V}_R$ = 0.06 at x_L= 0.156 m and d_L=0.02 m

Another test has been performed concerning the lance arrangement by changing the height of the lance from the bottom of the box from 26 mm to 100 mm. Figure 5.5 explains the contour plot of the O_2 concentration for the half of the test box in the BCC bed. The widths of the mixing jet are similar, but for a lance position of 26 mm, the mixing jet after 5 layers in height moved a distance of 1 sphere upstream. According to the figure of the bed with the lance position of 100 mm, the injection flow diffused in two directions, up and down from the injection position.

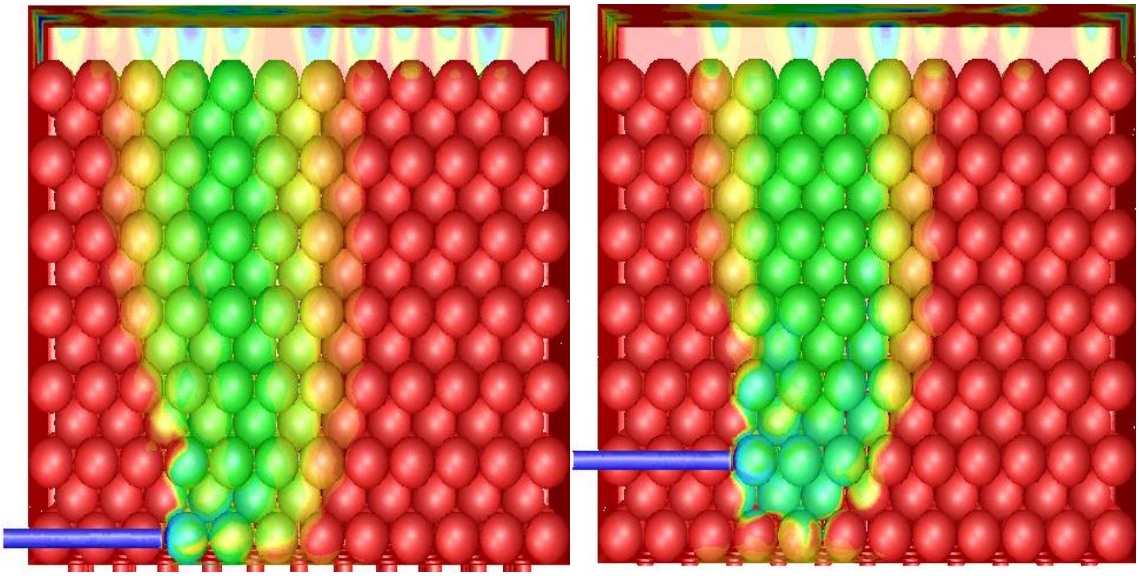

Figure 5.5: Influence of lance position on the O_2 concentration and contour plots for the BCC structured bed at $\dot{V}_R$ = 0.1 with x_L= 0.156 m and d_L=0.02 m

5.2.4 Influence of lance diameter

Figure 5.6 shows a part of the simulation domain with three diameters (6, 12 and 20 mm) of the lance inserted 0.156 m away from the wall of the box.

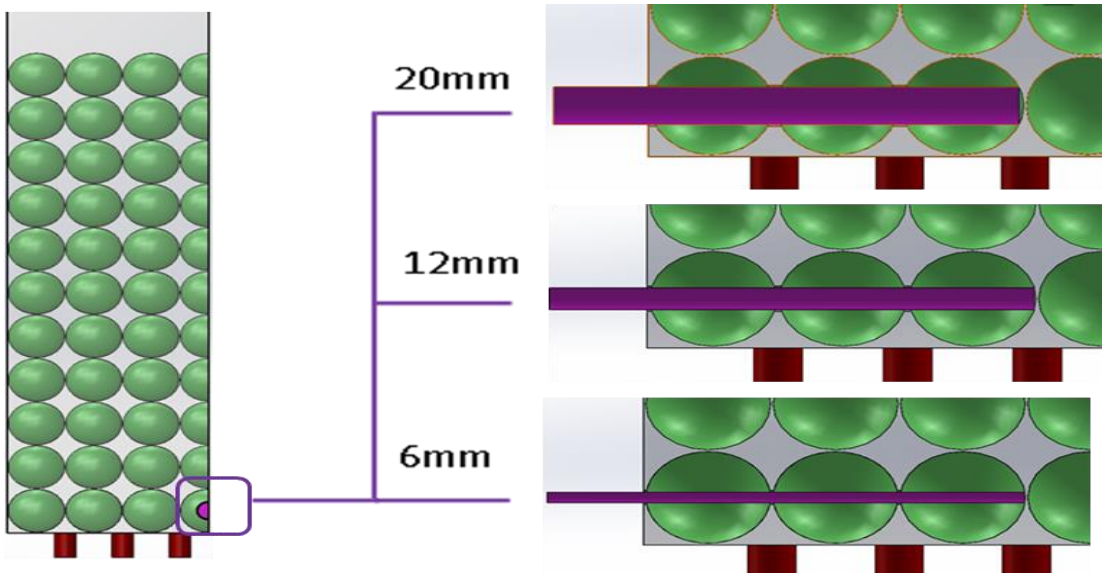

Figure 5.6: CFD domain for 3 diameters (d_L) of the lance inserted through the spheres for the SC bed

Figure 5.7 (a,b) shows the O_2 concentration curves for 3 different lance diameters with the same injection flow rate, which lead to different injection velocities. Hence, the contour plots are provided. Two flow rate ratios, i.e., 0.06 and 0.625, are considered. For the high flow rate ratio in Figure 5.7(a), the O_2 concentration curves for all lance diameters (6, 12 and 20 mm) appear to increase continuously to the end of the box. On the other hand, for the low flow rate ratio in Figure 5.7(b), the curves begin at a maximum O_2 concentration of 21% before the injection position. Next, they decreased to a minimum near the injection position. Then, the O_2 concentration curves increased again to the end of the box. The main reason for the jet shape for the curves at low flow rate ratio is the higher axial flow rate. However, the minimum shifts to a lower position with decreased velocity. It can also be concluded that the O_2 concentration is weakly affected by the diameter of the lance and thus the outlet velocity.

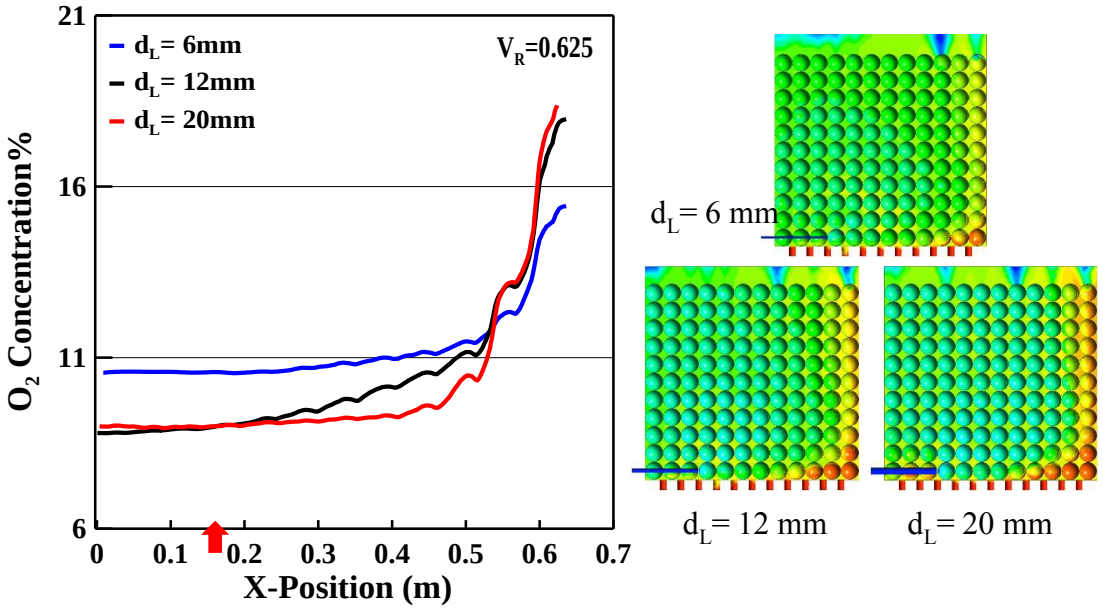

(a)

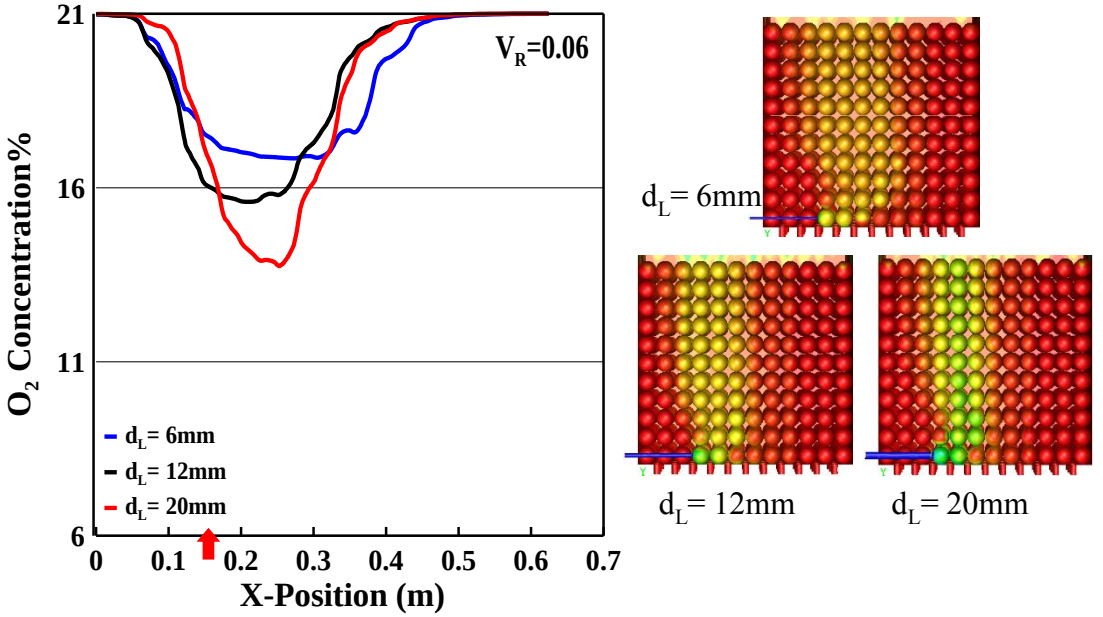

(b)

Figure 5.7: Effects of the lance diameter (injection velocity) on the O_2 concentration and contour plots for the gap method in the SC structured bed for (a) $\dot{V}_R$ = 0.625 and (b) $\dot{V}_R$ = 0.06, with x_L= 0.156 m and d_L= 0.02 m

5.2.5 Influence of volumetric flow

Figure 5.8 shows the effect of the total volumetric flow on the O_2 concentration at a lance position of 0.156 m. The curves show the same tendency and are nearly independent of the volumetric flow rate ratio $\dot{V}_R$.

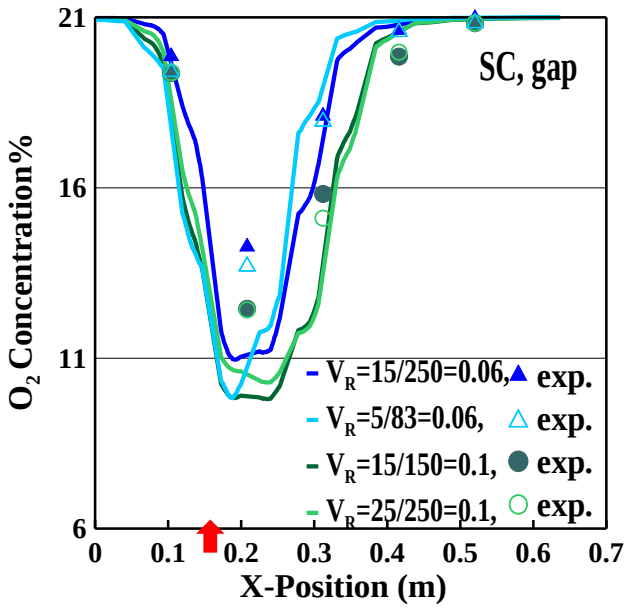

Figure 5.8: Volumetric flow effect on the O_2 concentration in the SC bed

5.2.6 Influence of volumetric flow rate ratio

The effect of the volumetric flow rate ratio on the oxygen concentration is shown in Figure 5.9 (a, b) for the gap method for the SC and BCC beds. The lance injection position is x_L= 0.156 m, and the lance diameter is d_L= 0.02 m. The volumetric flow rate ratio is varied by varying the air flow rate, i.e., the keeping N_2 flow $\dot{V}_I$ = 25 $m^3.h^{-1}$ constant. Figure 5.9 (a) shows the influence of the four different values of $\dot{V}_R$ (0.1, 0.166, 0.3 and 0.625) on the O_2 concentration in an SC structured bed. A higher $\dot{V}_R$ results in a wider O_2 concentration curve. The contour plots in the figure show that, when the volumetric flow rate ratio increases, more oxygen spreads across the bed. From the two figures, it is clear that the minimum O_2 concentration is obtained at a lower position for the BCC bed, as shown in Figure 5.9 (b), compared to the SC bed.

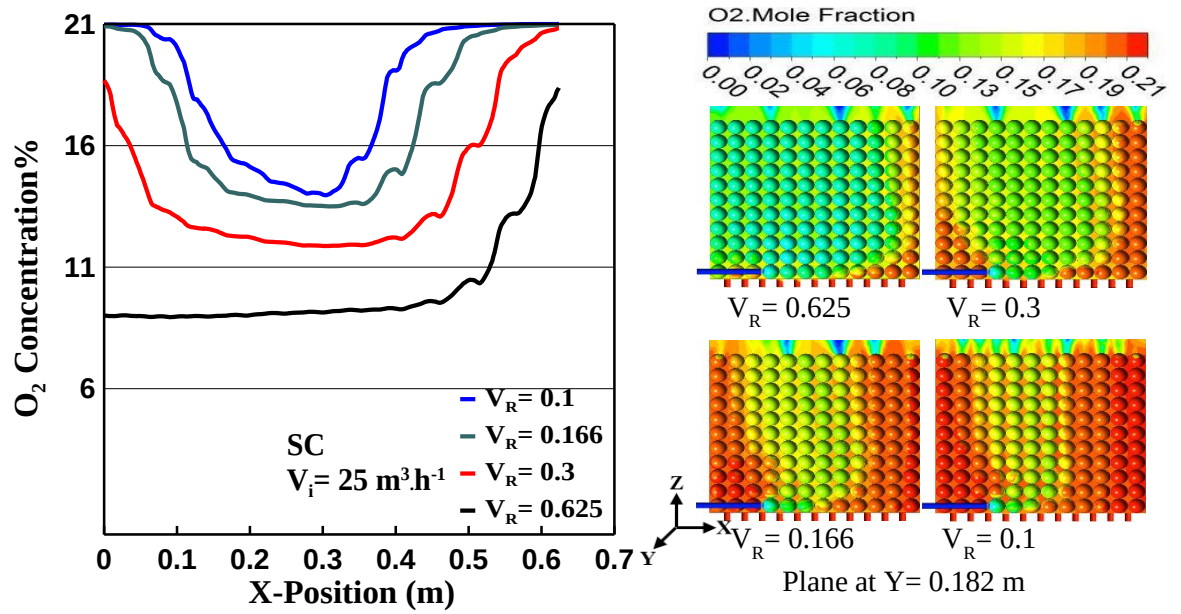

(a)

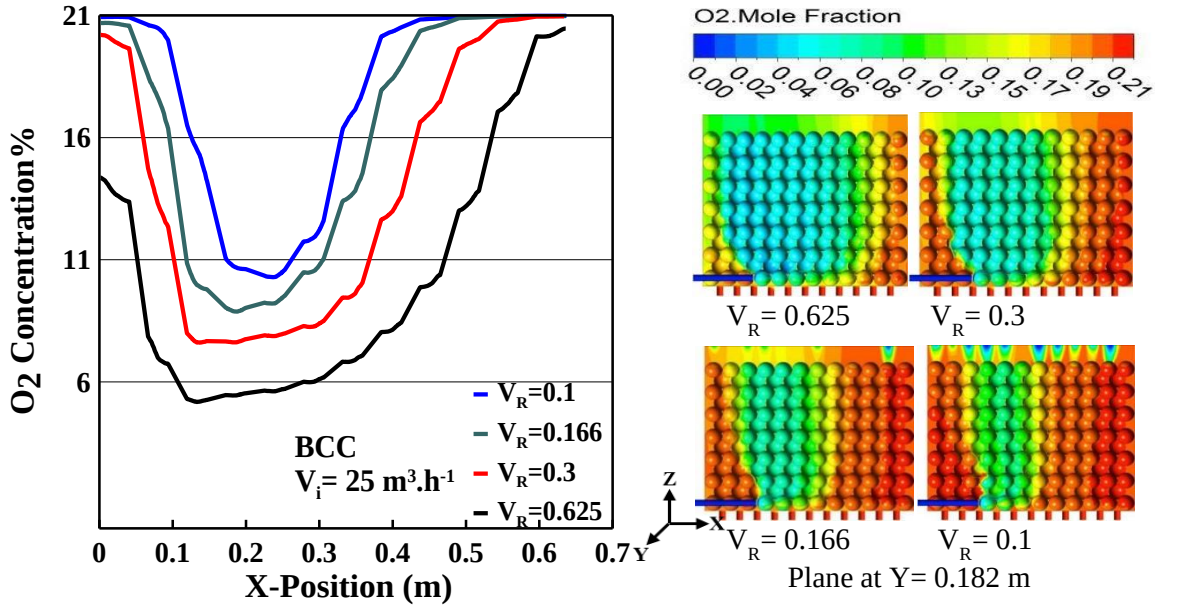

(b)

Figure 5.9: Influence of $\dot{V}_R$ on the O_2 concentration and contour plots in the structured bed for (a) SC and (b) BCC, with x_L= 0.156 m and d_L=0.02

5.2.7 Velocity profiles

Figure 5.10 shows the mixing velocity distribution for different measuring positions (lines) at the outlet plane, as shown in Figure 3.1(b). At each measuring position (line), 11 points are taken for the measurements. The velocity measurements were performed using a hot wire, therein obtaining an error of approximately ±0.01 m. s^{-1}. From the figure, it can be noted that there is a few difference in the mixing velocity distribution through the cross lines at the outlet of the box. Therefore, all the results can be taken at one line, and in this study, the measurements are taken at line 3.

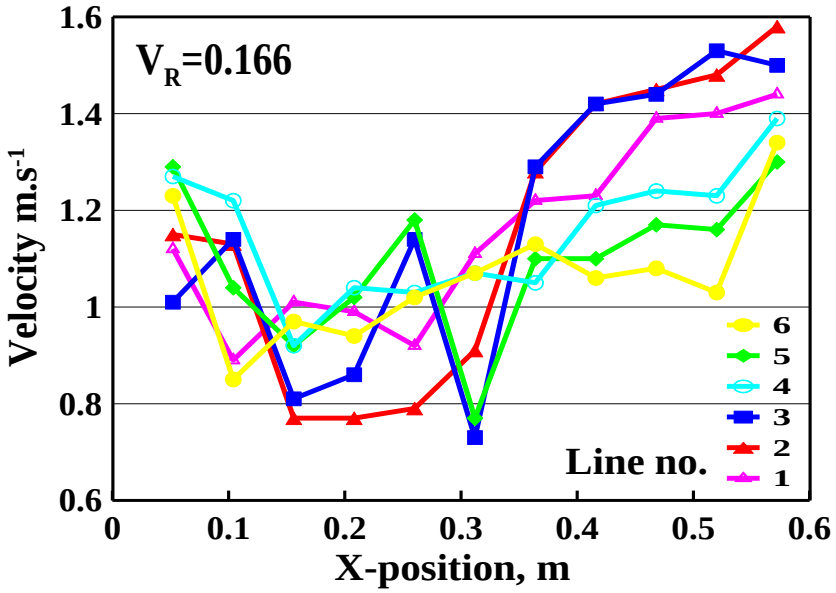

Figure 5.10: Mixing velocity distribution for different lines at the outlet plane, with x_L= 0.156 m and d_L=0.02 m

Figure 5.11 (a,b) presents the mixing velocity distribution for a volume ratio of 1.25 with two injection locations (0.156 m and 0.312 m) in an SC bed. The CFD results show the same trends for both lance positions. It can be seen that the CFD results agree with the experimental results after the injection position for both injection locations. Actually, the peaks in the simulation results represent the O_2 concentration. The results obtained from the experiments deviate from the results of the simulation. This could be due to the inability to manufacture exact spheres, which are different from the assumed spheres in the simulations. The figures show that the average mixing velocities at the outlet are 0.85 m.s^{-1} and 0.43 m.s^{-1} when the injection positions are 0.156 m and 0.312 m, respectively. However, the average velocities calculated through the simulation are nearly half the average velocities obtained in the experiments.

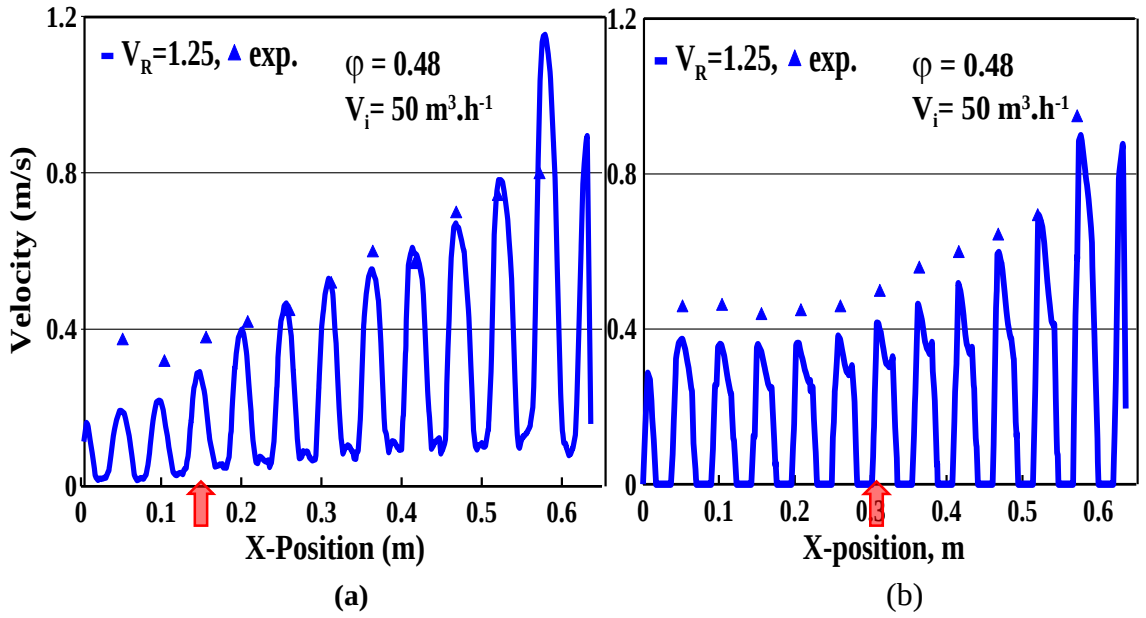

Figure 5.11: Comparison between CFD results and the experimental data for the mixing velocity distribution with volumetric flow rate ratio of 1.25 (a) at x_L= 0.156 m and (b) at x_L= 0.312 m

Figure 5.12 represents the mixing velocity distribution for the BCC bed with a volumetric flow rate ratio of 1.25 and an injection position of 0.312 m. The CFD results present the same trend as the experimental data. It can be seen by the contours shown in Figure 5.12 that channels can be found near the walls of the test box. These channels are created due to the arrangement of spheres in the BCC configuration. Thus, there is low resistance to the flow near the walls. The BCC configuration also leads to an increased resistance to flow in-between the spheres in the interior of the box. Furthermore, these channels exist in a real shaft kiln. The contour plot shown in the figure presents the contours of the magnitude of the velocity in the plane at the lance level Z= 0.026 m and at the plane Z= 0.5 m for the BCC bed. It can be seen that the velocity is higher at the circumference of the test box due to the channeling of the flow. The main reason for this is the space created between the spheres and walls of the test box under this arrangement. In addition, the average of the mixing velocity at the outlet was 0.43. However, for the simulated results, the CFD calculations of mixing velocity was nearly the velocity obtained from the experiments.

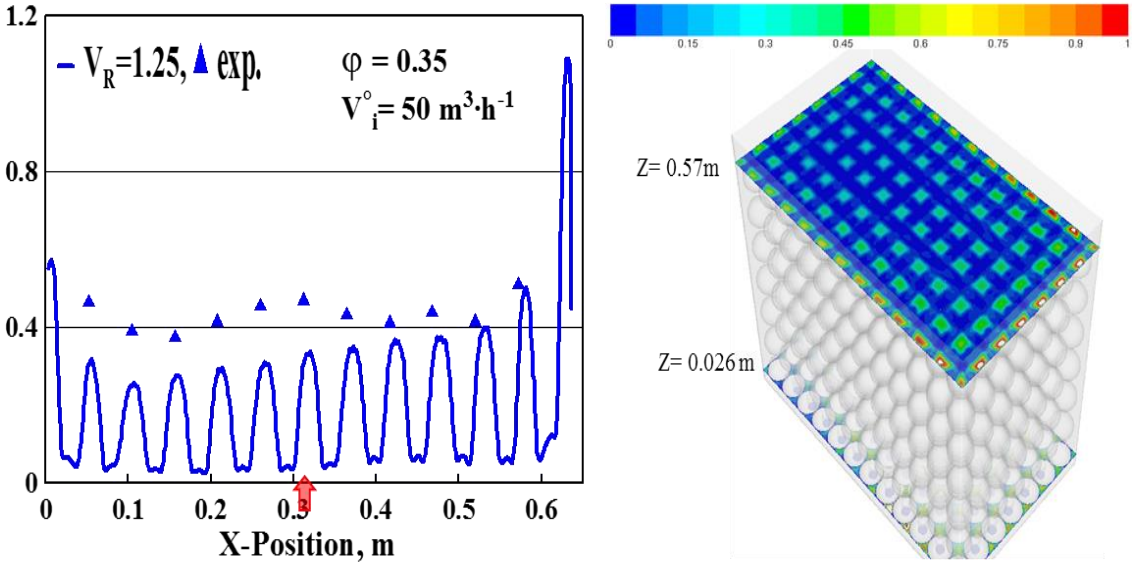

Figure 5.12: Comparison of CFD results and the experimental data for the mixing velocity distribution and contour plot at two planes with a volumetric flow rate ratio of 1.25, with x_L= 0.312 m

5.3 Simulations results of RPM (axial flow with parallel injection)

For the parallel flow, the nitrogen was injected through the bottom of the box parallel to the air flow, as shown in Figure 5.13 (a). The injection flow rate was $\dot{V}_i$ = 25 m³.h^{-1}, the air flow rate values were $\dot{V}_{ax}$= 40 m³.h^{-1} and 250 m³.h^{-1}, and the lance diameter for nitrogen injection was 20 mm. The experiments were performed with two lance injection positions of 0 m and 0.104 m in the Z direction. To bring the nitrogen gas into the test chamber, a bore with a diameter of 22 mm was attached at the perforated plate. The position of the nitrogen lance in both arrangements was kept the same in the experimental box. In the bed with the SC, the lance was fixed in the center with respect to the width and at a distance of 286 mm from either side with respect to length, as shown in Figure 5.13(b). In the BCC bed, the lance was fixed in one of the holes for the air inlet.

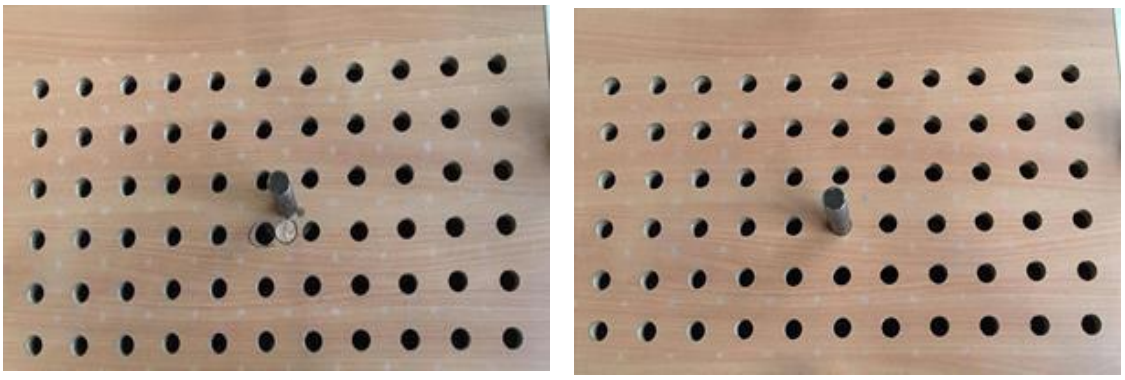

SC BCC

(a)

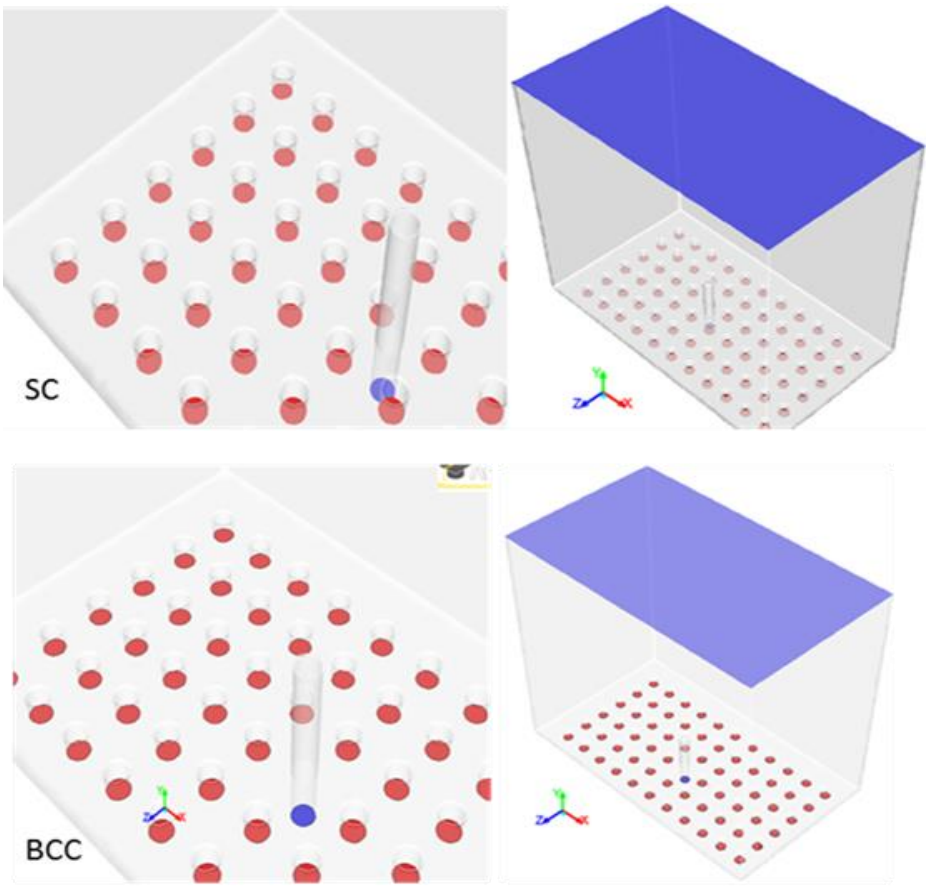

(b)

Figure 5.13: (a) Real perforated plate with two lance injection positions. (b) CFD domain with the perforated plate, injection lance and 66 holes for the axial air flow

5.3.1 Influence of contact point treatment method

Figure 5.14 (a, b) numerically compares the effects of the two contact point treatment methods (gap and overlap) on the O_2 concentration when the injection flow is parallel to the axial flow. The figure also shows contour plots of the flow mixing behavior. Two bed arrangements (SC and BCC) and two volumetric flow rate ratios $\dot{V}_R$ (0.625, 0.1) were studied. The overlap method predicts a lower minimum O_2 concentration compared to the gap method. This could be due to the slightly higher void fraction $\varphi = 0.51$ of the bed for the case of the gap method. Moreover, the minimum O_2 concentration has a lower value under the BCC arrangement compared to the SC arrangement for both methods, which could be due to the channeling through the packed bed.

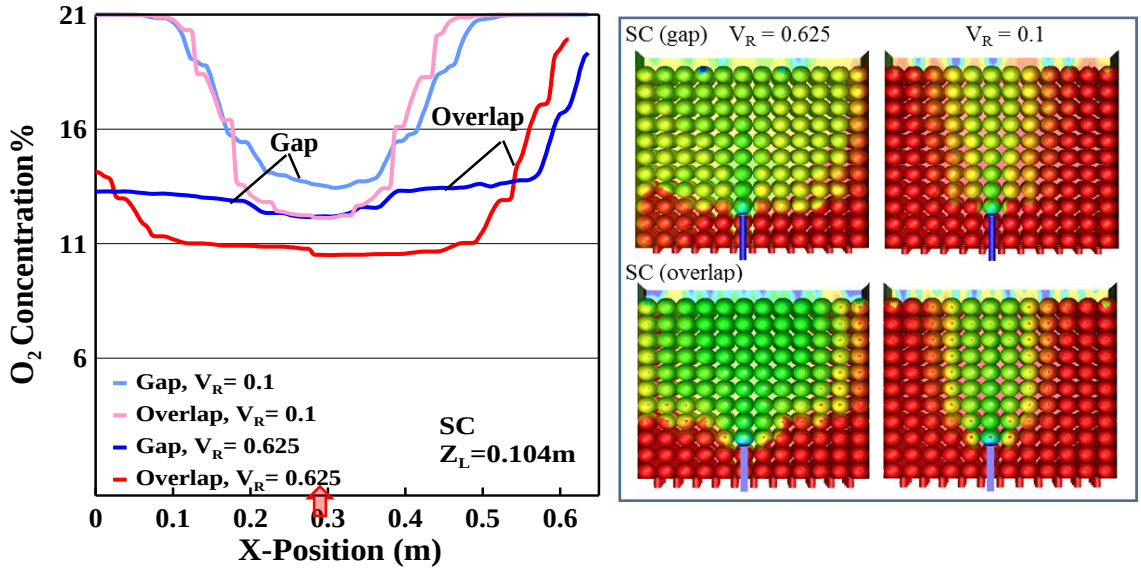

(a)

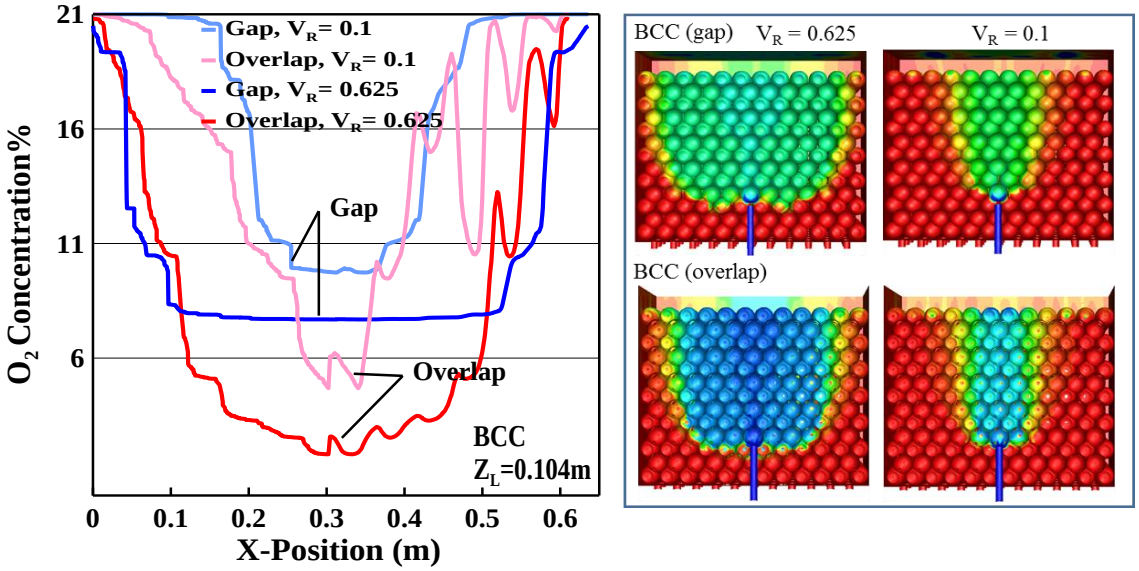

(b)

Figure 5.14: Influence of contact point treatment methods on the O_2 concentration in a structured bed for different volumetric flow rate ratios in parallel flow for a) SC and b) BCC, with z_L= 0.104 m and d_L=0.02 m.

The injection position in the z direction was 0.104 m away from the bottom. The injection position in the x direction varies for the SC and BCC beds depending on the arrangement of the layers. In the SC arrangement, the lance was inserted 0.286 m away from the box wall, as shown in Figure 5.15. The depth in the bed is equivalent to two sphere diameters. For the BCC bed, the lance was placed in the middle of the perforated plate, i.e., at 0.312 m from the wall. The lance was inserted through a hole in the spheres to again obtain a depth equivalent to two sphere diameters, as shown in Figure 5.16.

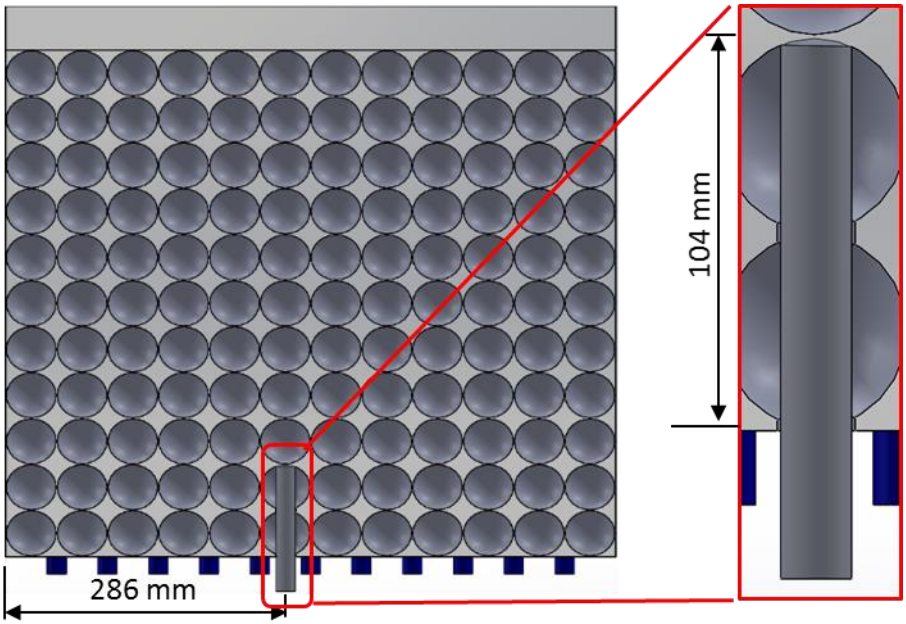

Figure 5.15: Lance injection position in the SC structured bed

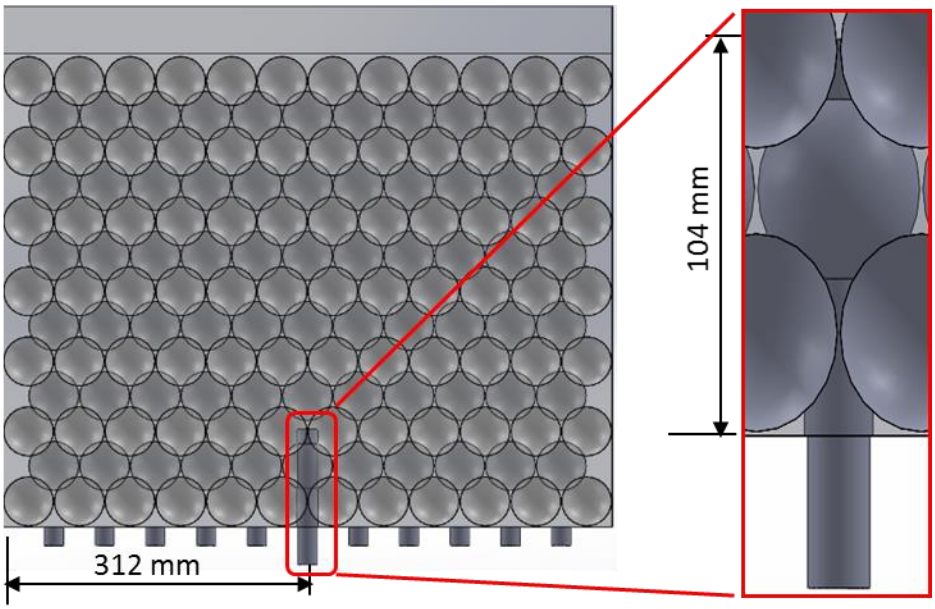

Figure 5.16: Lance injection position in the BCC structured bed

5.3.2 Influence of the flow rate ratio for the two bed arrangements

Figure 5.17 shows the contour plot of the parallel flow for the two bed arrangements. Two volumetric flow rate ratios were used for each type of arrangement. The injection position in the z direction was at a position of 0.104 m away from the bottom, and the lance diameter was 20 mm. A narrower jet is obtained when $\dot{V}_R = 0.1$ compared to the jet obtained when $\dot{V}_R = 0.625$ in both arrangements. An even narrower jet can be obtained under the SC arrangement, as the BCC results in a higher pressure drop in the z direction compared to the SC arrangement. Figure 5.18 shows the O_2 concentration profiles. The minimum O_2 concentration in the SC bed has a greater value than that in the BCC bed.

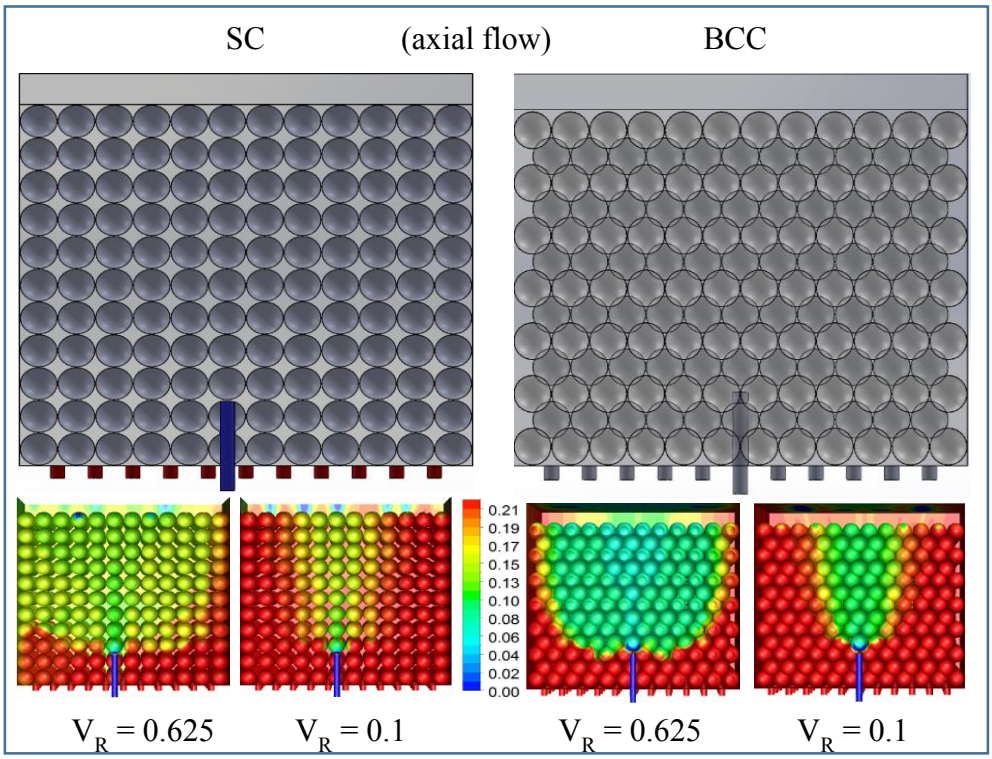

Figure 5.17: Axial flow in the SC and BCC structured bed domains and a contour plot of the O_2 concentration for two different $\dot{V}_R$, with z_L= 0.104 m and d_L=0.02 m

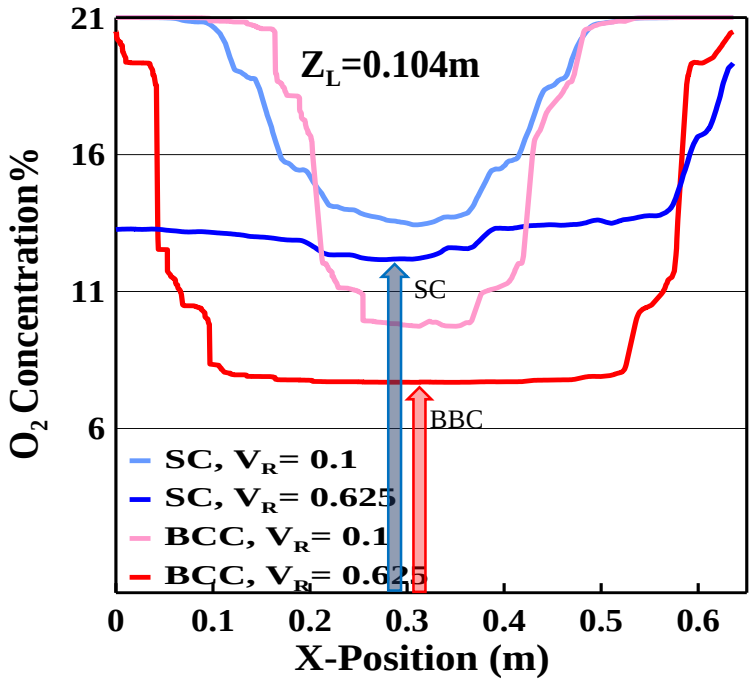

Figure 5.18: Influence of $\dot{V}_R$ on the O_2 concentration for axial flow with parallel injection flow in the SC and BCC arrangements, with z_L= 0.104 m and d_L=0.02 m

5.3.3 Influence of the axial lance injection position

Two injection positions of 0 m and 0.104 m in the Z direction were used in the parallel flow for the BCC structured bed. Figure 5.19 shows the O_2 contours, and Figure 5.20 shows the O_2 profiles for the two mixing ratios. There is no influence of the injection position on the O_2 concentration even with different volumetric flow rate ratios see Figure 5.20.

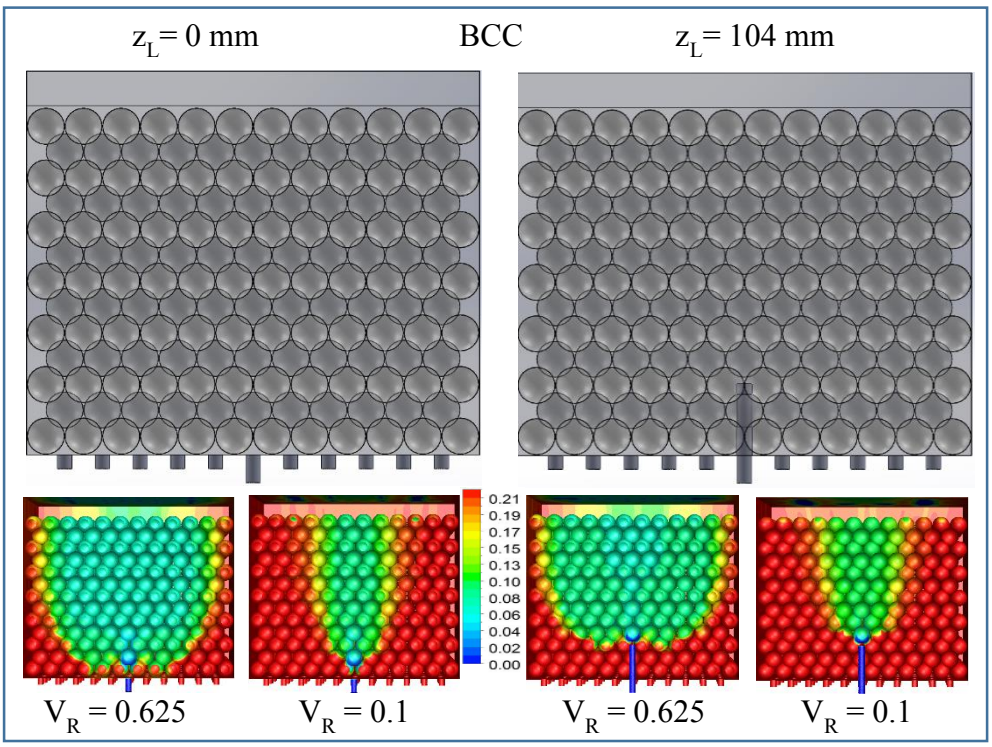

Figure 5.19: Axial flow domain with two injection positions, z_L = 0 and 104 mm, for the BCC structured beds and the contour plots of the O_2 concentration for two different $\dot{V}_R$

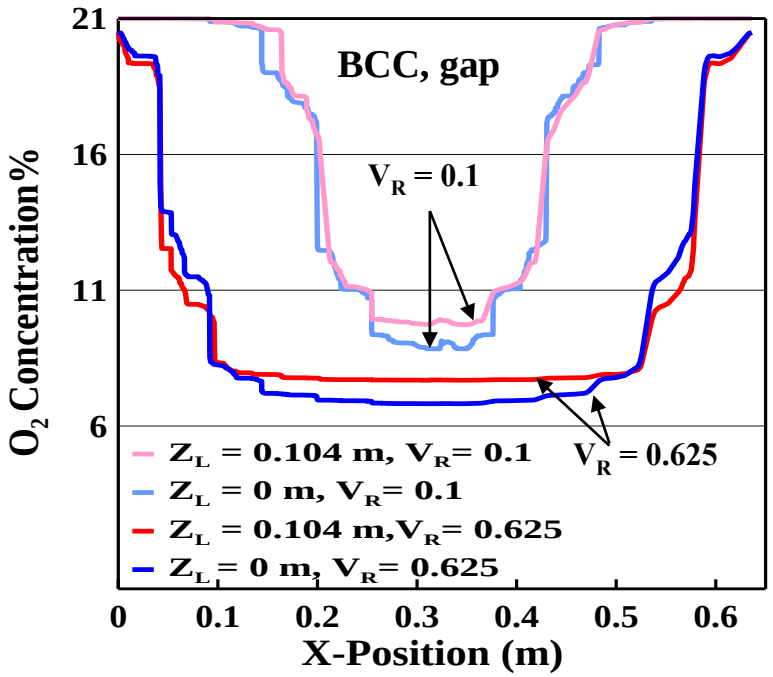

Figure 5.20: Influence of the axial lance injection position z_L and $\dot{V}_R$ on the O_2 concentration for the BCC bed.

The results of the simulation using the RPM employing the gap method for both the BCC and SC structured beds and their validation with experimental data are summarized in Figure 5.21. The results of the simulation and experimental data better agree when $\dot{V}_R$ is low for both beds.

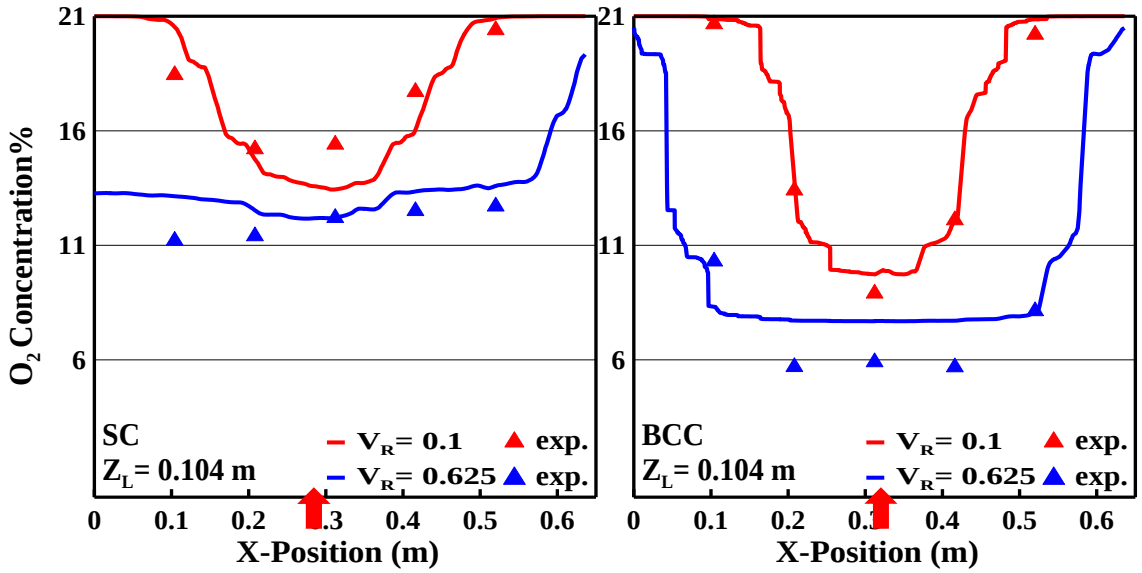

Figure 5.21: Comparison between the RPM gap method of the two structured beds with the experimental data, where $\dot{V}_R$ = 0.625 and 0.1

5.4 Comparison between cross and parallel injection

A comparison between the results of the O_2 concentrations for cross flow and axial flow through the BCC bed with two injection types is presented in Figure 5.22. In the cross flow, the lance was attached 101 mm away from the bottom, and the injection position was at x_L= 0.260 m; in parallel flow, the injection position was z_L = 0.104 m. The lance was inserted into the bed 0.318 m away from the wall box. The contour plots for the two types of injection are shown in Figure 5.23. The jet for the parallel flow was slightly wider than the jet for the cross flow. Additionally, the jet for the cross flow penetrates below the injection point.

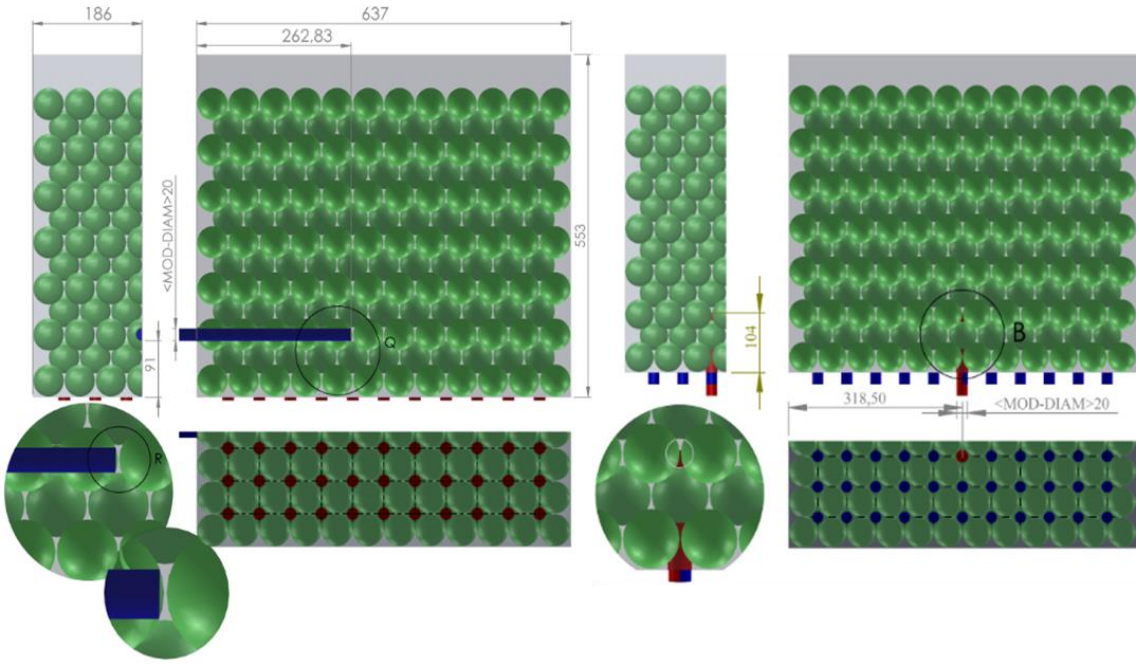

Figure 5.22: CFD domain of the BCC bed using the gap method for the two injection types

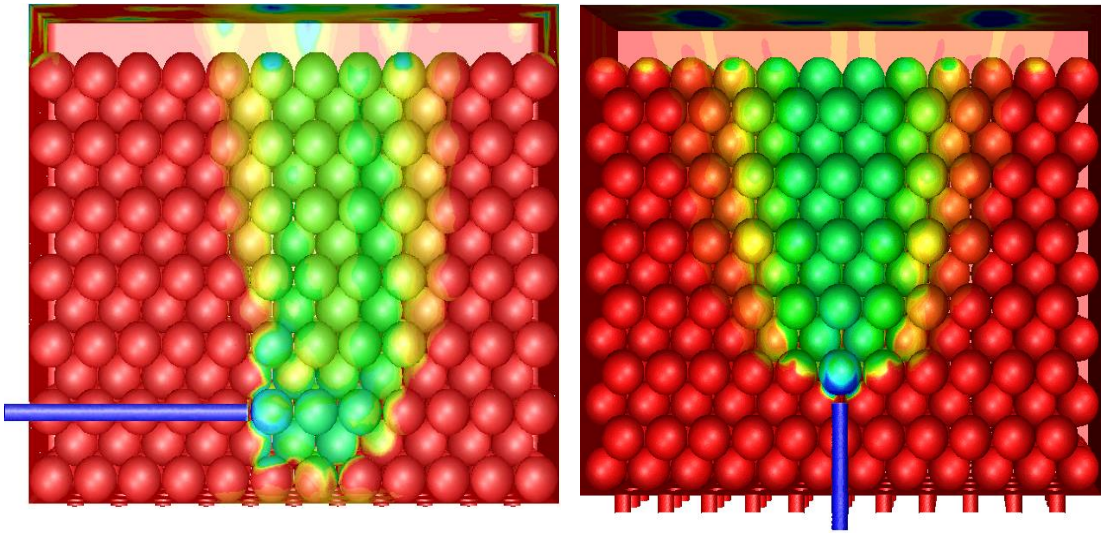

Figure 5.23: Contour plots of the O_2 concentration with the two injection types

Figure 5.24 shows the curves of the O_2 concentration for cross and axial flows. The volumetric flow rate ratio is 0.1. In the cross flow, the minimum O_2 concentration is approximately 11%, and the width of the jet from the upper point is 0.3 m.The minimum of the curve is not exactly facing the injection point. In the axial flow, the minimum O_2 concentration is approximately 10%, but the width of the curve is also 0.3 m. In this type of flow, the minimum O_2 concentration was facing the injection point. The CFD results were validated with experiment data. A slight deviation is seen at the fourth measuring point for the cross flow, whereas a better fit was found for the axial flow.

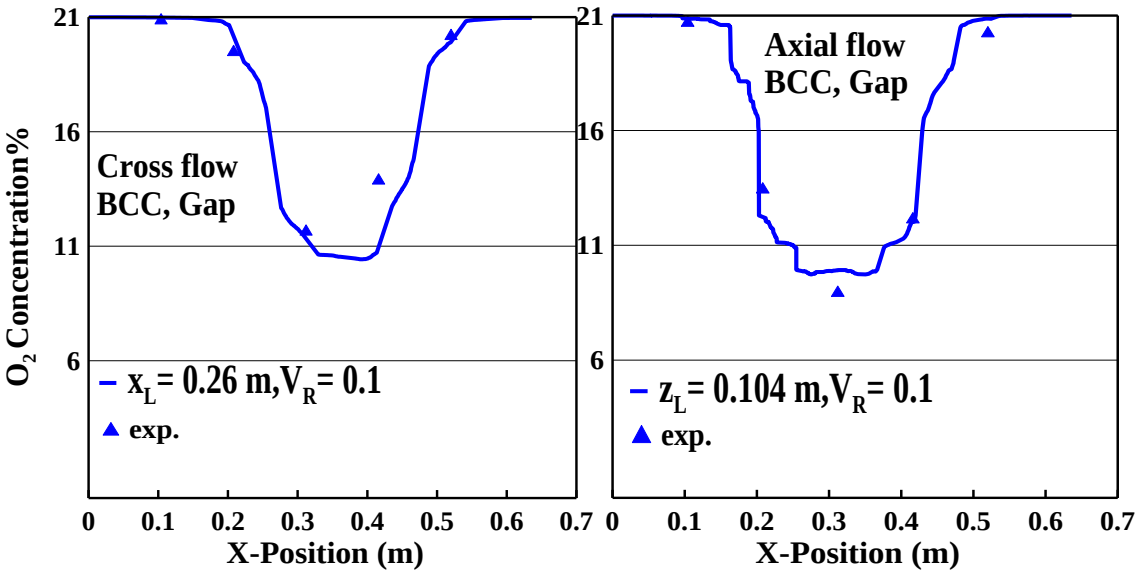

Figure 5.24: CFD results validated with experimental data for the cross and axial flow

Figure 5.25 shows the velocity distribution at three lines (measurement positions); see Figure 3.1. From the figure, it can be concluded that the results obtained from the CFD simulations for the mixing velocity distribution are the same as those at cross lines at the outlet of the box. The CFD results present similar trends for both types of injection. The figures show that the average mixing velocity at the cross flow was 1.5 $m.s^{-1}$ and approximately 1.6 $m.s^{-1}$ for the axial flow. The effect of air channeling is very clear at the two ends of the box.

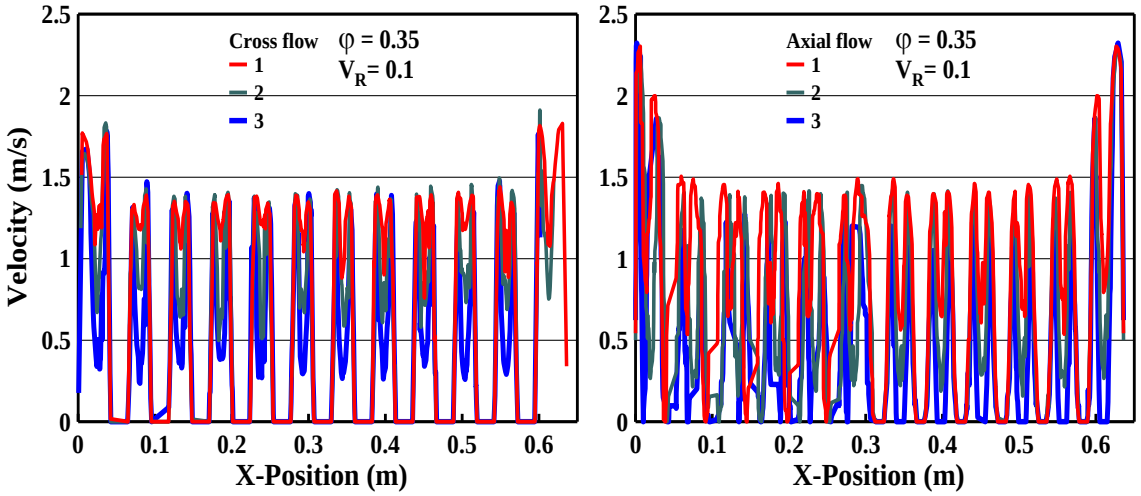

Figure 5.25: CFD results of the velocity distribution at three lines for axial and cross flows in the BCC bed

6. CFD Results of PMM

6.1 Porous media model

Modeling the shaft kiln using the RPM poses many challenges. This chapter reports on the results for when a packed bed is modeled by the PMM to visualize the flow mixing in the bed. The PMM is widely used for many problems, including flows through packed beds, filter papers, perforated plates, and tube banks [47-48]. Wu et al. [30] reported that the porous media approach for a closely packed geometry can help a CFD simulation to quickly and reasonably capture the averaged behavior of thermal-hydraulic parameters. The computation time under the PMM is very low compared to when using the RPM. In the PMM, the geometry can be easily created by substituting the resistance of the spheres by a resistance source in the momentum equation to obtain the same particle effect.

The superficial velocity porous formulation generally gives good representations of the bulk pressure loss through a porous region. However, because values of the superficial velocity within a porous region remain the same as those outside the porous region, it cannot predict the increase in velocity in porous zones, thus limiting the accuracy of the model

There are some restrictions placed upon the geometry of the porous media [49]:

(1) The void space of the porous media is interconnected.
(2) The dimensions of the void space must be large compared to the mean free path length of the fluid molecules.
(3) The dimensions of the void space must be sufficiently small so that the fluid flow can be controlled by adhesive forces at fluid-solid interfaces and by cohesive forces at fluid-fluid interfaces (multiphase systems).

The first assumption is obvious because no flow can occur in a disconnected void space. The second property will enable us to replace the fluid molecules in the void space by a hypothetical continuum. The third property excludes many cases from the definition of a porous medium. For example, beach sand, sandstone, wood, and the human lung are defined as natural porous media. Liapor spheres with a diameter of 0.5 cm and crushed limestone 1 cm in size can be regarded as granular porous materials [50]. However, the dimensions of the void space in the packed bed with 10 cm in diameter lime stones might be oversized.

6.1.1 Viscous and inertial resistance

Porous media are modeled by the addition of a momentum source term to the standard fluid flow equations. The source term is composed of two parts: a viscous loss term (Darcy, the first term on the right-hand side of Eq. 6.1) and an inertial loss term (the second term on the right-hand side of Eq. 6.1) [46].

$$S_i = -\left[\sum_{j=1}^{3} D_{ij}\mu v_j + \sum_{j=1}^{3} C_{ij}\frac{1}{2}\rho|v|v_j\right] \quad (6.1)$$

where S_i is the source term for the ith (x, y, or z) momentum equation, $|v|$ is the magnitude of the velocity, and D and C are prescribed matrices. This momentum sink contributes to the pressure gradient in the porous cell, therein creating a pressure drop that is proportional to the

fluid velocity (or velocity squared) in the cell. In the case of simple homogeneous porous media (isotropic media), this can be written as

$$S_i = -\left(\frac{\mu}{\alpha} v_i + C_2 \frac{1}{2} \rho |v| v_i\right) \qquad (6.2)$$

It can also be written in terms of the pressure drop per unit length as

$$\frac{\Delta P}{L} = -\left(\frac{\mu}{\alpha} v_i + C_2 \frac{1}{2} \rho |v| v_i\right) \qquad (6.3)$$

where α is the permeability and C_2 is the inertial resistance factor. To model a porous region without considering heat transfer, the main additional inputs for the problem setup are defining the porous zone, specifying the porosity of the porous medium, and setting the viscous resistance coefficient 1/α and the inertial resistance coefficient C_2. Because the porosity is known, finding the resistance coefficients is hence the first task.

6.1.2 Ergun equation for a packed bed

Considering the modeling of a packed bed, the appropriate constants can be derived using the Ergun equation. The Ergun equation is a semi-empirical correlation applicable for many types of packing:

$$\frac{\Delta P}{\mathrm{L}} = 150. \frac{(1-\varphi)^2}{\varphi^3} . \frac{\mu . U}{\overline{d_p}^2} + 1.75. \frac{1-\varphi}{\varphi^3} . \frac{\rho . U^2}{\overline{d_p}} \qquad (6.4)$$

where *dp* is the mean diameter.

Comparing Eq. 6.2 with Eq. 6.4, the permeability and inertial loss coefficient in each component direction can be derived as

$$\alpha = \frac{{d_p}^2 \varphi^3}{150(1-\varphi)^2} \qquad (6.5)$$

and

$$C_2 = \frac{(1-\varphi)}{d_p \varphi^3} \qquad (6.6)$$

As can be observed in Eqs. 6.5 and 6.6, both coefficients are determined by the geometry parameters.

6.1.3 Superficial velocity

The flow through a porous medium obeys the same relations as for basic fluid mechanics. The volume of fluid flowing per unit time or fluid flux transported through the bed is described by the volumetric flow rate, Q ($m^3.s^{-1}$). This is related to the superficial velocity (U), which is given below:

$$U = \frac{Q}{A} \qquad (6.7)$$

where A (m^2) is the cross sectional area of the tube. The superficial velocity is the velocity of the fluid as if there were no media in the bed. For instance, a flow-measuring device placed immediately before the media would measure the superficial velocity.
Another term used to describe the velocity is the interstitial velocity (U_i), which is the average velocity within the pores. This considers the bed porosity through the relation given below.

$$U_i = \frac{U}{\varphi} \qquad (6.7)$$

where φ is the porosity.

6.1.4 Model definition and Boundary conditions

The standard k-ϵ model with standard wall function is applied to model the turbulence and, species transport model is used to calculate flow mixing. The element size used in the computation using the PMM is similar to that in the case of the RPM. The first-order upwind schemes are selected to compute the field variables. The relaxation factors are set to the FLUENT default values. The resistance coefficients are computed using different porosities, as shown in Table 6.1.

Table 6.1: Values of the viscous and inertial resistance coefficients

Porosity		Viscous resistance (m^{-2})	Inertial resistance (m^{-1})
BCC	0.35	546647	1020
SC	0.48	135633	316
	0.60	41091	124
	0.70	14555	58
	0.80	4333	26

In addition, the volumetric flow rate ratio of air and N_2 is the same as that used for the calculations based on the RPM. Both inlets are set as velocity inlets, and the mixture outlet is defined as the pressure outlet. Table 6.2 shows the boundary settings.

Table 6.2: Inlet and outlet boundary conditions

		D_h (m)	I (%)	Velocity ($m.s^{-1}$)	Temperature (K)
	air	66*0.02	5	0.536, 1.1, 2, 3.35	300
	N_2	0.02	5	depend on Lance diameter used	300
Outlet		0.288	5	-	300

6.2 Geometry and computational mesh

The model strategy is applied again to reduce the computational effort. The model is assumed to be symmetrical to reduce the computational effort. The considered computational domain includes an inlet for the main flow (air) at the bottom and an inlet for the injection flow (N_2) at the side. The mixture leaves the domain at the mixture outlet.

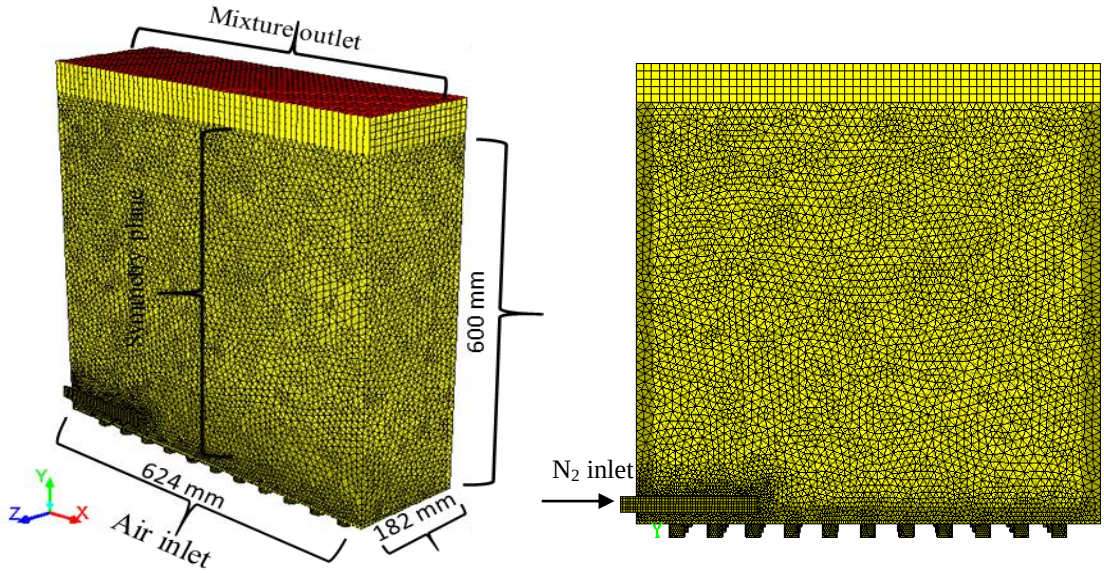

Figure 6.1: Geometry and computational mesh for the simulation

As depicted in Figure 6.1, the height of the geometry is 600 mm, which is the same as the dimensions of the geometry used for the RPM simulations. The lance has a diameter of 20 mm and is located 26 mm above the air inlet, with a lance depth of 156 mm. The mesh independence of the simulation is obtained by varying the number of mesh elements. Table 6.3 details the three meshes and the computation time.

Table 6.3: Mesh element and computation time for PMM

Size of elements	No. of elements	No. Of iterations	Time (min)
1 mm	881205	141	30 min
2 mm	538724	136	13 min
3 mm	239864	135	7 min

Figure 6.2 shows the mesh density for the computational domains and the contour lines of the O_2 concentration. The figure shows that there is no effect of the mesh element size on the obtained results. The grids were created with tetrahedral cells in the porous zone, and the remainder of the upper part of the computational domain was meshed with hexahedral cells.

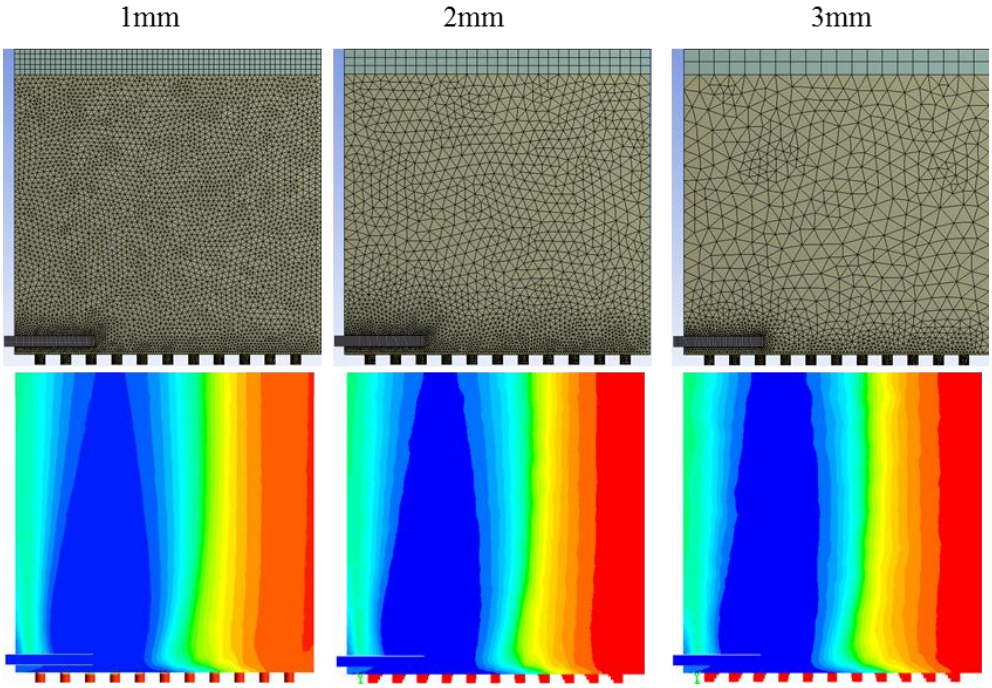

Figure 6.2: The mesh study using the PMM and the corresponding O_2 concentration contour plots for each grid

6.3 Simulation results of the PMM (axial flow with cross injection)

Simulations are performed to investigate how parameters affect the radial mixing in a packed bed using the PMM. The studies mainly focus on certain important factors such as the bed height, lance position, lance diameter, porosity value, particle size, and bed setting.

6.3.1 Influence of the turbulence model and the order of the upwind schemes

In Figure 6.3, the upper part shows the contour plots for the comparison of two turbulence models: the k-e model and the SST (k-w) model. Three lance positions were used, i.e., 0, 0.156, and 0.312 m, and the volumetric flow rate ratio was 0.625. The contour plots of the O_2 concentration are displayed for the plane Z = 0.468 m. It is clear that, with different injection positions, there is no large effect of the turbulence model on the O_2 concentration through the bed.

The bottom part of Figure 6.3 shows the contour plots for how the accuracy of the order of the upwind schemes affects the O_2 concentration. Three lance positions were used (0, 0.156, and 0.312 m), and the volumetric flow rate ratio was 0.625. The contour plots of the O_2 concentration are displayed for the planes Z = 0.468 m and Y = 0.182 m. The first-order upwind schemes are selected to compute the field variables as they were used in the RPM. To examine the influence of a higher order spatial accuracy, simulations are conducted under the same operating conditions but only with the second-order upwind schemes. The comparison shows that the second-order upwind schemes provide more accurate results.

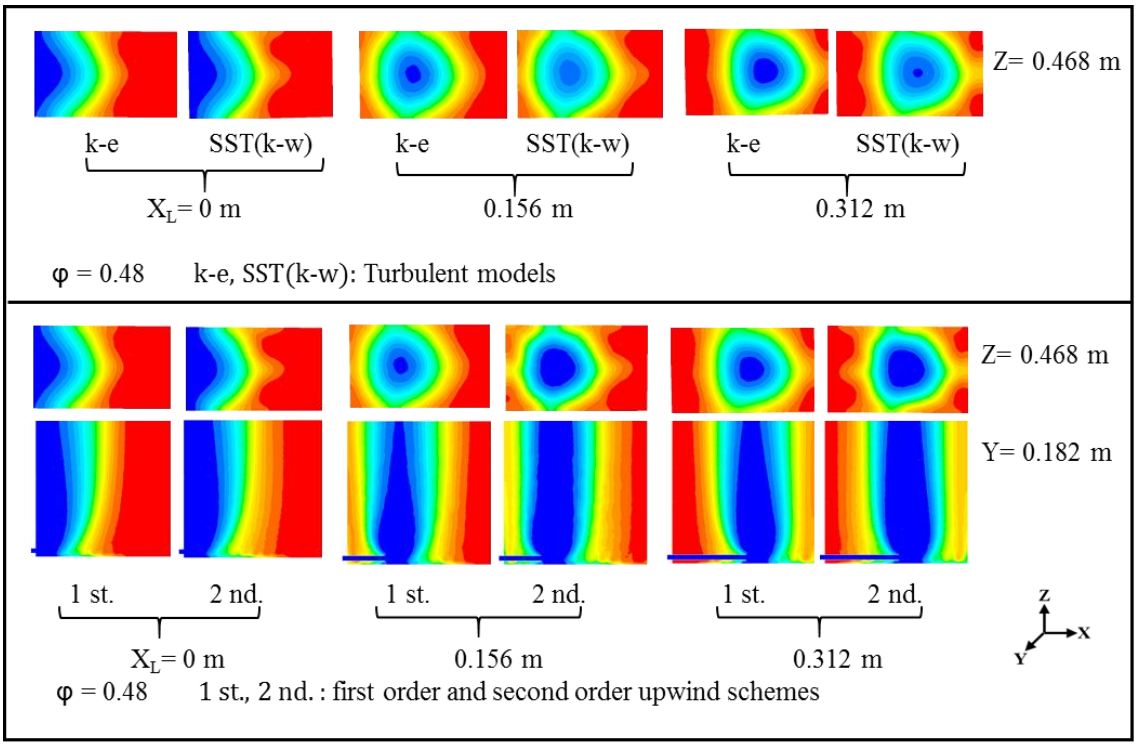

Figure 6.3: Contour plots of turbulent models and the influence of the first-order and second-order of the upwind schemes on the O_2 concentration, with d_L= 0.02 m and x_L = 0, 0.156 and 0.312 m.

6.3.2 Influence of measurement height

Figure 6.4 explains the influence of the measurement height on the O_2 concentration for the two beds (the structured bed with a porosity of 0.48 and the unstructured bed with a porosity of 0.4). As mentioned previously in Chapter 3, two levels are used for the SC arrangement. This choice of levels is limited due to the size of the spheres, d_P = 52 mm, and the type of arrangement. The levels are Z1 = 0.260 m and Z_2 = 0.468 m. Conversely, for the unstructured bed of small glass beads, there are no limitations for choosing measurement levels. The lance device could be inserted anywhere in the bed. Therefore, the new measurement levels are Z_1 = 0.223 m and Z_2 = 0.473 m, and the injection position is x_L= 0.156 m. The results of the simulations using the PMM revealed that the O_2 concentration was independent of the measurement level in the two beds. The curves of the O_2 concentration for the unstructured bed lie lower than those for the structured bed and are shifted slightly to the left side. Both curves obtain the maximum value of the O_2 concentration in the downstream direction up to the end of the test box. The reasons for these differences are due to the size of the particles used for the beds.

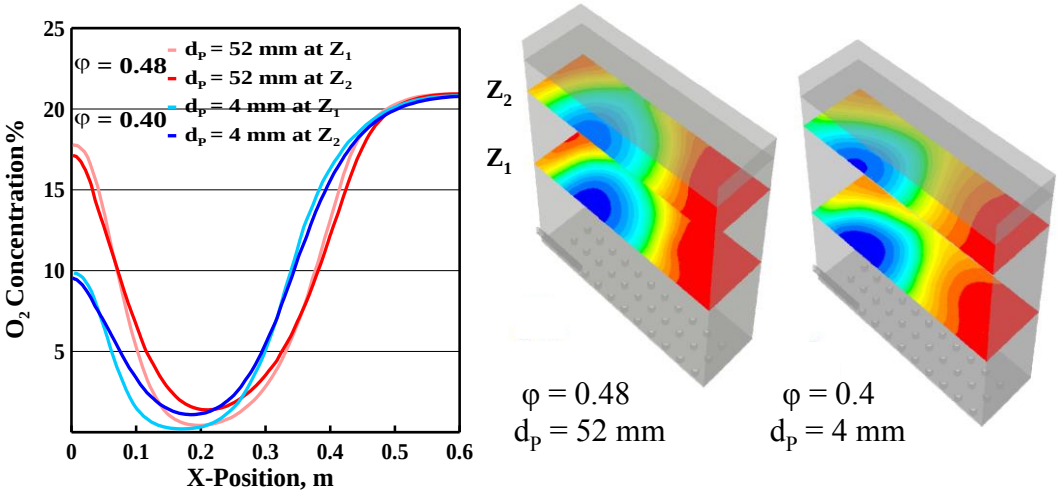

Figure 6.4: Effects of the measurement level on the O_2 concentration, with x_L= 0.156 m, d_L=0.02 m, and $\dot{V}_R$ = 0.625 for the PMM in the structured and unstructured beds.

6.3.3 Influence of porosity value

The simulation results obtained based on the PMM are validated against experimental data. Figures 6.5 and 6.6 show the comparison of the predicted results from the PMM at different porosities for the two arrangements, SC and BCC, of the structured bed and the data obtained based on the experimental work at porosities of 0.48 and 0.35, respectively. The simulations were conducted using two different values of the volumetric flow rate ratio $\dot{V}_R$ = 0.625 and 0.06. The lance diameter is d_P = 20 mm, and the lance position is x_L = 0.156 m. Figure 6.5 shows the results for a bed of porosity 0.48, which were used to find a porosity value that results in a simulation that better agrees with the experimental data. Simulations were performed for a porosities value of: 0.48, 0.6, 0.7, and 0.8. When the porosity of the geometry increases, the viscous and inertial resistance significantly decrease. The results

revealed that the O_2 concentration was under-predicted for a porosity of 0.48. It can also be seen that the O_2 concentration changes slightly as the porosity increases from 0.48 to 0.8. A good agreement with the results predicted by real particle model when the porosity is increased to 0.8. The shifting of the curve for the PMM could be due to the assumption of a homogeneous velocity of the axial flow through the 66 holes of the perforated plate. However, in reality, the homogeneity of the flow cannot be ensured. It is impossible to insert a hot wire inside the test box (through the spheres) to measure the velocity of the flow through the 66 inlet holes. Moreover, the real geometry of the manufactured spheres differs from the exact spheres created in the CFD domains; the manufactured spheres include a mold imprint on the surface of the spheres that could affect the flow. The contour plots of the studied cases of the variable porosities in the figure demonstrate how the injection flow varies with the change in porosity and the change in the volumetric flow rate ratios. The widths of the curves for the low ratio are smaller than those for the high ratio due to the increase in the axial flow.

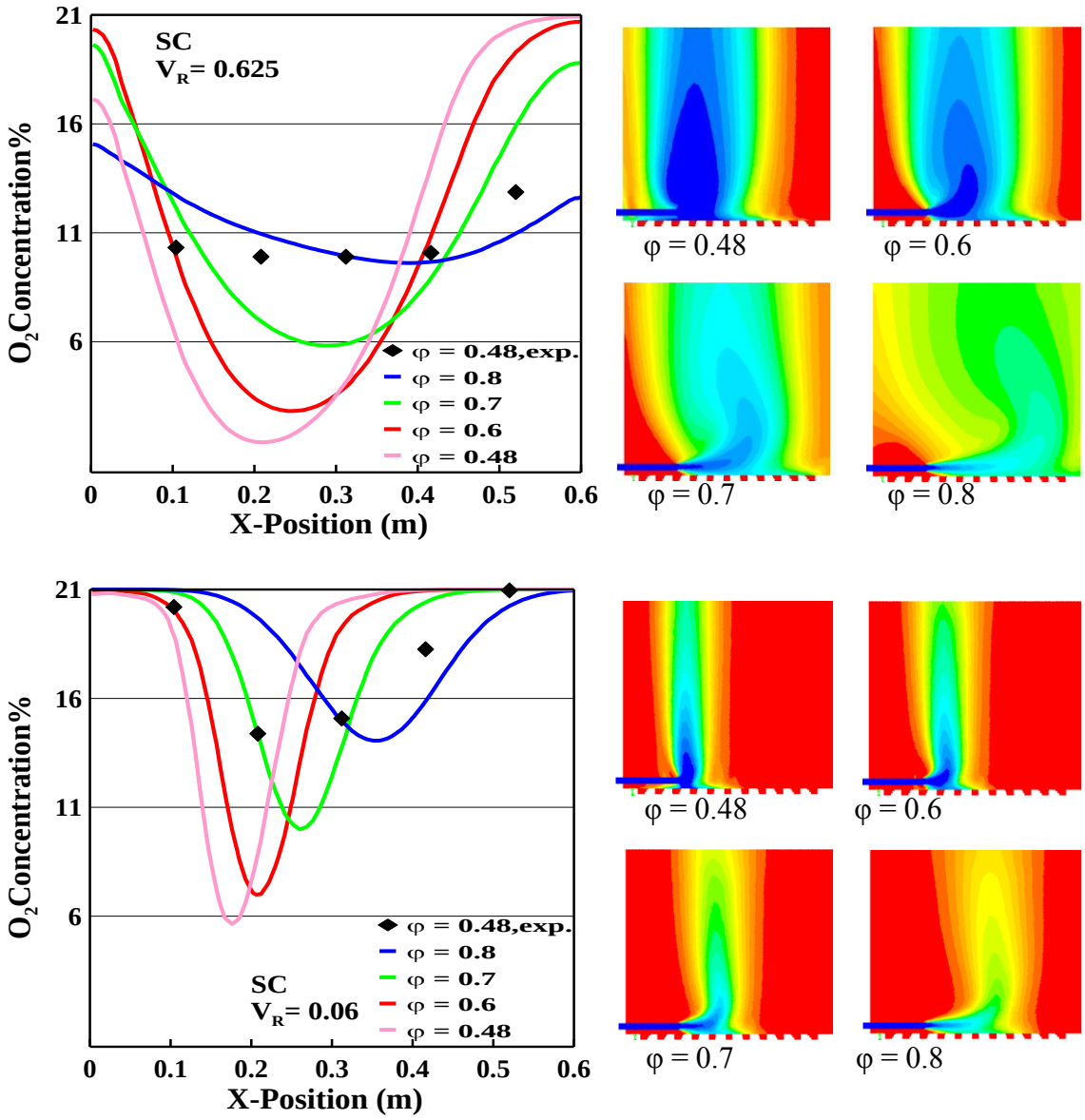

Figure 6.5: Comparison of the O_2 concentration for the SC packed bed with different porosities and experimental data at two $\dot{V}_R$ values, with x_L= 0.156 m and d_L=0.02 m

Figure 6.6 shows the comparison of the results of the simulation and the experimental data. The results of the simulation with a porosity of 0.7 show better agreement with the experimental results for the real bed with a porosity of 0.35. The BCC O_2 concentration curves have the same behavior as the SC curves. In addition, the contour plots in the figure clearly show the effect of the volumetric flow rate ratio on the mixing between flows from both inlets, i.e., the air inlet and the N_2 inlet.

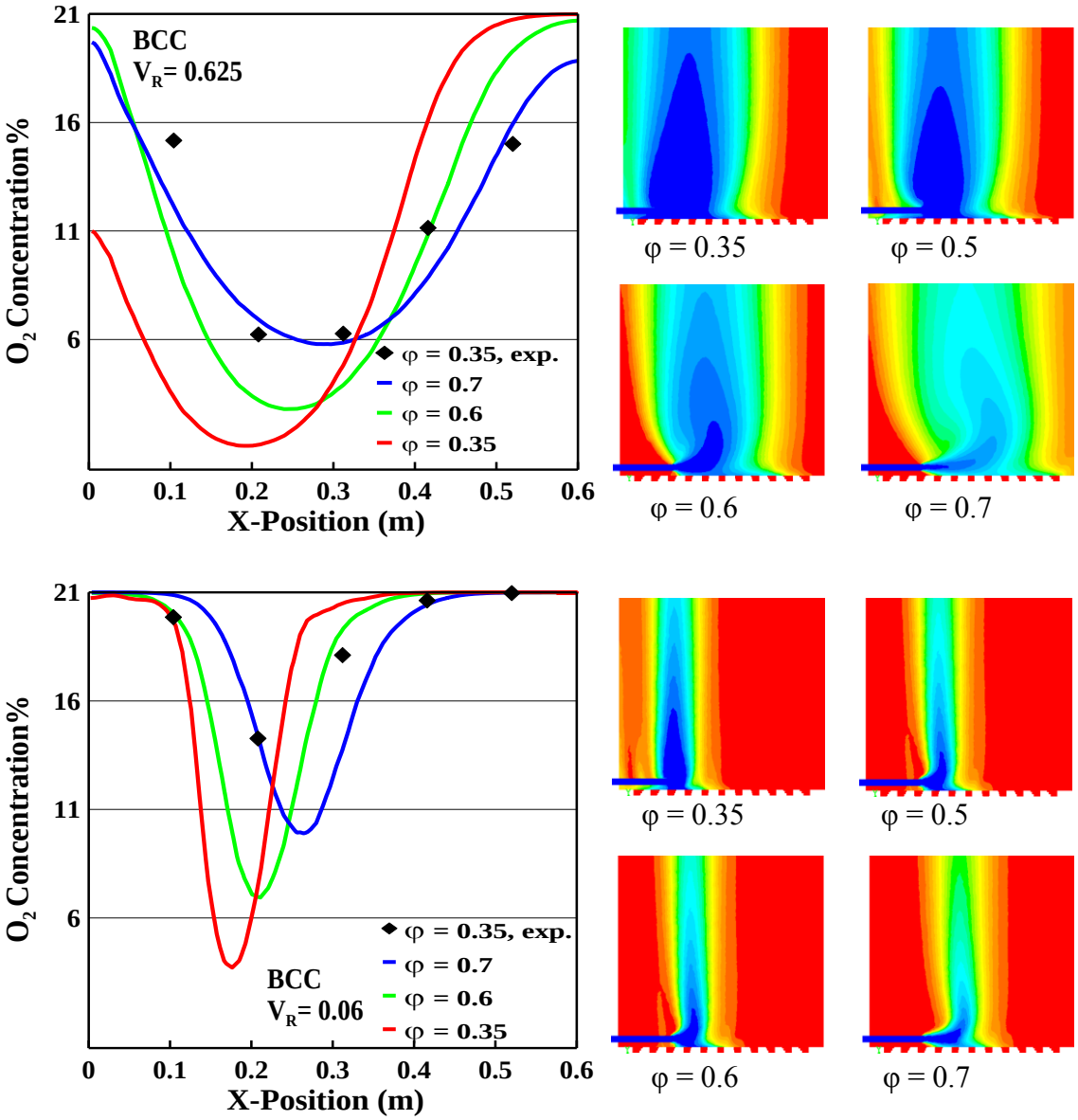

Figure 6.6: Comparison of the O_2 concentration for the BCC packed bed with different porosities and the experimental data at two $\dot{V}_R$ values, with x_L= 0.156 m and d_L=0.02 m

For the unstructured bed (glass beads), the comparison of the results obtained using the PMM with different porosities and the experimental results is explained in Figure 6.7. Two volumetric flow rate ratios are used for the comparison. The lance position and lance diameter are 0.156 m and 0.02 m, respectively. From the figure, it can be seen that, for $\dot{V}_R$ = 0.625, the curves of the O_2 concentration with different porosities are approximately identical, as is clear from the contour planes for the four porosities. A significant agreement between the simulation results and experiments is obtained at high $\dot{V}_R$. In the case of a low volumetric flow rate ratio, the effect of the change in porosity under the PMM is clear, and the agreement between the simulation results and experiments is not similar to that in the case of the high flow rate ratio. This fitting could be improved with increasing porosity. The simulation curves of the unstructured bed lie above the experimental curve, in contrast to the structured bed.

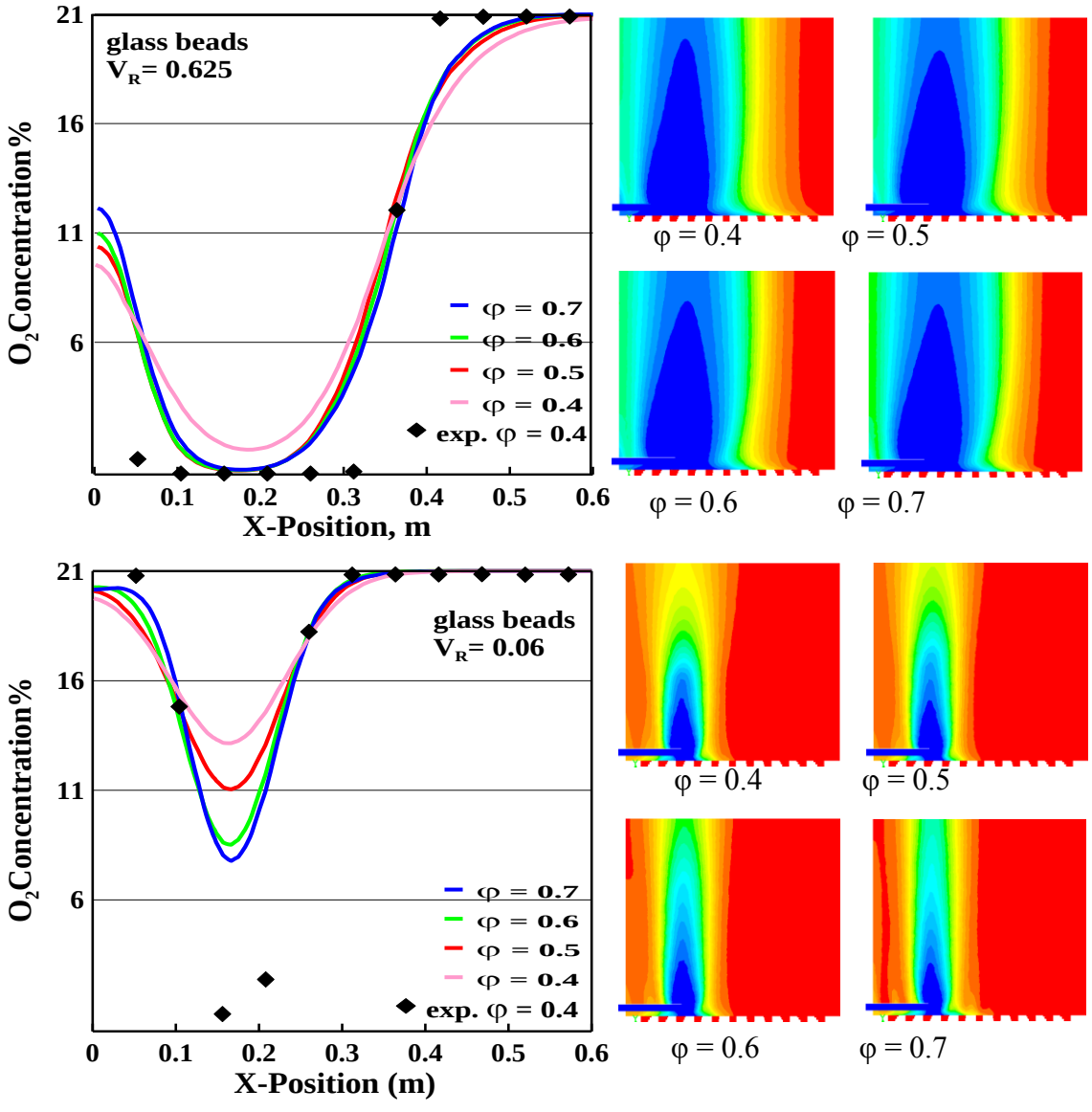

Figure 6.7: Comparison of the O_2 concentration for the unstructured bed with different porosities and experimental data at two $\dot{V}_R$ values, with x_L= 0.156 m and d_L=0.02 m

6.3.4 Influence of lance position

Figures 6.8 shows the influence of the lance position (injection position) on the O_2 concentration and the contour plot for high and low $\dot{V}_R$ in the PMM for a bed porosity of 0.48. The figures also include the experimental data at these positions.

The curves of the O_2 concentration for a lance position of 0.156 and 0.312 m are drawn such that the lance position is assumed to be at the origin of the coordinate system, i.e., (x = 0). From the figure, for $\dot{V}_R$ =0.625, it can be seen that all profiles decrease together and form a jet of N_2. Those O_2 concentration curves have a similar behavior as the experimental curves. For low $\dot{V}_R$, the figure shows a smaller width of the jet (the distance between the first two side flat points, on the top of the curve).

For high $\dot{V}_R$, the minimum O_2 concentration is approximately zero. In contrast, for low $\dot{V}_R$, the minimum O2 concentration for the lance position of 0 m is nearly 2%, and that for the other two lance positions is approximately 7%. This is due to the rising of the axial flow. Additionally, it can be seen that the minimum O_2 concentration for the lance position of 0 m is at a lower position than for the other two lance positions because the flow can only move in one direction. This means that the lance position has a strong influence on the O_2 concentration profiles in the bed. Moreover, the curve of the O_2 concentration lies away from the origin for the lance position of 0 mm compared to the case for the other lance positions.

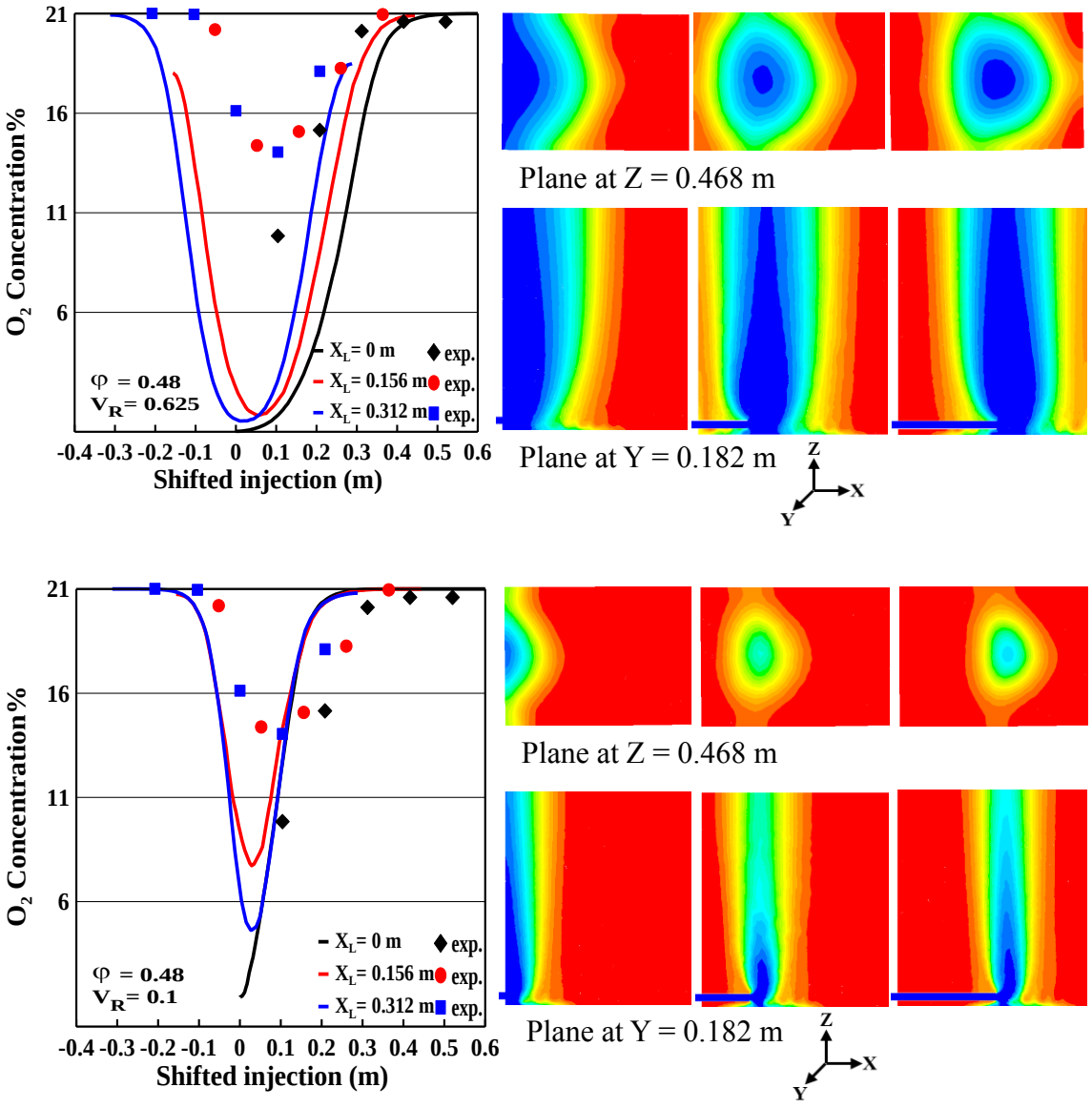

Figure 6.8: Effect of the lance position on the O_2 concentration for the SC structured bed and the experimental data at two $\dot{V}_R$ values, with x_L= 0.156 m and d_L=0.02 m

For the unstructured bed, the results of the simulation for the PMM are shown in Figure 6.9 again for two different $\dot{V}_R$. The O_2 concentration curves are in good agreement with the experimental curves for both low and high volumetric flow rate ratios.

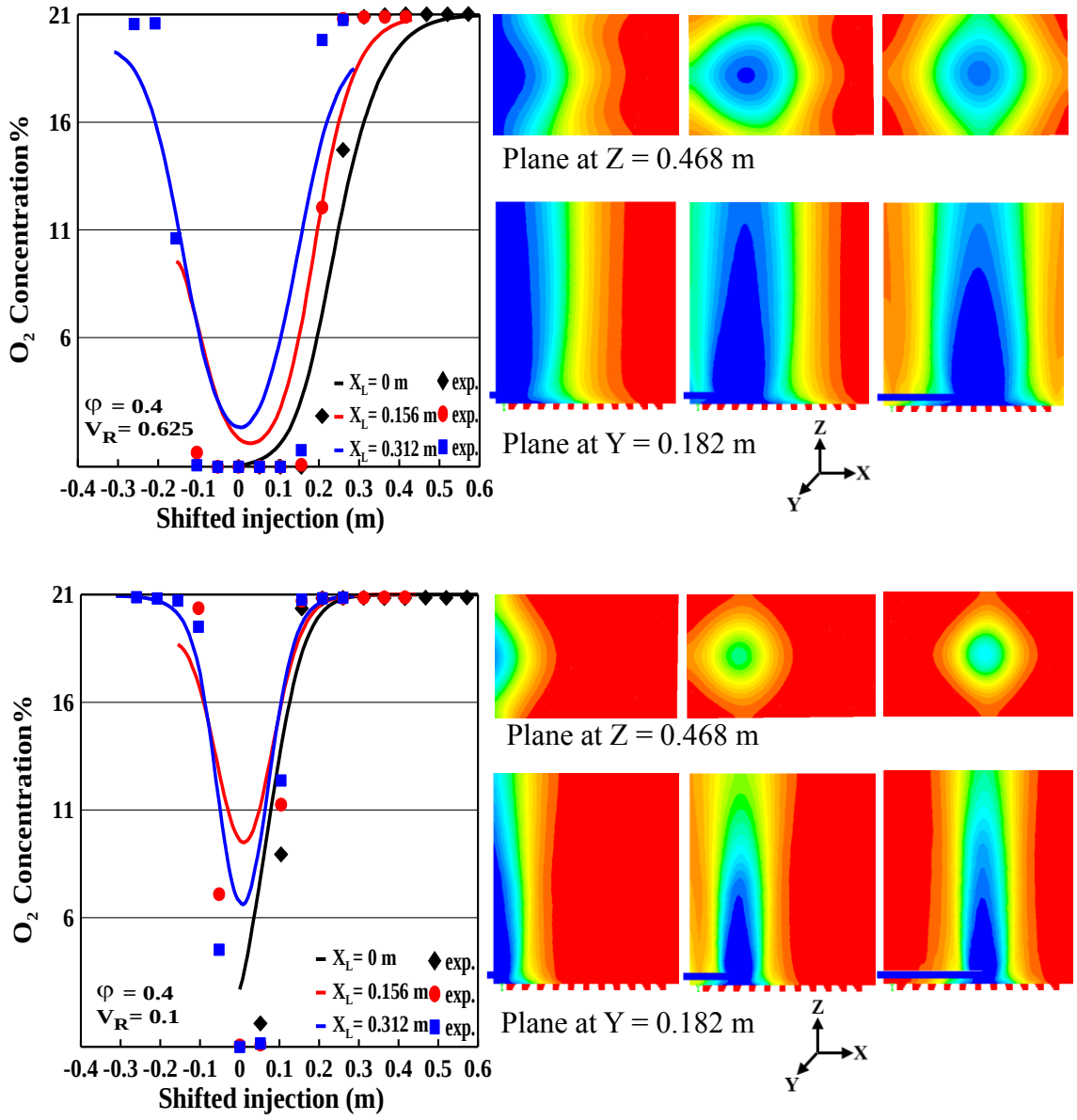

Figure 6.9: Effect of the lance position on the O_2 concentration for the unstructured bed and the experimental data at two $\dot{V}_R$ values, with x_L= 0.156 m and d_L=0.02 m

In both beds (structured and unstructured), the behavior of the O_2 concentration curves is similar. The contour planes for the unstructured bed are shown for the lance positions x_L = 0.156 m and x_L = 0.312 m in Figure 6.9. The presence of unmixed nitrogen can be seen up to the end of the bed (shown in blue) in the case of high $\dot{V}_R$. However, in the case of low $\dot{V}_R$, the blue color cannot be seen after the position becomes almost half the bed height, thereby indicating the absence of unmixed nitrogen. This is due to the increased axial flow rate (air). On the other hand, the contour planes for the structured bed (ceramic spheres) show that the blue color (N_2) is missing after approximately four or five sphere diameters from the bed height.

6.3.5 Influence of lance diameter

Figure 6.10 shows the O_2 concentration curves of the PMM for three different lance diameters with the same injection flow rate, which leads to different injection velocities and hence the contour plots. Two flow rate ratios, i. e., $\dot{V}_R$ = 0.06 and $\dot{V}_R$ = 0.625, are considered. The CFD results of the O_2 concentration are compared with the experimental data for both volumetric flow rate ratios.

For the high volumetric flow rate ratio, the O_2 concentration curves from the simulation for all lance diameters (6, 12 and 20 mm) are shaped as a jet and are approximately identical. The experiment curves for the same $\dot{V}_R$ as shown in the figure are also close to each other; however, they increase continuously to the end of the box. The minimums of the simulation curves are shifted by approximately 0.07 m from the injection point. In the case of a low volumetric flow rate ratio (increased axial flow rate), both curves of the CFD simulation and experiments form a jet shape. They appear to achieve a better agreement than under higher $\dot{V}_R$. In this case, the minimum of the simulation curves still faces the injection point.

It can also be concluded that the O_2 concentration is not strongly affected by the diameter of the lance or by the outlet velocity. The agreement between the results for the PMM and the experimental data little bit improved but to a little extent when decreasing the volumetric flow rate ratio or in other words by increasing the axial flow rate.

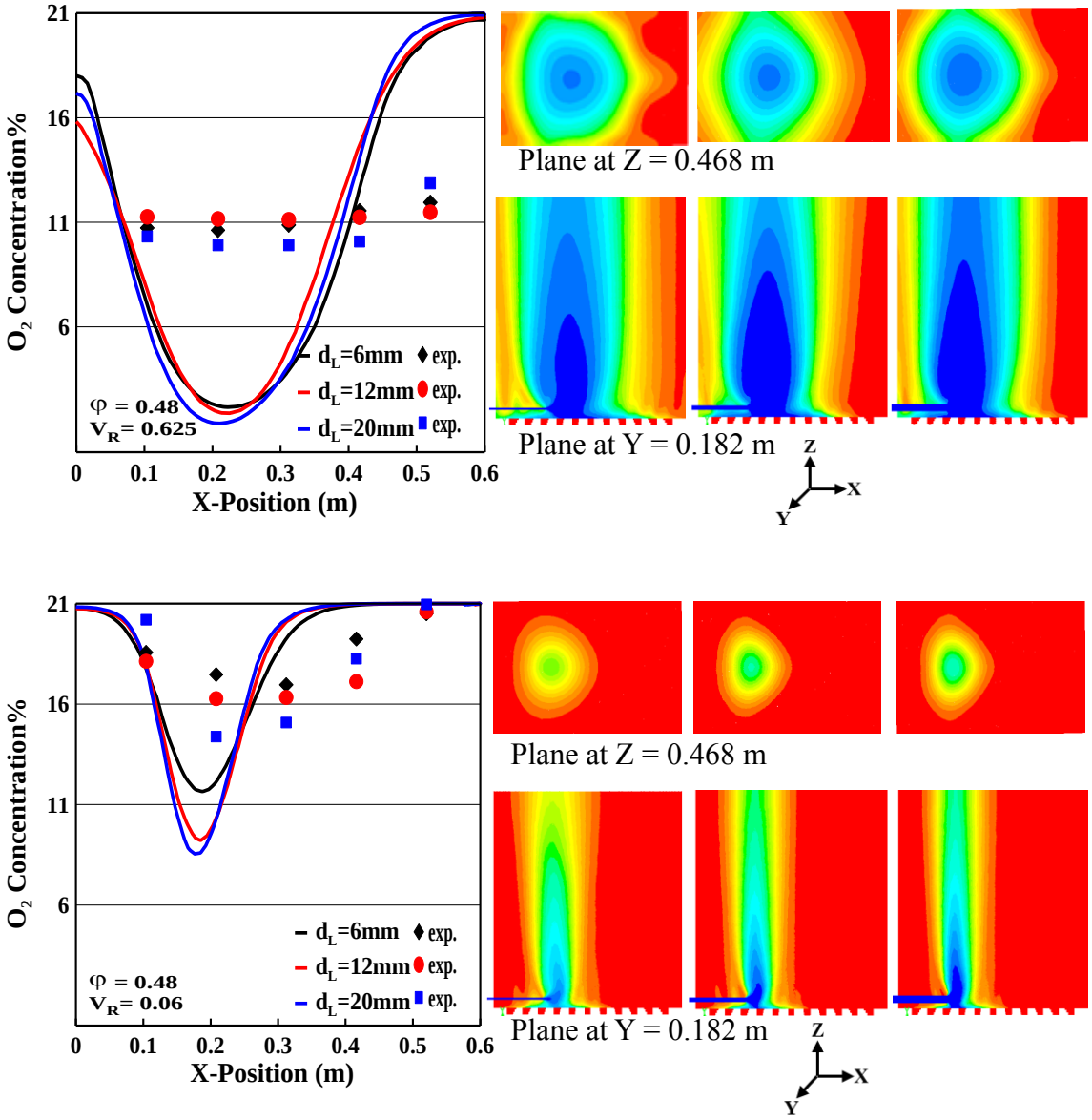

Figure 6.10: Effect of the lance diameter (injection velocity) on the O_2 concentration for the SC packed bed and the experimental data at two $\dot{V}_R$ values, with x_L= 0.156 m and d_L=0.02 m

The influence of the lance diameter (injection velocity) on the O_2 concentration is shown in Figure 6.11 for the unstructured bed. The contour planes of the O_2 concentration for the high and low volumetric flow rate ratios show that there is a small effect of the change in the injection velocity. From the figure, it can be concluded that the minimum O_2 concentration at high $\dot{V}_R$ for the three lance diameters ranges between 0 and 3%, similar for the structured bed. For low $\dot{V}_R$, the minimum O_2 concentration ranges between 13 and 15%, whereas for the structured bed, the minimum O_2 concentration ranges from 8 to 11%.

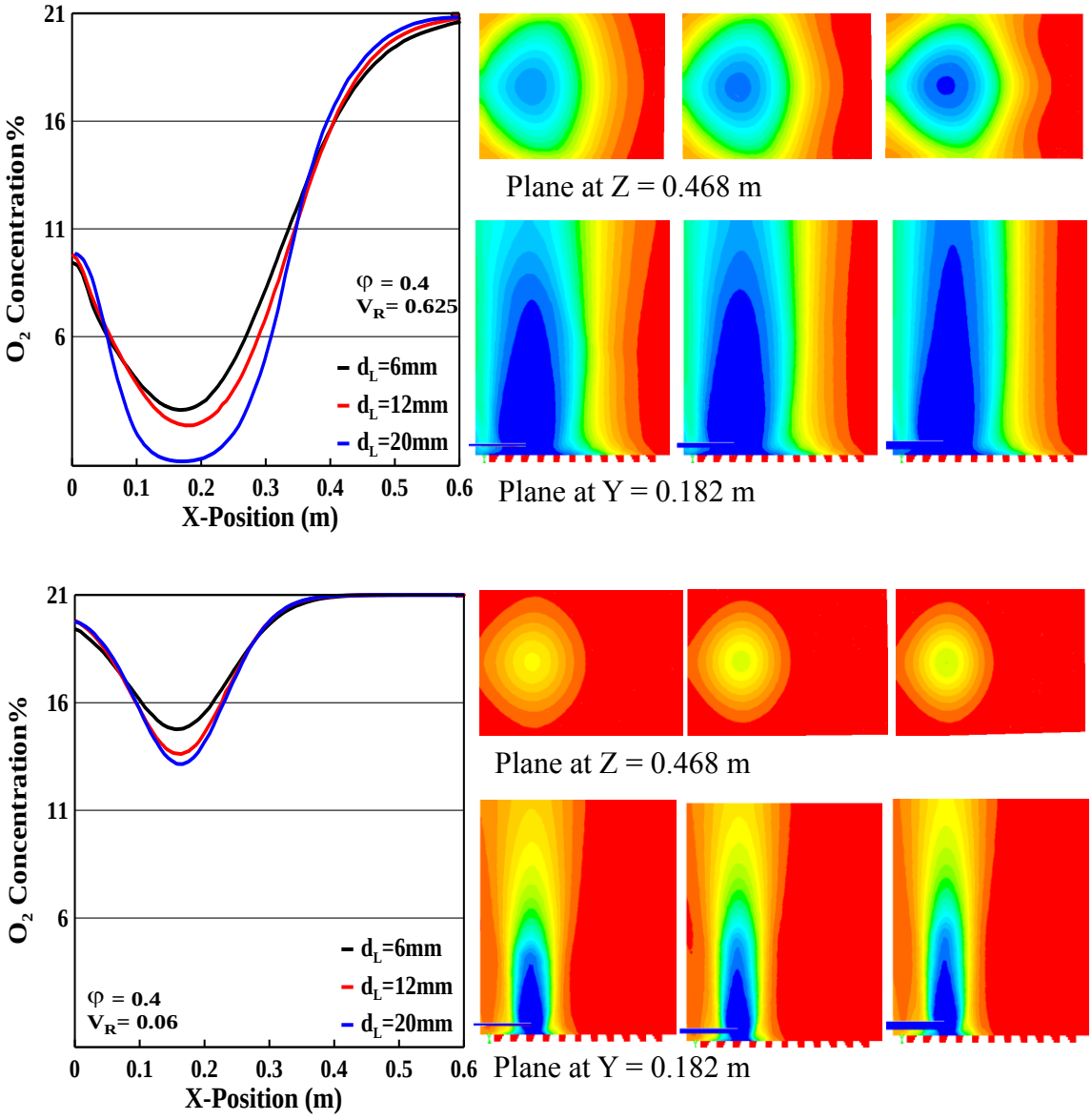

Figure 6.11: Effect of the lance diameter (injection velocity) on the O_2 concentration for the unstructured bed at two $\dot{V}_R$ values, with x_L= 0.156 m and d_L=0.02 m

6.3.6 Influence of particle size with different bed porosities

Figure 6.12 (a, b) shows the combined influence of two parameters, i.e., porosity and particle size, on the O_2 concentration. Three values of the porosity (0.35, 0.5 and 0.7) and three particle sizes (4, 52, and 100 mm) are used. The contour planes are displayed for two cases: (a) high $\dot{V}_R$= 0.625 and (b) low $\dot{V}_R$= 0.06. Figure 6.12 (a), for the high $\dot{V}_R$, shows that, for small particles (d_P = 4 mm), the mixing through the bed seems to be unaffected by the increasing porosity. For larger particles (d_P = 52 mm), mixing can be observed when the porosity is greater than or equal to 0.7. For even larger particles (d_P = 100 mm), the mixing starts when the porosity is equal to 0.5.Figure 6.12 (b) shows the contour planes of the mixing through the bed at low $\dot{V}_R$= 0.06. The mixing behavior for the three particle sizes is similar for the different porosities. A change in the penetration depth of the mixing zone can be seen with increasing porosity and particle size.

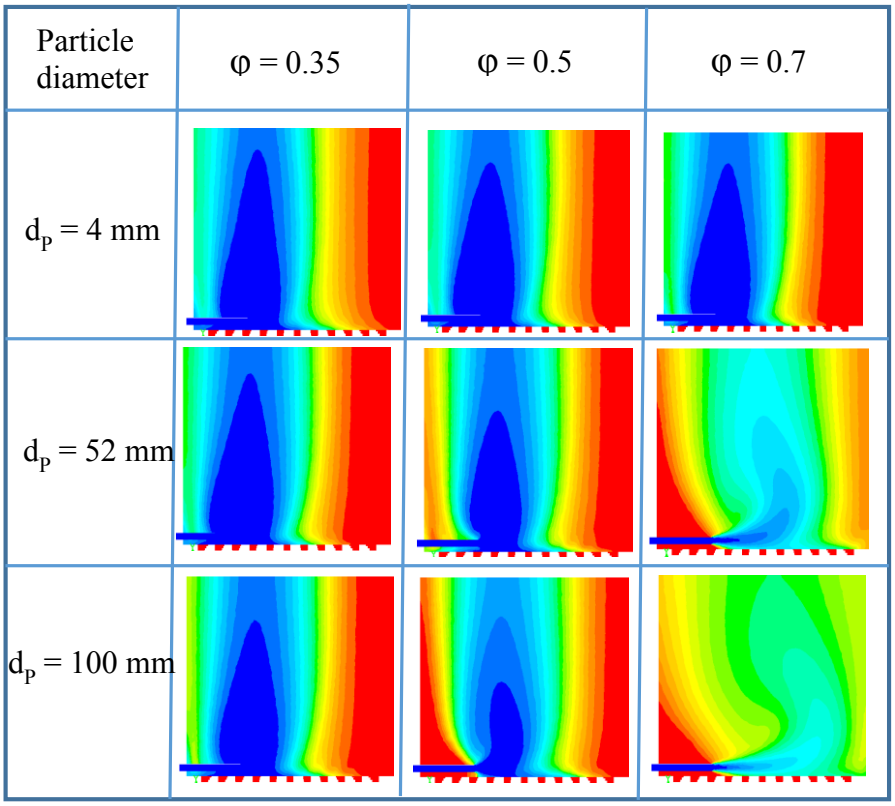

(a)

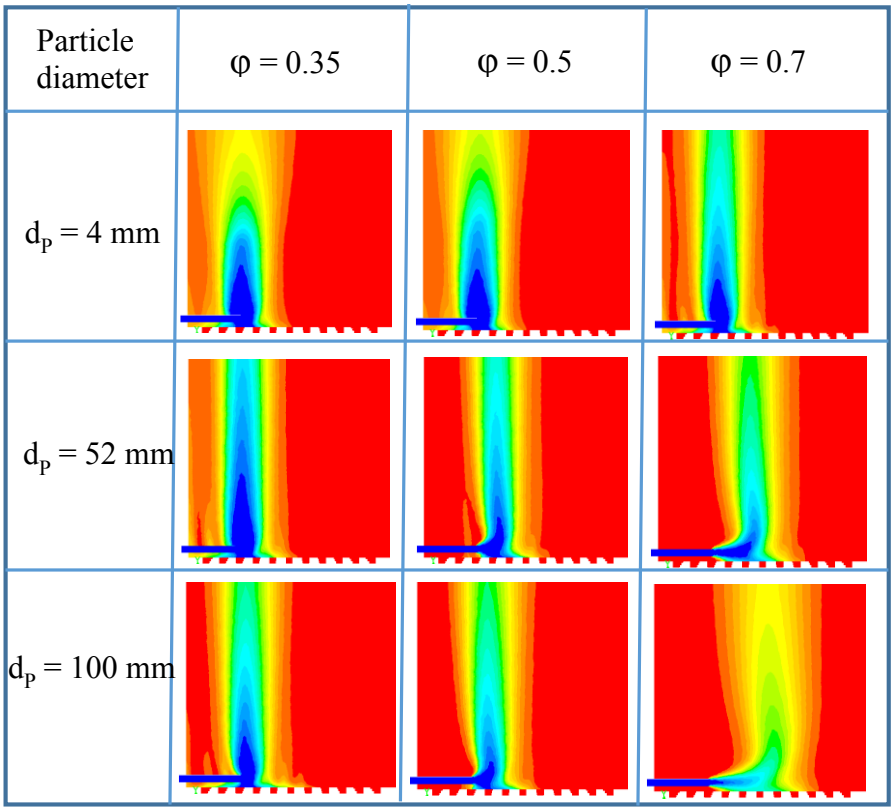

(b)

Figure 6.12: Influence of the bed particle size crossing with different bed porosities, with x_L= 0.156 m and d_L=0.02 m. (a) $\dot{V}_R$= 0.625 (b) $\dot{V}_R$= 0.06

6.3.7 Comparison between results of the PMM and the RPM

Figure 6.13 shows a comparison between the results obtained under the PMM and the RPM with three contact point treatment methods. This comparison is for the structured bed in two arrangements, SC and BCC, with a porosity of 0.48 and 0.35, respectively, where x_L= 0.156 m, d_L=0.02 m, and the volumetric flow rate ratio is 0.625. For the BCC bed arrangement, the results of the PMM with the overlap method show a good agreement with the results of the RPM. For the SC bed, the results of the PMM, irrespective of the porosity, do not match the results obtained under any method for the RPM at the same porosity.

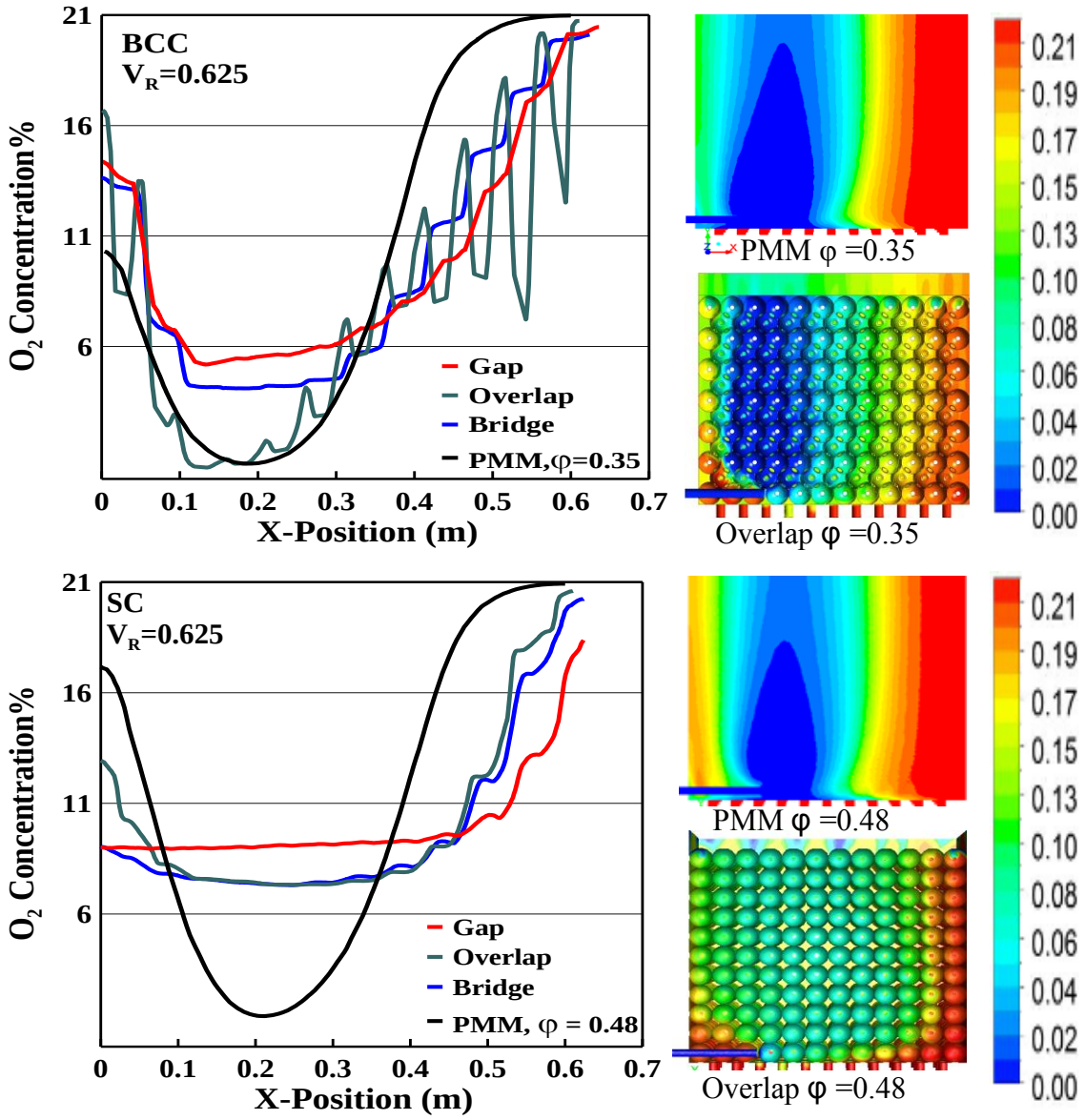

Figure 6.13: Effect of the contact point treatment in the RPM in comparison with the PMM at the same porosity, with x_L= 0.156 m and d_L=0.02 m

6.4 Simulations results of the PMM (axial flow with parallel injection)

6.4.1 Influence of the lance position and the porosity value

Figure 6.14 shows the contour figures for the O_2 concentration for axial flow with parallel injection through the BCC bed using the PMM. The figures show three planes: the first plane is at the air inlet, the second plane is at the outlet, and the third plane is passing through the center of the injection position. Two lance positions were used, z_L= 0 mm and z_L= 104 mm, and four values of porosity (0.35, 0.5, 0.7, and 0.8) and two volumetric flow rate ratios (0.625 and 0.1) were used. For z_L= 0 mm and low $\dot{V}_R$, the nitrogen concentration remains constant around the injection position up to the outlet of the bed with porosities of 0.35 and 0.5. For the other two values of the porosity, i.e., 0.7 and 0.8, the nitrogen concentration changes. The change in the concentration of N_2 shows that mixing occurs. For z_L= 104 mm, the contour planes show that the mixing occurs directly after the injection position regardless of the change in porosity, which means that the lance position strongly affects the mixing through the bed.

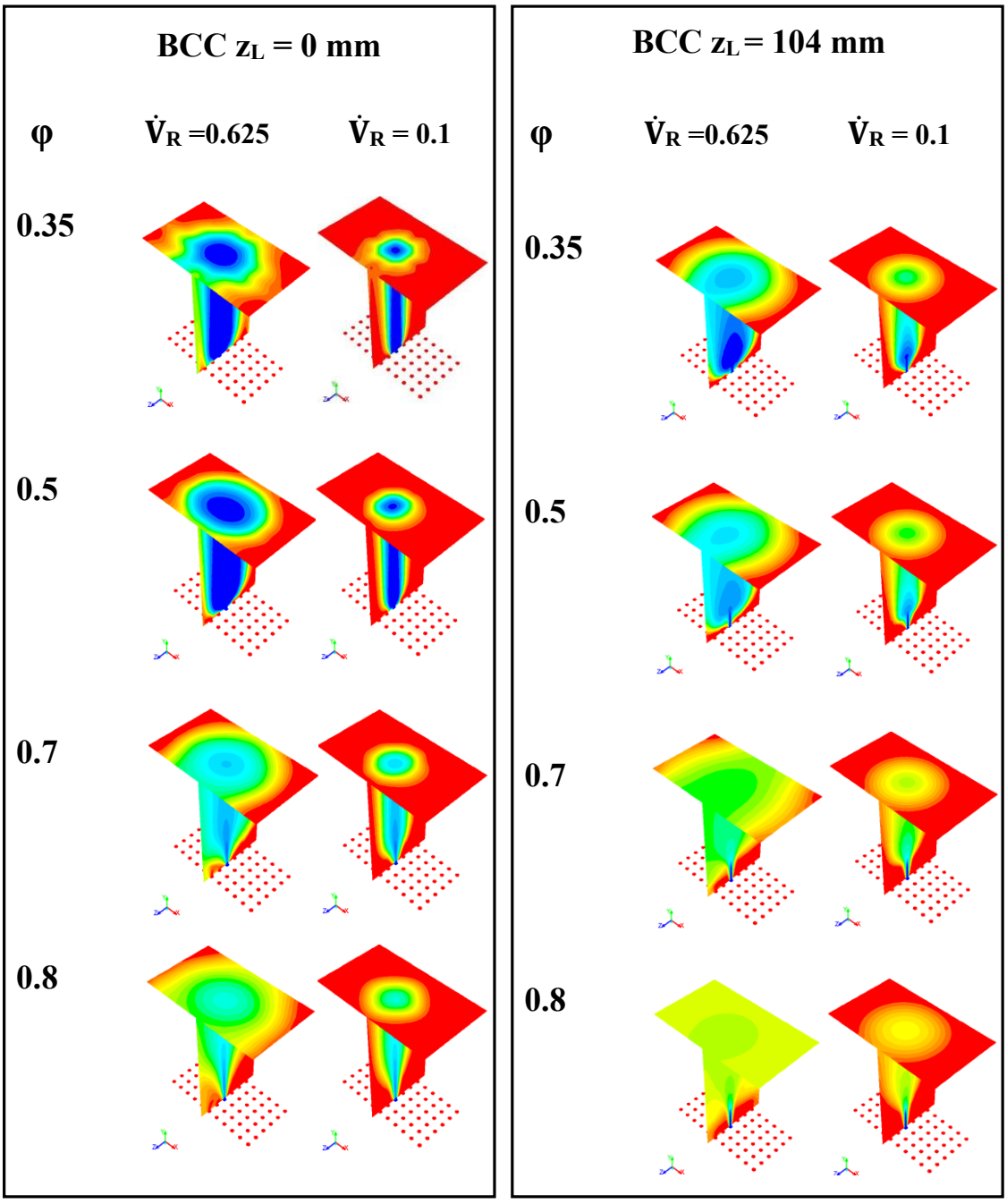

Figure 6.14: Influence of the lance injection position on the O_2 concentration for the BCC bed at two different $\dot{V}_R$ and four values of porosity, with d_L = 0.02 m

In Figure 6.15, the simulation results of the BCC bed with different porosities are compared with the experimental data for the BCC bed with a porosity of 0.35. Two values of $\dot{V}_R$, 0.625 and 0.1, have been used in the comparison. The lance position was z_L = 0.104 m. The figure shows that there is a better agreement between the results of the PMM with a porosity of 0.35 and the experiment in the case of low $\dot{V}_R$ than that for high $\dot{V}_R$.

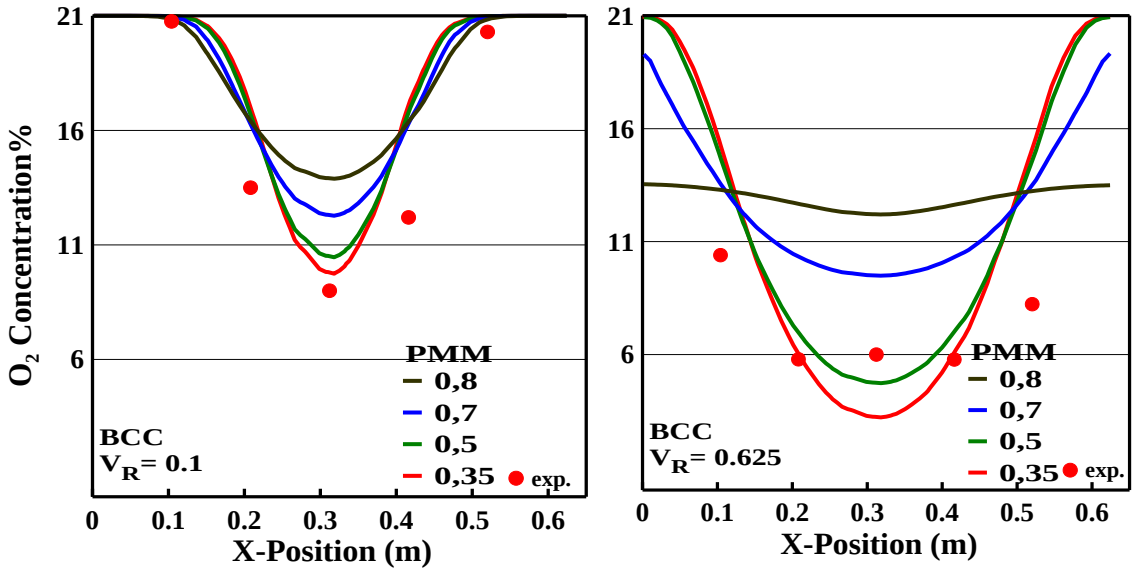

Figure 6.15: Validation of the PMM results with different porosities for the O_2 concentration and experiments in the BCC bed at two different $\dot{V}_R$, with x_L= 0.104 m and d_L = 0.02 m

6.4.2 Influence of lance position with different bed porosities

Figure 6.16 shows the contours of the O_2 concentration obtained using the PMM to demonstrate the influence on the mixing through the bed for beds with different arrangements, i.e., BCC and SC. The injection position is z_L= 104 mm for both the SC and BCC arrangement. In the SC bed with a porosity of 0.48, the air and nitrogen mix directly after the injection point, whereas for the BCC bed with a porosity of 0.35, the air and nitrogen do not mix until a comparatively longer distance from the injection position.

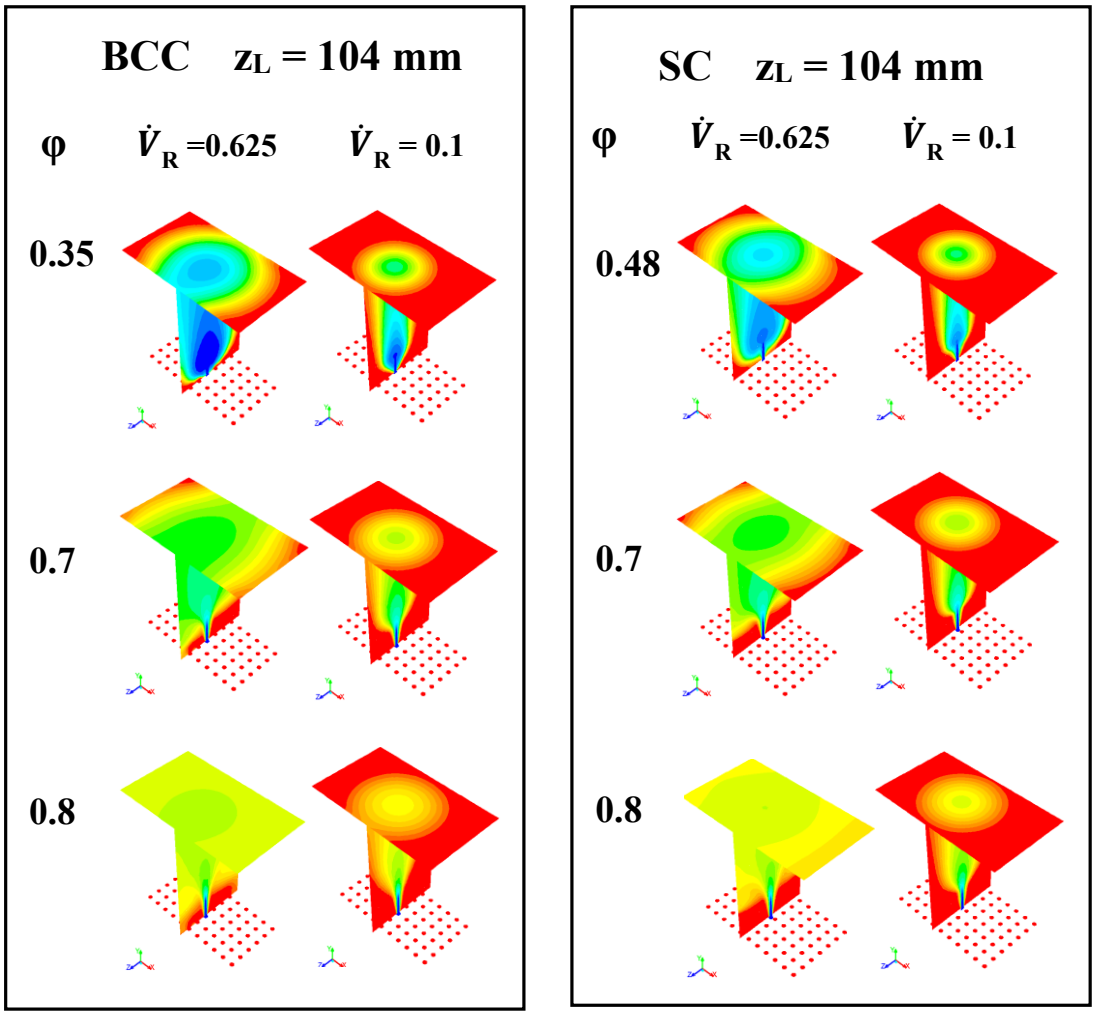

Figure 6.16: influence of the bed arrangement on the O_2 concentration for the BCC bed at two different $\dot{V}_R$ and four values of porosity, with d_L = 0.02 m

The simulation results of the SC bed with a porosity of 0.48 and the experiment data are compared in Figure 6.17. The deviation between the simulation results and the experimental data can be clearly seen at high $\dot{V}_R$. From the comparisons of the BCC and SC beds presented in Figures 6.15 and 6.17, it can be concluded that the mixing and the agreement between the results of the simulation and the experimental data are greatly influenced by the values of the volumetric flow rate ratio.

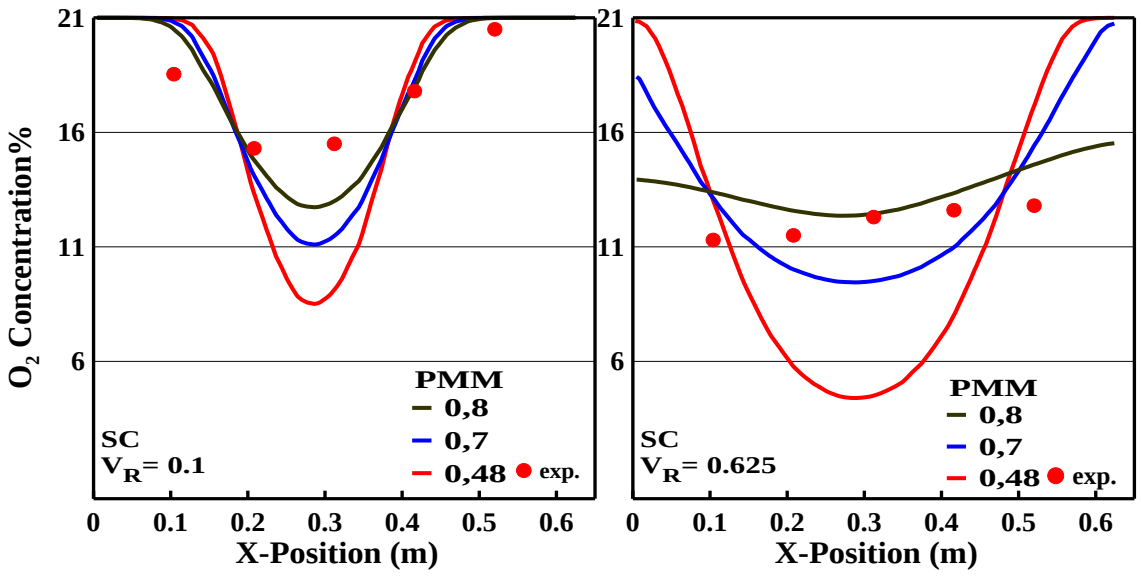

Figure 6.17: Validation of the PMM results with different porosities for the O_2 concentration and the experiments in the SC bed at two different $\dot{V}_R$, with x_L= 0.104 m and d_L = 0.02 m

6.4.3 Influence of the particle size and the porosity value

Figure 6.18 shows the combined influence of two parameters, porosity and particle size, on the O_2 concentration based on the contours of the O_2 concentration. Three values of the porosity (0.35, 0.5 and 0.7) and three particle sizes (4, 52, and 100 mm) are considered. The volumetric flow rate ratio $\dot{V}_R$= 0.1 is used. The mixing behavior for the three particle sizes is different at different porosities. For instance, at a porosity of 0.35, with small particles 4 mm in diameter, the nitrogen penetrates above and below the injection point at 0.104 m. For the other two beds, with particle sizes of 52 and 100 mm, the mixing starts from the injection point. The width of the jet remains constant for the bed of small particles, i.e., with d_P = 4 mm, irrespective of its porosity. On the other hand, the width of the jet increases with the increasing porosity of the beds composed of larger particles, i.e., with d_P = 452 mm and d_P = 100 mm.

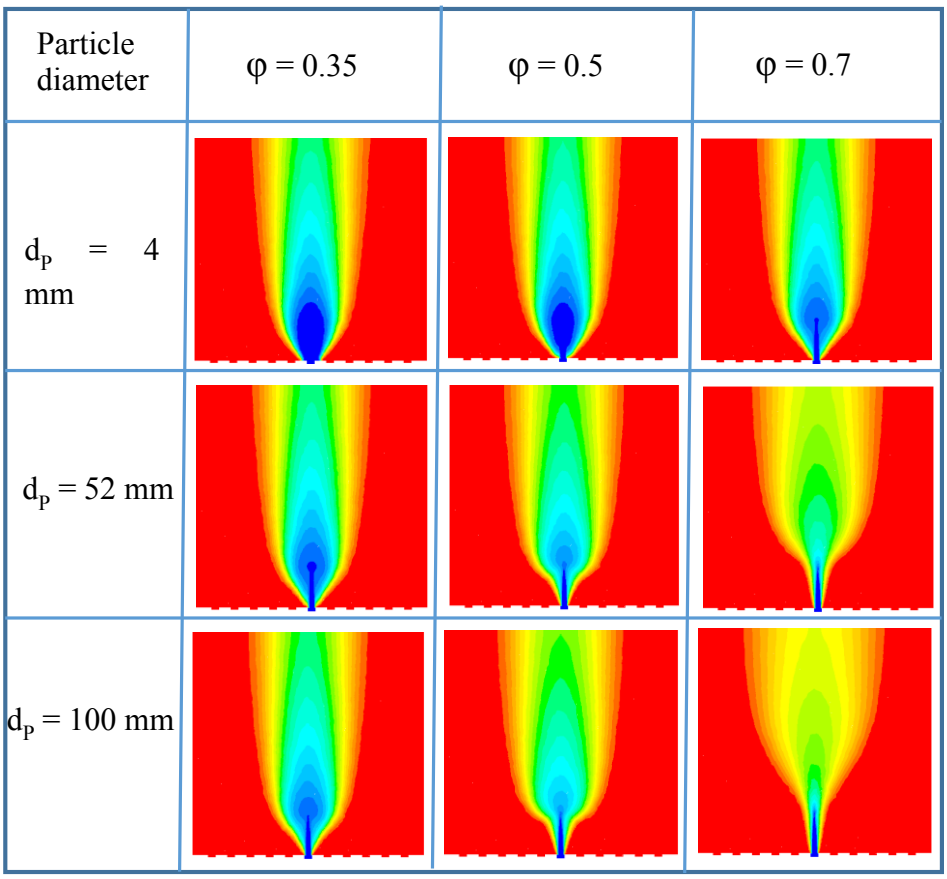

Figure 6.18: Influence of the bed particle size crossing with different bed porosities, with x_L= 0.104 m, d_L=0.02 m and $\dot{V}_R$= 0.1

6.4.4 PMM comparison with RPM

Figure 6.19 shows a comparison between the results of the PMM and those of the RPM with two contact point treatment methods: the gap and overlap methods. Structured beds with BCC and SC arrangements and porosities of 0.35 and 0.48, respectively, are used. The injection position z_L= 0.104 m and the lance diameter d_L=0.02 m were considered. The volumetric flow rate ratio was 0.1. The figure shows the results of the PMM as well as the experimental data compared to the results of the RPM with the gap and overlap method for the BCC bed. However, for the SC bed, there is a small deviation between the PMM and the RPM for both methods.

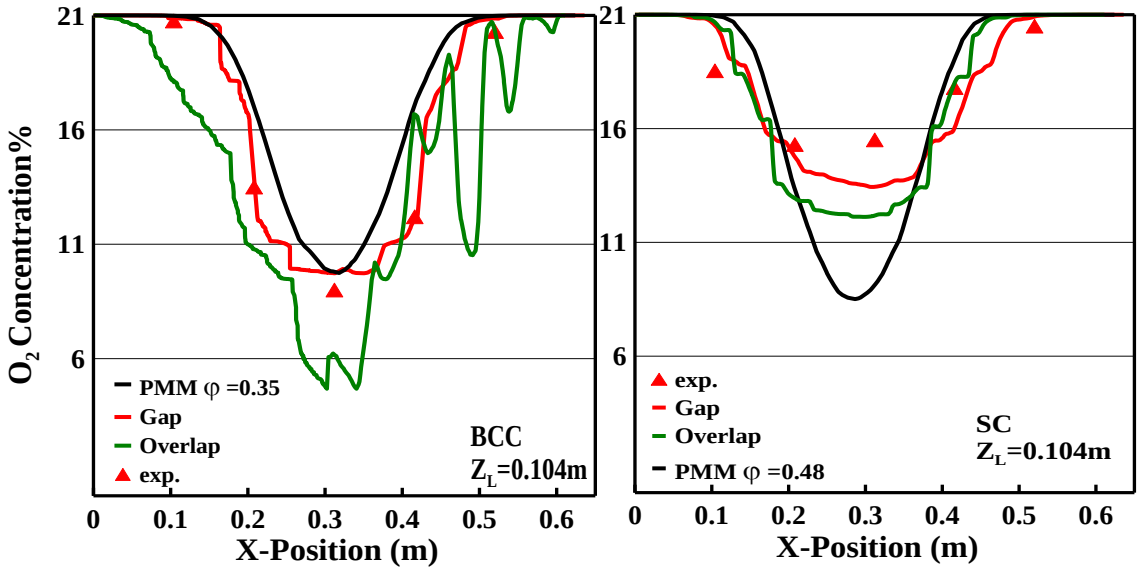

Figure 6.19: Effect of the contact point treatment in the RPM compared to the PMM at the same porosity, with $\dot{V}_R$ = 0.1, x_L= 0.104 m, and d_L = 0.02 m

6.5 Comparison between cross and parallel injection

A comparison between the results of the O_2 concentrations for cross flow and axial flow through the BCC bed with the two injection types is presented in Figure 6.20. In the cross flow, the lance was attached 100 mm away from the bottom. The injection position was at x_L= 0.260 m, whereas in the parallel flow, the injection position was at z_L = 0.104 m. The lance was inserted inside the bed 0.312 m away from the wall box.

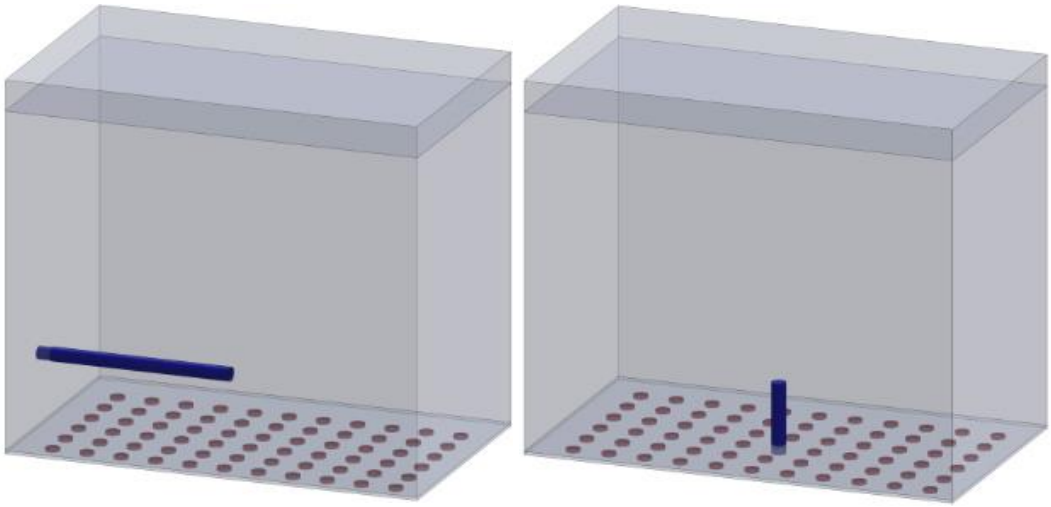

Figure 6.20: CFD domain of the PMM for two injection types: cross and axial

The PMM was used to obtain contour plots of the O_2 concentration for the two types of injection, as shown in Figure 6.21. Two different $\dot{V}_R$ values and the same porosity of 0.35 were used. It can be seen from the figure that the mixing behaviours between the two flows through the bed are different. The jet for the axial flow is slightly wider than the jet for the cross flow for both values of $\dot{V}_R$.

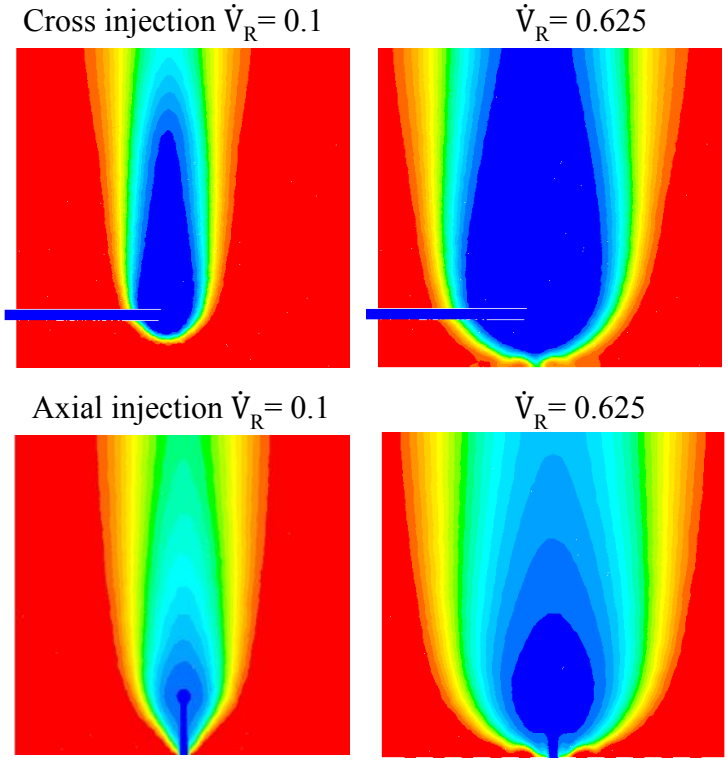

Figure 6.21: Contour plots of the O_2 concentration with two injection types: cross and axial

Figure 6.22 shows the O_2 concentration curves for the cross and axial flows. The volumetric flow rate ratios of 0.1 and 0.625 were used. For $\dot{V}_R$ = 0.625, the minimum O_2 concentration for the cross flow is zero, and that for the axial flow is approximately 3%.For $\dot{V}_R$ = 0.1, the minimum O_2 is approximately 2% for the cross flow, and that for the axial flow is approximately 10%

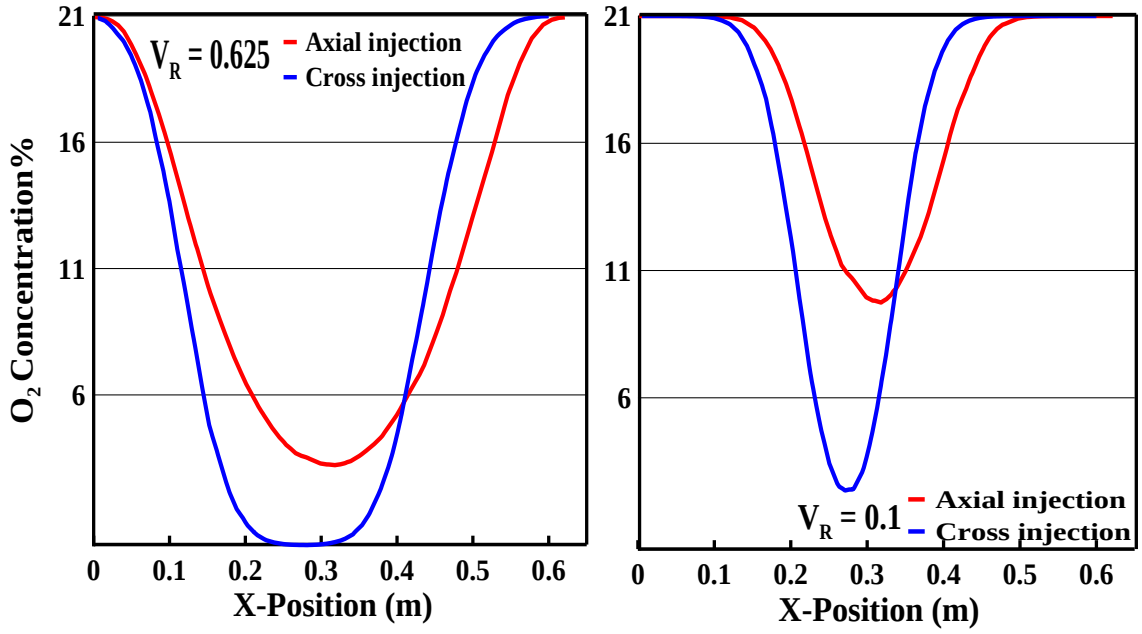

Figure 6.22: CFD results validating the experimental data for the cross flow and the axial flow in the BCC bed

7. Conclusion

The experimental work reveals that measurements the O_2 molar concentration are independent of both the height of the bed and the lance diameter. The shape of the jet curve of the O_2 molar concentration distribution is independent of the injection position. However, the injection position strongly influences the oxygen concentration profiles in the bed. Moreover, with increased volumetric flow rate ratio, the width of the jet (the distance between the first two side flat points, on the top of the curve) increases. The jet penetration and width of the jet only depend on the ratios of the two flows, not on their absolute values.

The CFD simulation employing the RPM can predict the radial and axial (cross and parallel) flow mixing in the structured packed bed using the O_2 molar concentration as a new method for data reporting. The model combined with the gap method generates results for the oxygen molar concentration that better agree with the experimental results. As the volumetric flow rate decreases, the agreement between the results of the CFD simulations and the experimental data is satisfactory. The simulation results show that the bridge method generates results for the pressure drop that agree with the results from Brauer's correlation for spherical particles. In addition, the results obtained using the overlap method are in better agreement with the PMM results at the same porosity but not with the experimental data. The CFD results of two injection types, i.e., radial and axial, are validated with the experiment data, and a better fit is found for the axial flow.

Simulations were also performed using the PMM to reduce the computational effort and time. The CFD results for the unstructured bed (small particles with a diameter of 4 mm) are in good agreement with the experimental data compared to those for large spheres in the structured bed at the same porosity. The results of the PMM for the structured bed (spheres with a diameter of 52 mm) with a cross flow revealed that the O_2 concentration is under-predicted for a porosity of 0.35. The PMM results of the O_2 concentration for the parallel flow are in good agreement with the experimental results, especially for low $\dot{V}_R$. In addition, it can be concluded that the width of the O_2 concentration for the PMM in the case of increasing porosity for small particles remains constant. Moreover, the width increases with increasing porosity for larger particles.

References

[1] Specht, E.:Wärme- und Stoffübertragung in der Thermoprozesstechnik.
Vulkan-Verlag, 2014.
[2] Internet sources: https://www.**maerz**.com/?lang=de
[3] Z. Xu, "Reduced model for flow simulation in the burner region of lime shaft kilns," Otto-von-Guericke-University Magdeburg, PhD thesis, 2010.
[4] Z.Y. Zhou, H.P. Zhu, A.B. Yu, B. Wright, P. Zulli, "Discrete particle simulation of gas–solid flow in a blast furnace," Computers & Chemical Engineering, Volume 32, Issue 8, pp. 1760–1772, 2008.
[5] T. Bluhm-Drenhaus and E.Simsek, "A coupled fluid dynamic-discrete element simulation of heat and mass transfer in a lime shaft kiln," Chemical Engineering Science, vol. 65, pp. 2821–2834, 2010.
[6] Anthony G. Dixon, Gregory Walls, Helen Stanness, Michiel Nijemeisland, E. Hugh Stitt, "Experimental validation of high Reynolds number CFD simulations of heat transfer in a pilot-scale fixed bed tube," Chemical Engineering Journal, Volumes 200–202, pp. 344–356, 2012.
[7] M.Rasul and D.Saotayanan, "Modeling and simulation of thermodynamic processes of vertical shaft kiln used for producing dead burned magnesia," International journal of energy and environment, vol. 1, pp. 37–44, 2007.
[8] M.J. Baker, G.R. Tabor, "Computational analysis of transitional air flow through packed columns of spheres using the finite volume technique," Computers & Chemical Engineering, Volume 34, Issue 6, pp. 878–885, 2010.
[9] H. P. A. Calis, J. Nijenhuis, B. C. Paikert, F. M. Dautzenberg, C. M. van den Bleek, "CFD modeling and experimental validation of pressure drop and flow profile in a novel structured catalytic reactor packing," Chemical Engineering Science, Vol. 56, pp. 1713–1720, 2001.
[10] Nihad Dukhan, Özer Bağcı, Mustafa Özdemir, "Experimental flow in various porous media and reconciliation of Forchheimer and Ergun relations," Experimental Thermal and Fluid Science, Vol. 57, pp. 425–433, 2014.
[11] Yi Xu, Li-Ping Wang, Yan-Qian Zhong, Yi-Hua Zheng, "Experimental research of fluid flow and effective thermal parameters in micro-particle packed bed as a thermal biosensor reactor under constant wall temperature conditions," Experimental Thermal and Fluid Science, Vol. 45, pp. 34–42, 2013.
[12] R. Srinivasan, B.N. Raghunandan, "Experiments on thermal response of low aspect ratio packed beds at high Reynolds numbers with varying inflow temperature," Experimental Thermal and Fluid Science, Vol. 44, pp. 323–333, 2013.
[13] A.H. Ahmadi Motlagh, S.H. Hashemabadi, "3D CFD simulation and experimental validation of particle-to-fluid heat transfer in a randomly packed bed of cylindrical particles," International Communications in Heat and Mass Transfer, Vol. 35, Issue 9, pp. 1183–1189, 2008.
[14] H. Freund, Thomas Zeiser, Florian Huber, Elias Klemm, Gunther Brenner, Franz Durst, Gerhard Emig, "Numerical simulations of single phase reacting flows in randomly packed fixed-bed reactors and experimental validation," Chemical Engineering Science, Vol. 58, Issues 3–6, pp. 903–910, 2003.
[15] T. Atmakidis and E. Kenig, "A numerical study on the residence time distribution in low and moderate tube/particle diameter ratio fixed bed reactor", Chemical Engineering Transactions, volume 18, pp. 581-586, 2009.
[16] A.G.Dixon and E.Taskin, "Cfd method to couple three-dimensional transport and reaction inside catalyst particles to the fixed bed flow field," Ind. Eng. Chem. Res, vol. 49, pp. 9012–9025, 2010.

[17] T.Eppinger and K.Seidler, "Dem-cfd simulations of fixed bed reactors with small tube to particle diameter ratios," Chemical Engineering Journal, vol. 116, pp. 324–331, 2011.
[18] A.G.Dixon and E.Taskin, "Systematic mesh development for 3d cfd simulation of fixed beds: Single sphere study," Computers and Chemical Engineering, vol. 35, pp. 1171–1185, 2011.
[19] H.Freund and J.Bauer, "Detailed simulation of transport processes in fixed-beds," Ind. Eng. Chem. Res., vol. 44, pp. 6423–6434, 2005.
[20] P.Gunjal and V. Vivek, "Computational study of single-phase flow in packed beds of spheres," AIChE Journal, vol. 51, pp. 365–378, 2005.
[21] Yuh Ferng and Kun-Yueh Lin, "Investigating effects of BCC and FCC arrangements on flow and heat transfer characteristics in pebbles through CFD methodology," Nuclear Engineering and Design, vol.258, pp. 66–75, 2013.
[22] Shanshan Bu, Jian Yang , Qingtai Dong, Qiuwang Wang, "Experimental study of flow transitions in structured packed beds of spheres with electrochemical technique," Experimental Thermal and Fluid Science, vol.60, pp. 106–114, 2015.
[23] Jian Yang, Qiuwang Wang , Min Zeng , Akira Nakayama, "Computational study of forced convective heat transfer in structured packed beds with spherical or ellipsoidal particles," Chemical Engineering Science, vol.65, pp. 726–738, 2010.
[24] P.Ward,Y.Hassan, E.Merzari,P.Fischer, "Direct Numerical simulation and linear stability analysis of the flow in a pebble bed," Proceedings of the ASME 2014 4th Joint US-European Fluids Engineering Division Summer Meeting FEDSM 2014 August 3–7, 2014, Chicago, Illinois, USA.
[25] M. Nijemeisland and A.G. Dixon, "CFD study of fluid flow and wall heat transfer in a fixed bed of spheres," AIChE Journal, vol. 50, pp. 906–921, 2004.
[26] S. Sachdev, S. Pareek, B. Mahadevan and A. Deshpande, "Modeling and Simulation of Single Phase Fluid Flow and Heat Transfer in Packed Beds,"
Excerpt from the Proceedings of the 2012 COMSOL Conference in Bangalore.
[27] Anthony G. Dixon, Michiel Nijemeisland, E. Hugh Stitt, "Systematic mesh development for 3D CFD simulation of fixed beds: Contact points study," Computers and Chemical Engineering, vol.48, pp. 135–153, 2013.
[28] K. Vollmari, T. Oschmann, S. Wirtz, H. Kruggel-Emden, "Pressure drop investigations in packings of arbitrary shaped particles," Powder Technology, vol.271, pp. 109–124, 2015.
[29] Michiel Nijemeisland, Anthony G Dixon, "Comparison of CFD simulations to experiment for convective heat transfer in a gas–solid fixed bed," Chemical Engineering Journal, vol. 82, Issues 1–3, pp. 231–246, 2001.[30] C.Wu and Y.Ferng, "Investigating the advantages and disadvantages of realistic approach and porous approach for closely packed pebbles in cfd simulation," Nuclear Engineering and Design, vol. 240, pp. 1151–1159, 2010.
[31] J. Lee and G. Park, "Numerical treatment of pebble contact in the flow and heat transfer analysis of a pebble bed reactor core," Nuclear Engineering and Design, vol. 237, pp. 2183–2196, 2007.
[32] F. Augiera and F. Idouxa, "Numerical simulations of transfer and transport properties inside packed beds of spherical particles," Chemical Engineering Science, vol. 65, pp. 1055–1064, 2010.
[33] H. Freunda and T. Zeiser, "Numerical simulations of single phase reacting flows in randomly packed fixed-bed reactors and experimental validation," Chemical Engineering Science, vol. 58, pp. 903–910, 2003.
[34] Y. A. Hassan, "Large eddy simulation in pebble bed gas cooled core reactors," Nuclear Engineering and Design, vol. 238, pp. 530–537, 2008.
[35] B.Eisfeld and K.Schnitzlein, "A new pseudo-continuous model for the fluid flow in packed beds," Chemical Engineering Science, vol. 60, pp. 4105– 4117, 2005.

[36] W. Van-Rooyen and D. Krueger, “Simulation and optimisation of gas storage tanks filled with heat sink,” Nuclear Engineering and Design, vol. 236, pp. 156–163, 2006.
[37] K. Vafai and C. Tien, “Boundary and inertia effects on flow and heat transfer in porous media,” Int. J. Heat Mass Transfer, vol. 24, pp. 195–203, 1981.
[38] A.Khaled and K.Vafai, “The role of porous media in modelling flow and heat transfer in biological tissues,” Int. J. Heat Mass Transfer, vol. 46, pp. 4989–5003, 2003.
[39] Jiang, P.X., Li,M., Ma,Y.C., Ren, Z.P., “Boundary conditions and wall effect for forced convection heat transfer in sintered porous plate channels,” Int. J. Heat Mass Transfer, vol. 47, pp. 2073–2083, 2004.
[40] J. Wu and B. Yu, “A resistance model for flow through porous media,” Trans Porous Med, vol. 71, pp. 331–343, 2008.
[41] J. Hellstrm and T. Lundstrm, “Flow through porous media at moderate Reynolds number,” International Scientific Colloquium, Modelling for Material Processing, June 8–9, 2006.
[42] H. Bai, J. Theuerkauf, and P. Gillis, “A Coupled DEM and CFD Simulation of Flow Field and Pressure Drop in Fixed Bed Reactor with Randomly Packed Catalyst Particles,” Industrial Engineering Chemical Research, vol. 48, pp. 4060–4074, 2009.
[43] Patankar, “numerical heat transfer and fluid flow,” McGRAW-HILL BOOK COMPANY, 1980.
[44] ANSYS, \ Ansys fluent 12.0, users guide, 2009.
[45] Pedras, M. H. J., de Lemos, M. J. S., “Macroscopic turbulence modeling for incompressible flow through undeformable porous media,” Int J Heat and Mass Transfer, vol. 44, pp. 1081–1093, 2001.
[46] M. Brauer. Grundlagen der Einphasen-und Mehrphasenstroemungen. Sauerlaender Verlag, Frankfurt, 1 edition, 1971.
[47] W. Guo and A. Ying, “Influence of 2d and 3d convection diffusion flow on tritium permeation in helium cooled solid breeder blanket units,” Fusion Engineering and Design, vol. 81, pp. 1465–1470, 2006.
[48] H. A. Jakobsen and H. Lindborg, “A numerical study of the interactions between viscous flow, transport and kinetics in fixed bed reactors,” Computers and Chemical Engineering, vol. 26, pp. 333–357, 2002.
[49] A. Corey, “Mechanics of Immiscible Fluids in Porous Media,” Water Resources Publications, 3 edition, 1994
[50] D.A. Nield and A. Bejan, “Convection in Porous Media,” Springer, 3 edition, 2005.

List of Publications

1. **A. Alkhalaf**, H. Woche, and E. Specht, “Experimental investigation of cross flow mixing in an unstructured bed”, Journal of Chemical Technology and Metallurgy, 51, 6, 2016, 639-648.

2. **A. Alkhalaf** and E. Specht, "Prediction of cross flow mixing in the structured packed bed through CFD simulation using (FBM and PMM) and validation with experiments". Engineering Applications of Computational Fluid Mechanics, 11, 1, 2017, 1–14

3. **Ali Alkhalaf**, H. A. Refaey, Nabeh Al-durobi, E. Specht, "CFD Simulation and Experimental Validation of Cross Flow Mixing in Body Center Cubic Packed Bed and Comparison with PMM". Accepted in the (Twelfth International Conference of Fluid Dynamics 19-20 December, 2016, Le Méridien Pyramids Hotel,Cairo,EGYPT)..

4. Specht, E.; Mohammadpour, K.; **Alkhalaf, A**.:Ermittlung der Flammenlänge von gasförmigen Brennstoffen in Schachtöfen.VDI-Berichte Nr. 267, 2015. VDI Verlag GmbH Düsseldorf, 291-299.(ISBN 978-3-18-092267-6).

Curriculum Vitae

Personal data

Name:	Ali Al-Khalaf
Date of Birth:	26.Feb.1964
Place of Birth:	Najaf, Iraq
Marital status:	Married
Nationality:	Iraqi

School Education

1970–1976	Primary School, Al Tedhia Primary School, Baghdad, Iraq.
1976–1979	Secondary School, Al Resala Secondary School, Baghdad, Iraq.
1979–1982	High School, Al Tameem High School, Baghdad, Iraq.

University Education

1982–1986	B.Sc. in Mechanical Engineering, UOT, Baghdad, Iraq.
1989–1992	M.Sc. in Power Generation, UOT, Baghdad, Iraq.
2013–2016	**PhD** student, Institute of Fluid Dynamics and Thermodynamics, Otto von Guericke University, Magdeburg, Germany.

Professional Occupation

1993-1998	Asst. Lecturer at Steam Plant Lab., Mech. Eng. Dept. UOT Baghdad, Iraq
1998-2001	Asst. Lecturer at Higher Institute of Mechanical Professions, Tripoli, Libya
2007-2012	Asst. Lecturer at Steam Plant Lab., Mech. Eng. Dept. UOT Baghdad, Iraq

Contact alialkhalaf64@yahoo.com
ali-mohammed.ridha@ovgu.de